Electronic Thesis and Dissertation Repository

11-30-2011 12:00 AM

Mechanistic Mixed-Mode Failure Criterion for Continuous Fiber-Polymer Composites

Thomas P. Bruce, *The University of Western Ontario*

Supervisor: Dr. Jeff T. Wood, *The University of Western Ontario*
A thesis submitted in partial fulfillment of the requirements for the Doctor of Philosophy degree in Mechanical and Materials Engineering
© Thomas P. Bruce 2011

Follow this and additional works at: https://ir.lib.uwo.ca/etd

Part of the Polymer and Organic Materials Commons

Mechanistic Mixed-Mode Failure Criterion for Continuous Fiber-Polymer Composites

(Spine title: Mechanistic Composite Failure Criterion)

(Thesis format: Monograph)

by

Thomas P. <u>Bruce</u>

Graduate Program in Mechanical and Materials Engineering

A thesis submitted in partial fulfillment
of the requirements for the degree of
Doctor of Philosophy

The School of Graduate and Postdoctoral Studies
The University of Western Ontario
London, Ontario, Canada

THE UNIVERSITY OF WESTERN ONTARIO
School of Graduate and Postdoctoral Studies

Certificate of Examination

Supervisor

_____
Dr. J. T. Wood

Examiners

_____
Dr. J. R. Dryden

_____
Dr. A.V. Singh

_____
Dr. A. Rizkalla

_____
Dr. J.R. Reeder

The thesis by

Thomas Philip <u>Bruce</u>

entitled:

Mechanistic Mixed-Mode Failure Criterion for Continuous Fiber-Polymer
Composites

is accepted in partial fulfillment of the
requirements for the degree of
Doctor of Philosophy

Date: <u>November 30, 2011</u>

_____
Chair of the Thesis Examination Board

ii

ABSTRACT

Design of continuous fiber-polymer (CFP) composite components with optimized and predictable energy dissipation requires a failure criterion able to predict the fracture energy of CFP composites for all mixed-mode loading conditions. Existing mixed-mode failure criteria are empirical and show poor correlation for a range of CFP composites. Therefore, a universally applicable criterion based on constituent material properties and operative failure mechanisms is required. A novel mechanistic failure criterion for CFP composites is proposed. The criterion considers resin fracture strength, hackle formation, interfacial debonding, the crack tip plastic zone and interply vs interyarn delamination. Experimental data obtained by mixed-mode testing of continuous fiber-polymer composites and evaluation of the properties of the associated polymer and reinforcement is used to support the criterion.

Keywords: Continuous Fiber-Polymer Composites, Mixed-Mode, Delamination, Failure Criterion, Critical Strain Energy Release Rate, Fibre/Matrix Bond

DEDICATION

I would like to dedicate the writing of this thesis to my grandfather, Thomas Bruce, who always encouraged me to strive toward higher education.

ACKNOWLEDGEMENTS

TABLE OF CONTENTS

LIST OF TABLES

LIST OF FIGURE

xi

xvi

LIST OF APPENDICES

LIST OF SYMBOLS

a	crack length
A	cross-section area of a filament
a_0	initial delamination length from support
B	rectangular specimen thickness
B_{cal}	calibration specimen width
C	compliance
c	distance from point of loading to midspan of mixed-mode fixture
C_{sys}	compliance of the loading system
d	fiber diameter
da	incremental change in fracture length
dC	incremental change in the material compliance
d_E	effective diameter
d_F	displacement at fracture
D_f	filament diameter
dP	incremental change in load
dU	incremental change in strain energy
dW	Incremental change in work
$d\delta$	incremental change in displacement
E	Young Modulus
E_{11}	Young's modulus in the longitudinal direction

E_{1f}	bending elastic modulus of the laminate in a fiber direction
E_{22}	Young's modulus in the transverse direction
E_b	specimen bending modulus
E_{cal}	calibration specimen modulus
E_f	fiber Young's modulus
F_f	ratio of fiber dedond length per unit crack length
$F_{f\text{-}IP}$	ratio of fiber dedond length for interply failure
$F_{f\text{-}IY}$	ratio of fiber dedond length for interyarn failure
F_r	ratio of resin debond length per unit crack length
$F_{r\text{-}IP}$	ratio of resin debond length for interply failure
$F_{r\text{-}IY}$	ratio of resin debond length for interyarn failure
G	strain energy release rate
G_C	critical strain energy release rate
G_f	fiber shear modulus
G_I	mode I strain energy release rate
G_{IC}	mode I critical strain energy release rate
G_{ic}	interfacial debonding energy
G_{II}	mode II strain energy release rate
G_{IIC}	mode II critical strain energy release rate
G_m	matrix shear modulus
h	specimen half thickness
H_f	hackle function: hackle angle as a function of mixed-mode loading

I	moment of inertia
K	stress intensity factor
K_C	critical stress intensity factor
K_I	mode I stress intensity factor
K_{IC}	mode I critical stress intensity factor
K_{II}	mode II stress intensity factor
K_{IIC}	mode II critical stress intensity factor
L	half-length of supported specimen length
L_c	critical transfer length
L_d	debond zone length
L_e	filament debond length
L_{Mi}	unit crack length of for mode I induced cleavage
L_{MM}	crack length of hackles as a function of principal stress angle
L_s	resin fracture length
L_u	unit fracture length
m	slope of the load-displacement plot of the calibration specimen
M	mode mixture - varies from 0 for pure mode I to 1 for pure mode II
m_{cal}	slope of calibration curve
M_t	mode mixture at which transition from interyarn to interply occurs
n	number of filaments embedded in a fiber fragmentation specimen
P	applied load
P_c	critical load

P_F	load at fracture
P_I	mode I loading component
P_{II}	mode II loading component
R	matrix radius
r	distance from crack tip to the point at which the stress is evaluated
r_f	fiber radius
r_p	plastic zone radius
t	specimen thickness
U	elastic strain energy
V_f	fiber volume fraction
W	energy for crack growth
Y_t	half yarn thickness
Γ_c	transverse modulus correction parameter
Γ_f	fiber fracture energy
δ	displacement
δ_c	critical displacement
ε_f	fiber strain to failure
θ	direction from crack tip to the point at which the stress is evaluated
θ_P	direction of the maximum principal stress
σ	applied normal stress
$\sigma_1, \sigma_2, \sigma_3$	principal stresses
σ_c	stress at the crack tip at which crack growth occurs

σ_f	Fiber fracture strength
σ_o	far field applied normal stress
σ_{tip}	normal stress at the crack tip
σ_x	normal stress in the x-direction at a point (r, θ) from the crack tip
σ_{xI}	mode I normal stress in the x-direction
σ_{xII}	mode II normal stress in the x-direction
σ_{ys}	Yield Strength
σ_y	normal stress in the y-direction at a point (r, θ) from the crack tip
σ_{yI}	mode I normal stress in the y-direction
σ_{yII}	mode II normal stress in the y-direction
τ_i	interfacial bond strength
τ_o	far field applied shear stress
τ_{xy}	shear stress at a point (r, θ) from the crack tip
τ_{xyI}	mode I shear stress
τ_{xyII}	mode I shear stress
υ	Poisson's ratio
Φ	ASTM 5045 calibration factor
χ	critical transfer length non-dimensional correction factor
χ_c	crack length correction parameter

1. INTRODUCTION

Continuous fiber polymer (CFP) composites constitute an important class of high strength, low weight materials. CFP composites are currently being utilized in blast resistant structures for which high toughness-to-weight materials are required. Studies related to design optimization of blast resistant structures constructed from CFP composites are limited. Many studies of CFP composite materials are driven by the aerospace industry, and relate to optimization of the material strength rather than its toughness. Additionally, blast resistant structures are subjected to mixed-mode loading conditions, while many traditional studies focus on either pure mode I or pure mode II loading cases.

Existing studies regarding the energy absorbing properties of CFP composites under mixed-mode loading sometimes propose failure criterion for these materials. An effective failure criterion would be an ideal predictive tool for the design of CFP composites with optimized energy absorbing properties. However, though many criteria have been proposed, they are universally empirical in nature, require extensive composite material fabrication and testing to evaluate empirical parameters, and have proven largely ineffective in predicting failure over a range of composite materials.

The goal of this research is to develop a non-empirical mixed-mode failure criterion for CFP composites. The criterion is to be mechanistic, founded on an understanding of the operative fracture mechanisms involved in material failure,

and requiring knowledge only of the reinforcement and matrix material properties related to fracture. Therefore, the criterion should be generally applicable to a broad range of CFP composites. The criterion is to be employed to design composite material structures that effectively absorb energy for a minimal weight. Design optimization will utilize finite element analysis, where the only input parameters are the related energy absorbing properties of the constituent materials.

Studies of the fracture of CFP composites under mixed-mode loading have shown that failure occurs predominantly through delamination. For these materials, the energy associated with delamination has been found to vary with the mixed-mode loading condition. In this study, the operative failure mechanisms involved in delamination were determined, characterized and quantified. As well, the material properties related to energy absorption during delamination were measured for a specific fiber-resin system. The insight and understanding achieved through these studies was employed to formulate expressions to predict the energy at which failure will occur through delamination of CFP composites under mixed-mode loading conditions. Predicted values were compared to experimental values to substantiate the model.

This research provides an important contribution to the scientific community by providing a fundamental and detailed understanding of the failure mechanisms involved in the fracture of CFP composite materials, and by proposing a non-

empirical failure criterion for these materials based on an application of this understanding.

The research presented here is separated into nine chapters. Chapter 2 provides a review of composite materials with particular attention to CFP composites; a quick overview of fracture mechanics; a summary of the process of delamination and a review of the specific failure mechanisms involved; and lastly a discussion on energy absorption with regards to delamination within CFP composites, with an emphasis on research activities in the field.

Chapter 3 provides a summary of the failure criterion proposed to date, and an evaluation of their relative merits. The framework for development of a mechanistic criterion is then presented.

Chapter 4 discusses results of the studies performed as part of this research on unidirectional (UD) composites. These studies are performed to determine the failure mechanisms that occur during delamination, and to evaluate which of these provide the principal contributions to the associated energy absorption. The experimental methods used are reviewed and the results from the testing are presented, and an interpretation of the results is given.

Chapter 5 discusses results of the studies performed as part of this research on fabric composites. These studies are conducted to characterize the failure

mechanisms involved in delamination of fabric composites that occur in addition to those observed in UD composites. The experimental methods employed are reviewed and the results from the testing are presented, and an interpretation of the results is given.

Chapter 6 presents results of the studies performed as part of this research on the material properties of polymers. Those material properties of the polymer determined by testing of UD and fabric composites to contribute significantly to the delamination energy absorption are characterized and measured. Experimental methods and test results are reviewed, and an interpretation of the results is given.

Chapter 7 presents results of the studies performed as part of this research on the interfacial properties of reinforcing fibers and polymers. Experimental methods available to determine these properties are reviewed. Test results are presented, and an interpretation of the results is given.

Chapter 8 proposes a mechanistic failure criterion based on the understanding and knowledge gained from this study. The methodology by which the criterion is derived is reviewed in detail. The criterion is used to predict failure of the UD composites tested in this study. Predicted values are compared to measured values determined experimentally for the UD composites to substantiate the validity, effectiveness, and accuracy of the model.

Finally chapter 9 summarizes the major insights gained through this research, the nature of the proposed failure criterion, and conclusions regarding the value and impact of the research finding, particularly in regards to the proposed failure criterion. A comparison is provided demonstrating the predictive capability of the proposed criterion to existing criteria.

2. LITERATURE REVIEW

This chapter begins with a brief overview of composite materials in general, and a detailed review of unidirectional and fabric CFP composites. A summary of the principles of material fracture is then provided. Next a description of delamination of laminated structures is given with an emphasis on the conditions necessary to induce delamination. Then a summary of studies conducted in regards to delamination and the associated energy absorption is presented.

2.1 Composite Materials

Composite materials are defined in their most general form as engineered materials consisting of two or more component materials, each with unique physical properties that remain distinct at a macroscopic level in the finished material. Every composite consists of a reinforcement and a matrix component. The matrix component acts to physically constrain the reinforcement component. The reinforcement component provides a desirable functional property. The two components function together to result in a material with properties that cannot be achieved with either component alone. A wide range of material properties can be achieved by altering the matrix and reinforcement components [1]. Composites may be orthotropic, as when the reinforcement is symmetric and well dispersed, or highly anisotropic, as when aligned fibers are used as the reinforcement [1].

Fiber reinforced polymer composites utilize fibers as the reinforcing material because of the very high strength and stiffiness of many fibers along the fiber direction. Fibers are materials consisting of continuous elongated structures. Fibrous materials include individual filaments or strands of a material, such as steel wire. Fibrous materials also include products produced by mechanically interlocking filaments together, by methods such as twisting, weaving and braiding. These products are referred to as threads, tows, yarns, ropes and cables, depending on the materials used and industrial application [2]. The mechanical interlocking of filaments is advantageous as the product often possesses properties superior to the constituent filament properties. Additionally, increased fiber length and width can be attained, providing for a broader range of engineering applications [2].

Fiber composites are typically classified as short fiber or continuous fiber composites. The term short fiber composite is applied to those composites produced by using randomly arranged short fibers, often referred to as chopped fiber. Short fiber composites are relatively inexpensive when compared to continuous fiber composites, and therefore are typically selected when the mechanical property requirements are not high, and cost is a significant engineering factor [3].

Continuous fiber composites use aligned continuous fibers as the reinforcement material. Continuous fiber composites preserve the mechanical properties of the fibers more effectively than short fiber composites and are typically stronger and

stiffer. Continuous fiber composites became popular with the advent of fiberglass. Glass fiber is employed in approximately 95% of manufactured composite structures [4]. Other common fibers used in continuous reinforced polymer composites are carbon fibers and polymer fibers [5].

Use of a polymeric matrix is often employed with a fiberous reinforcement as polymers are light weight and possess the capacity in their liquid state to mold around the fibers. This provides effective surface coverage to the fibers, ensuring strong adhesion between the matrix and reinforcement [3]. Termed continuous fiber polymer (CFP) composites, they are commonly employed when high strength and stiffness to weight is required [1]. Both thermoset and thermoplastic polymers are used as matrix materials in CFP composites [3]. Epoxy is commonly selected when high temperature performance, good price-to-performance ratio, availability, manufacturability and dimensional stability are required. Epoxies however require elevated temperatures to cure, resulting in higher manufacturing costs when compared to resin systems that can cure at room temperatures [3].

A CFP composite can be regarded as consisting of multiple levels of structure, ascending from individual fiber filaments, to bundles of fibers embedded in resin, to layers of aligned fibers with resin rich layers between them. Figure 2.1.1 schematically illustrates the various levels of structure with a typical CFP composite. Filaments are aligned into tows, or twisted into yarns. Tows and yarns are then either aligned into 2-dimensional sheets, known as unidirectional

(UD) cloth or tape, or woven together into fabrics. Each layer of arranged fibers constitutes a ply. A CFP composite is constructed by the stacking together of multiple plies to produce a laminated structure. Plies are also frequently referred to lamina, and a composite as a laminate [1].
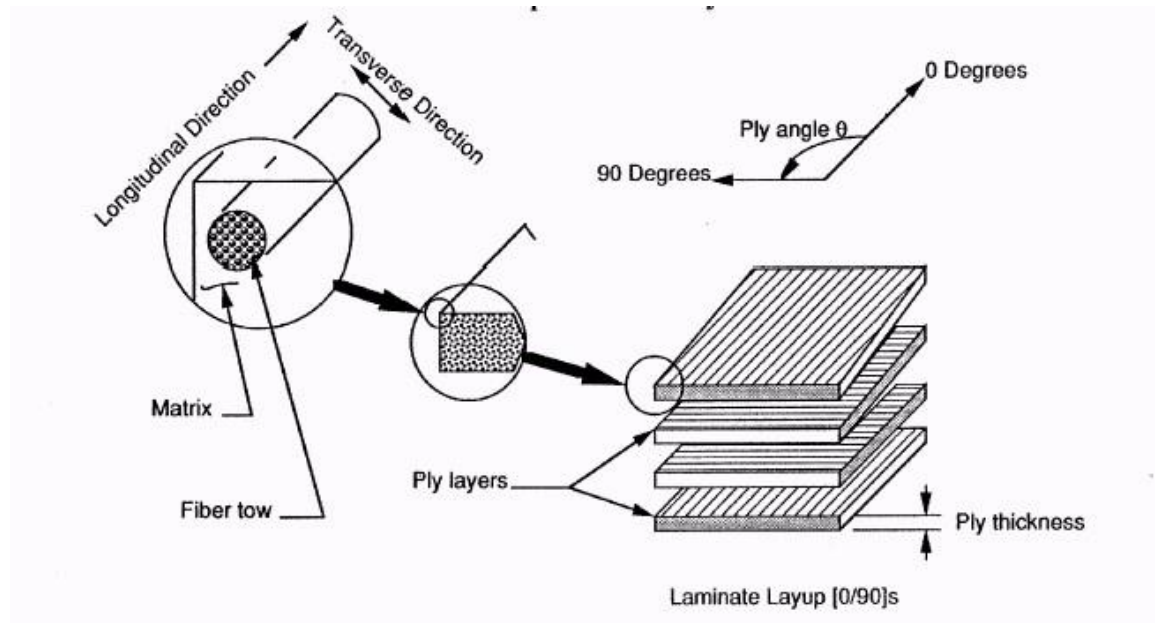
Figure 2.1.1: Levels of structure within a typical fiber-polymer composite (0/90 UD composite shown).

UD plies can be all arranged in the same direction to produce a highly anisotropic material. This construction technique is commonly employed when high strength and stiffness properties are required in a material in only one direction, such as in the aerospace industry. A UD laminate may also be constructed by alternating UD plies at some angle to each other. Lay-ups of 0°/90°, 0°/ 90°/-45°/45°, and 0°/60°/120° are commonly selected. Alternating layers results in a blending of the fiber mechanical properties throughout the composite. Alternating

unidirectional composites are commonly employed when consistent mechanical properties are required which are higher than those that can be achieved with short fiber composites [1].

Woven fabrics are produced by weaving a yarn, known as the weft yarn, across a pre-arranged set of parallel yarns, known as the warp yarns. The direction parallel to the warp yarns is known as the warp direction, and the direction parallel to the weft yarn is known as the weft direction. A typical woven fabric is shown in Figure 2.1.2. Fabrics can be woven into a large variety of weave patterns, each possessing unique characteristics, increasing the range of manufacturing options. Typical weaves, and the unit cell associated with different weave patterns, is shown in Figure 2.1.3.
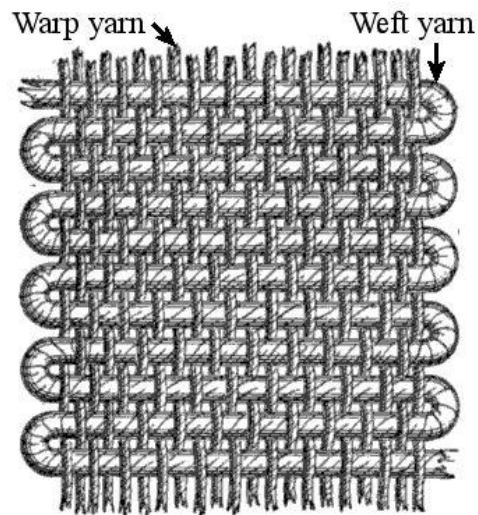
Figure 2.1.2:   Construction of a typical woven fabric.
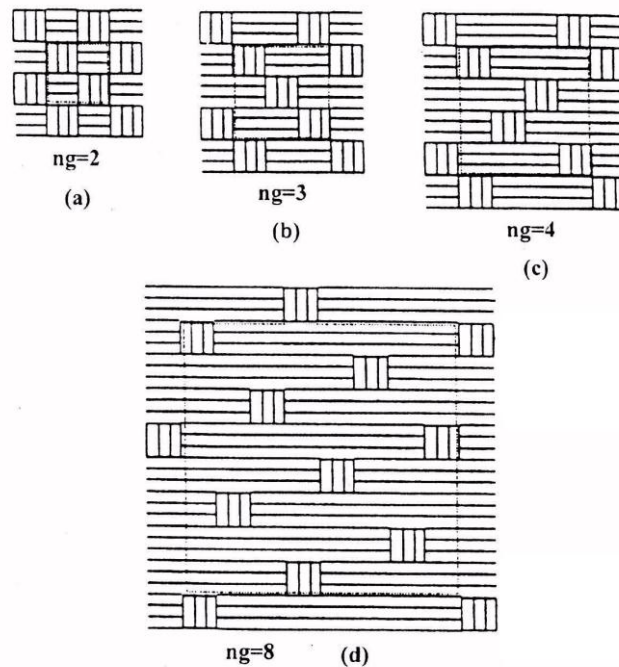
Figure 2.1.3: Woven fabrics; (a) plain weave; (b) twill weave; (c) 4-harness satin weave; (d) 8 harness satin weave. ng is the weave index, which characterizes the number of warp yarns in the repeat structure.

Woven fabrics are commonly used in the military, boating and automotive industries and have largely displaced the use of alternating UD cloths because of their superior manufacturability characteristics. Fabrics can be positioned by hand or machine, and worked without the presence of resin to hold the fibers position with respect to other fibers, unlike UD cloths. Fabrics drape over contoured surfaces better than UD cloths, permitting them to be molded into complex contours without the occurrence of bunching or wrinkling. Therefore more complex shapes can be produced, and more cost effective manufacturing techniques can be used [3].

2.2 Fracture of Materials

Fracture is defined as the separation of a material into sections as a result of the failure strength of the material being exceeded [6]. Fracture occurs through crack growth, involving both crack initiation and crack propagation. The ability of a material to resist fracture is described by the toughness of the material. Toughness is defined as the amount of energy per unit volume absorbed by a material to induce fracture [7]. Fracture may occur in either a ductile or in a brittle manner. Ductile fracture involves plastic deformation in the material during crack growth. Ductile materials are tough as energy is required to plastically deform the material. Brittle fracture is characterized by the lack of plastic deformation in the material during crack growth, and therefore brittle materials are typically not tough [8]. Expressions developed to describe fracture typically assume the existence of a crack and describe propagation of the crack. Testing designed to measure the toughness of a material typically involve introducing a pre-existing crack or opening into the test specimen to act as a crack initiator.

CFP composites are often composed of two brittle components. Many commercial fibers and thermosetting polymers are quite brittle. However, the resulting composite typically exhibits toughness much greater than the reinforcement and matrix. The toughness of CFP composites often exceeds that of many toughened metals on a per weight basis [1]. When the components materials of a composite are brittle, mechanisms of energy dissipation other than ductility must occur to account for the relatively high toughness [1]. The significant energy dissipating mechanisms in a CFP composite are fiber pullout

and delamination. Fiber pullout occurs when composites experience pure tension. Delamination is more common when bending loads are applied [9]. Pullout involves fiber-resin interfacial debonding and frictional sliding, while delamination involves fiber-resin interfacial debonding and ply separation. Though fiber-resin interfacial debonding is not in itself a significant contributor to energy dissipation, the occurrence of interfacial debonding is essential for delamination and fiber pullout [1].

2.2.1 Critical Strain Energy Release Rate

A.A. Griffith performed significant early studies on the nature of brittle fracture [8,10]. He determined that crack growth occurred only when both the failure strength of the material is exceeded, and sufficient energy has been introduced into the material. Griffith noted that there is necessarily surface energy associated with the creation of the surfaces resulting from crack growth, and that a critical amount of energy would be required to be introduced into the crack tip to provide for this surface energy. Griffith determined that the source of the energy is the elastic strain energy introduced to the material as a result of an applied load [6].

Griffith stated that crack growth can occur for brittle materials when the energy consumed by the corresponding surface creation is exceeded by the elastic strain energy (or work) introduced into the material. The Griffith fracture criterion is expressed as [6]:

$$\frac{dU}{da} = \frac{dW}{da} \qquad\qquad (2.2.1)$$

Strain energy is introduced into the material through an applied load, or through performing work on the material. When the introduced strain energy is equal to the energy required for crack growth for that material, crack propagation can occur. The value of the energy required per unit length of crack growth, dW/da, is a constant. The term dU/da per unit thickness is frequently referred to as the Strain Energy Release Rate (SERR), denoted G. Therefore a unique value of the change in elastic strain energy with respect to crack length will correspond to the onset of crack growth. This value is frequently referred to as the Critical Strain Energy Release Rate (CSERR), and is denoted G_c. The CSERR has a unique value for a given material under a specific mode of loading, and represents the capacity of the material to resist crack growth [6]. This is illustrated in Figure 2.2.1.
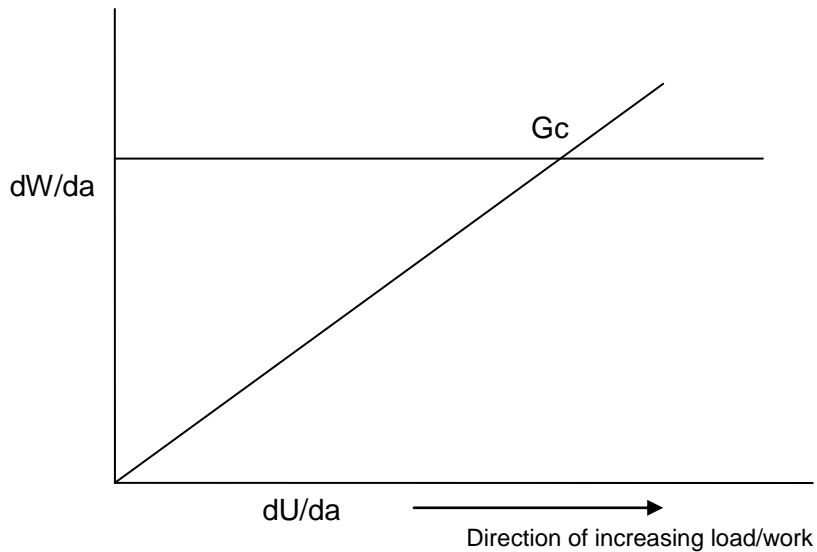
Figure 2.2.1: The critical strain energy release rate, G_c, corresponds to the strain energy release rate, dU/da, that is equal to the energy required for crack growth, dW/da, per unit length of crack growth.

The concept of CSERR can be illustrated by an example. Consider the case of a specimen with an existing crack oriented perpendicular to an applied load. For a load applied at a constant displacement rate, the material is constrained from deforming in the event of crack growth. With increasing displacement, the load increases linearly, as shown in segment A-B of Figure 2.2.2. Once the applied load is large enough to induce a stress at the crack tip that exceeds the material failure strength and the introduced strain energy exceeds that required for crack growth, the crack increases in length. As the displacement remains fixed for the constrained specimen at the moment of cracking, the load drops due to the lengthening of the crack and the resulting decrease in the material compliance. In Figure 2.2.2, crack growth initiates at point B and terminates at point C. The

modulus of the specimen decreases from the slope of the segment A-B to the slope of the segment A-C. The area A-B-D in Figure 2.2.2 corresponds to the amount of elastic strain energy introduced into the material when crack growth occurred, and is referred to as the Work of Fracture. Area A-B-C corresponds to the decrease in elastic strain energy resulting from extension of the crack and is therefore also the amount of energy consumed by the corresponding surface creation. This energy per unit length of crack growth is a measure of the CSERR [6].
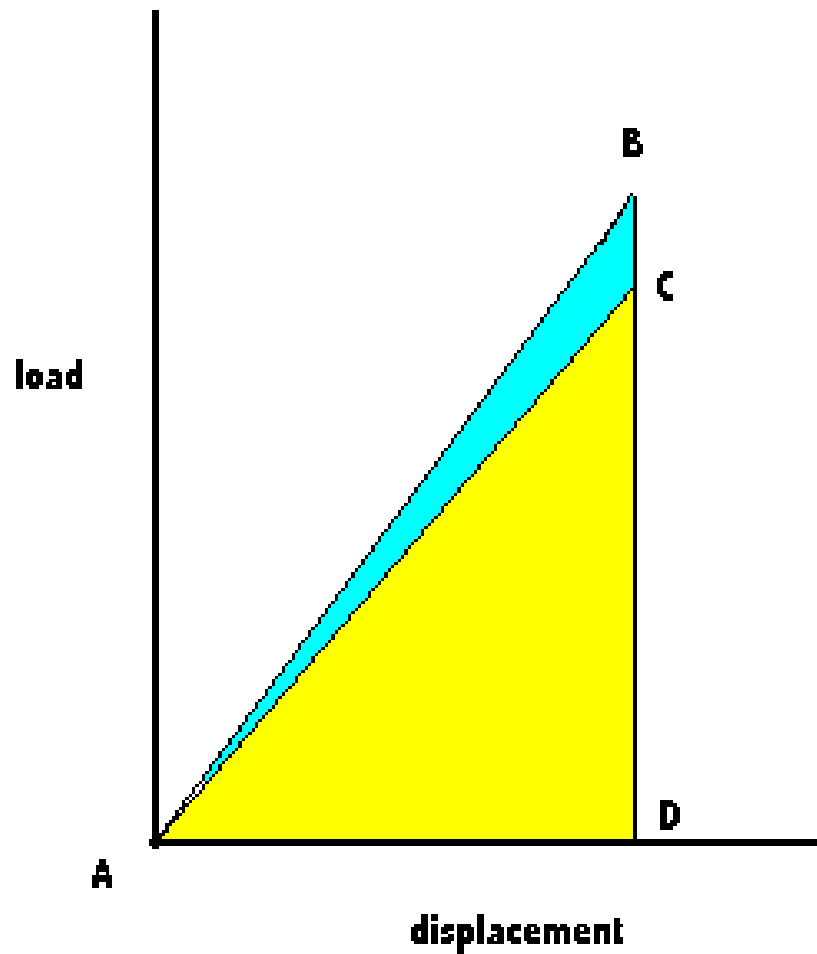
Figure 2.2.2: Load-displacement curve of a typical constrained material.

The CSERR is a constant for a given material. However, this value is unique for each mode of loading. Growth of a crack may occur through three modes of loading, or through a combination of these. These are Mode I (opening), Mode II (in-plane shear) and Mode III (out-of-plane shear, or tearing), as illustrated in Figure 2.2.3. Mixed-mode loading occurs when more than one mode of loading occurs simultaneously. There is a unique CSERR associated with each possible combination of mixed-mode loading [6].

Mode I:
Opening

Mode II:
In-plane shear

Mode III:
Out-of-plane shear
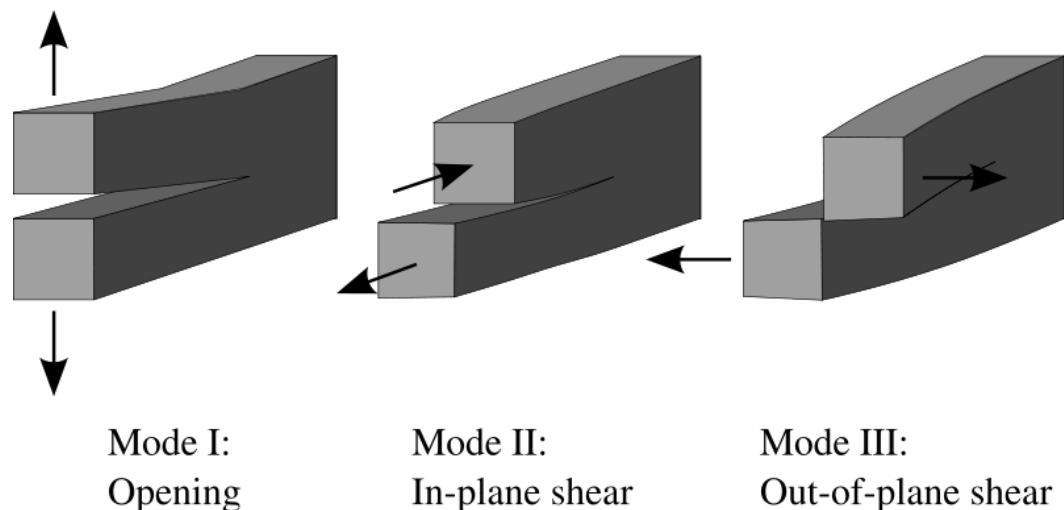
Figure 2.2.3: The three modes of loading.

2.2.2 Crack Tip Plastic Zone

Griffith assumed the case of a perfectly brittle material. However, all real materials will experience some degree of plasticity at the crack tip [10]. G.R. Irwin [7.11] developed Linear Elastic Fracture Mechanics (LEFM) to describe crack growth for the case where the deformation of the material is predominantly

linear elastic, and for which plastic behaviour is limited to the crack tip. H.M. Westergaard [12] developed a function from which can be derived an expression that provides the state of stress at the tip of a crack for a material that experiences limited plastic deformation. The general form of the expression is [6]:

$$\sigma_{tip} = \frac{Kf(\theta)}{\sqrt{2\pi r}}$$

(2.2.2)

For the case where $\theta=0$, the equation simplifies to [6]:

$$\sigma_{tip} = \frac{K}{\sqrt{2\pi r}}$$

(2.2.3)

The Stress Intensity Factor, K, is related to the Strain Energy Release Rate, G, each a measure of the capacity of a material to resist fracture. The former term relates to stress, while the latter term relates to energy. The critical value for K at which crack growth occurs is denoted K_C. The value of the stress at the crack tip at which crack growth occurs is called the critical stress and is denoted σ_C. Re-arrangement of Equation 2.2.3 in terms of the size of the plastic zone, r_p, and with the critical values for σ_{tip} and K substituted yields [6]:

$$r_p = \frac{K_c^2}{2\pi\sigma_c^2}$$

(2.2.4)

Plastic yielding at the crack tip dictates that the maximum stress that can occur at the crack tip under plane stress conditions (ignoring work hardening) is the yield strength of the material. Plane stress conditions, typical for thin cross-sections, exist when a material strained in one direction is able to contract or expand in other directions, with no resulting residual stresses. For plane strain conditions the maximum stress at the crack tip can exceed the material yield strength by as much as three times the yield strength. Plane strain conditions, typical for thicker cross-sections, exist when the material is unable to contract or expand in out-of-plane loading directions. The additional material behaves to constrain surrounding material in the thickness direction and a tri-axial stress state results. The stress field and the extent of the plastic zone at and near the crack tip are shown in Figure 2.2.4 for plane stress and plane strain conditions. The plastic zone associated with plane strain is less than that associated with plane stress [6].
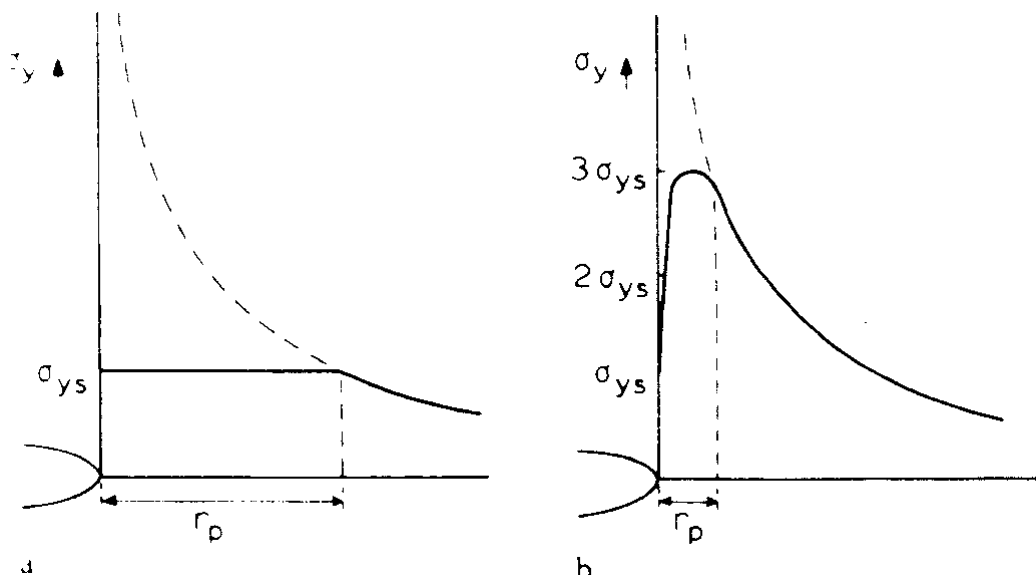
Figure 2.2.4: Stress field and plastic zone at crack tip for; (a) plane stress; (b) plane strain (6).

As the stress at the crack tip is limited to the yield strength of the material for plane stress conditions and to approximately three times the yield strength for plane strain conditions, values for the maximum plastic zone radius can be given for plane stress and plane strain conditions [6]:

$$r_p = \frac{K_c^{\,2}}{2\pi\sigma_{ys}^2} \qquad \text{(plane stress)} \qquad\qquad (2.2.5)$$

$$r_p = \frac{K_c^{\,2}}{18\pi\sigma_{ys}^2} \qquad \text{(plane strain-ideal)} \qquad\qquad (2.2.6)$$

In practice, plane strain conditions cannot exist across the full width of a material due to the plane stress conditions at the surface and a transition region to plane strain; the numerical denominator in Equation 2.2.6 has been experimentally determined to be closer to 6 rather than 18 [6].

The shape and extent of the plastic zone occurring at a crack tip varies with the stress condition and loading mode. The profile of the plastic zone can be assessed by considering equation 2.2.2 and Von Mises material failure criterion. For an isotropic and homogenous material, Figure 2.2.5 illustrates the plastic zone shape at the crack tip for mode I and mode II loading under plane stress and plane strain conditions [6].

<center>(a)   (b)</center>
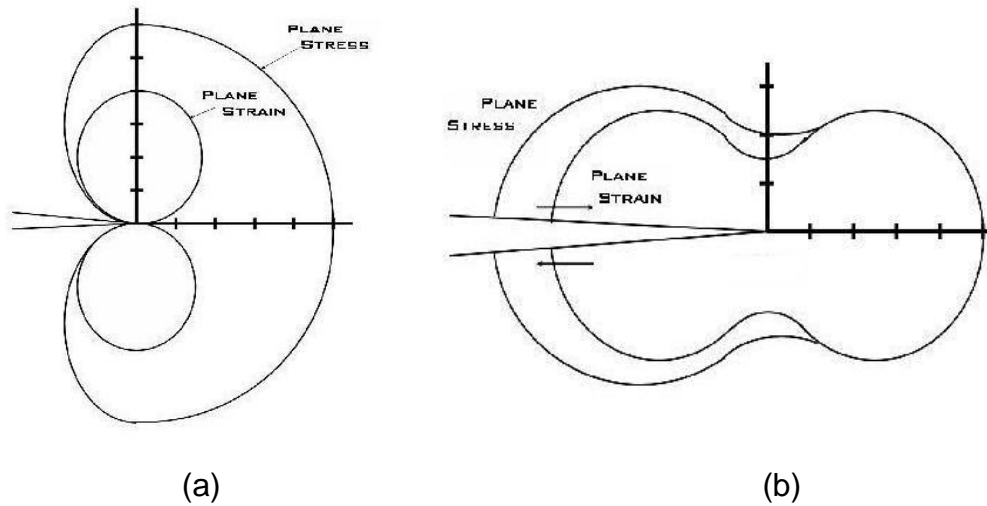
Figure 2.2.5: Shape and relative size of crack tip plastic zone for plane stress and plane strain conditions; (a) for mode I loading; (b) for mode II loading [6].

2.3 Delamination

Crack growth within a homogeneous material typically results in propagation of the crack perpendicular to the applied load direction. However, when loading results in cracking within laminated structures, the crack direction is frequently constrained by the reinforcing material. Consequently, the fracture path will occur between plies. This type of fracture is known as delamination [6], and is defined as the propagation of a crack within a laminated structure resulting in separation of adjacent plies. It may occur in any material that possesses a laminated structure, including some metals, wood and fiber-polymer composites. The principle of delamination is illustrated in Figure 2.3.1.
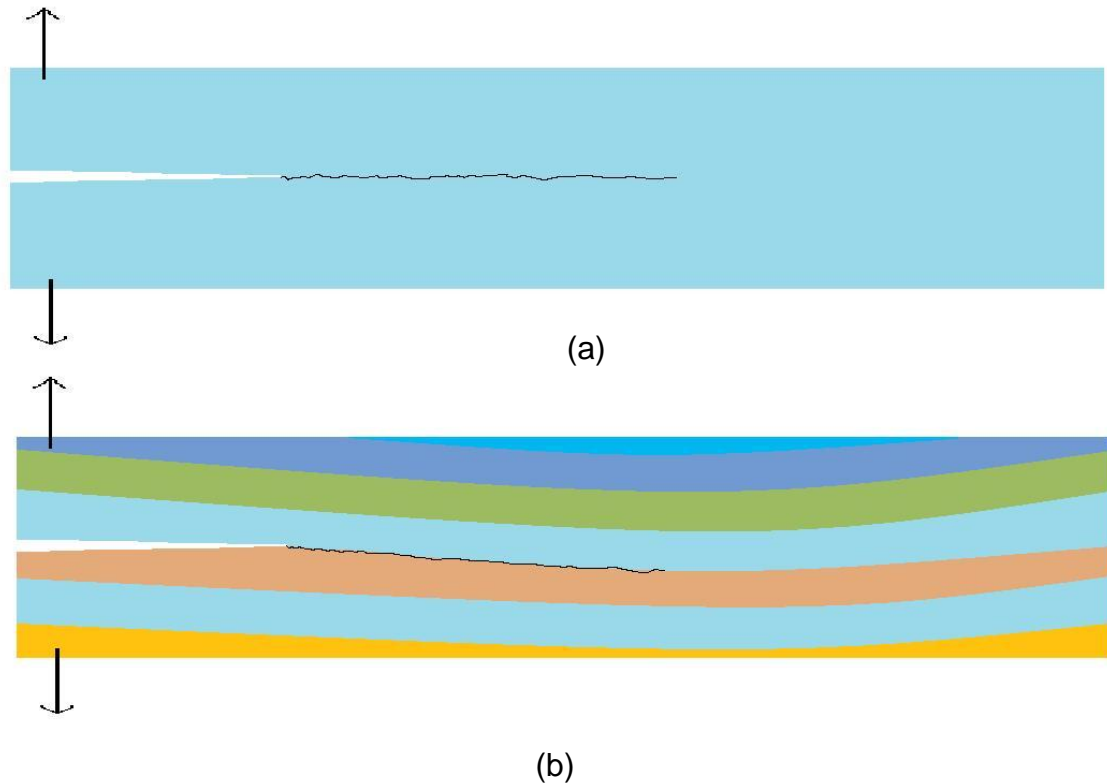
Figure 2.3.1: (a) Fracture growth in an isotropic homogeneous material; (b) constrained fracture growth in a laminated material (delamination).

For isotropic materials, only the mode I CSERR is typically studied in detail, as this value is often lower than the mode II or III CSERR's [13]. Therefore, regardless of the mode of loading that induces a fracture in an isotropic material, the fracture typically transitions and propagates in mode I. It is important to distinguish between loading mode and fracture mode. A single fracture mode may dominate over a wide range of loading conditions.

In CFP composites, the mode II CSERR is also typically larger than the mode I value [13]. However, delamination of CFP composites is typically studied under both mode I and mode II loading conditions. The constraints imposed on crack

growth by the geometry of the material provide that crack growth will not necessarily transition to mode I. Similar to isotropic materials, the mode III CSERR of CFP composites is typically neglected as the mode III component of loading is small for most engineering applications, while the mode III CSERR is typically large [14]. Therefore, for delamination through CFP composite, the CSERR for mode I, mode II and ratio's of these is of interest.

Delamination of fiber-polymer composites may occur through a number of failure mechanisms [15]. Fracture may proceed through the resin rich layer between plies as shown in Figure 2.3.2(a), referred to as resin fracture. Fracture may occur along the resin-fiber interface between plies as shown in Figure 2.3.2(b), and is known as interply failure or interlaminar failure. Fracture may also proceed within a ply as shown in Figure 2.3.2(c), and is known as interyarn failure or intralaminar failure. Fracture may also occur through a combination of these failure mechanisms. Each failure mechanism will have a unique CSERR, influenced by the properties of the composite's constituent materials [16]. For CFP composites, the CSERR typically increases with increasing toughness of the matrix and increasing strength of the fiber-matrix bond [10].
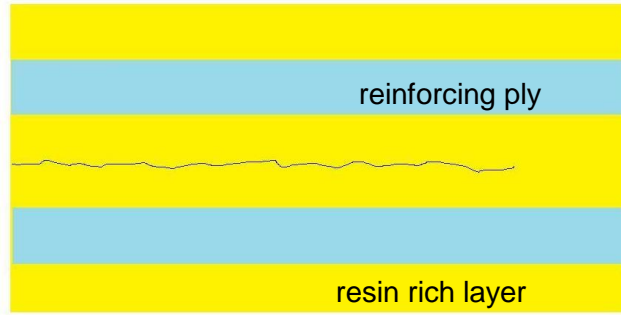
(a)
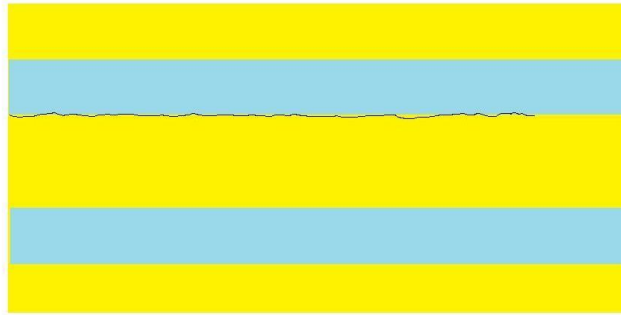
(b)
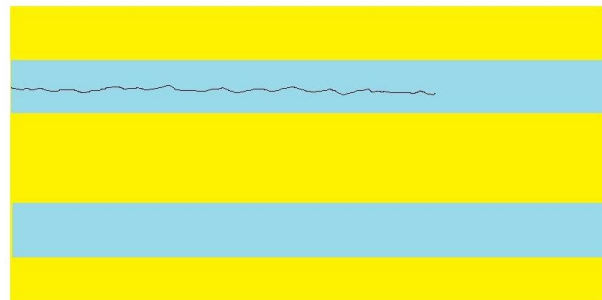
(c)

Figure 2.3.2: Delamination occurring through the three possible failure mechanisms; (a) resin fracture; (b) interply; (c) interyarn.

2.3.1 Fiber-Matrix Debonding

Delamination is the dominant energy absorbing mechanism during failure of laminated structures subjected to through-thickness forces, such as bending, impact and mixed-mode loading [17]. Though the reinforcing fiber and polymer matrix of CFP composites are typically relatively brittle materials and possess comparatively low energy absorbing properties, delamination of CFP composites can absorb significant amounts of energy as a result of extensive surface creation [3]. This occurs by separation of adjacent plies through interfacial debonding and resin fracture [1]. Delamination differs from interfacial debonding in that debonding occurs along a specific fiber, while delamination involves extensive debonding along an entire ply [18].

Delamination occurs through a process called crack tip blunting and crack deflection. Crack tip blunting and deflection can be understood by considering the case of two materials with unique mechanical properties, A and B, bonded along a common interface, C, with a pre-existing crack in material A, as shown in Figure 2.3.3(a). For the axial loading condition shown there exists an axial stress and a transverse stress at the crack tip, as shown in Figure 2.3.3(b). The magnitude of the transverse stress will be approximately 20% of the axial stress [1]. When loading is sufficient to produce an axial stress that exceeds the fracture strength of material A, the crack will grow toward the interface. Once the crack intersects with the interface, the crack will either be halted by the interface, as shown in figure 2.3.3(c), penetrate into material B as shown in Figure 2.3.3(d), or be blunted by the interface as shown in Figure 2.3.3(e).

Halting of the crack will occur if the fracture strength of material B is greater than that of material A and the strength of the bond along the interface between materials A and B, referred to as the interfacial bond strength, is greater than the transverse stress at the crack tip. Penetration will occur if the interfacial bond strength exceeds the transverse stress at the crack tip and the fracture strength of material B is less than that of material A. Blunting will occur when the transverse stress at the crack tip exceeds the interfacial bond strength. With further loading, the blunted crack grows along the interface, as shown in Figure 2.3.3.(f), resulting in delamination. This process is referred to as crack tip blunting and crack deflection [1].

(a)

Transverse Stress

Axial Stress

(b)

(c)

(d)

(e)

(f)
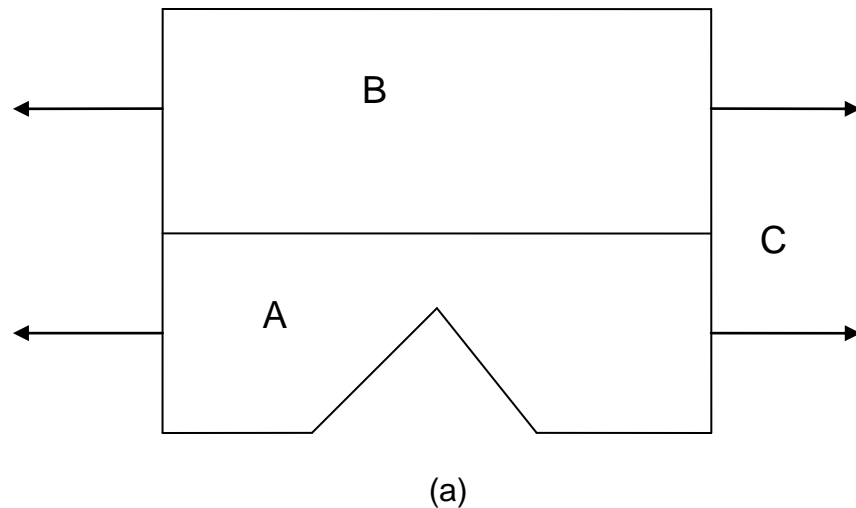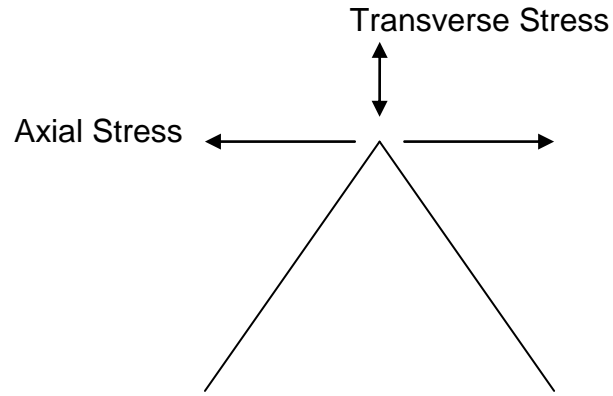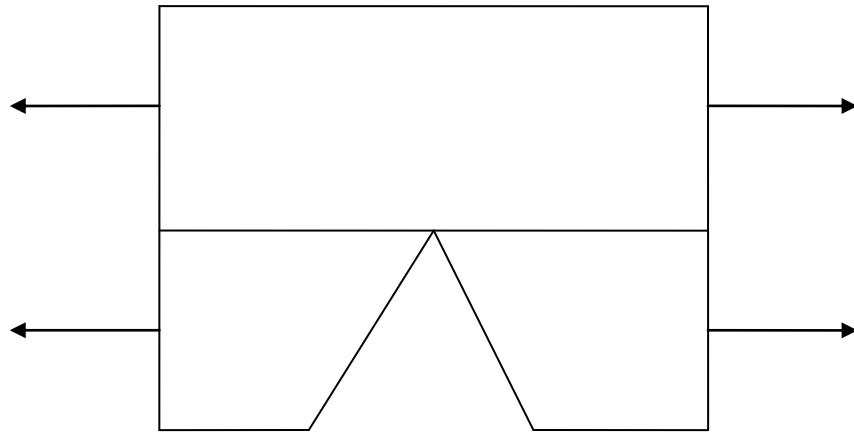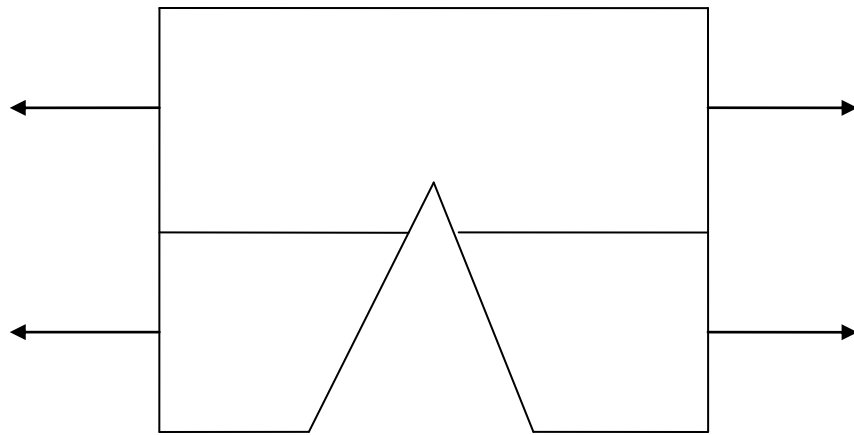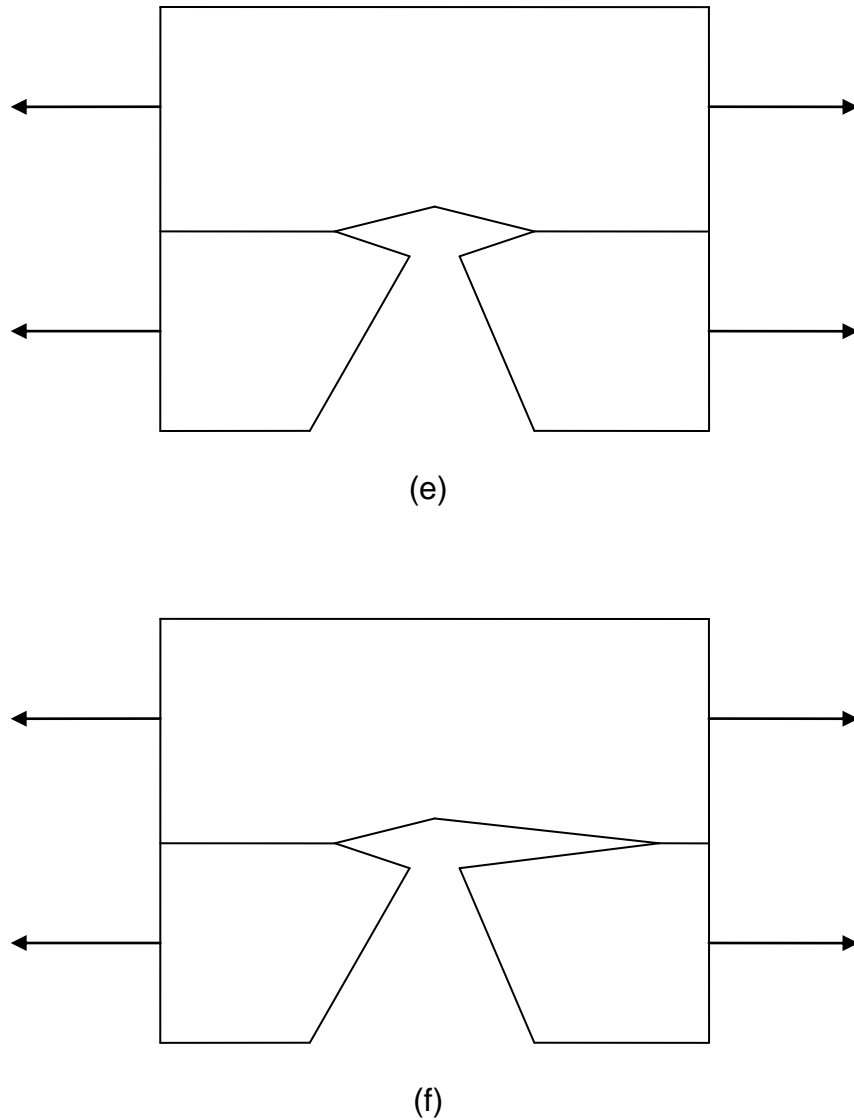
Figure 2.3.3: Stages involved in crack tip blunting; (a) axial loading of material A bonded to material B along interface C, with a pre-crack in A; (b) axial and transverse stresses at the crack tip; (c) crack halted at the interface; (d) penetration of the crack into material B; (e) crack tip blunting at the interface; (f) crack deflection along the interface.

Crack tip blunting and crack deflection comprise the key mechanisms for the occurrence of delamination in CFP composites under mode I loading conditions. Transverse crack penetration through plies absorbs little energy, as

reinforcements are generally of a brittle nature in CFP composites. Therefore the occurrence of crack tip blunting and crack deflection are essential for CFP composites to behave as effective energy absorbing materials. Though these mechanisms do not directly absorb significant energy, they do provide for the key energy absorbing mechanisms to become engaged [1]. Due to the large surface area produced by crack growth between plies, delamination can absorb significant amounts of energy. Therefore the toughness of a composite is strongly related to the fiber matrix interfacial properties.

The interfacial bond strength is key to how a composite will fracture and the energy absorbing properties of the material. As mentioned, for the case of mode I and mixed-mode loading of CFP composites, delamination occurs when the interfacial bond strength is less than approximately 20% of the resin fracture strength. Therefore relatively weak interfacial bond strength is desired to promote crack tip blunting and permit the high energy absorbing failure mechanisms associated with delamination to occur. However, an interfacial bond strength significantly lower than that required to permit crack deflection to occur reduces the associated energy absorption [18].

Similar to initiation of a crack through a homogeneous material, initiation of fracture along the fiber-matrix interface requires a distinct amount of energy input per unit length. This property is referred to as the Critical Interfacial Strain Energy Release Rate (CISERR), and is denoted G_{ic}. The value of the CISERR will be unique for each fiber-matrix interface [1], but will be relatively constant for

a given fiber-resin system, regardless of the mixed-mode loading condition [19].

It is important to note that the CISERR, G_{ic}, is not the same term as the mode I

plane-strain CSERR, G_{IC}. The former applies to fracture along the interface of a

laminated structure, while the latter applies to fracture within a homogeneous

material under mode I loading.

2.3.2 Matrix Fracture

The CSERR of CFP composites is reported to increase with increasing matrix

toughness, and well as with increasing thickness of the matrix layer plies [20].

As mentioned, polymeric resins may fracture in a brittle or ductile manner.

Cleavage is typical for brittle resins subjected to high mode I loading conditions

and is characterized by a smooth fracture surface [21]. Shattering of the resin

may occur for brittle resins subjected to high mode II loading and is characterized

by multiple crack path formation through the resin and the creation of shards.

Plastic fracture is observed with ductile resin systems under high mode I loading

and is characterized by an irregular fracture surface. Hackle formation occurs in

resin systems able to experience limited plasticity under high mode II loading,

and is characterized by an irregular, jagged, saw-tooth type appearance to the

fracture surface [15,22,23].

The principal factor influencing resin surface area creation during propagation of

a crack through resin in CFP composites is the occurrence of hackle formation

[21]. Hackles, also referred to as shear cusps, occur when a mode II loading

component is present. Superposition of the mode I and mode II components

cause the principal stress at the fracture tip to be oriented in a non-zero direction (i.e., not along the direction of the reinforcement). The stress state causes a sequence of non-linear micro-cracks to develop through the resin ahead of the crack tip. Therefore, though mode II loading is occurring, hackle formation involves mode I induced tension cracking. These micro-cracks extend with increased loading, approaching the fiber reinforcement. The fibers restrain further extension, and the cracks coalesce through formation of additional cracks perpendicular to the specimen length direction [21,24]. The process is illustrated in Figure 2.3.4. Hackle formation is characterized by an irregular, jagged, saw-tooth type appearance to the fracture surface.
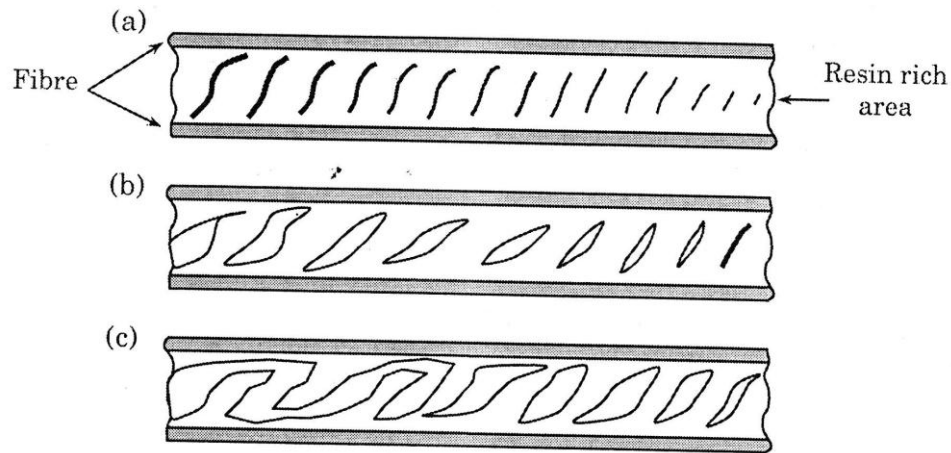
Figure 2.3.4: Hackle formation process that occurs within the resin rich layer between reinforcing plies in a CFP composite; (a) microcrack formation; (b) crack formation; (c) crack coalescence [25].

The angle of the hackles with respect to the crack growth direction increases from zero degrees for pure mode I loading (cleavage fracture), to a maximum of 45 degrees for the pure II case. The result is increased effective crack length

and an increase in the associated energy absorption, due to the increased surface energy required to create the increase in crack length. It is important to note that hackle formation is observed in CFP composites consisting of a thermosetting polymer matrix, for both glass and carbon reinforcing fibers, but that it is not generally observed in CFP composites with a thermoplastic matrix [21, 23].

2.3.3 Interyarn and Interply Failure

For a CFP composite material subjected to bending, delamination typically involves initiation through matrix cracking between plies [9]. The unbalanced stress state in bending induces the crack to propagate toward the ply face in compression [26]. Delamination may proceed by either interply or interyarn failure. Interply failure involves crack deflection resulting in fiber-matrix debonding and resin fracture along the interface between a ply and the resin-rich region between plies. Interyarn failure involves crack deflection resulting in fiber-matrix debonding and resin fracture between filaments and the surrounding resin within a ply. For interyarn failure, both fracture faces will consist of filaments with thin regions of resin between them. For interply failure, one face will consists of filaments and resin similar to interyarn, but the other face will consist predominantly of resin with evident linear concave pockets from which filaments were extracted. The typical appearance of each is shown in Figure 2.3.5.
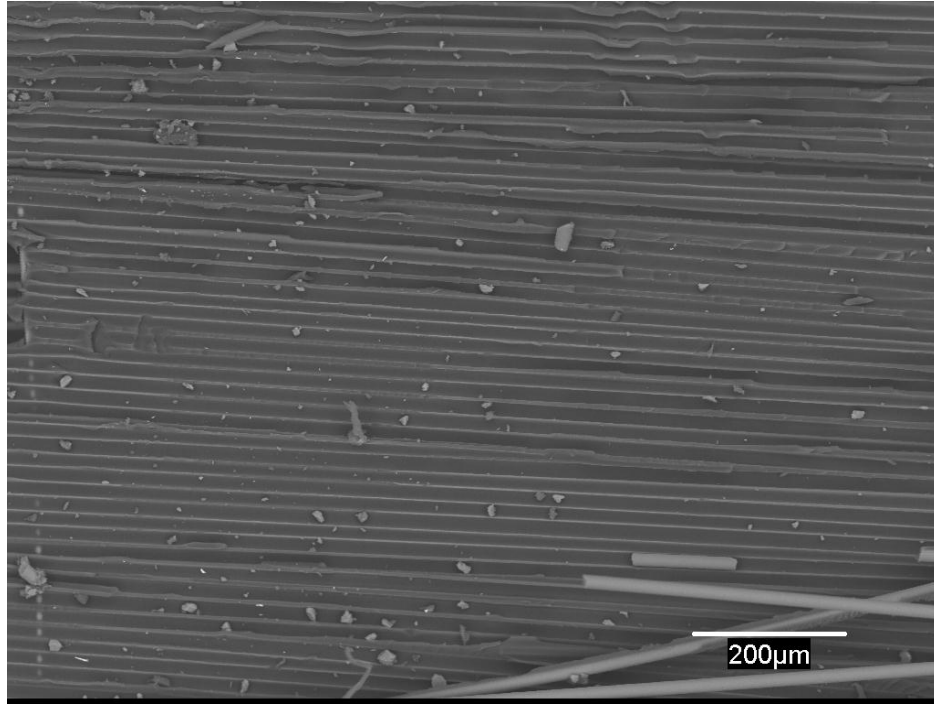
(a)
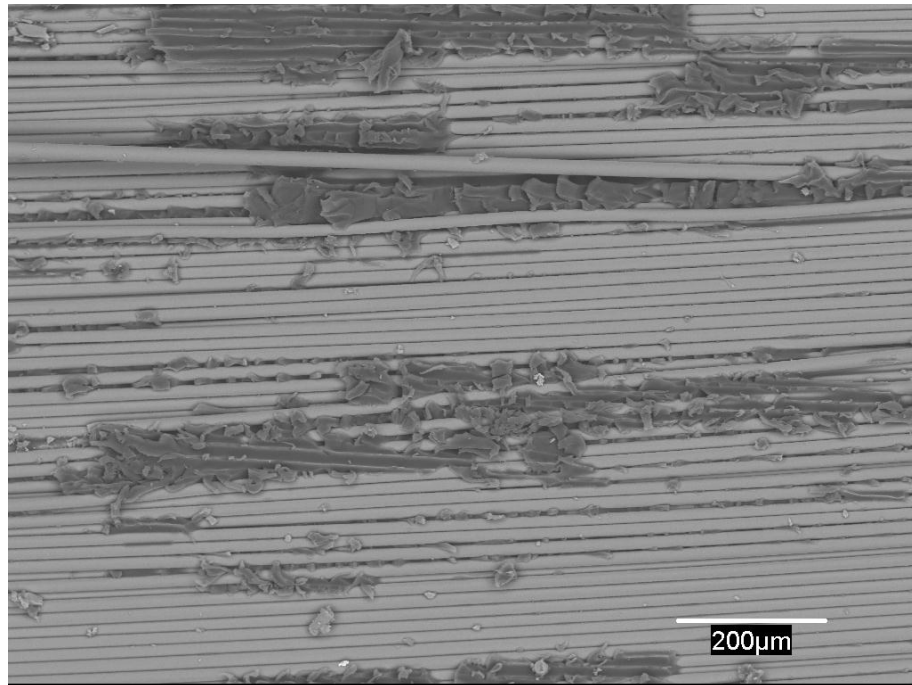
(b)

Figure 2.3.5: SEM micrographs of the typical delamination fracture surfaces; (a) resin rich face; (b) fiber rich face

The CSERR for interply failure is typically reported to be greater than that for interyarn. It has been suggested that this is due to the greater toughness provided by the thicker resin rich layer surrounding the yarns associated with interply failure as compared to interyarn failure [22]. For interply failure the resin is unconstrained on the resin rich side of the crack but constrained on the reinforcement side; while for interyarn failure the resin is constrained on both sides of the crack [27]. The imposed constraints limit the size of the plastic zone within the resin ahead of the crack tip. Plastic deformation immediately ahead of the crack tip is the principal process by which energy is absorbed during crack growth within a polymer [6]. Inhibiting development of the plastic zone inhibits the energy absorption process.

The mode II CSERR is generally found to be several times greater than for mode I [20]. This is the result of the tendency of interply failure to dominate over interyarn failure for high mode II. Mode II loading produces high in-plane shear stresses, which tend to increase the occurrence of crack tip blunting [15,21]. The increase in CSERR with increases mode II loading has also been attributed to the increase in crack path due to hackle formation [15,23]. Mode II loading also tends to induce crack migration and crack branching [21]. Crack migration involves a single crack that progresses along a convoluted path. Crack branching involves the formation of multiple crack formation. In both cases, significant fiber fracture and increased crack path length through the resin result [21].

2.4 Energy Absorption in Laminates

The study of methods to analyze the delamination of CFP composites is relatively recent. Early studies initiated in the 1960's [28] considered the initiation and propagation of delamination cracks by attempting to assess the state of stress at the crack tip by using the Linear Elastic Fracture Mechanics (LEFM) techniques developed by G.R. Irwin. However, this resulted in the difficulties of singularities at the crack tip and lack of accuracy in values for the state of stress near the crack tip. Various approaches were suggested to improve the validity of studying delamination using LEFM. Crack growth was considered as progressing through a cohesive zone [29], just inside one of the plies near the interface [30] or through an isotropic layer between the plies [31]. These approaches avoided having to consider the crack tip stress and the occurrence of the singularity. However, there were weaknesses to each of these approaches that continued to result in inaccuracies.

Methods based on an analysis utilizing the Mechanics of Materials approach (i.e., strength-based) were recognized as inherently limited by the stress singularity and sensitivity to assumptions. Therefore during the 1980's, studies shifted toward analyzing interlaminar crack growth through a Fracture Mechanics approach (i.e., energy-based). NASA was among the leaders in utilizing energy methods to predict the initiation and growth of interlaminar cracks.

O'Brien conducted a study to evaluate the mode I/II CSERR of a carbon-epoxy composite in 1982 [34] and in 1987 [35] calculated the stresses at the crack tip of

specimens subjected to Mode I loading to evaluate correlation with measure values. Other researchers studied delamination with glass-epoxy [36] and carbon-epoxy composites [37]. As well, principles of fracture mechanics were employed to understand delamination through complex shaped CFP's, such as curved composite frames for the UH Black Hawk and V22 Osprey aircraft [38].

In many of these studies, the ability of strength-based and energy-based criteria to accurately predict material failure was compared. Martin [36] considered both a strength-based failure criterion, utilizing the Tsai Hill criterion, and an energy-based failure criterion. While the energy-based criterion was found to accurately predict the onset of failure, the strength-based method did not. The author noted that the weakness in the strength-based approach is due to the lack of adequate test methods being available to determine the material through thickness strength, and the inability to evaluate the stresses at the crack tip due to the presence of a singularity. The author strongly recommended the use of energy-based criterion to predict crack propagation in composite materials. Following NASA's lead, others investigated delamination through a similar approach. It was concluded that energy-based methods provided a more reliable and accurate method than strength-based methods for predicting the initiation and growth of interlaminar delamination cracks [37].

As a result of these studies, a number of test methods were produced to evaluate the CSERR associated with delamination of CFP composites over a range of mixed-mode conditions. These included the double cantilever beam (DCB)

method for pure mode I loading, and the End Notched Flexural (ENF) method for pure mode II loading. To determine the CSERR for mixed-mode I/II loading, the Cracked Lap Shear method, the Edge Delamination Tension method, the Arcan method, the asymmetric DCB method, the Mixed-Mode Flexure test, and the Variable Mixed-mode test were developed [9]. Each of these methods however could only determine the CSERR over a limited range of mixed-mode conditions, required the use of numerical analysis or involved a challenging test set-up [9]. Inconsistent and incomplete sets of data resulted, and comparison of data across studies was unreliable.

Reeder and Crews [9] then proposed a mixed-mode bending test procedure in 1988 that offered a simple and reliable method of testing composite materials under all mode I to mode II loading ratios. The procedure permitted the development of consistent sets of data for CSERR over the full range of mixed-mode loading conditions. In 1991, Reeder and Crews [38] refined the procedure to account for non-linear behaviour. Their technique was proposed for UD CFP composites, though some limited testing has been performing using the technique with fabric CFP composites. Their method, ASTM D6671, Standard Test Method for Mixed-mode I – Mode II Interlaminar Fracture Toughness of Unidirectional Fiber Reinforced Polymer Matrix Composites, has become the standard accepted test for conducting mixed-mode testing.

A number of significant studies investigating the CSERR of UD CFP composites and the evaluation of the material properties that account for variations in the CSERR have been performed using ASTM D6671. Zhao [26] in 1995 studied

mixed-mode loading under both static and fatigue loading conditions for carbon/epoxy composites. Zhao reviewed the fracture surfaces of the specimens following testing using SEM to evaluate the fracture mechanisms involved in delamination. Zhao found that stable crack growth occurred over the full spectrum of mixed-mode ratios that were investigated under cyclic (fatigue) loading conditions.

Benzeggagh and Kenane [15] in 1996 studied glass/epoxy composites to determine a mixed-mode delamination failure criteria. Values of the CSERR were graphed as a function of the percentage of mode II loading. Then curve fitting was employed to produce a semi-empirical failure criteria. They presented the CSERR under mixed-mode loading by two useful graphical methods. Firstly, as shown in Figure 2.4.1(a), total CSERR is plotted as a function of the percentage of mode II loading, often referred to as mode mixture. Secondly, as shown in Figure 2.4.1(b), mode I and mode II components of the CSERR are plotted along separate axis. Both methods have become standard practice in the field. To convert the Figure 2.4.1(b) format to the Figure 2.4.1(a) format, the term G_c is obtained by accumulating G_I to G_{II}, and the mode mixture is the ratio of G_{II} to G_c.

Gc

GII / Gc

(a)

GI

GII
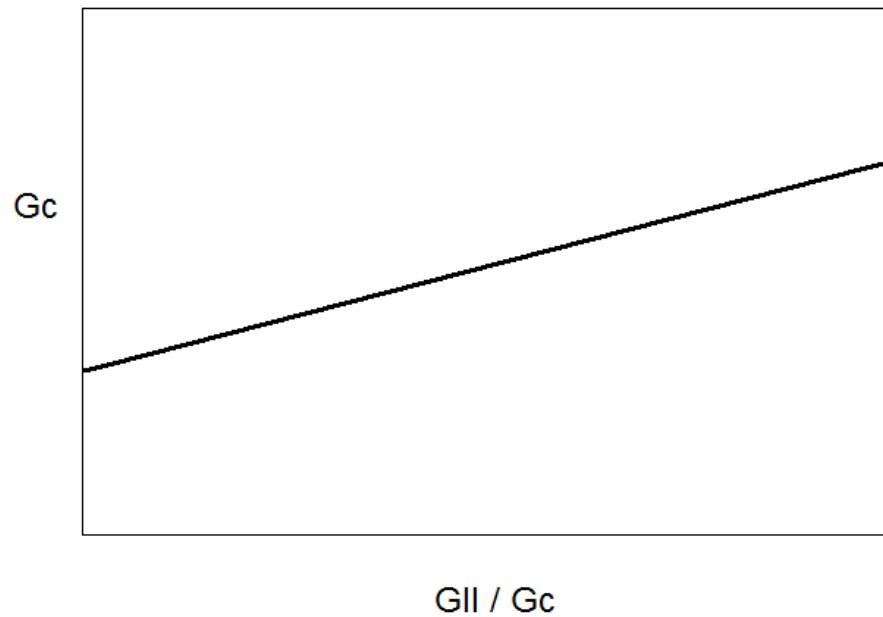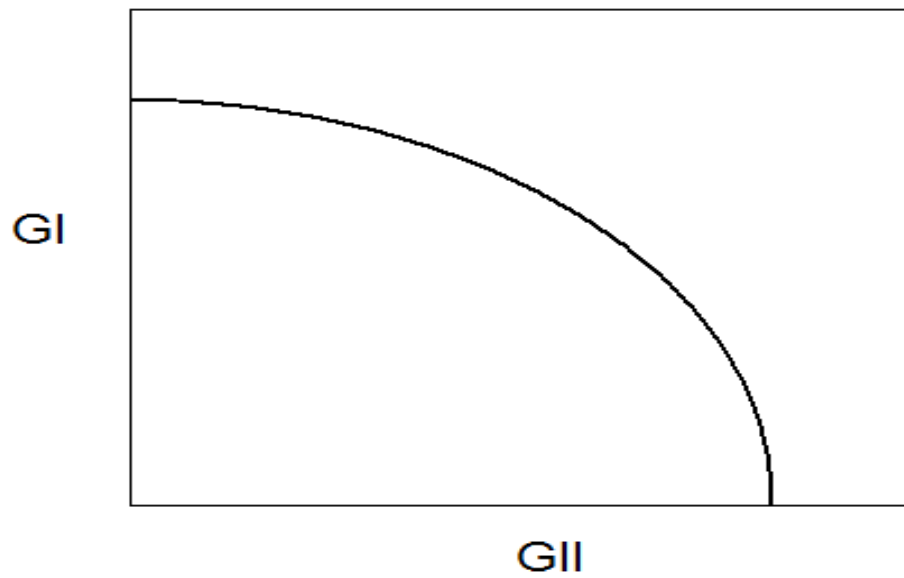
(b)

Figure 2.4.1: Two typical methods to plot mixed-mode loading CSERR data; (a) total CSERR plotted as a function of mode mixture; (b) mode I and mode II components of the CSERR plotted along separate axis [15].

Ducept et al. [39] in 1997 conducted a thorough review on the reliability of mode I, mode II and mixed-mode testing for determining delamination fracture energy of fiber-polymer composite materials. They compared the double cantilever beam (DCB) technique used for mode I testing, the end notch flexural (ENF) technique used for mode II testing, and the Reeder and Crews mixed-mode bending technique. They concluded a high degree of reliability of Reeder's mixed-mode test procedure.

Additional important testing performed using the Reeder and Crews test procedure include Singh and Greenhalgh [21] in 1998, studying the micromechanisms of delamination fracture growth of multidirectional plies under Mode I, Mode II and mixed-mode loading conditions; Greenhalgh et al. [40] in 1999, studying delamination fracture toughness of carbon epoxy composites constructed with delaminated upper plies at various non-zero orientations to the lower plies; and Greenhalgh and Singh [41] in 2002, studying the effect of moisture on the delamination fracture toughness of carbon epoxy composites under mixed-mode loading conditions.

Greenhalgh [21,40,41] observed that crack growth from the delamination tip occurs through coalescence of microvoids in front of the existing crack tip. With increasing load, the microcracks coalesce into a single propagating crack. The resulting crack propagates at 0 degrees to the pre-existing crack direction for pure mode I loading, and at 45 degrees for pure mode II loading. For mixed-mode loading, the crack direction transitions from 0 to 45 degrees with increasing

hackle formation as the mode II component increases.

Greenhalgh [21,40] also observed that the mode II CSERR is typically higher than the mode I CSERR for a UD CFP composite, and attributed this to the increase in the total fracture area associated with hackle formation. Significantly, Greenhalgh observed that the material toughness was directly related to the failure mechanisms involved, and that these failure mechanisms are related to the mechanical properties of the matrix and reinforcement.

Araki et al. [16] in 2005 applied a failure criterion to predict the direction of crack growth for neat epoxy to determine the relationship between material properties and the corresponding fracture mechanisms. He determined that the resin fracture mode was dependent on the mode mixture, and that variations in the fracture mode contributed to variations in the CSERR with mode mixture.

Mixed-mode testing of fabric composites is not widely reported. The interply CSERR has been reported to be higher than the interyarn CSERR for fabric composites [42], similar to UD composites. Additionally, the CSERR is reported to typically be higher for fabric composites than for UD composites constructed from the same fiber-resin system [27,42,43,44]. Figure 2.4.2 illustrates the key differences in the geometry of a fabric composite as compared to a UD composite. It has been suggested that fabric composites absorb more energy than UD composites due to the more complex stress state within the fabric composites, and the presence of resin rich pockets within fabrics, both of which

act to increase the load required to cause fracture propagation [27,44]. Ebeling et al. [42] noted that the resin pockets act to pin crack growth and explain the start/stop nature of crack growth at intersecting yarns and account for the saw-tooth pattern observed in the load-displacement curves for mixed-mode testing of fabric CFP composites.
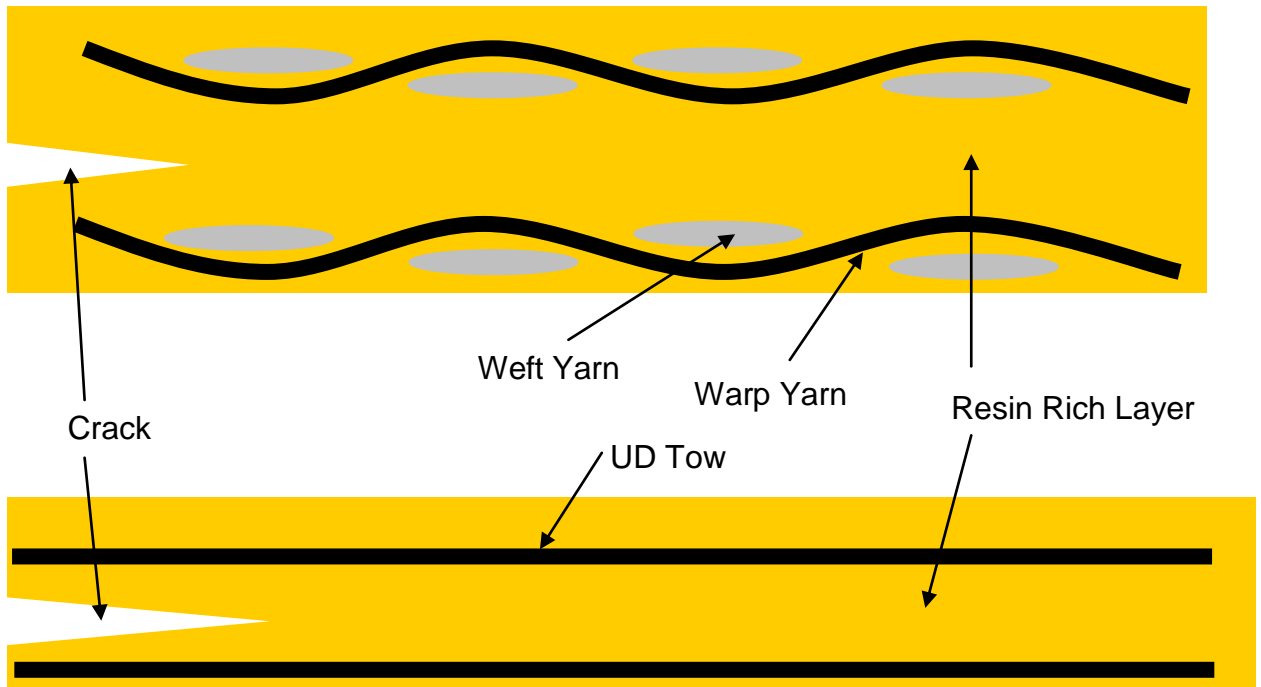
Figure 2.4.2: Illustration of the comparative geometry of a fabric composite (top), and a UD composite (bottom).

Paris et al. [43] have used the techniques outlined in ASTM D6671 for testing fabric polymer matrix composites. Paris evaluated the CSERR at four loads; the non-linear transition, visual crack growth, the maximum load, and for a 5% offset

to the linear portion of the load-displacement data. A typical load-displacement curve and the loads for which she calculated CSERR are shown in Figure 2.4.4. The saw-tooth pattern resulting from crack pinning is evident in the figure. Paris [43] concluded that the CSERR for the material she studies under mode I loading was 2.6 times greater for a fabric construction than for a UD construction (720 vs 269 J/m^2), and 3.1 times higher under mode II loading (2350 vs 750 J/m^2).
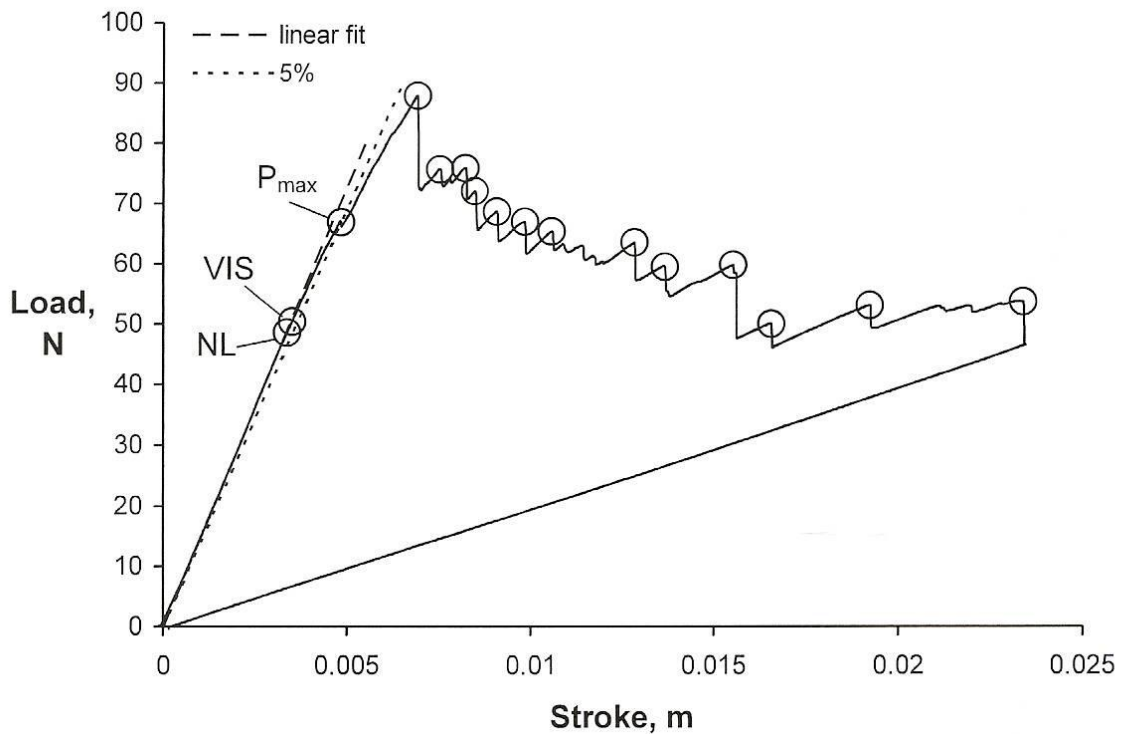
Figure 2.4.3: Typical load-displacement curve for mixed-mode load testing of CFP composite and the loads for which CSERR is calculated [43].

3. FRAMEWORK

The design of CFP composite components with optimized and predictable energy dissipation requires a failure criterion able to predict fracture energy under mixed-mode loading conditions. Existing mixed-mode failure criteria are empirical and show poor correlation for a range of CFP composites. Therefore, a universally applicable criterion based on constituent material properties and operative failure mechanisms is required.

3.1 Existing CFP Mixed-Mode Failure Criteria

Composite materials exhibit a wide range of behaviours in the values of the CSERR as a function of the mixed-mode loading percentage. Figure 3.1.1 [45] shows a plot of the CSERR with respect to the mode mixture for a number of composite materials, demonstrating the range of behaviours. A wide number of criteria have been proposed to predict these curves. In all, more than 18 distinct failure criteria have been proposed for the delamination of CFP composites under mixed-mode loading conditions.

The fact that there are so many criteria suggests that there is still significant disagreement within the scientific community in understanding mixed-mode delamination. All existing criteria are empirical, requiring the evaluation of arbitrary parameters by curve fitting to experimentally measured CSERR values. In general, these criteria fail to predict with any accuracy the failure response of

CFP composites other than the one used to calculate the parametric values. The more well-known or significant criteria are reviewed below.
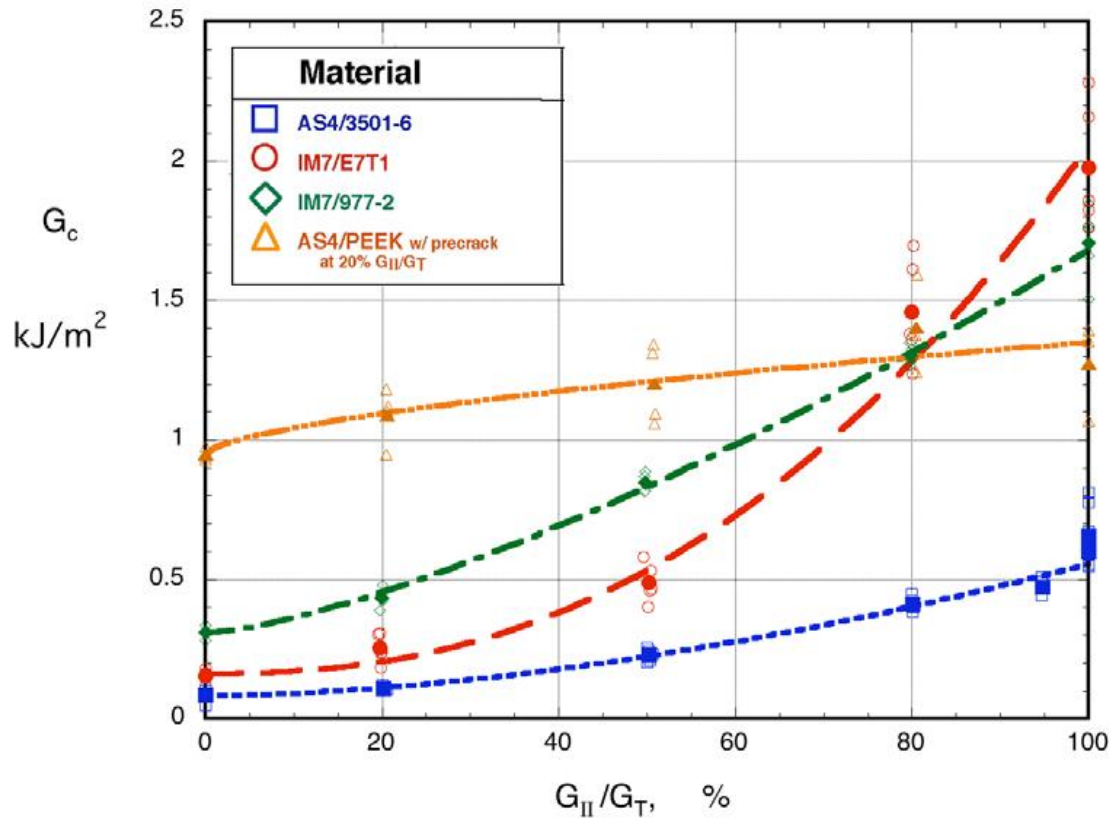
Figure 3.1.1: CSERR vs mode mixture for some common composite materials. Vertical axis is CSERR, and the horizontal axis is the mode mixture [45].

3.1.1 Linear Type Criteria

A number of Linear Criteria are proposed by Whitcomb [46,47]. The first, and simplest of these, is the Constant Fracture Energy Criterion. This criterion predicts a very conservative estimate of the mixed-mode loading CSERR. The criterion is based on the Mode I CSERR, G_{IC}. As mentioned, the Mode II CSERR is typically higher than the Mode I CSERR for CFP composites. Therefore

fracture is predicted to occur when the mode I SERR exceeds the mode I CSERR. The criterion can be expressed as [46]:

$$G_{Ic} = G_I \tag{3.1.1}$$

As a conservative criterion, it results in inefficient designs with high cost and weight penalties [3]. Therefore an alternate Constant Fracture Energy Criterion [46] is proposed, in which the total fracture energy is the sum of the mode I and mode II components of strain energy. This criterion can be expressed as [46]:

$$G_c = G_I + G_{II} \tag{3.1.2}$$

Fracture is predicted to occur when the sum of the mode I and mode II components of the SERR under mixed-mode loading are equal to the material CSERR. The Linear Criterion, which accounts for the fact that the mode II CSERR is typically higher than the mode I CSERR, is produced by normalizing this Equation 3.1.2 [23]:

$$\left(\frac{G_I}{G_{Ic}} \right) + \left(\frac{G_{II}}{G_{IIc}} \right) = 1 \tag{3.1.3}$$

The Linear Criterion is the most frequently employed expression to predict fracture in CFP composites used by industry [41]. Values for G_{IC} and G_{IIC} must be evaluated experimentally for each CFP composite considered. This is a

common feature of all failure criteria proposed to date and considered in this chapter. Figure 3.1.2 shows the values of G_I to G_{II} at which fracture is predicted to occur by the linear type criteria [23]. In the diagram, as well as for all other diagrams from this author, for simplicity it is assumed that the mode II CSERR is 3 times the value of the mode I CSERR. The author has also substituted the nomenclature G_I and G_{II} with G^m_{IC} and G^m_{IIC}.
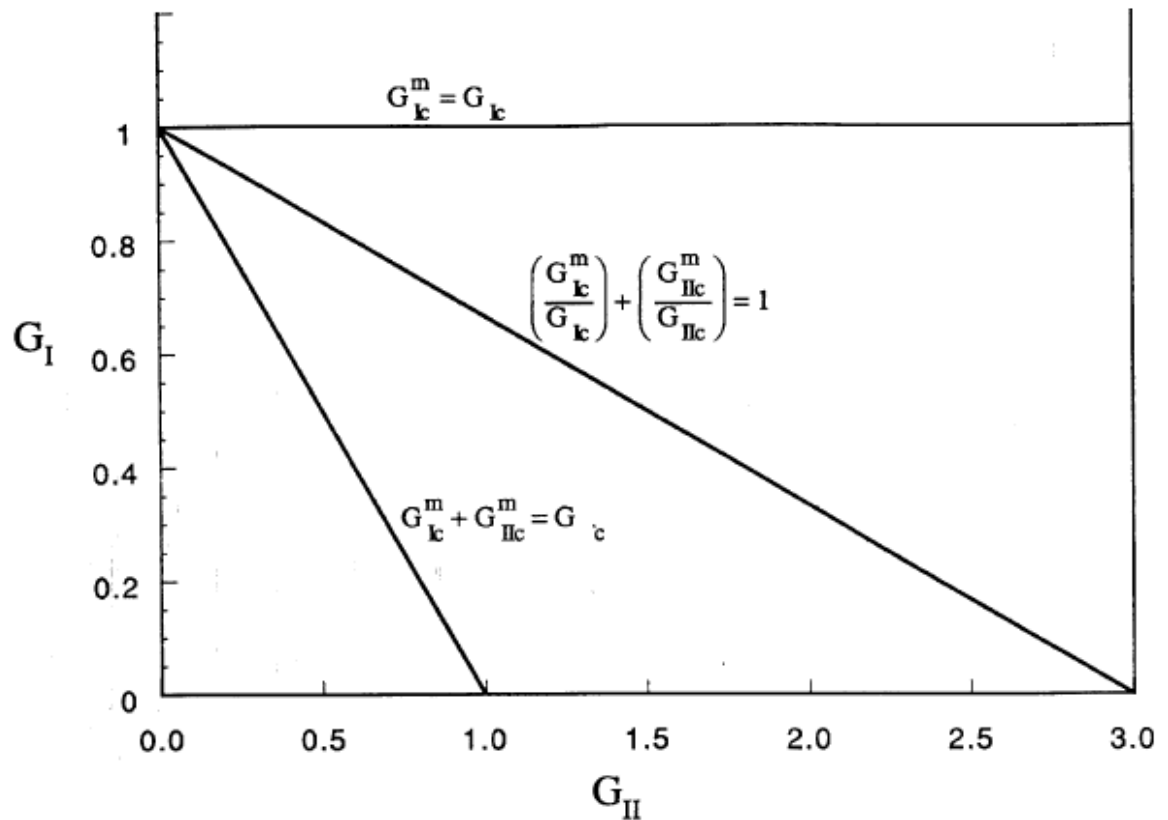
Figure 3.1.2: Mixed-mode CSERR diagram for various linear criteria [23].

3.1.2 Power Law Criterion

Whitcomb [46] also proposed the Power Law Criterion, which is a generalized version of the Linear Criterion. In its most general form, the Power Law Criterion can be expressed as [46]:

$$\left(\frac{G_I}{G_{Ic}}\right)^{\alpha} + \left(\frac{G_{II}}{G_{IIc}}\right)^{\beta} + \left(\frac{G_{III}}{G_{IIIc}}\right)^{\lambda} = 1 \tag{3.1.4}$$

The Mode III loading component is typically insignificant in practical applications, and so is usually considered negligible, reducing the expression to [48]:

$$\left(\frac{G_I}{G_{Ic}}\right)^{\alpha} + \left(\frac{G_{II}}{G_{IIc}}\right)^{\beta} = 1 \tag{3.1.5}$$

The exponents *α, β and λ* are parameters with values that provide a best fit to experimental CSERR data. For the case of making predictions for a CFP composite, G_{IC} and G_{IIC} of the composite require experimental determination, and then the mixed-mode CSERR's are calculated using parametric values obtained by curve fitting the full CSERR curves of other CFP composites. This is a common feature of all failure criteria proposed to date and considered in this chapter which involve parametric values. Where adequate data is not available, the parameters can be assumed to have a linear form (they are all equal to 1) or a quadratic form (they are all equal to 2). Note that setting the exponents to a value of unity reduces the expression to the Linear Criterion.

The Power Law Criterion permits a wide range of material behaviours to be modeled. When the exponents are assumed to be greater than 1, the resulting failure curve is convex. The curve is concave when the exponents are less than 1. Skewing of the curve occurs when the exponents are not equal. Even though a range of material behaviours can be modeled, there is nothing inherent in the equation to suggest how a given material will behave. Therefore, the criterion does not provide a predictive capability. Figure 3.1.3 shows the values of G_I to G_{II} at which fracture is predicted to occur by the criterion for a range of parametric values [23].
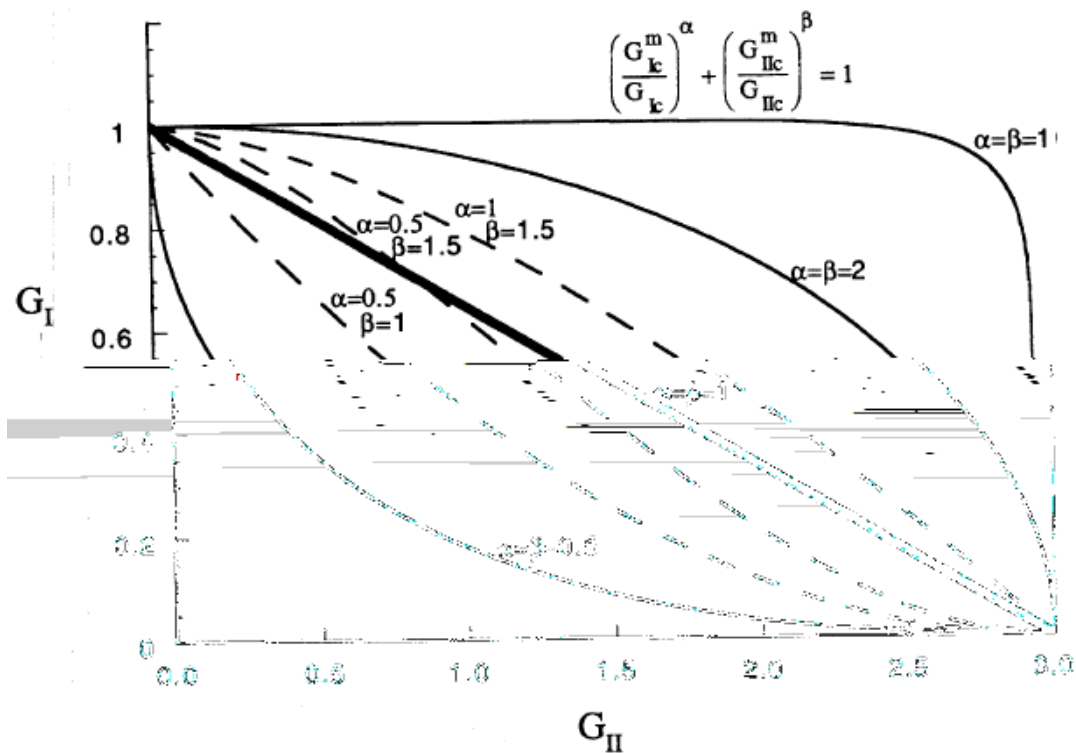
Figure 3.1.3: Mixed-mode CSERR diagram for the power law criterion [23].

3.1.3 Polynomial Criterion

The Polynomial Criterion was proposed by Yan et al. in 1991 [49]. The criterion assumes that fracture can most accurately be predicted through a polynomial expression. The expression they proposed is [49]:

$$G_c = G_{Ic} + \rho \left(\frac{G_{II}}{G_I} \right) + \tau \left(\frac{G_{II}}{G_I} \right)^2 \qquad (3.1.6)$$

Where ρ and τ are fitting parameters. Adjustment of these parameters provides for a large variation in curve shape. However, the curves that can be produced are unrealistic. They either loop back on themselves or extend indefinitely, and result in G_{IC} and G_{IIC} values approaching zero for low and large mode mixture [23]. Figure 3.1.4 shows the values of G_I to G_{II} at which fracture is predicted to occur by the criterion for a range of parametric values [23].
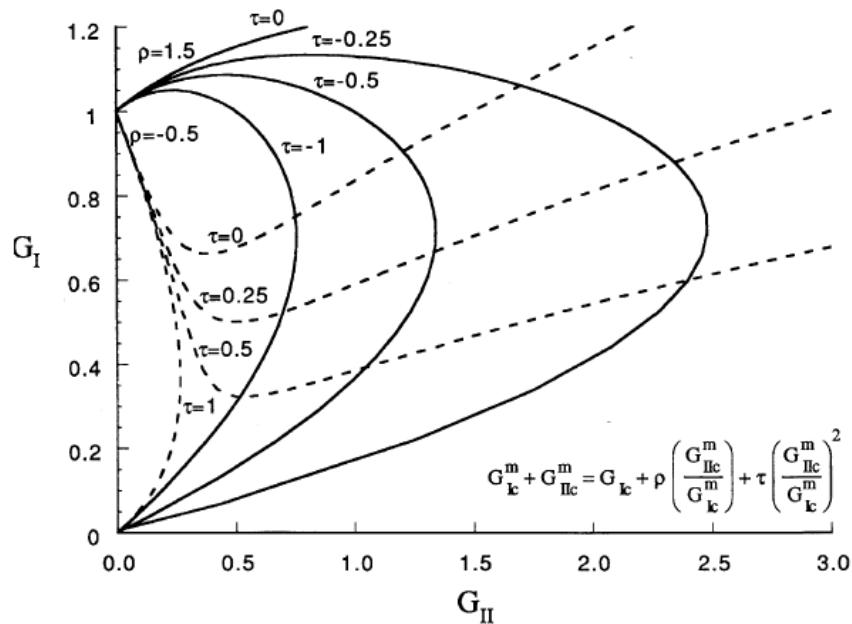
Figure 3.1.4: Mixed-mode CSERR diagram for the polynomial criterion [23].

3.1.4 Stress Intensity Factor Criterion

The Stress Intensity Factor Criterion was proposed by Hahn in 1983 [50]. The criterion assumes that fracture can be predicted as a linear function of the Mode I stress intensity factor, K_{IC}. The criterion is expressed as [50]:

$$G_I + G_{II} = G_{IIc} - \left(G_{IIc} - G_{Ic}\right)\sqrt{\frac{G_I}{G_{Ic}}}$$

(3.1.7)

For the case that G_{IIC} is equal to G_{IC} the criterion reduces to the Linear Criterion. When G_{IIC} is significantly greater than G_{IC} the criterion becomes the Power Law criterion. Figure 3.1.5 shows the values of G_I to G_{II} at which fracture is predicted to occur by the criterion [23].
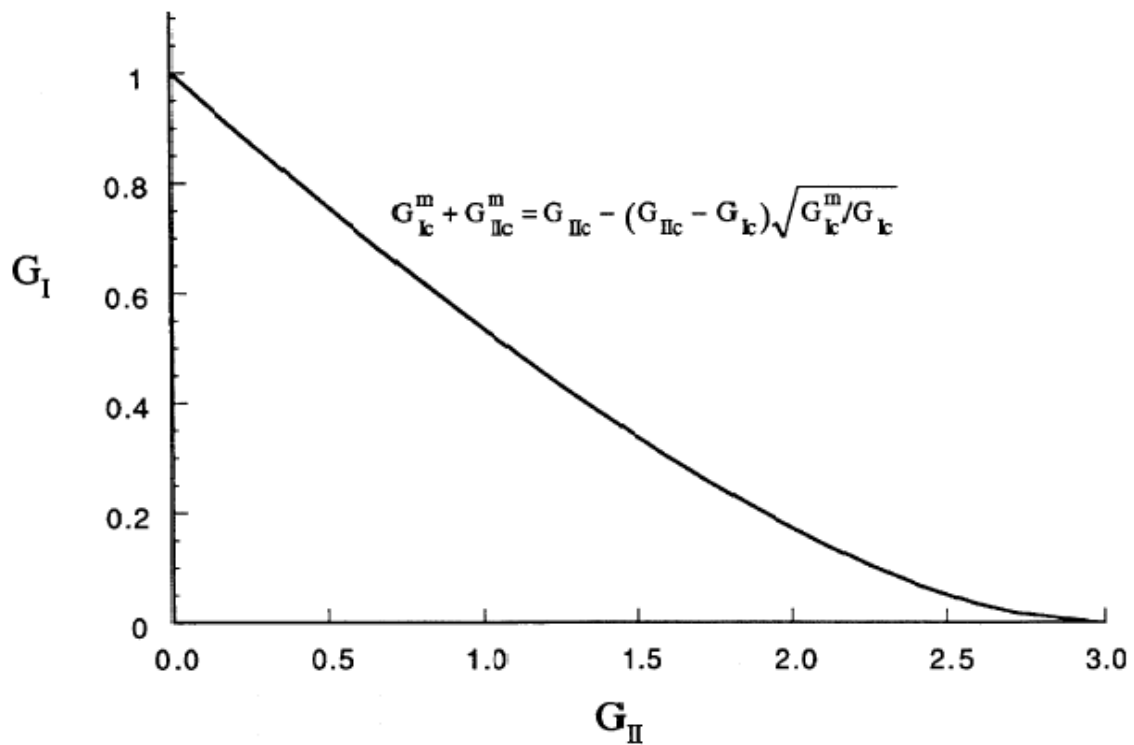
Figure 3.1.5: Mixed-mode CSERR diagram for the stress intensity criterion [23].

3.1.5 Bilinear Model Criterion

Due to the empirical nature of most criteria, others were proposed that considered the physical behaviour of the failure mechanisms involved in delamination. Reeder in 1992 [23] proposed the Bilinear Model Criterion, which sought to account for the apparent existence of multiple failure mechanisms becoming engaged during the transition from Mode I to Mode II loading. The Bilinear model determines the transition in the failure mechanism by evaluating the intersection as dependent on the parameters. One expression describes the SERR between zero and 50% mode II loading, while the other expression describes the SERR between 50% and 100% mode II loading. A linear relationship for each expression is assumed. The expressions are [23]:

$$G_I = \xi G_{II} + G_{Ic} \qquad (3.1.8)$$

$$G_I = \zeta G_{II} - \zeta G_{IIc} \qquad (3.1.9)$$

Where ζ and ξ are arbitrary parameters. When each of these parameters are equal to the negative ratio of the mode I to the mode II critical strain energy release rates, the equations reduce to the Linear Criterion. The criterion provides a positive step forward by accounting for a frequently observed transition in failure mechanisms during mixed-mode testing of CFP composites. However, the criterion does not involve characterization or incorporation of the behaviour of particular failure mechanisms [23]. Figure 3.1.6 shows the values of

G_I to G_{II} at which fracture is predicted to occur by the criterion for a range of parametric values [23].
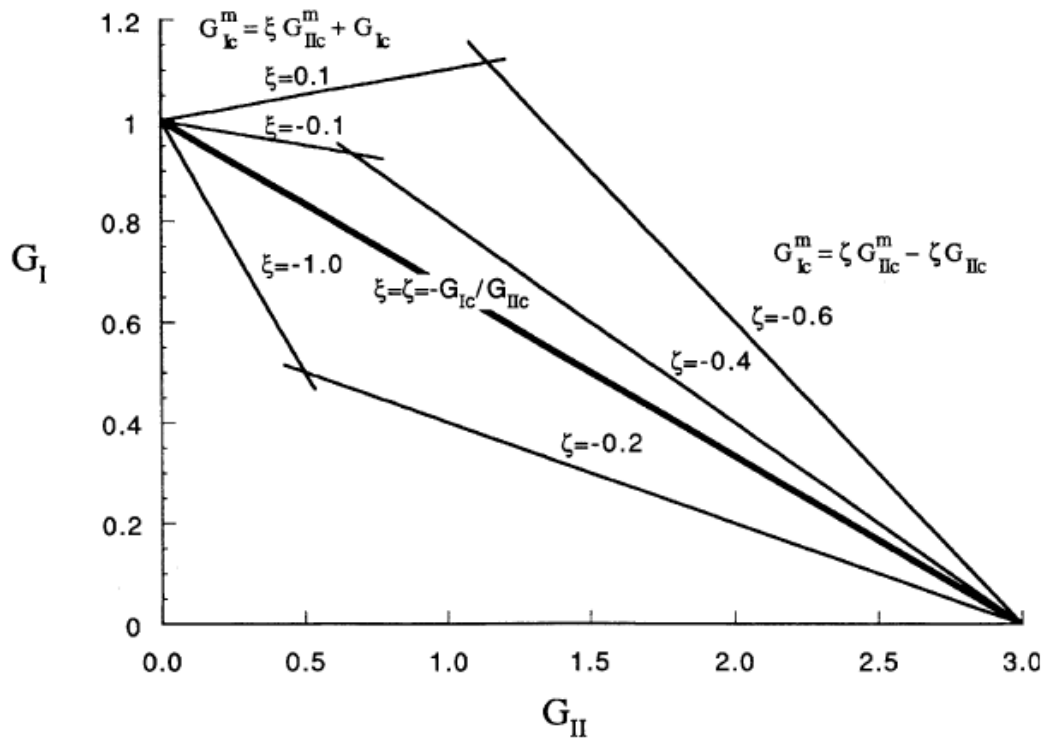
Figure 3.1.6: Mixed-mode CSERR diagram for the bilinear criterion [23].

3.1.6 Hackle Criterion

Hahn and Johannesson proposed the Hackle Criterion 1983 [51]. This is one of the more significant physically-based criteria, in that material fracture properties are directly considered. The criterion attempts to predict the occurrence of delamination failure by modelling the hackle formation process in the delamination zone. Hahn and Johannesson concluded that the hackle angle was a linear function of the mode I and mode II SERR, and therefore expressed the

Hackle Criterion as [51]:

$$G_I + G_{II} = (G_{Ic} - X) + X\sqrt{1 + \frac{G_{II}}{G_I}\sqrt{\frac{E_{11}}{E_{22}}}}$$ (3.1.10)

The difficulty with the Hackle criterion is that for values of X other than zero, the mode II CSERR is always predicted to be infinite. And for a value of X of zero, the expression collapses to a Linear Criteria. Figure 3.1.7 shows the values of G_I to G_{II} at which fracture is predicted to occur by the criterion for a range of parametric values [23].
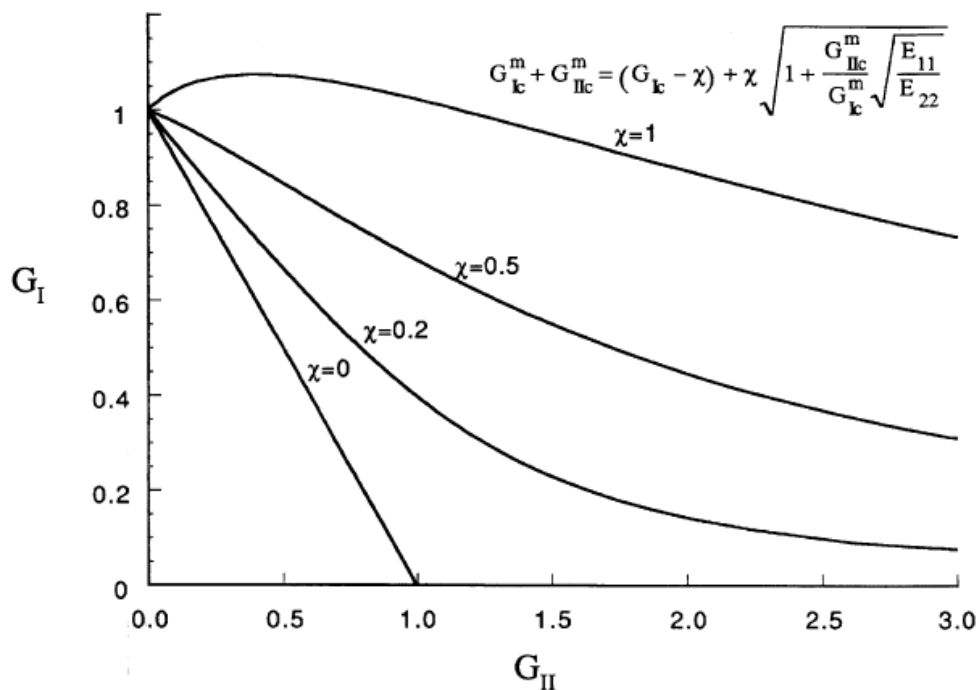
Figure 3.1.7: Mixed-mode CSERR diagram for the hackle criterion [23].

3.1.7 Benzeggagh and Knane (B-K) Criterion

Benzeggaph and Knane [15] proposed a semi-empirical criterion in 1996 that is relatively successful and widely used by researchers. The criterion is stress based, and considers the stress intensity factor at the crack tip. The criterion is expressed as [15]:

$$G_c = G_{Ic} + (G_{IIc} - G_{Ic})\left(\frac{G_{II}}{G_I + G_{II}}\right)^n \qquad (3.1.11)$$

The arbitrary parameter n is determined experimentally by curve fitting. Ducept [24] in 2000 reviewed the Benzeggaph and Knane criterion and proposed a value of n of 3/2 for glass-epoxy composites, and a value of n of 5/2 for glass-epoxy bonded joint. Benzeggagh and Knane suggest a best-fit expression for glass-epoxy for the CSERR as given below [15].

$$G_c = 118.3 + 2795.18\left(\frac{G_{II}}{G_I + G_{II}}\right)^{2.6} \qquad (3.1.12)$$

3.2 Comparative Reviews

Extensive comparative testing of the mixed-mode delamination failure criteria proposed to date has been conducted [23,40,41,45,52]. Greenhalgh [40,41,52] studied composite systems consisting of UD carbon with bismalemide resin (T800/5245), and with epoxy resin (T800/924). He determined the mixed-mode CSERR's for these materials, and then evaluated the data against twelve criteria,

including the Linear, Power Law, Polynomial, Stress Intensity, Hackle, and B-K. Results of Greenhalgh's studies are shown in Figure 3.2.1 [52]. For some of the criteria assessed, Greenhalgh references the author's name rather than the criterion name.
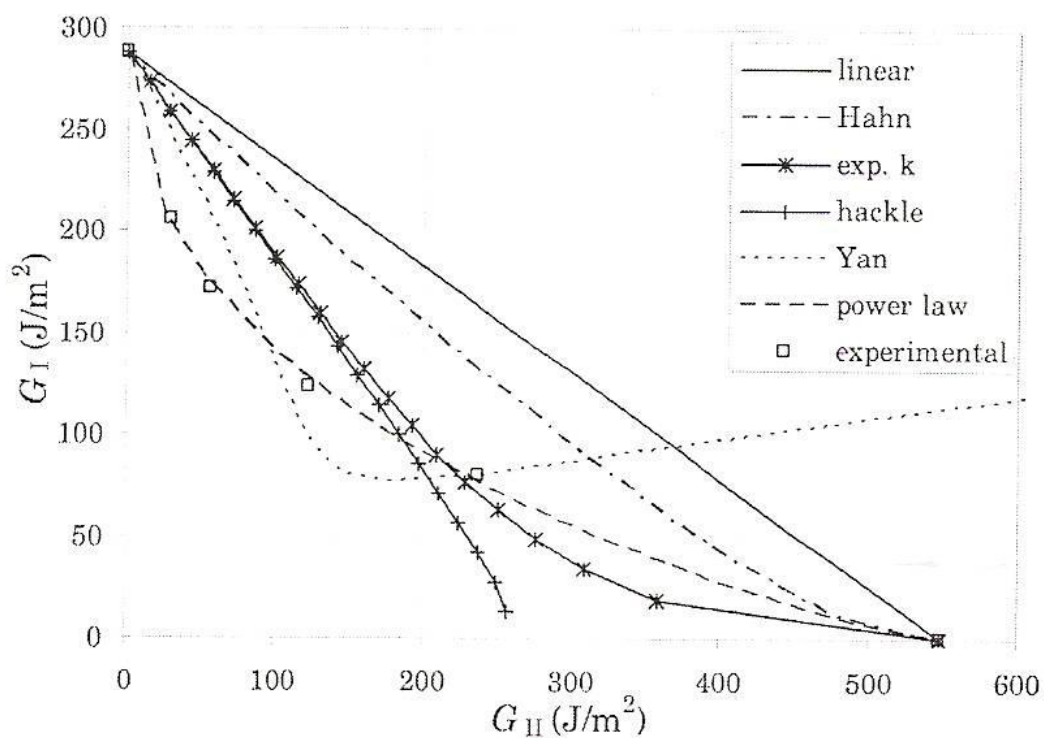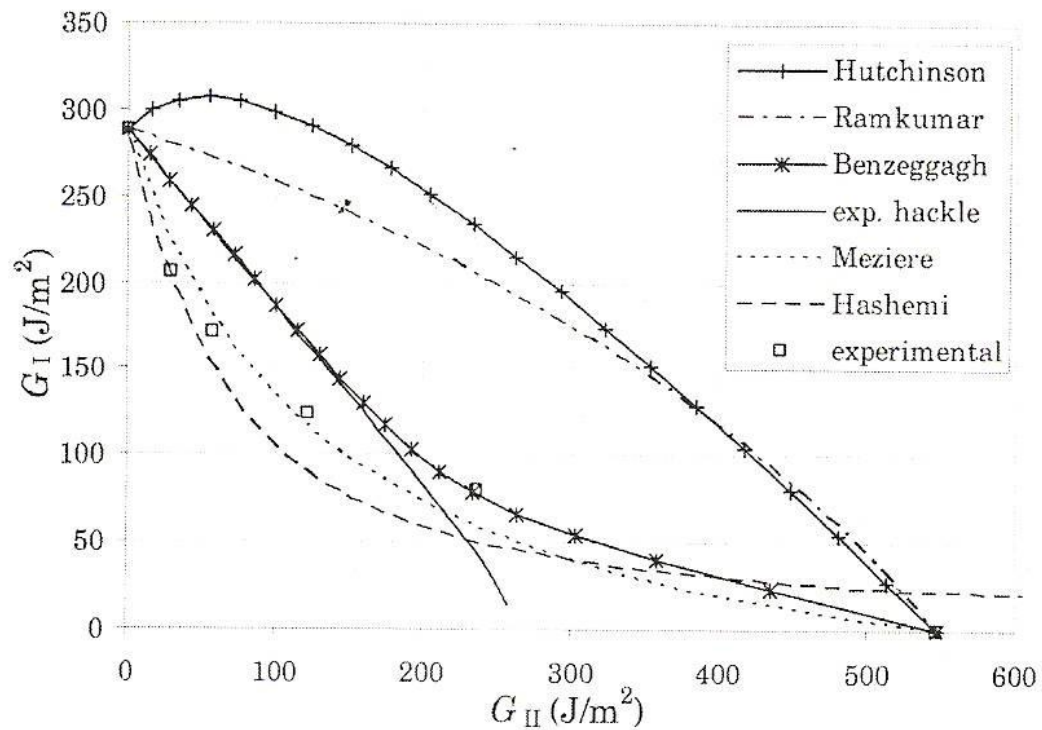
Figure 3.2.1: Comparison of the fit of various mixed-mode delamination failure criteria to the experimental data of Greenhalgh [52].

Reeder [23,45] studied composite systems consisting of UD carbon and brittle epoxy resin (AS4/3501-6), a toughened epoxy resins (IM7/E7T1 and IM&/977-2), and a thermoplastic resin (AS4/PEEK). He similarly determined the mixed-mode CSERR's for these materials, and then evaluated the data against six failure criterion, including the Linear, Power Law and Bilinear. Figure 3.2.2 shows the plot of the Power Law fit to the various CFP composites studied [45]. Figure 3.2.3 shows the fit of various failure criteria to one of the materials studied [23].
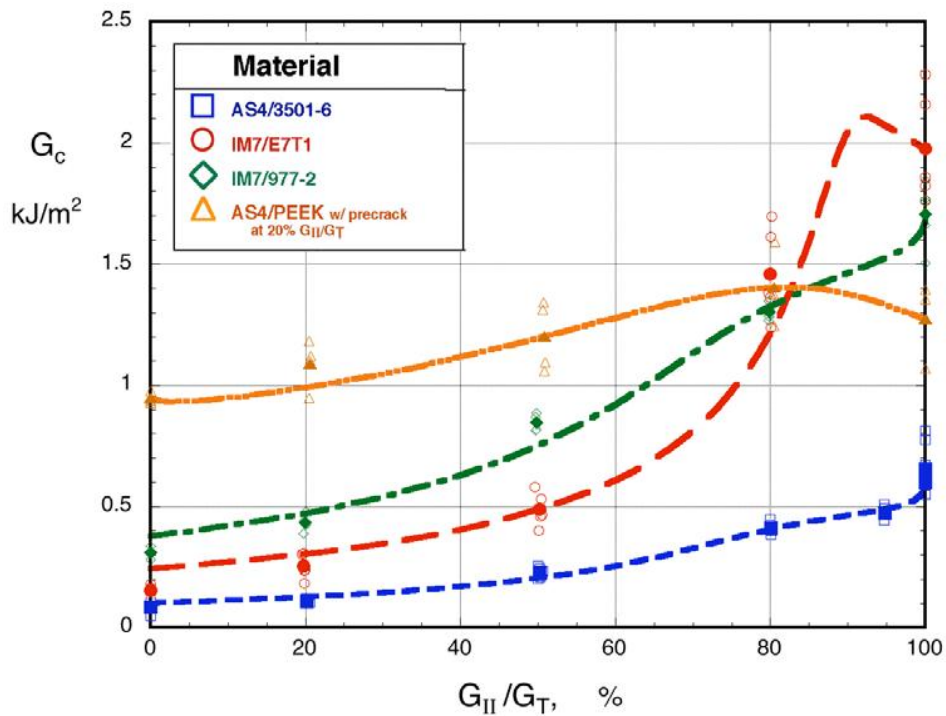
Figure 3.2.2: Fit of the power law criterion to experimental data plotted as G_c vs % mode II loading [45].
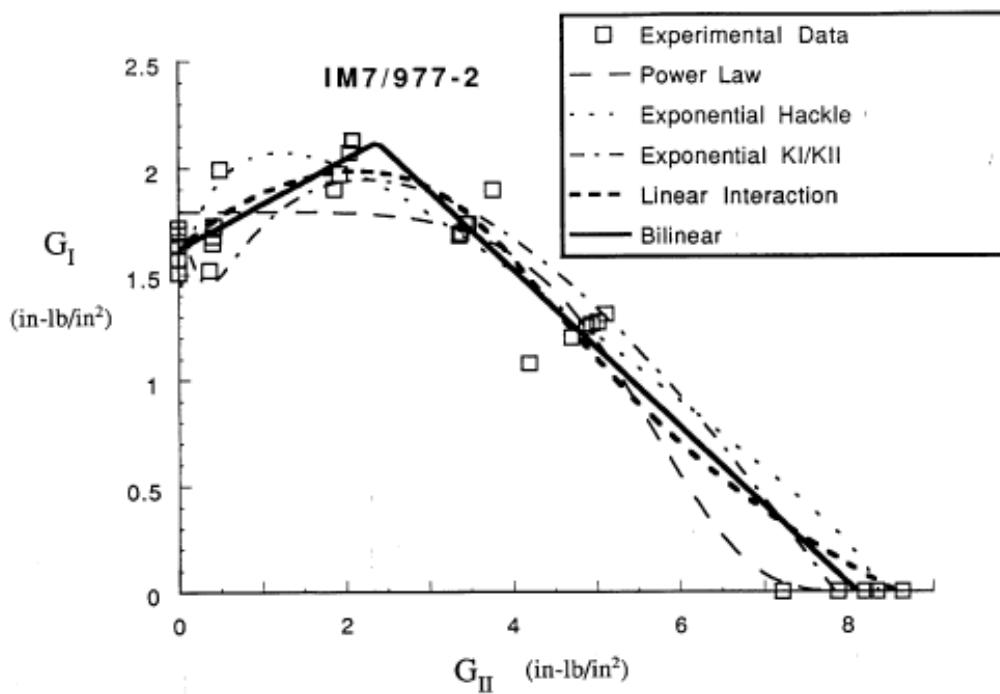
Figure 3.2.3: Fit of various failure criterion for the CFP composite IM7/977-2 [23].

In summation, Greenhalgh's and Reeder reported that the Polynomial and the Hackle criteria failed to model the behaviour of the composite materials reviewed; the Linear and the Stress Intensity Factor criteria poorly modeled the behaviour; and the Bilinear, Benzaeggah and Kenane, and the Power Law criteria modeled the fracture behaviour with some accuracy. The general conclusion of the authors was that none of the criteria accurately predicted the fracture behaviour of a range of composite materials for mixed-mode loading.

Greenhalgh and Singh [21,41] concluded for most of the criteria they reviewed that "… in general, the criteria are empirical fits to experimental data, and do not model the physical processes that occur during fracture" [41] and "that most of the failure criteria bore no relationship with the delamination mechanisms" [21]. Singh and Greenhalgh [21] did find however that those failure criteria that were physically based did show some degree of fit to the data, but only poorly [21]. Reeder [23] noted that the shape of the G_I/G_{II} plotted data varies with the different resins and suggested that multiple criteria may be necessary to reflect the different failure mechanisms that are engaged for a given composite construction due to the transition of failure mechanisms as the load shifts between pure mode I and pure mode II [23].

3.3 Mechanistic Criterion

A mechanistic mixed-mode failure criterion for CFP composites would be based on application of constituent material properties and operative failure mechanisms. The advantage of a mechanistic failure criterion compared with

empirical criteria is two-fold. Firstly, as it incorporates an understanding of the material mechanics, it will generally be more applicable over a wider range of composite materials. Secondly, it can be used as a design tool to customize constituent material selection to optimize the resulting composite's energy absorbing properties.

A generalized mechanistic failure criterion would ideally require only knowledge of the mechanical properties of the matrix and reinforcement materials that affect energy absorption, and a characterization of the key energy absorbing failure mechanisms involved in delamination. Application of the principles of linear elastic fracture mechanics (LEFM) will be employed to integrate these properties and processes into a cohesive and comprehensive predictive model.

The development of a mechanistic failure criterion will involve a number of steps. First, the dominant failure mechanisms that occur during delamination must be determined. Second, the particular energy absorbing mechanisms that are involved for each failure mechanism must be understood. Third, the related CSERR for each of these energy-absorbing mechanisms must be evaluated. Fourth, the total crack path associated with each energy absorbing mechanism must be assessed.

The failure criterion would then consist of an accumulation of the energy terms associated with each energy absorbing process over the relative areas of the fracture surfaces for each mode mixture. For a proposed CFP composite, the

corresponding constituent component (resin, fiber and resin-fiber interface) energy terms would be introduced. The result would be a curve describing the predicted CSERR as a function of the mode mixture for that composite. This curve would define the failure conditions for that material.

Determination of the required information appears to require a very complex and exhaustive investigation. Studies performed with UD and fabric composites as part of this research were able to isolate and characterize the relevant failure mechanisms and key energy absorbing processes. Fortunately, the number of significant terms that need to be defined are manageable. The dominant failure mechanisms that occur during delamination of CFP composites are interyarn failure and interply failure. Prediction of which failure mechanism will occur is a function of the stress state. The principle energy absorbing processes involved for both interyarn and interply failures are resin fracture and fiber-resin debonding. These processes can be fully characterized by measuring the associated mechanical properties, which are the resin mode I CSERR and the resin-fiber debond energy, respectively.

Development of the mechanistic failure criterion proposed here involves the systematic study of the energy related properties of the constituent components of a composite (matrix and reinforcement), and investigation using LEFM of the operative physical processes involved in the failure mechanisms involved in delamination. The proposed criterion then predicts CSERR for a given fiber/resin system by integrating the energy terms of the fracture processes involved in

delamination as a function of their relative area of the crack surface. The value of the CSERR associated with resin fracture is derived as a function of hackle formation and the degree of constraint placed on the development of the plastic zone.

This thesis is structured with a framework that provides in separate chapters a comprehensive discussion of each subject area of investigation, offering the reader a systematic flow to the ideas and concepts presented. Investigation into the fracture processes involved in delamination of unidirectional (UD) composites is first provided, followed by a consideration of fabric composites. Then the experimental studies and related analysis of the polymeric matrix is accumulated and presented, followed by the study of the matrix/reinforcement interfacial properties is presented. Lastly, the cohesion of the key concepts and ideas is presented as a mechanistic failure criterion. Experimental data is used to support the criterion, and the value and impact of the criterion and major insights gained through this research are considered.

4. UNIDIRECTIONAL COMPOSITE STUDIES

4.1 Introduction

Fracture studies are performed on unidirectional (UD) CFP composites to define the specific failure mechanisms that are the most significant contributors to the energy absorption associated with delamination. These studies sought to determine specific details regarding the failure mechanisms involved in delamination to gain insight into how the CSERR relates to composite geometry and material properties. As mentioned, existing fracture test methods to induce and study delamination in CFP composites include mode I, mode II and mixed-mode testing. Each of these is reviewed. Mode III testing is not performed in this study and will not be considered further.

4.1.1 Mode I Fracture Test Methods

Mode I loading, also referred to as the opening mode, results when a force acts normal to the plane of an existing crack. The method most commonly used to evaluate the mode I CSERR is the Double Cantilever Beam (DCB) test, as described in ASTM D5528, Standard Test Method for Mode I Interlaminar Fracture Toughness of Unidirectional Fiber-Reinforced Polymer Matrix Composites. The DCB test has been developed for unidirectional materials, but has been used to successfully study other ply lay-ups such as fabric composites [13].

CFP composite specimens for the DCB test are prepared as thin long rectangular

sections with a constant cross-sectional area. A pre-existing delamination is introduced into one end of the specimen during fabrication by placing a piece of non-adhesive material in the mid-plane of the specimen, aligned along the laminate direction. The introduced delamination will ensure that failure is induced along the mid-plane of the specimen. Midplane symmetry of the specimen is essential to ensure proper Mode I delamination growth [13]. Hinges or tabs are glued to the specimen so that loading can be applied. A typical DCB test specimen arrangement is shown in Figure 4.1.1.
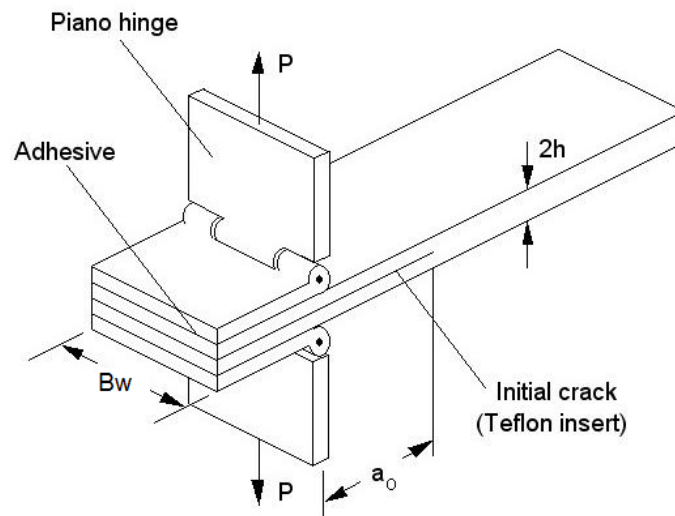
Figure 4.1.1: Mode I Test Specimen.

To perform a DCB test, force is applied at the loading points of the specimen at a constant rate of displacement, the load and displacement data are recorded, and values corresponding to crack growth are noted. For a DCB test of a CFP composite, the load-displacement curve will remain relatively linear until crack

growth occurs, at which point the load will drop. The crack will grow for a given length and stop. Then re-loading of the specimen occurs until the crack grows by another incremental amount. This cycle repeats, and is known as stable crack growth [53].

A theoretical mode I CSERR test load-displacement curve is shown in Figure 4.1.2. The serrated, saw-tooth type pattern corresponds to re-loading of the specimen following each incremental crack growth. Each increment of crack growth is indicated by the abrupt decrease in the load. As the crack length increases, the compliance of the specimen decreases. Also, the load at which subsequent crack growth occurs is less than that for the previous growth cycle [3].
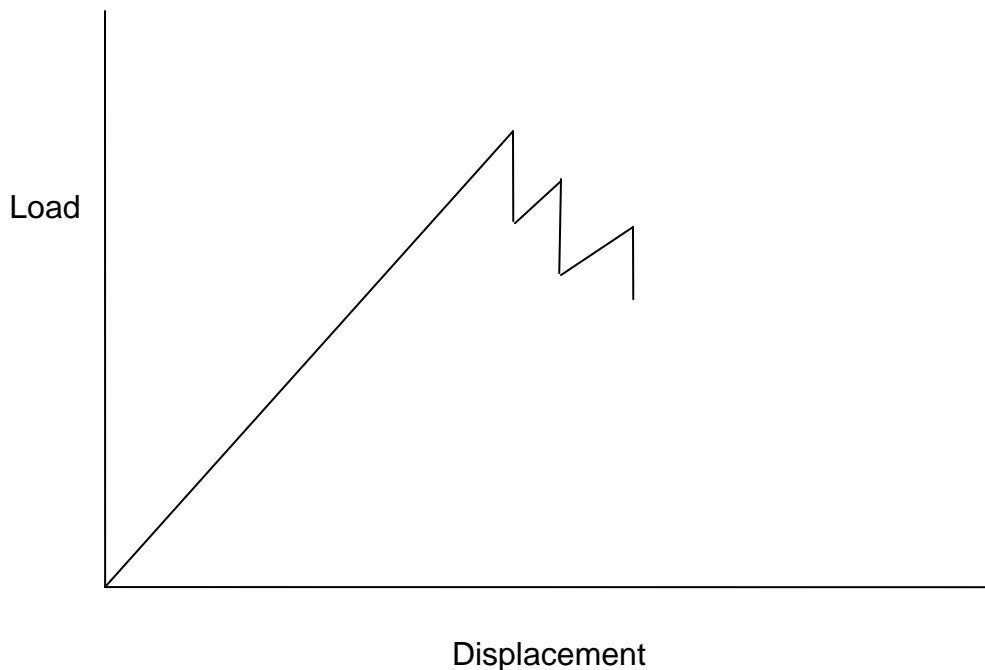
Figure 4.1.2: Appearance of typical DCB test load-displacement curve.

The Mode I CSERR is calculated as a function of the strain energy input into the beam with respect to crack growth [3,53]. The CSERR calculated for the initial crack growth will typically not be the same as the value determined for subsequent crack growth. Therefore two values of Mode I CSERR are defined. The value corresponding to the initial crack growth is referred to as the initiation CSERR; while the value calculated for subsequent crack growth is referred to as the propagation CSERR.

For a mode I test, the strain energy introduced into a material up to the onset of crack growth can be found by calculating the area under the corresponding load-displacement curve from initial loading until crack growth occurs. This can be expressed as [6]:

$$U = \frac{1}{2} P\delta$$
(4.1.1)

Forming a differential equation:

$$dU = \frac{1}{2}\left(Pd\delta + \delta dP\right)$$
(4.1.2)

Strain energy release rate, G, is defined as:

$$G = -\frac{1}{B}\frac{dU}{da}$$
(4.1.3)

Compliance is defined as the displacement over the applied load:

$$C = \frac{\delta}{P} \tag{4.1.4}$$

Alternatively, this can be re-arranged as follows:

$$\delta = CP \tag{4.1.5}$$

Taking the derivative of this expression:

$$d\delta = CdP + PdC \tag{4.1.6}$$

Substituting Equation 4.1.4 into Equation 4.1.6 yields:

$$d\delta = -\frac{\delta}{P}dP + PdC \tag{4.1.7}$$

Multiplying by force:

$$Pd\delta = -\delta dP + P^2 dC \tag{4.1.8}$$

Re-arranging terms:

$$Pd\delta + \delta dP = P^2 dC \tag{4.1.9}$$

The left hand side of Equation 4.1.9 is twice the right hand side of Equation 4.1.2. Substitution provides an expression for dU in terms of the load and the

compliance:

$$dU = \frac{P^2 dC}{2} \qquad (4.1.10)$$

Substituting Equation 4.1.10 into Equation 4.1.3 yields:

$$G = \frac{P^2}{2B}\frac{dC}{da} \qquad (4.1.11)$$

From simple beam theory for a cantilever beam:

$$\delta = \frac{8Pa_o^{\,3}}{EBt^3} \qquad (4.1.12)$$

Substituting Equation 4.1.12 into Equation 4.1.4 for the compliance yields:

$$C = \frac{8a_o^{\,3}}{EBt^3} \qquad (4.1.13)$$

Taking the derivative of compliance with respect to crack length yields

$$\frac{dC}{da} = \frac{24a_o^{\,2}}{EBt^3} \qquad (4.1.14)$$

Substituting the expression for dC/da into Equation 4.1.11 yields an expression for strain energy release rate:

$$G_I = \frac{12P^2 {a_o}^2}{EB^2 t^3}$$
(4.1.15)

The expression is often simplified by introducing displacement into the expression by substituting Equation 4.1.12 into Equation 4.1.15.

$$G_I = \frac{3P\delta}{2Ba_o}$$
(4.1.16)

The CSERR is the value of G_I at which crack growth is observed.

$$G_{IC} = \frac{3P_C \delta_C}{2Ba_o}$$
(4.1.17)

The simplified expression given in Equation 4.1.17 tends to over-estimate the value of the fracture toughness and typically correction factors are applied. Therefore ASTM D5528 recommends three data reduction techniques, each of which are considered equal. These are the Modified Beam Theory (MBT), the Compliance Calibration Method (CCM) and the Modified Compliance Calibration Method (MCCM). A description of these methods is provided in ASTM D5528 and will not be reproduced here. Data presented in this research were evaluated using the Modified Beam Theory method. Appendix A provides a comparison of variations noted in this study between the three methods.

4.1.2 Mode II Fracture Test Methods

Mode II loading, also referred to as the sliding mode, results when a force acts parallel to the plane of an existing crack. The method most commonly used to evaluate the mode II CSERR is the End Notch Flexure (ENF) test. There is currently not an ASTM standard to conduct the ENF test. However a draft is in process as of September 15, 2009 by Barry Davidson, entitled Standard Test Method for Determination of the Mode II Interlaminar Fracture Toughness of Unidirectional Fiber Reinforced Polymer Matrix Composites Using the End-Noticed Flexure (ENF) Test.

Specimens for the ENF test are prepared similarly to the mode I test method already described, but with an absence of the end tabs. During testing, the two ends of the specimen are constrained vertically, and a load is applied at a constant rate of displacement to the center of the specimen. A typical test specimen and the testing arrangement is shown in Figure 4.1.3. This is the standard 3-point loading test configuration. Load and displacement data are recorded, and the values corresponding to crack growth are noted. For Mode II testing, crack growth typically occurs in an unstable manner, resulting in significant propagation of the crack across the specimen length once crack initiation occurs [13,54,55]. Therefore there is not a unique propagation CSERR.
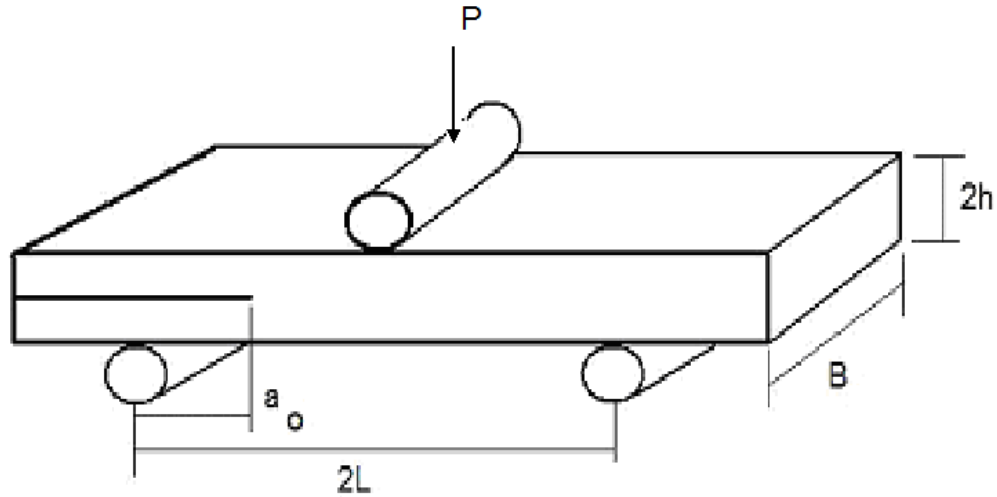
Figure 4.1.3: Mode II specimen and 3 point bend loading arrangement.

An expression for the Mode II SERR, G_{II}, can be derived by starting with Equation 4.1.11. From geometry, the compliance for the specimen arranged under 3-point loading is:

$$C = \frac{\delta}{P} = \frac{2L^3 + 3a_o^{\;3}}{8E_b Bh^3} \qquad (4.1.18)$$

Re-arranging terms:

$$\frac{1}{8E_b Bh^3} = \frac{\delta}{P(2L^3 + 3a_o^{\;3})} \qquad (4.1.19)$$

While differentiating with respect to crack length yields:

$$\frac{dC}{da} = \frac{9a_o^{\,2}}{8E_b Bh^3} \tag{4.1.20}$$

Substituting Equation 4.1.20 into Equation 4.1.11 provides:

$$G = \frac{P^2}{2B_w} \frac{9a_o^{\,2}}{8E_b Bh^3} = \frac{9P^2 a_o^{\,2}}{16E_b B^2 h^3} \tag{4.1.21}$$

And substituting Equation 4.1.19 into Equation 4.1.21 produces an expression for the mode II SERR:

$$G_{II} = \frac{9a_o^{\,2} P\delta}{2B(2L^3 + 3a_o^{\,3})} \tag{4.1.22}$$

The value for the Mode II CSERR occurs at the critical load and displacement corresponding to crack growth:

$$G_{IIC} = \frac{9a_o^{\,2} P_C \delta_C}{2B(2L^3 + 3a_o^{\,3})} \tag{4.1.23}$$

4.1.3 Mixed-Mode Fracture Test Methods

Mixed-mode loading results from the superposition of loading modes. For this study, mixed-mode loading will be limited to the case of mode I and mode II. As mentioned, the method most commonly used to perform mixed-mode testing is ASTM D6671, Standard Test Method for Mixed-mode I – Mode II Interlaminar Fracture Toughness of Unidirectional Fiber Reinforced Polymer Matrix

Composites. The method combines both the Double Cantilever Beam (DCB) mode I loading the End Notch Flexure (ENF) mode II loading test methods, and is commonly referred to as the mixed-mode bend (MMB) test. Test specimens are constructed identically as for ASTM D5528. The test arrangement of ASTM D6671 permits specimens to be tested over a range of mixed-mode loading conditions. The MMB test fixture and specimen loading arrangement is shown in Figure 4.1.4 [38].
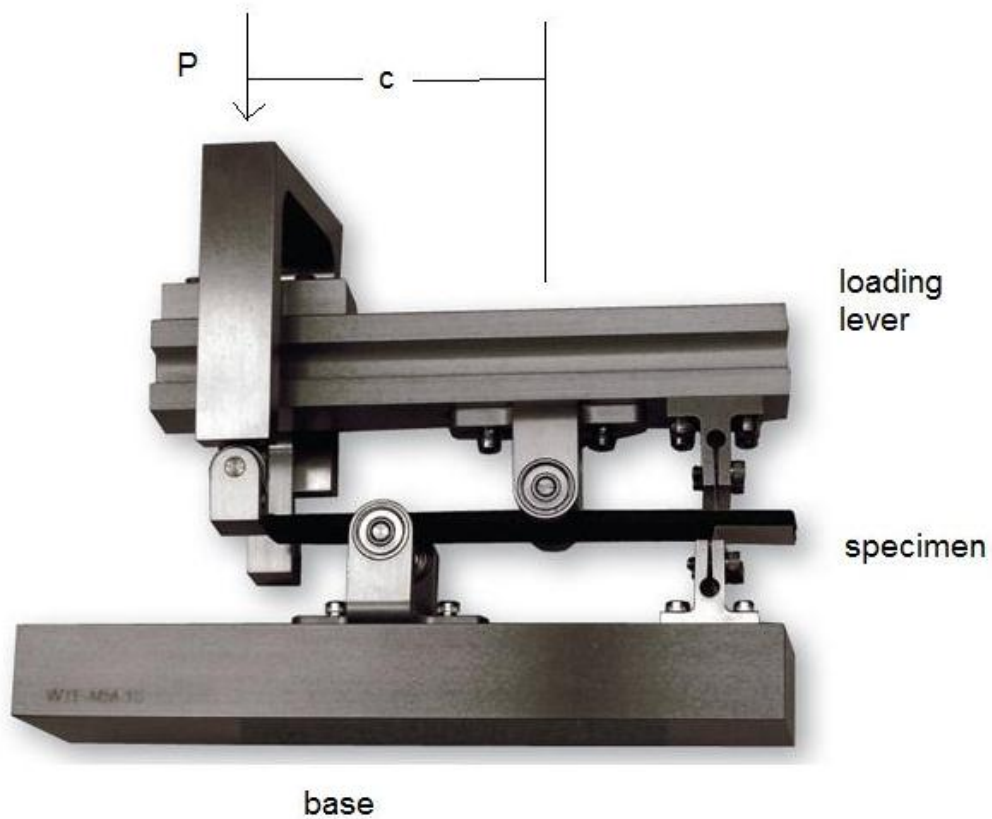
Figure 4.1.4: Mixed-mode bend test fixture with specimen.

For the MMB test, adjustment of the point along the fixture at which the load, P, is applied varies the ratio of the Mode I and Mode II loading.   Pure mode II loading occurs when the load is applied above the beam midspan, or where the dimension c, as shown in Figure 4.1.4 is equal to zero.   Mixed-mode loading is attained by increasing the loading dimension c, where a higher value of c produces a lower percentage of mode II loading.   Pure mode I loading is attained by removing the beam and applying the load directly through the hinges attached to the specimen.   The loading lever is made of aluminium to minimize the impact of the fixturing weight on the specimen, maintaining a controlled state of stress in the specimen throughout the testing duration, while simultaneously remaining rigid throughout the test.   The base is made of steel to maintain stability [9], and the bearings act to reduce friction and to ensure that all applied forces are vertical to the fixturing and that no horizontal force components are developed [38].

With the MMB test, the basic expressions to calculate the CSERR values are determined through application of simple beam theory equations and superposition of Mode I and Mode II loading.   Figure 4.1.5 illustrates the forces applied to the specimen by the test as a function of specimen geometry and the position of the applied load.   Derivation of the equations for calculating the G_{IC} and G_{IIC} components of the total CSERR is reviewed.   All derivations and expressions are taken from Reeder [9,38] and ASTM D6671, unless stated otherwise.

(a) MMB specimen loading.   (b) Mode I loading.   (c) Mode II loading.
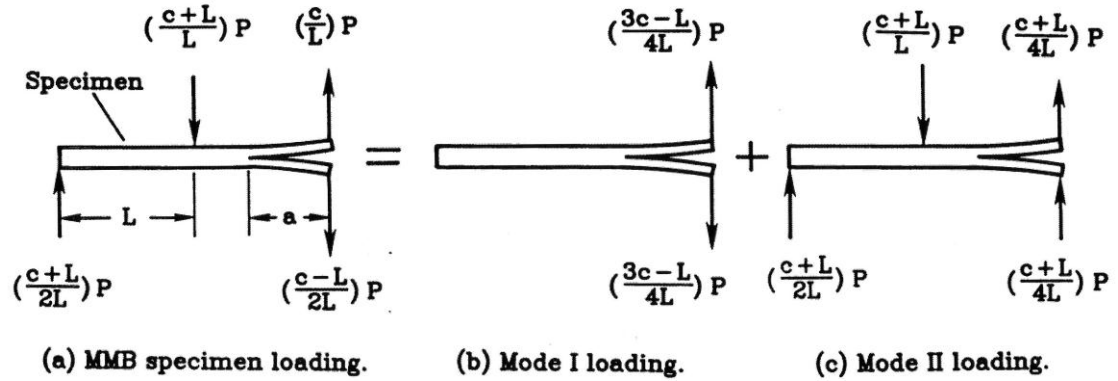
Figure 4.1.5: Mixed-mode loading through superposition of mode I and mode II loading conditions [38].

The mode I loading force component is:

$$P_1 = P\frac{3c - L}{4L} \qquad (4.1.24)$$

From simple beam theory analysis, the mode I component of the strain energy release rate is given as:

$$G_1 = \frac{12a_0^2 P_1^2}{B^2 h^3 E_{11}} \qquad (4.1.25)$$

And by substitution of Equation 4.1.24 into Equation 4.1.25 provides:

$$G_1 = \frac{\left(3a_0^2 P_1^2\right)\left(3c - L\right)^2}{4B^2 h^3 L^2 E_{11}} \qquad (4.1.26)$$

The mode II loading force component is:

$$P_{II} = P\frac{c + L}{L}$$

(4.1.27)

From Russel [56], the mode II component of the strain energy release rate is given by:

$$G_{II} = \frac{\left(9a_0{}^2 P_{II}{}^2\right)}{16B^2 h^3 E_{11}}$$

(4.1.28)

And by substitution of Equation 4.1.27 into Equation 4.1.28 yields:

$$G_{II} = \frac{\left(9a_0{}^2 P_{II}{}^2\right)(c+L)^2}{16B^2 h^3 L^2 E_{11}}$$

(4.1.29)

Dividing Equation 4.1.29 into Equation 4.1.26, the G_I / G_{II} ratio is given as:

$$\frac{G_I}{G_{II}} = \frac{4}{3}\left(\frac{3c-L}{c+L}\right)^2$$

(4.1.30)

This expression is valid where the point of loading $c \geq L/3$. At $c = L/3$ the expression is equal to zero. Therefore the expression is not valid for $c < L/3$. Conveniently, the ratio of G_I to G_{II} is only a function of c and L.

The Equation for the total critical strain energy release rate can be found by adding Equation 4.1.29 and Equation 4.1.26 and substituting the critical load:

$$G_C = G_I + G_{II} = [4(3c-L)^2 + 3(c+L)^2]\frac{3a_0{}^2 P_c{}^2}{16B^2 h^3 L^2 E_{11}}$$

(4.1.31)

Equation 4.1.31 under estimates the value of the CSERR by about 15% [39]. Most of this error results from the assumptions made in calculating the mode I component. The simple beam theory presented makes the assumption that the two arms of the specimen are fixed against rotation at the delamination tip. This is not the actual case. In fact, they do rotate slightly due to the elastic support that they provide one another. This effect was studied by Kanninen [57]. There is also a shear deformation energy associated with bending, which was analyzed by Aliyu and Daniel [58]. The shear deformation energy also contributes to the Mode II strain energy term. This was studied by Carlsson et al. [59]. Applying these modifications to the original equations produces a set of expressions which more accurately capture the stress state specimens experience during testing. Comparison of CSERR values calculated with these expressions from experimental data to those predicted by Finite Element Analysis found the calculated values accurate to within approximately 6%.

The final form of the expressions for calculating the mode I and mode II CSERR components as provided in ASTM D6671 are given below, and reflect further refinements performed to improve the precision of the calculations. These corrections are based on research performed by Williams [60], Wang and Williams [61] and Kinlock and Wang [62]. Crack length correction parameter, χ_C, and a transverse modulus correction parameter, Γ_C, were introduced.

$$G_I = \frac{12 P_c^2 (3c - L)^2 (a_0 + \chi_c h)^2}{16 B^2 h^3 L^2 E_{1f}}$$ (4.1.32)

$$G_{II} = \frac{9 P_c^2 (c + L)^2 (a_0 + 0.42 \chi_c h)^2}{16 B^2 h^3 L^2 E_{1f}}$$ (4.1.33)

Where:

$$E_{1f} = \frac{8(a_0 + \chi_c h)^3 (3c - L)^2 + [6(a_0 + 0.43 \chi_c h)^3 + 3L^3)(c + L)^2}{16 L^2 B h^3 \left(\dfrac{1}{m} - C_{sys} \right)}$$ (4.1.34)

$$\chi_C = \sqrt{\frac{E_{11}}{11 G_{13}} \left(3 - 2 \left(\frac{\Gamma_c}{1} + \Gamma_c \right)^2 \right)}$$ (4.1.35)

$$\Gamma_c = 1.18 \left(\frac{\sqrt{E_{11} E_{22}}}{G_{13}} \right)$$ (4.1.36)

The final expressions for the mode I and mode II components of CSERR account for both the elastic interactions between the two arms of the specimen and the shear deformations. The test maintains a high degree of consistency in the ratio G_I/G_{II} as the delamination extends, keeping the ratio within 5%. Though this test method was designed for testing unidirectional laminates, the test is applicable to woven laminates [9].

4.2 Methods

4.2.1 Specimen Preparation

Two E-glass/epoxy CFP composites were fabricated. A 17.8 oz/yd^2 unidirectional (UD) E-glass fabric, style TG-18-U, supplied by J B Martin (St-Jean-sur-Richelieu, Quebec, Canada) was selected as the reinforcement. The matrix consisted of a two-part epoxy supplied by Crosslinks Technology (Toronto, Ontario, Canada), consisting of 100 parts of CLR 1180 and 30 parts CLH6560. Specimens were constructed by the hand lay-up technique. UD plies were aligned by hand on a sheet of vacuum bag material and saturated with resin by pouring the resin evenly over the surface and spreading with a 25 mm paint brush. Subsequent plies are applied similarly. During the lay-up process, a 20 μm Teflon (polytetrafluoroethylene (PTFE)) -coated polymer film was inserted between the center plies to act as a crack initiator, per ASTM D6671. The lay-up was sealed inside the vacuum bag material with high temperature tape and inserted into a heated platen press and cured at 120 °C for 90 minutes, per the resin curing instructions.

Two UD composites were constructed with the same reinforcement and resin by varying the pressure of the heated platen press. Curing at 200 Pa resulted in a layered structure (UD-L) that maintained resin rich layers between each ply. While curing at 400 Pa produced a cross-section with a continuous reinforcement distribution (UD-H), for which plies are no longer discernible as separate. Figure 4.2.1 shows an SEM micrograph of the cross-section of UD-L with a resin rich layer between plies. The resin rich layer was typically between 300 and 340 μ in

thickness. Figure 4.2.2 shows UD-H, with adjacent plies fused together and the

absence of a resin rich layer.
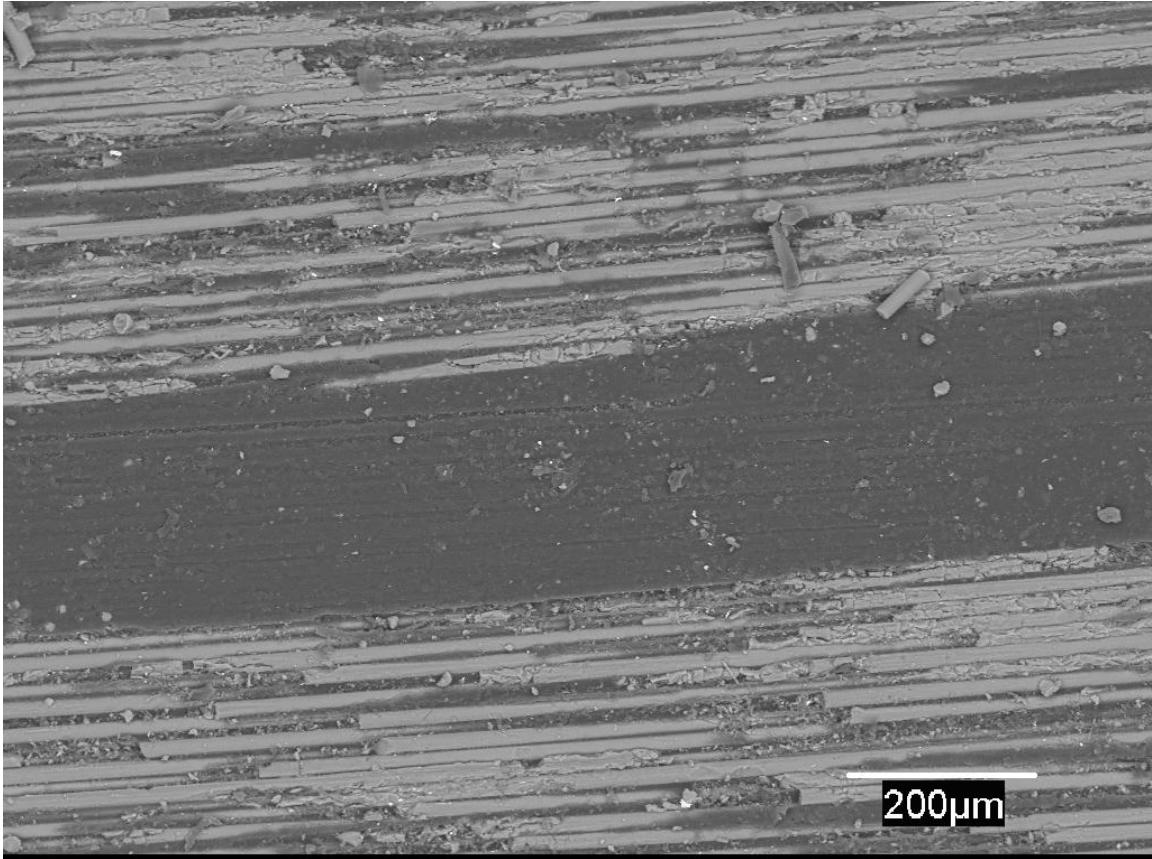
Figure 4.2.1: SEM micrograph of the cross-section of UD-L with a resin rich layer between plies. The resin rich layer was typically between 300 and 340 µm in thickness.
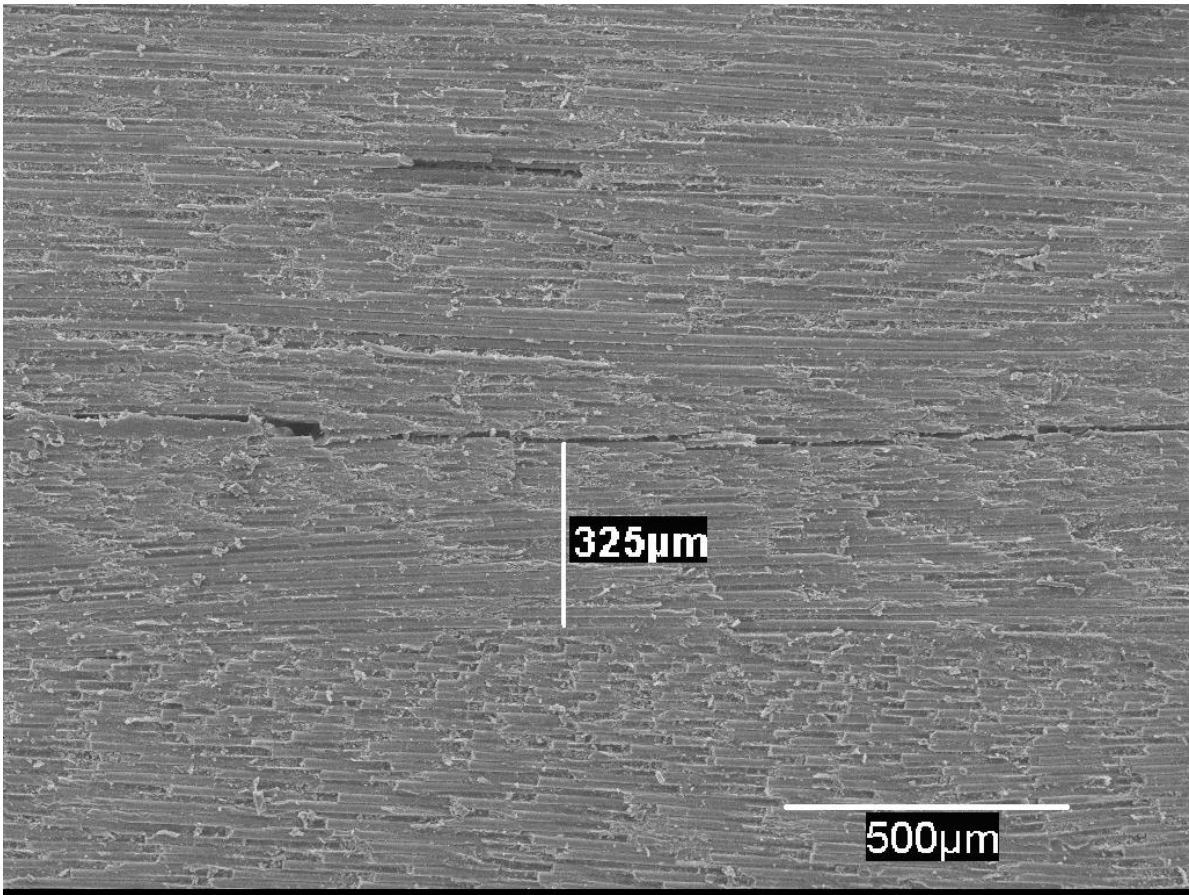
Figure 4.2.2: SEM micrograph of the cross-section of UD-H, with fused plies and no resin rich layer.

Specimens were prepared in compliance with ASTM D5528 and D6671, for which the specimen geometry is identical. Specimens were cut from the composite materials by using a table saw with a fine steel blade. Cut surfaces were ground and polished so that the specimen length and width were maintained within a tolerance of +/- 1% across the specimens. Specimen dimensions were 150 mm in length, 25 mm in width, and ranged in thickness between 3.5 mm and 4 mm. Piano hinge was cut to lengths of 25 mm and attached to the specimens with a two-part epoxy glue. The surfaces of both the

hinges and the specimen were prepared by sanding with 600 grit sandpaper and wiping clean with methanol.

Initial testing resulted in frequent debonding of the hinges prior to test termination. Therefore a wide range of commercial and industrial adhesives were evaluated to determine which adhesive provided the maximum bond strength. Huntsman Araldite 2011 high-strength epoxy was determined to provide the strongest bond between the metal hinges and the composite specimens. White-out was applied to one edge of each specimen to facilitate observation of the fracture growth, as recommended by ASTM D6671.

4.2.2 Testing

Mixed-mode fracture testing of the UD composites was performed in compliance with ASTM D5528 and D6671. Load was applied at a constant crosshead rate of 5 mm/min using a servo-hydraulic load frame with a 5000 Newton load cell. From the manufacturer's information it was found that the load cell is accurate for loads greater than 1% of the load cell capacity, or 50 Newtons.   Crack growth was observed and recorded using a magnifying lamp and a finely marked steel measurement gauge with 1 mm increments. Fracture tip growth was recorded as a function of the load and displacement as indicated by the load cell and cross-head movement of the load frame. Testing was performed on UD specimens at 0%, 25%, 50%, 75% and 100% mode II loading. A minimum of five specimens were tested per material for each mixed-mode condition.   The CSERR was calculated for each specimen tested per the methodology provided in ASTM D6671.

A typical mixed-mode load-displacement curve for the UD composites tested in this study is shown in Figure 4.2.3. The load-displacement curve is consistent with that described in ASTM D6671. Load increases linearly until near the maximum load, at which non-linear behaviour is observed. Following the maximum load, corresponding to delamination growth, the load drops off abruptly. CSERR values are calculated from the maximum load for each specimen tested. The force required to induce delamination in the UD specimens can be seen to be in the hundreds of Newtons. The resolution for the data is high, showing the capacity of the 5000 Newton load cell to be accurate above 1% of the load cell capacity.

As per ASTM D6671 for pure mode I testing, the fixture is removed and mode I testing is performed per ASTM D5528. Both ASTM D6671 and ASTM D5528 specify that a pre-crack is not required. Round robin activities regarding the use of pre-cracks found that their presence did not influence the measurements [38]. Additional studies [9] also found that the presence of a pre-crack did not affect the mode I initiation CSERR or propagation CSERR. Therefore a pre-crack was not introduced for the mode I and mixed-mode specimens.
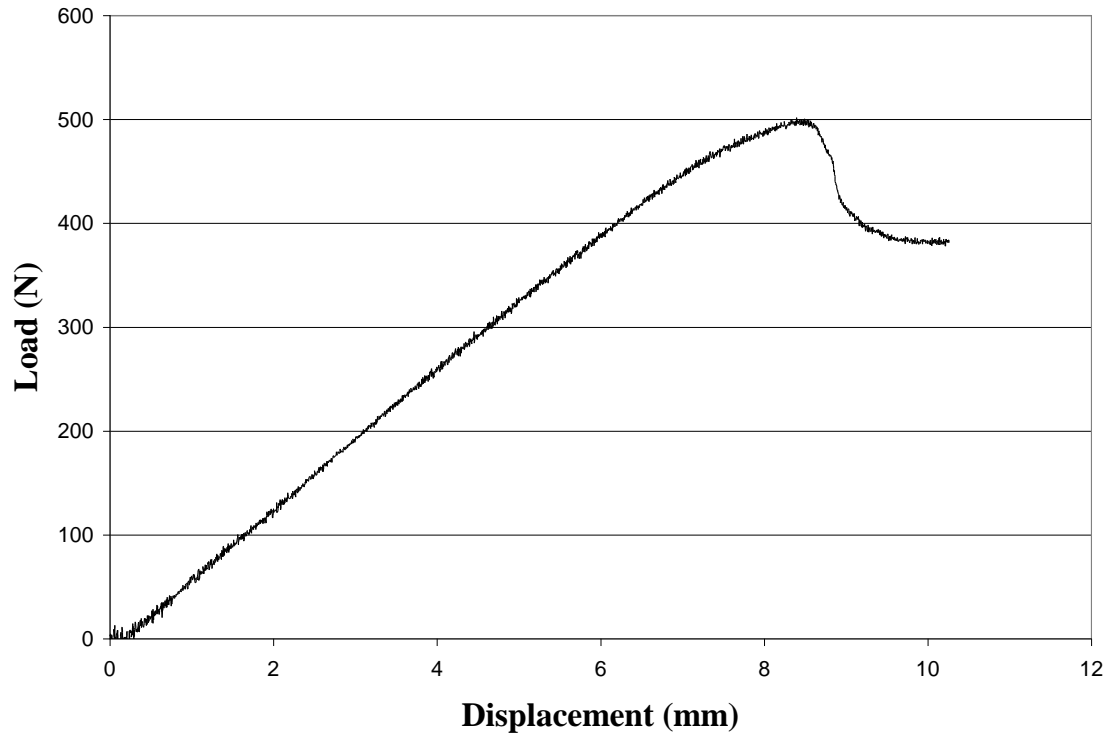
Figure 4.2.3: A typical load-displacement curve for UD composite following mixed-mode bend testing. The data shown is for UD-H subjected to 80% mode II mixed-mode loading.

4.3 Results

4.3.1 Delamination of UD-L

The measured CSERR values as a function of mixed-mode loading for UD-L is shown in Figure 4.3.1. The CSERR increases noticeably with increasing mode II loading. The average pure mode II CSERR for UD-L is 236% greater than that of pure mode I.
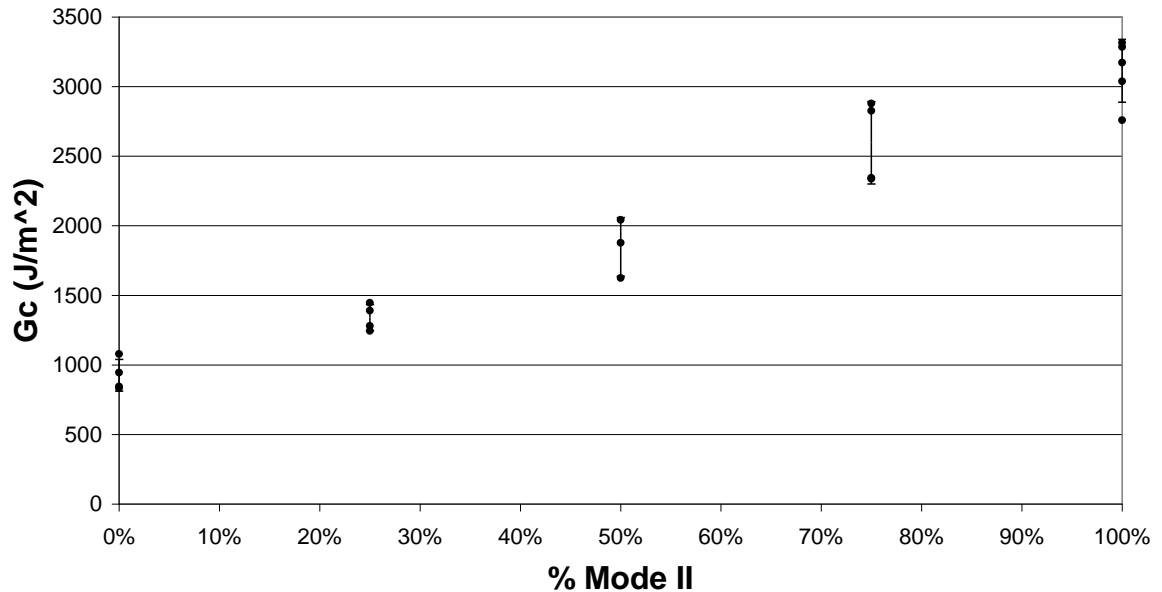
Figure 4.3.1: Critical strain energy release rate, G_C, vs. percent mode II loading of UD-L.

Examination of the fracture surface by scanning electron microscopy (SEM) determined that UD-L delaminated by interyarn failure at and below 25% mode II loading, and by interply failure at and above 50% mode II loading. It was also observed that the depth of interyarn failure within the ply decreased as the mode II loading increased, causing the interyply cracking to progress from approximately the center of the fiber bundle for 0% mode II loading, to near the fiber/resin interface for 25% mode II loading. This is shown in Figures 4.3.2 through 4.3.5. To confirm that the edge appearance was characteristic of the crack through the entire specimen thickness, specimens were mounted in polyester and incrementally ground down through the specimen cross-section. No variation in cross-sectional morphology was observed.
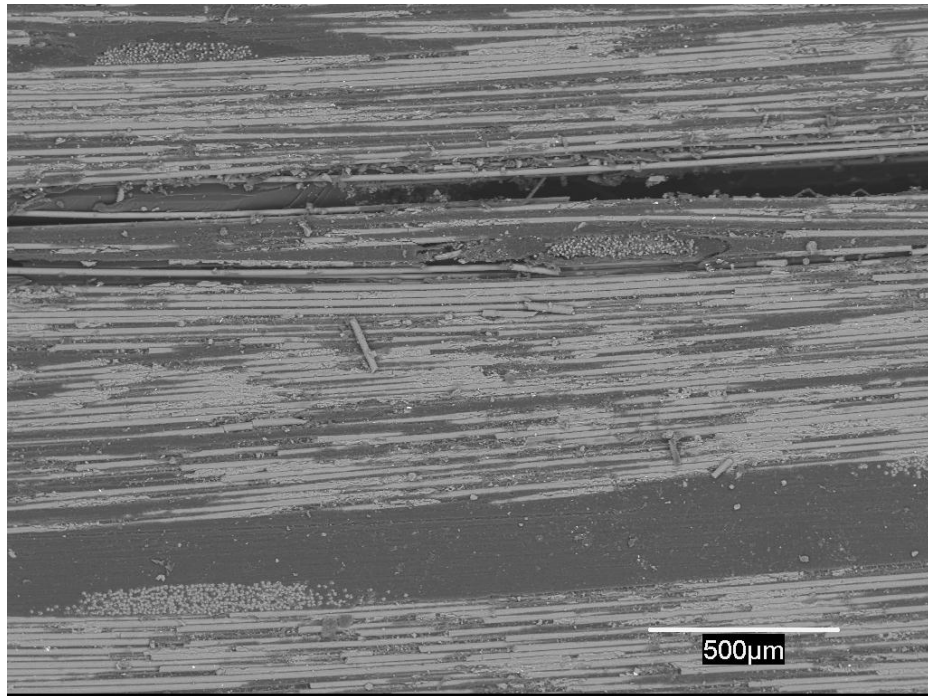
Figure 4.3.2: Edge SEM micrograph of 0% mode II loading specimen with delamination occurring by interyarn failure deep within the yarn bundle.
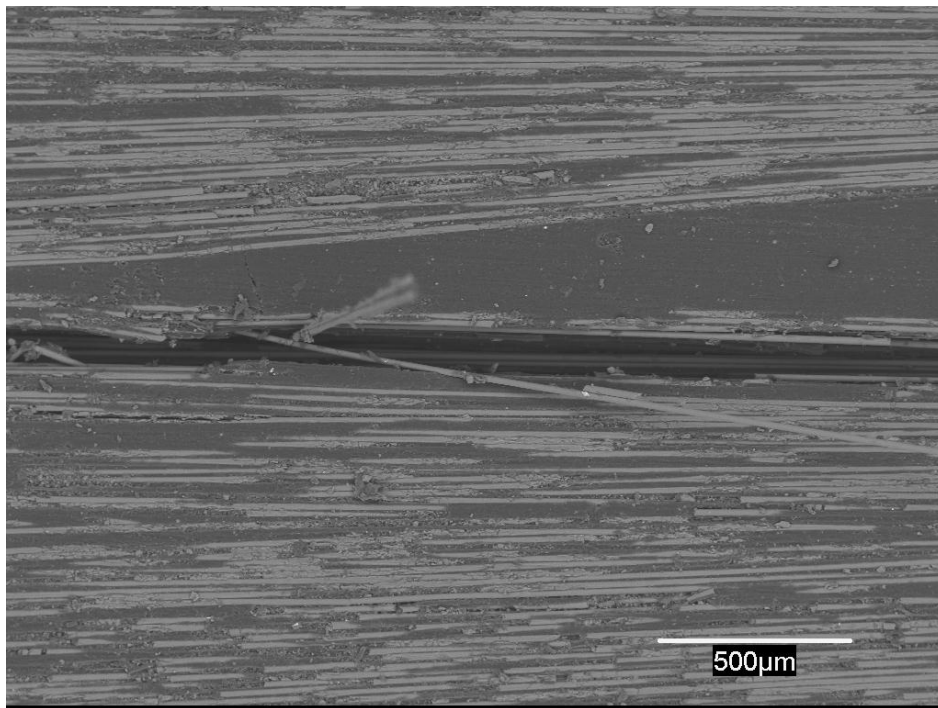
Figure 4.3.3: Edge SEM micrograph of 25% mode II loading specimen with interyarn failure occurring within the yarn bundle very near resin rich layer.
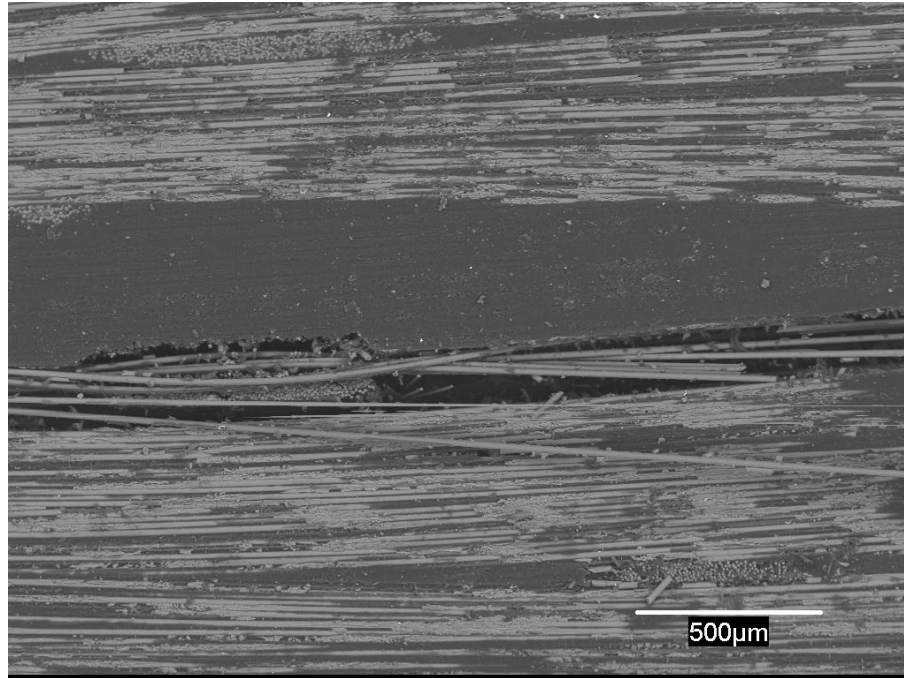
Figure 4.3.4: Edge SEM micrograph of 50% mode II loading specimen with delamination occurring at interface between yarn and the resin rich layer between plies.
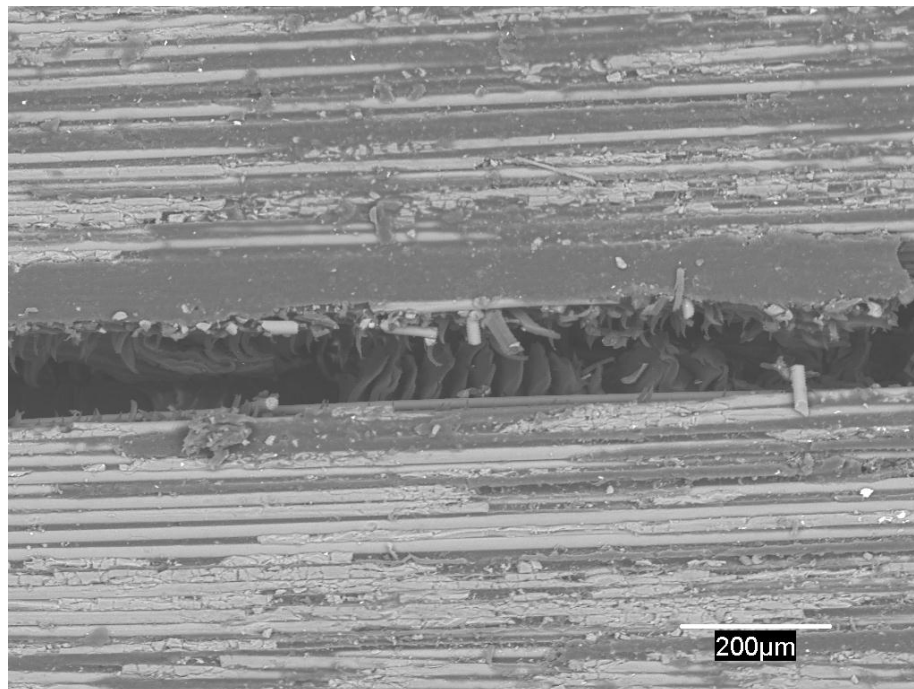
Figure 4.3.5: Edge SEM micrograph of 100% mode II loading specimen with delamination occurring at interface between yarn and the resin rich layer between plies. Hackling can clearly be discerned.

Where interyarn failure occurred (within a yarn), both fracture faces were fiber rich. Where interply failure occurred (at the yarn/resin rich layer interface), a fiber rich face and a resin rich face were observed. These are shown in Figures 4.3.6 and 4.3.7. Debonding between filaments and resin can be seen to occur cleanly at the interface, involving very little tearing out of resin or filament material. For lower mode II loading, hackle angles are shallow, and hackling is intermittent, with large cleavage fracture regions between hackles. This can be seen in Figure 4.3.6. Hackle formation increases in frequency and angle as the mode II loading component increases, as shown in Figure 4.3.8. No crack path branching or crack migration is observed to occur for either interyarn or interply delamination.
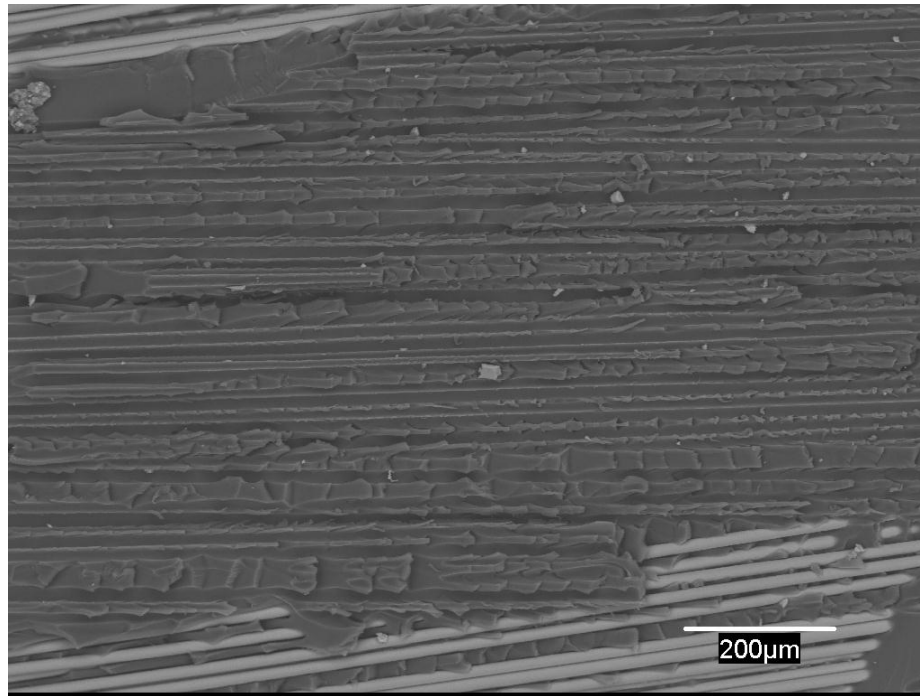
Figure 4.3.6: Surface SEM micrograph of resin rich delamination face of 50% mode II loading specimen. Resin with extracted filaments exhibiting some hackle formation is evident. Embedded filaments appear in the bottom region.
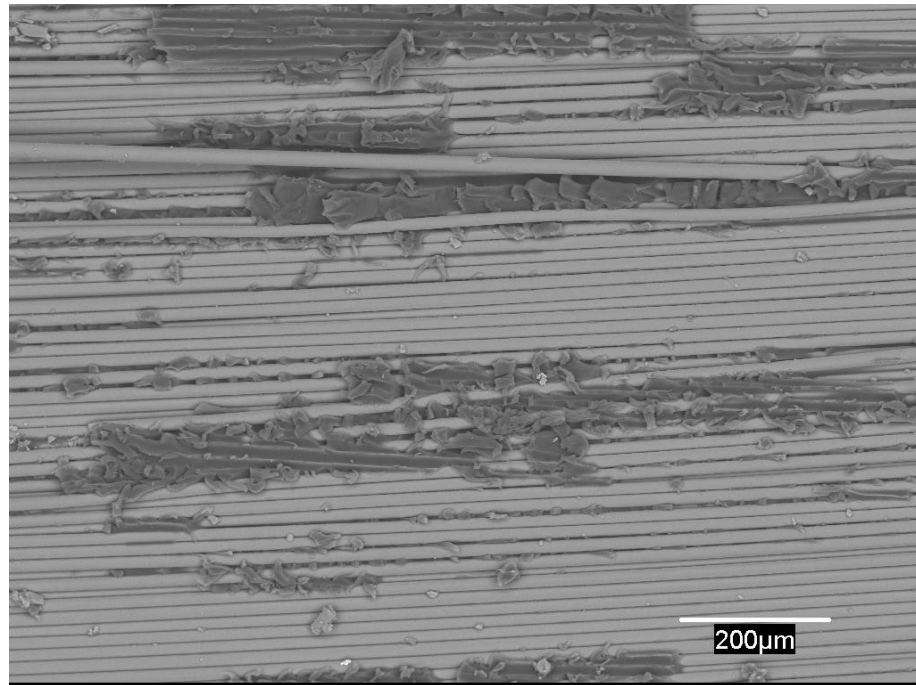
Figure 4.3.7: Surface SEM micrograph of fiber rich delamination face of 50% mode II loading specimen.
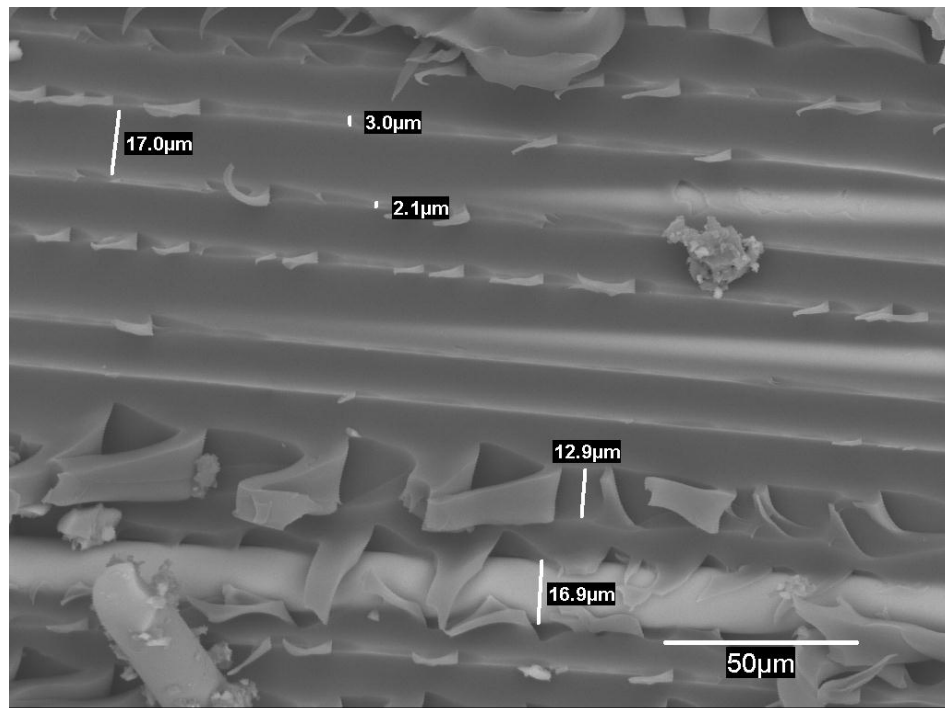
Figure 4.3.8: Surface SEM micrograph of resin rich delamination face of 100% mode II loading specimen. Dimensions of important features are noted. The high frequency of hackling and the steep hackle angle is evident.

4.3.2 Delamination of UD-H

The CSERR curve as a function of mixed-mode loading for UD-H is show in Figure 4.3.9. The CSERR of UD-H was relatively insensitive to loading mode and increases only slightly with increased mode II loading. The average pure mode II CSERR is only 25% greater than the average pure mode I CSERR. The CSERR of UD-L is in general larger than that for the UD-H. The average pure mode I CSERR for UD-L is 50% greater than for UD-H. While the average pure mode II CSERR for UD-L is 305% greater than for UD-H.
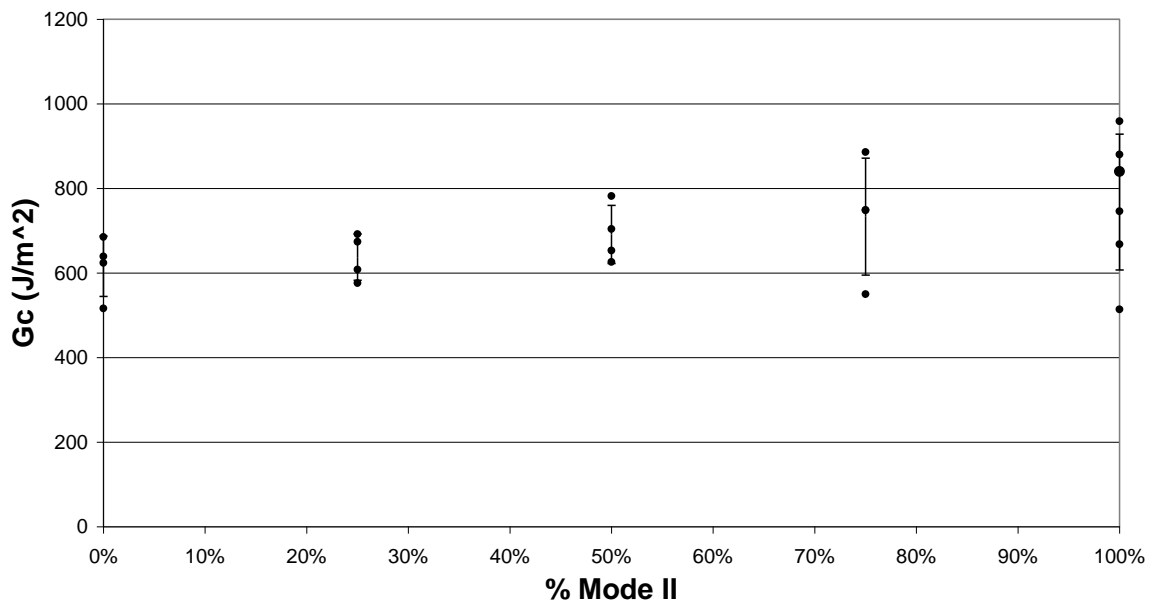
Figure 4.3.9: Critical strain energy release rate, G_C, vs. percent mode II loading of UD-H.

Scatter in the CSERR data for UD-L and UD-H is typical for mixed-mode bend testing. In general, the scatter increases as the percentage of mode II loading increases. High scatter in the data for mixed-mode bend testing of composites is

well documented [44]. It has been proposed that the scatter is due to the variations in alignment of yarns in successive plies resulting from hand lay-up techniques [44]. The particularly high Mode II scatter is typically attributed to the highly unstable nature of mode II fracture [44].

Examination of the fracture surface of the specimens following testing with a scanning electron microscope confirms that UD-H composite delaminated by interyarn failure for all loading conditions. This occurs due to the UD-H not having a distinct laminated structure with a resin rich layer between plies. Therefore the entire composite behaves similar to a single yarn. Interyarn failure within the yarn is shown in Figure 4.3.10.
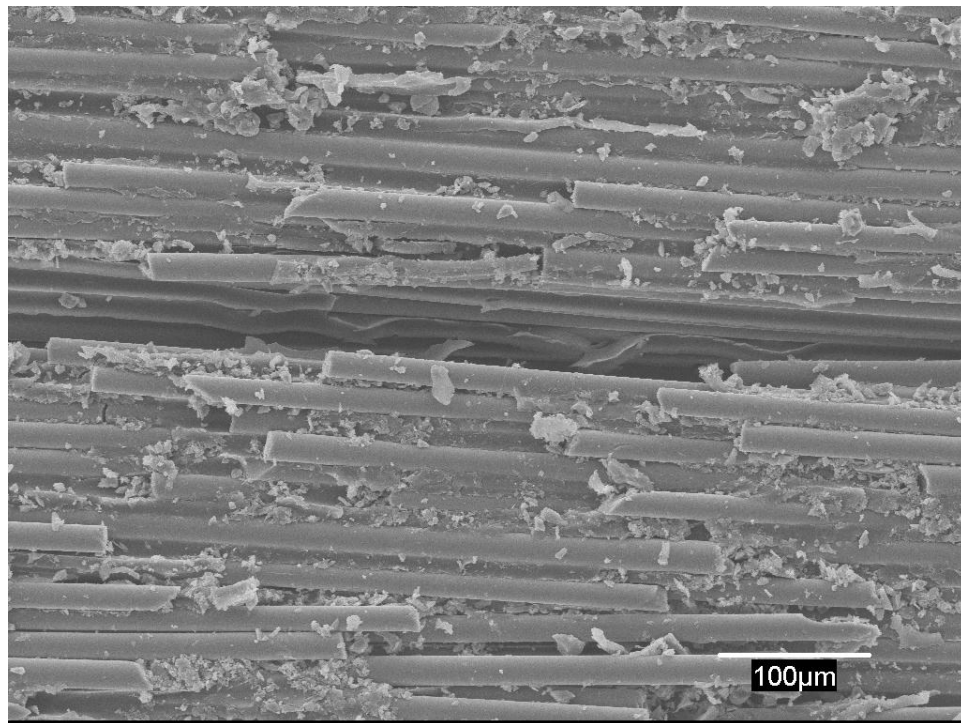
Figure 4.3.10: Edge SEM micrograph of 0% mode II loading specimen showing the typical cross-section appearance of interyarn failure through the UD-H composite. The appearance of some limited plastic deformation of the resin at the interface is evident.

No crack path branching or crack migration is observed to occur. Hackle formation is evident in Figure 4.3.11 as the mode II loading component increases.
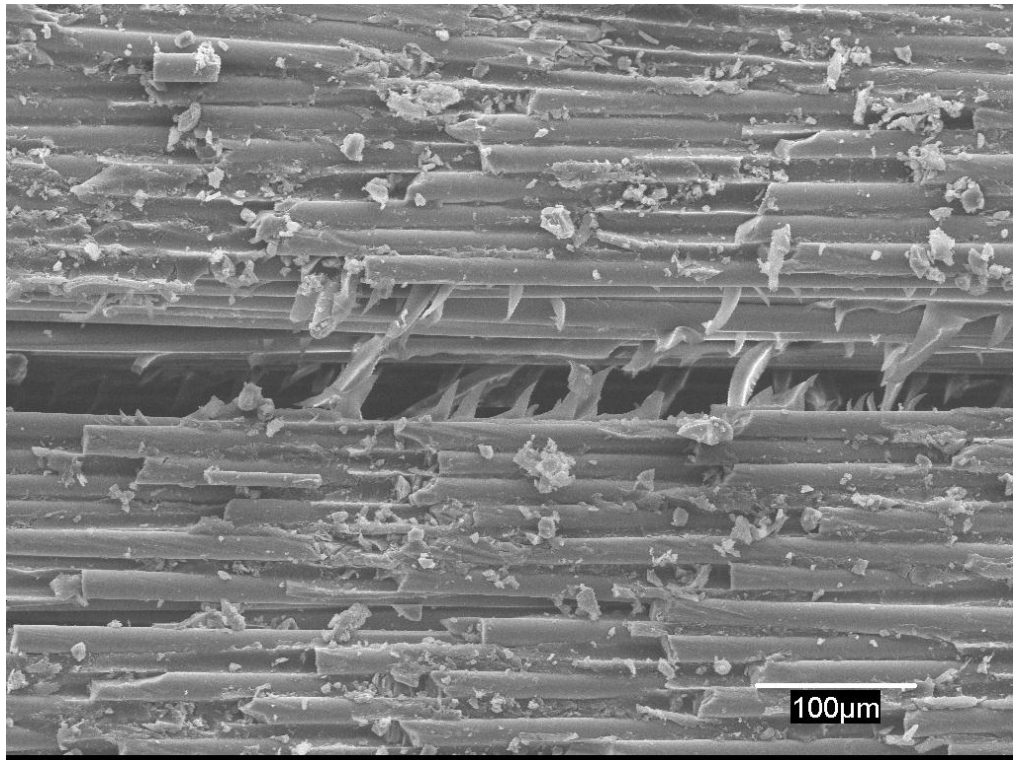
Figure 4.3.11: Edge SEM micrograph of 100% mode II loading specimen showing hackling.

SEM analysis determined that the thickness of resin occupied space between filaments was significantly thinner for interyarn failure than was observed for interply failure.   For interyarn failure, the spacing varied from 1.5 to 12 µm, with an average spacing of approximately 7 µm. This can be seen in Figure 4.3.12. As can be seen in Figures 4.3.6 and 4.3.8, the resin thickness between filaments for interply failure is on average wider - ranging from 3 µm to over 45 µm, with an

average spacing of approximately 25 μm. The range in spacing between

filaments observed in interyarn failure is most probably a result of variation in the

degree of yarn twist during manufacturing. While the broader range evident in

interply failure appears to be the consequence of the boundary effects, in which

filaments at the boundary between the plies and the resin rich layer are not

constrained by adjacent filaments, and therefore permitted to spread out with

respect to each other.
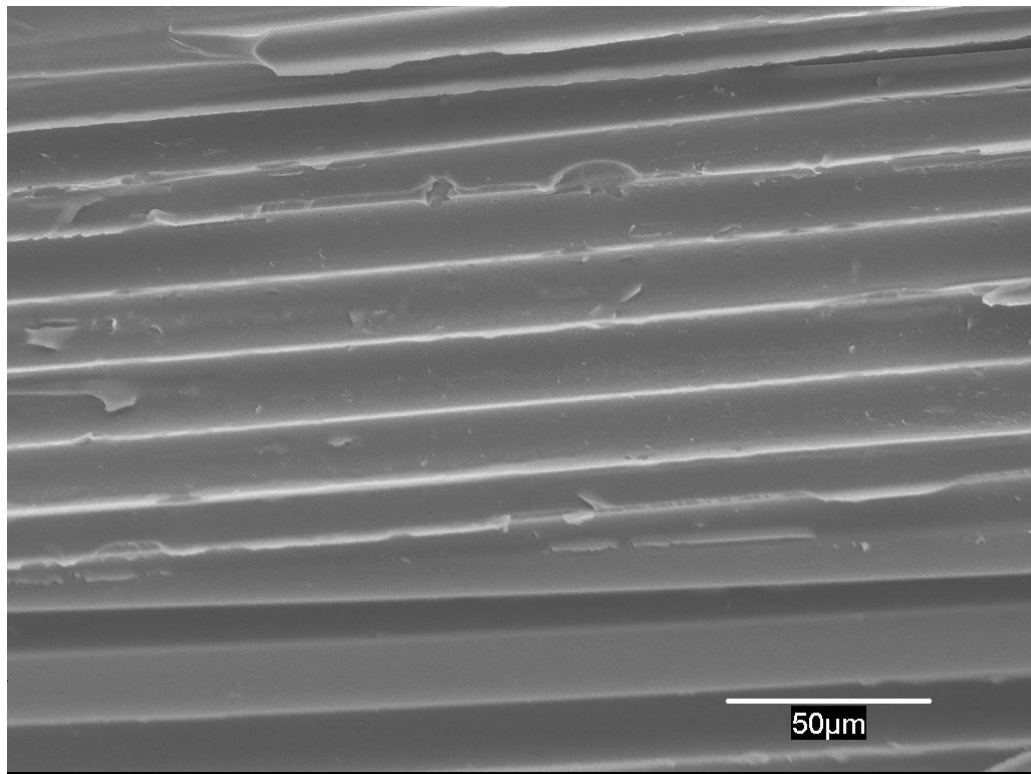
Figure 4.3.12: Surface SEM micrograph of 0% mode II loading specimen showing resin rich delamination face. Resin with extracted filaments without hackle formation is evident.

4.4 Discussion

4.4.1 Crack Initiation and Growth

Crack initiation is observed to occur through the formation of microcracks for all mixed-mode ratios. With increasing load, the microcracks coalesce into a visible crack that remains tightly closed. For pure mode II loading, crack growth is unstable due to test instability, and occurs rapidly across the specimen width once a critical load is reached. However, for all other mixed-mode ratios, with increasing load, the crack is observed to grow incrementally toward and then along the upper ply. It is assumed that the crack remains closed as fracture has not occurred across the entire specimen crack width. Crack opening is observed to occur at a critical load, after which the load rapidly drops. At this point, continuous fracture has occurred across the entire width of the delamination face. The critical load at which crack opening is observed always is the maximum load measured for each specimen tested. Micrographs showing a typical crack prior to and following opening are shown in Figure 4.4.1.
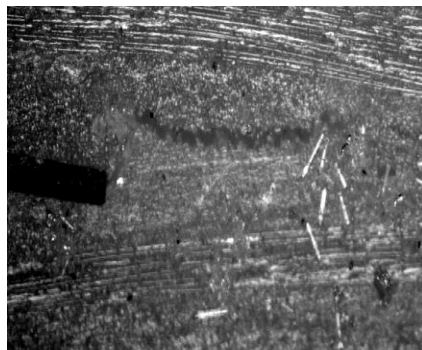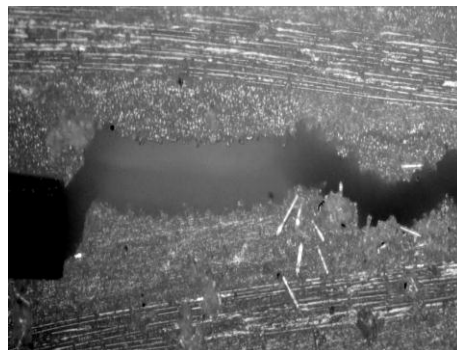
(a)   (b)

Figure 4.4.1. Micrographs of fracture formation steps; (a) micro-crack formation and coalescence; (b) coalescence across the full specimen width, resulting in crack opening.

With further loading, the process of the formation of a closed crack from the tip of the open crack, crack extension, and crack opening repeated. The process of fracture initiation and growth is shown in Figure 4.4.2. The point of each transition is shown with respect to a typical load-displacement curve. Load was recorded when the closed crack became visible, at each incremental growth of the crack, and when the crack was observed to open. CSERR's provided in Figures 4.3.1 and 4.3.8 were calculated using the maximum measured load.

Pre-existing crack   Resin rich layer between plies   UD ply

(A)

(B)

(C)

(D)
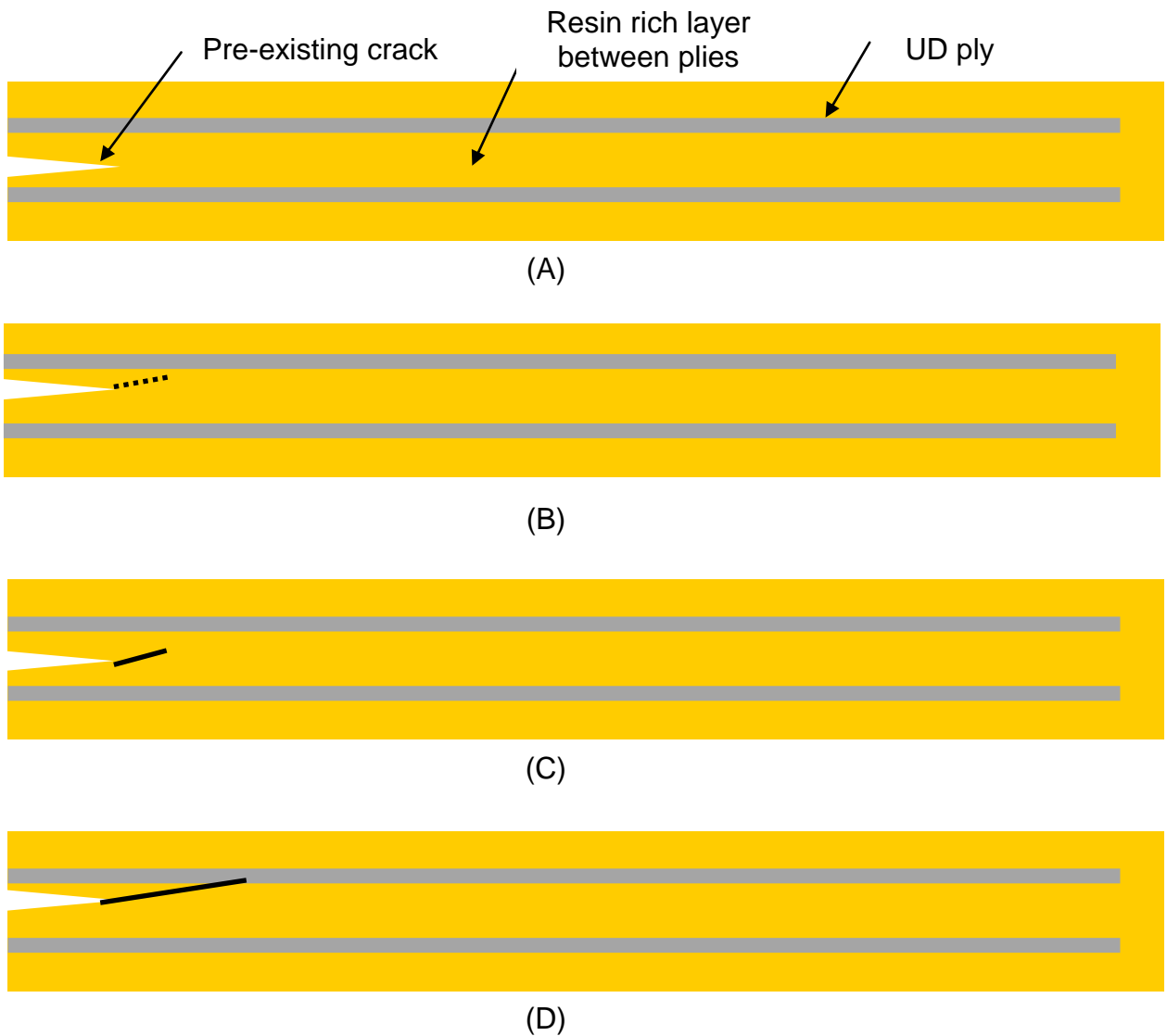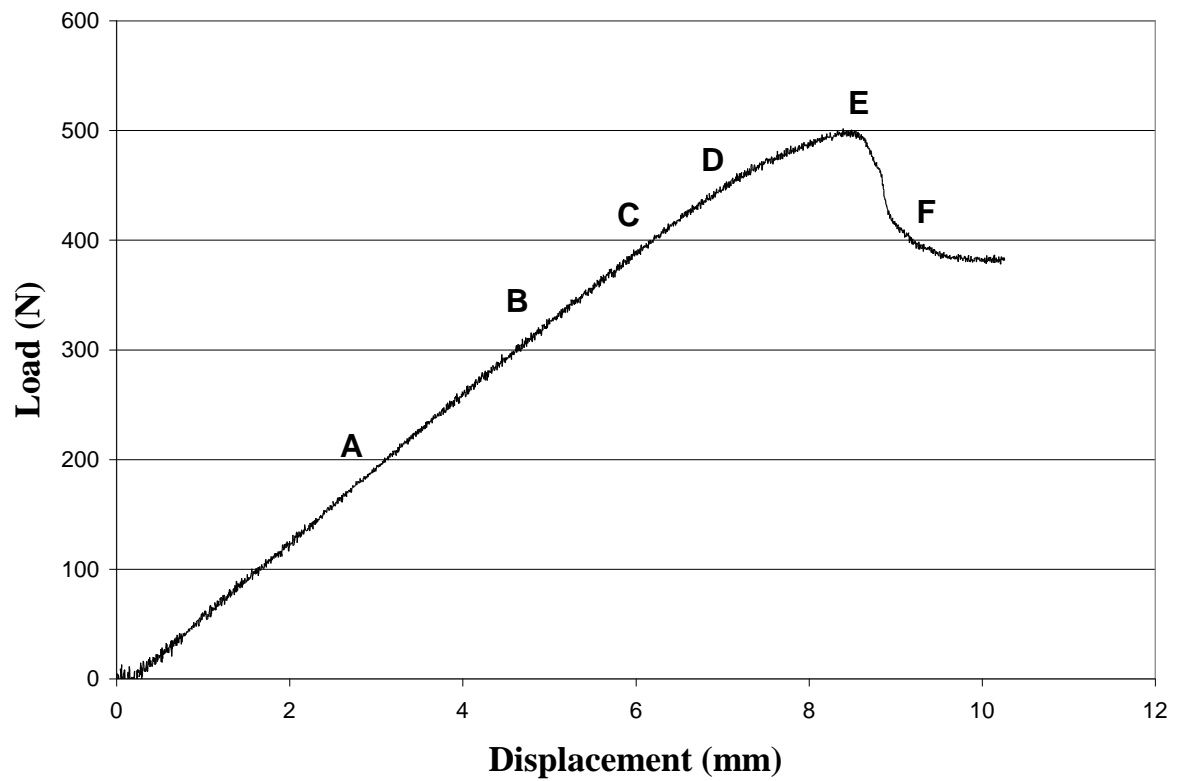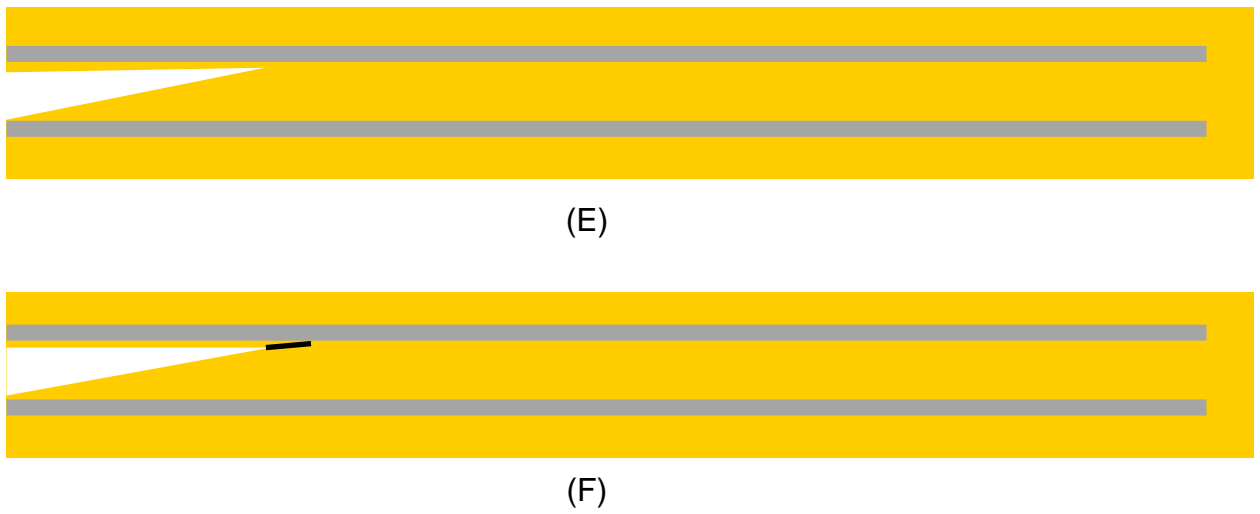
Figure 4.4.2: Illustration of the crack formation process in UD-L with corresponding points for each stage illustrated along a typical load-displacement curve for the material; A) UD-L composite with pre-existing crack; B) Micro-crack formation; C) Visible crack formation; D) Incremental growth of closed crack; E) Crack opening; F) Propagation by repeating of process.

4.4.2 Delamination Surface Morphology

Investigation of the surface morphology of UD composites following delamination demonstrates that there are only two failure processes involved for both interyarn and interply failure. These are debonding of the filaments from the resin, and fracture of the resin between filaments. Debonding results in filament extraction from the surrounding matrix. Resin fracture may involve a level of hackle formation. The only significant difference observed between interyarn and interply failure was the thickness of the resin between the filaments. These two failure processes are the key energy absorbing processes involved in delamination. The energy absorbed during delamination can therefore be evaluated by accumulation the energy associated with debonding and resin fracture over their respective areas of the fracture surface.

The respective area associated with these two processes can be defined through a simplified cross-section of the delamination surface of a UD composite, as illustrated in Figure 4.4.3. Fiber debonding occurs along the pockets from which filaments are extracted, while resin fracture occurs along the material between adjacent filaments. The filament debond length, L_e, is equal to the filament diameter, D_f, multiplied by the value of $\pi/2$. The resin fracture length, L_s, is the distance between adjacent filaments. Total fracture length is equal to the sum of debond length, L_e, and the filament spacing, L_s. Note that this value will exceed the unit fracture length, L_u, which is equal to the fiber diameter, D_f, and the Filament Spacing, L_s. The ratio of fiber dedond length per unit crack length, F_f, is

then equal to L_e/L_u, and the ratio of resin debond length per unit crack length, F_r, is equal to L_s/L_u.
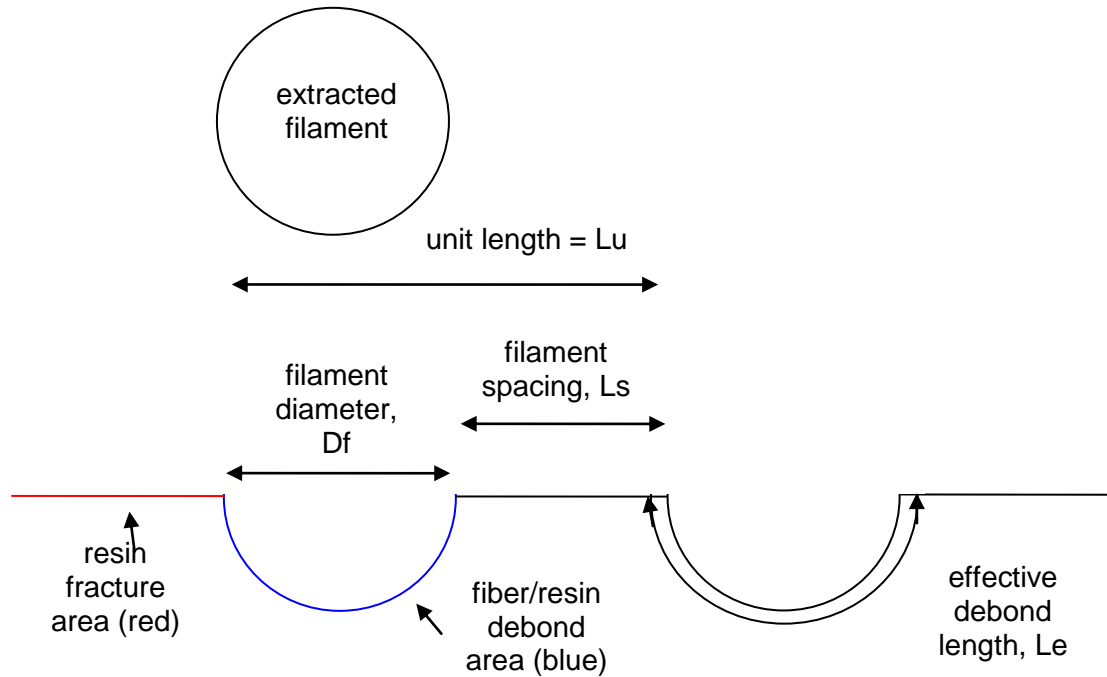
Figure 4.4.3: Illustration of the relationship between filament diameter and spacing.

4.5 Summary

Mixed-modes testing was performed on two glass – epoxy composites. The CSERR associated with delamination was measured over a range of mixed-mode conditions. The process by which crack initiation and growth occurred was observed and characterized. The occurrence of interyarn and interply failure was investigated and described. For a laminated CFP composite, delamination occurred by interyarn failure for low mode II loading, and by interply failure for high mode II loading. Therefore a unique mixed-mode loading condition exists at

which a transition occurs from interyarn to interply failure. It was noted that the

thickness of the resin between filaments was appreciably wider for interply failure

than it is for interyarn failure.

5. FABRIC COMPOSITE STUDIES

5.1 Introduction

Woven fabric polymer composites possess higher fracture resistance than uni-directional composites and therefore are preferred in the design of blast resistant structures. In an effort to investigate the failure mechanisms associated with delamination, fabric composites are fabricated and tested in accordance with the mixed-mode bending test. The behaviour of the delamination process has been investigated, and the unique energy absorbing processes associated with the delamination of fabric composites are characterized.

5.2 Methods

5.2.1 Specimen Preparation

Two fabric - epoxy composite materials were constructed and tested. These were an 8-harness satin weave E-glass fabric with a high toughness epoxy (8HHT), and a plain weave E-glass fabric with a low toughness epoxy (PWLT). The 8HHT specimens were fabricated with pre-preg manufactured by Fibercote Industries (E-glass/E-766B). The pre-preg consisted of an 8-harness 7781 satin weave E-glass fabric pre-impregnated with E-776B toughened epoxy. The diameter of the E-glass filaments as determined by SEM wass 6 µm. PWLT was fabricated with pre-preg manufactured by SP Epoxy. The pre-preg consists of a plain weave E-glass fabric pre-impregnated with a SE84LV non-toughened

epoxy. The diameter of the E-glass filaments as determined by SEM ranged between 9 and 12 μm.

The fabric composites were constructed by cutting the pre-preg into 250 mm by 300 mm squares. The squares were layered and aligned by hand onto a sheet of vacuum bag material. Orientation of the squares was maintained to ensure fiber direction and the face-up side of the material was consistent. During lay-up, a 20 μm Teflon (polytetrafluoroethylene (PTFE)) coated polymer film was inserted between the center plies as a crack initiator, per ASTM D6671. The composite materials were wrapped in vacuum bag material, sealed with high temperature tape and placed into a heated platen press. The materials were cured at the manufacturers recommended temperature, pressure and duration. The cure cycles are 90 minutes at 120° C and 310 Pa for the Fibercote system, and 60 minutes at 120° C and 600 Pa for the SP Epoxy system.

Specimens were prepared in compliance with ASTM D6671, and cut from the composite materials by using a table saw with a fine steel blade. Cut surfaces were ground and polished so that the specimen length and width were maintained within a tolerance of +/- 1% across the specimens. Specimen dimensions were 150 mm in length, 25 mm in width, and ranged in thickness between 3.5 mm and 4 mm. Piano hinge was cut to lengths of 25 mm and attached to the specimens with a two-part epoxy glue. The surfaces of both the hinges and the specimen were prepared by sanding with 600 grit sandpaper and wiping clean with methanol. White-out was applied to one edge of each

specimen to facilitate observation of the fracture growth, as recommended by ASTM D6671.

Efforts were made to measure the mechanical properties of the neat resins used to manufacture the pre-preg fabric material, but these were unsuccessful. The epoxy used in the PWLT pre-preg material (SP Epoxy SE84LV) is considered proprietary by the manufacture. They would not sell the resin separately, nor disclose the epoxy's properties. The epoxy used in the 8HHT pre-preg material (Fibercote Industries E-766B) could be procured separately. However, it was determined that neat resin specimens could not be prepared. Gas generation during curing resulted in excessive foaming and an inconsistent final product. Various methods were employed to restrict foaming including curing under vacuum, under pressure, at room temperature and in cold temperature. The foaming issue could not be solved. Therefore independent constituent material property characterization for the fabric composites considered in this study could not be performed.

5.2.2 Testing

Testing was performed in compliance with ASTM D5528 and D6671. Load was applied at a constant crosshead rate of 5 mm/min using a servo-hydraulic load frame with a 5000 Newton load cell. The load cell manufacturer information states that the load cell is accurate for loads greater than 1% of the load cell capacity, or 50 Newtons. Peak loads during testing ranged between 200 and 800 Newtons. Fracture growth was observed and recorded through use of a

finely marked steel measurement gauge with 1 mm increments, and a magnifying lamp. Testing was conducted on the woven fabric specimens at 0%, 20%, 40%, 50%, 60%, 80% and 100% mode II loading. A minimum of 5 specimens were tested for each material, for each loading mode. Fracture tip growth was recorded as a function of the load and displacement as indicated by the load cell and cross-head movement of the load frame.

Calculation of the Mode I CSERR was performed using the Modified Beam Theory correction method described in ASTM D5528. Calculation of the mixed-mode CSERR was performed per the methodology provided in ASTM D6671. The Mode II CSERR was determined using both ASTM D6671 and the End Notched Flexural (ENF) method to compare results. Mode II ENF testing was performed in the mixed-mode bending fixture by removing the constraints of the piano hinge. Mode II ASTM D6671 testing was performed identically, but the hinges were bolted to the frame, per ASTM D6671. The fabric composites were tested by the two methods to evaluate consistency in results from alternative test methods. Comparison of the two methods is presented in Appendix A. Values used in this study are those determined by the ASTM D6671 testing and interpretation method.

Mode II delamination of brittle materials is often unstable [66]. Stable growth permits more accurate measurements to be taken. Literature suggests [66] that stable delamination can be achieved for Mode II testing if a pre-crack is introduced. However, it was also found [64,67] that specimens under mode II ENF tests continued to extend in an unstable manner even when a pre-crack

was present. Additionally, when a pre-crack was introduced, the values of the maximum CSERR were more conservative than without the pre-crack, and the non-linear transition occurred appreciably earlier in the test [66]. Therefore no pre-crack was introduced into the mode II ENF specimens. Per ASTM D6671, mode II ASTM D6671 specimens were also not pre-cracked.

5.3 Results

5.3.1 Delamination of 8HHT

Satin weave fabrics have both a warp and a weft yarn dominated ply face. Figure 5.3.1 shows schematically the opposing faces of a satin weave fabric. Delamination of 8HHT is observed to occur along either the warp yarn dominated face or along the weft yarn dominated face. This is because the face along which delamination occurs is sensitive to specimen orientation. As mentioned, delamination is observed to proceed along the ply face that experiences compression during testing. Therefore, inverting a specimen in the mixed-mode bending apparatus reversed the ply face along which delamination occurred. For mode I testing, where both faces experience the same stress state, delamination always occurred along the warp yarn dominated ply face.

(a)   (b)
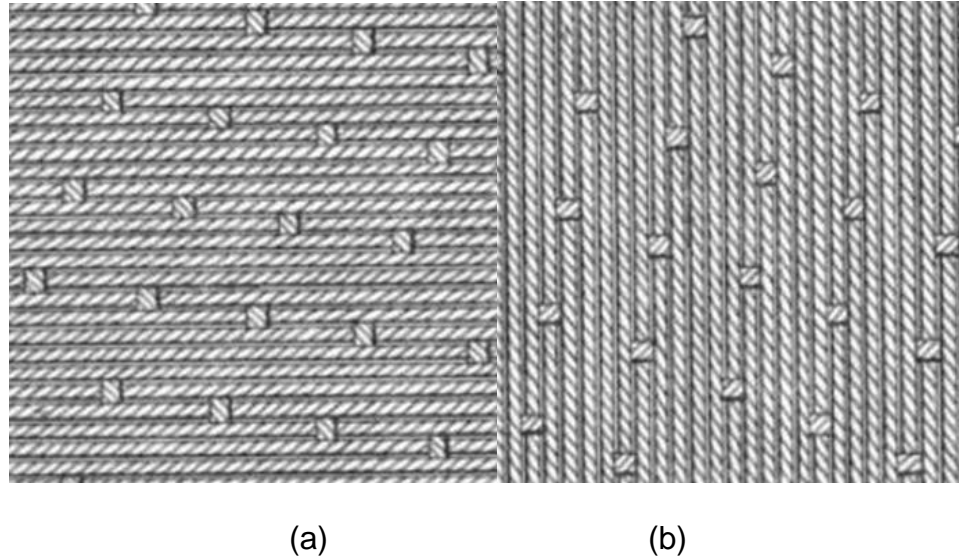
Figure 5.3.1: Illustration of the opposing faces of a typical 8 harness satin weave fabric showing. For the case of a crack progressing from left to right are shown: (a) the warp face; (b) and the weft face.

5.3.1.1 Delamination of 8HHT along Warp Yarn Dominated Ply Face

The warp yarn dominated ply face of an 8-harness satin weave composite is similar to a UD composite, as can be seen in Figure 5.3.1(a). The flow of the yarns in the warp direction is only interrupted by the presence of a weft yarn periodically. However, the mixed-mode testing load-displacement curve for delamination of the 8HHT along the warp yarn dominated ply face differs from that of a UD composite. The load-displacement curve displays a distinct saw-tooth type pattern as shown in Figure 5.3.2, which was not seen in the mixed-mode load-displacement curves for either UD-H or UD-L.
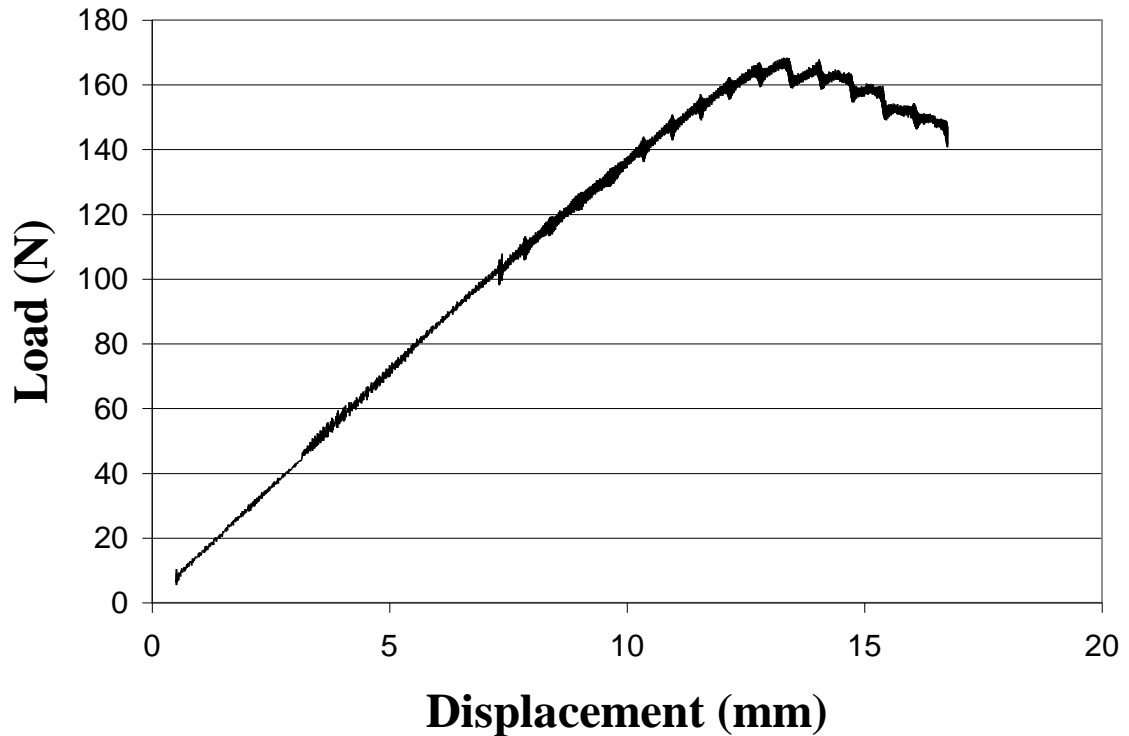
Figure 5.3.2: A typical load-displacement curve for delamination along the warp yarn dominated ply face of 8HHT subjected to 20% mode II loading.

Delamination of 8HHT along the warp yarn dominated ply face occurred by different mechanisms depending on the mixed-mode ratio. For low values of mode II loading, fracture occurred by interyarn failure, similar to UD-L. At intermediate mixed-mode ratios, delamination occurred by combined interyarn and interply failure. At high mixed-mode ratios, delamination occurred by interply failure along the warp yarns and around intersecting weft yarns. Interyarn and interply failures along the warp yarn dominated ply face of 8HHT are shown in Figure 5.3.3. Resin-rich pockets at the intersection of warp and weft yarns are an evident feature of 8HHT (highlighted with white arrows).
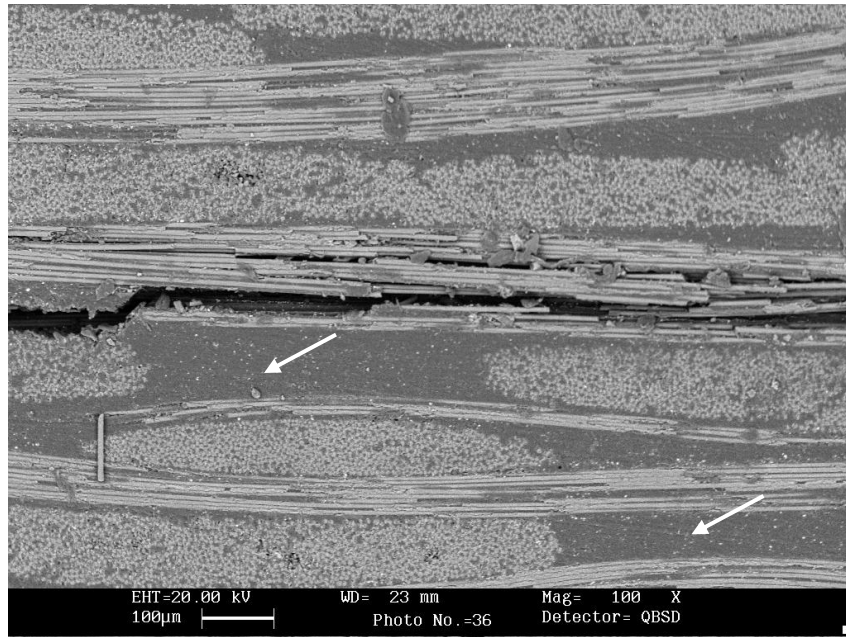
(a)
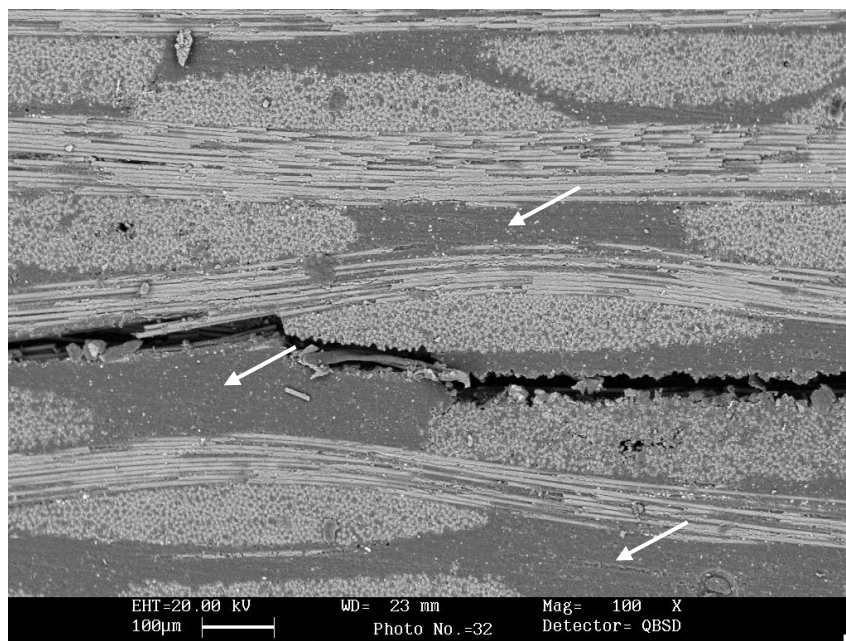
(b)

Figure 5.3.3: SEM micrographs showing typical appearances of delamination along the warp yarn dominated face of the 8HHT material ; (a) interyarn failure within warp yarn for pure mode I loading ; (b) interply failure along warp yarn and around intersecting weft yarn for 60% mode II mixed-mode loading. Crack growth is from left to right.

5.3.1.2 Delamination of 8HHT Along Weft Yarn Dominated Ply Face

The mixed-mode testing load-displacement curve for delamination of 8HHT along the weft yarn dominated ply face differs from that of the UD composites tested, and from 8HHT along the warp ply face. The load is observed to drop more abruptly and more deeply, as shown in Figure 5.3.4. The saw tooth pattern observed for 8HHT along the warp ply face is not evident.
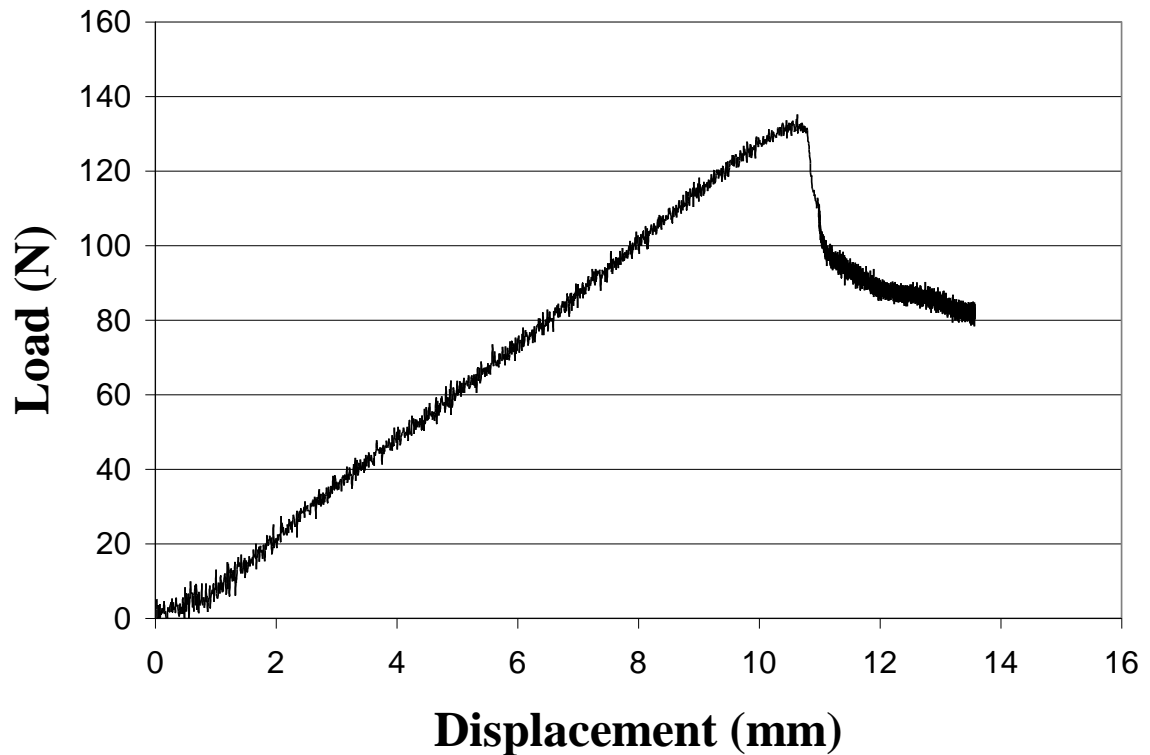
Figure 5.3.4: Typical load-displacement curve for delamination of 8HHT along the weft yarn dominated ply face for 20% mode II loading.

Delamination of 8HHT along the weft yarn dominated ply face occurred predominantly by interply failure along a single face of the weft yarns for low mode II loading, along both faces of the weft yarns for intermediate mode II loading, and by both interply failure along weft yarns and interyarn failure within

weft yarns for high mode II loading. Interply and interyarn failure along the weft

yarn dominated ply face of 8HHT is shown in Figure 5.3.5.

(a)

EHT=20.00 kV   WD= 26 mm   Mag=   50   X
100µm ├──┤   Photo No.=24   Detector= QBSD
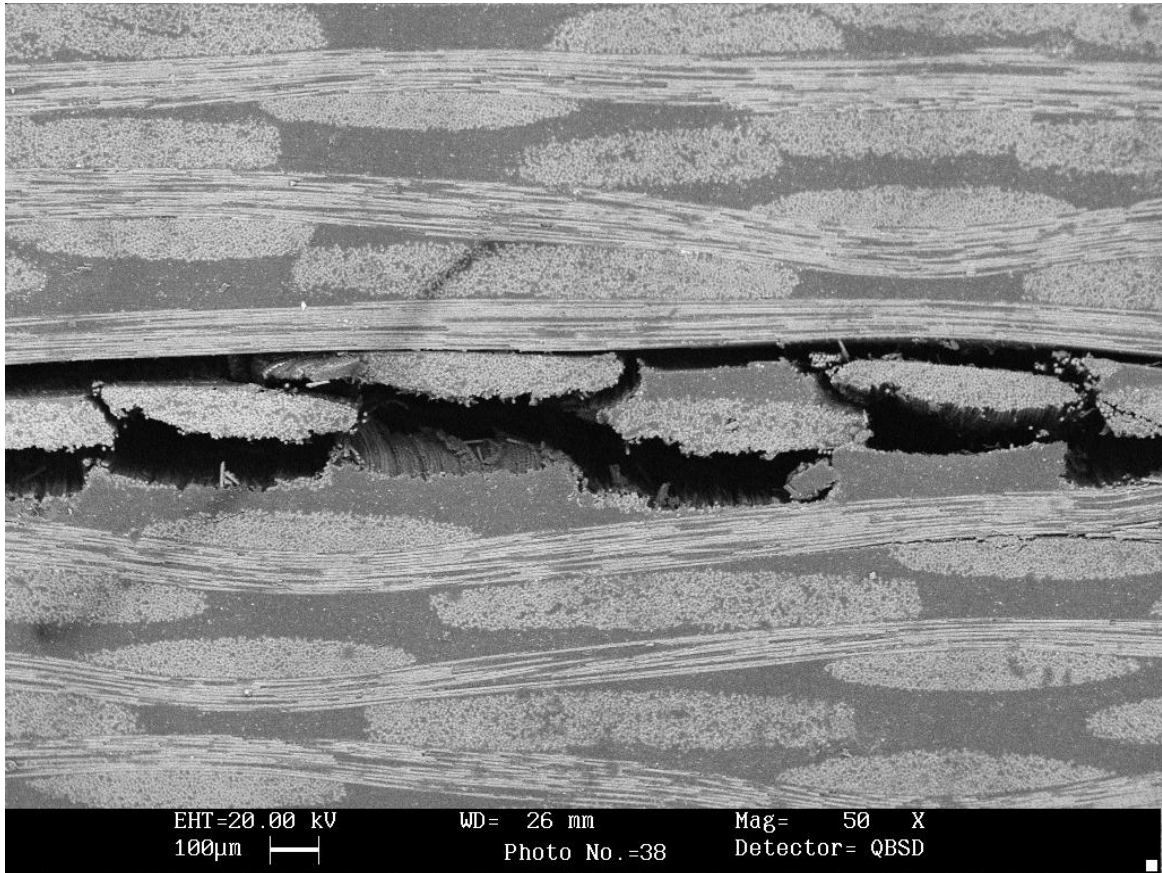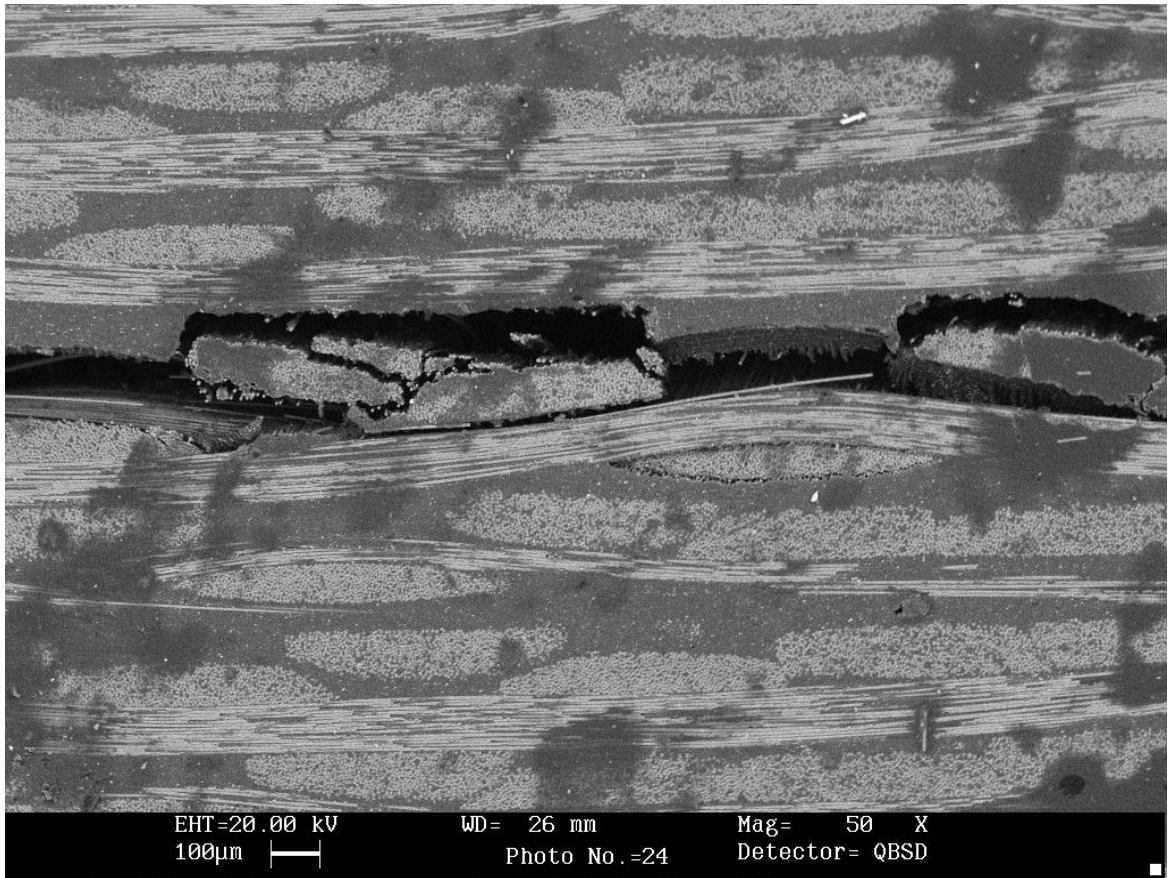
(b)

Figure 5.3.5. SEM micrographs showing delamination of 8HHT along the weft yarn dominated ply face; (a) interply failure under and over weft yarns for 40% mode II loading; (b) interply failure under and over weft yarn and interyarn failure through weft yarn for pure mode II loading.

5.3.2 Delamination of PWLT

Plane weave fabric does not possess the warp and weft yarn dominated ply faces as does satin weave fabric. Rather, opposing faces are essentially the same. Therefore PWLT does not show the specimen orientation sensitivity observed with 8HHT. The mixed-mode testing load-displacement curves for delamination of PWLT displayed a wide range of behaviours, with no apparent

trend or consistency, as shown in Figure 5.3.6. The curves often do not show a distinct maximum load at which crack initiation can be determined to occur.
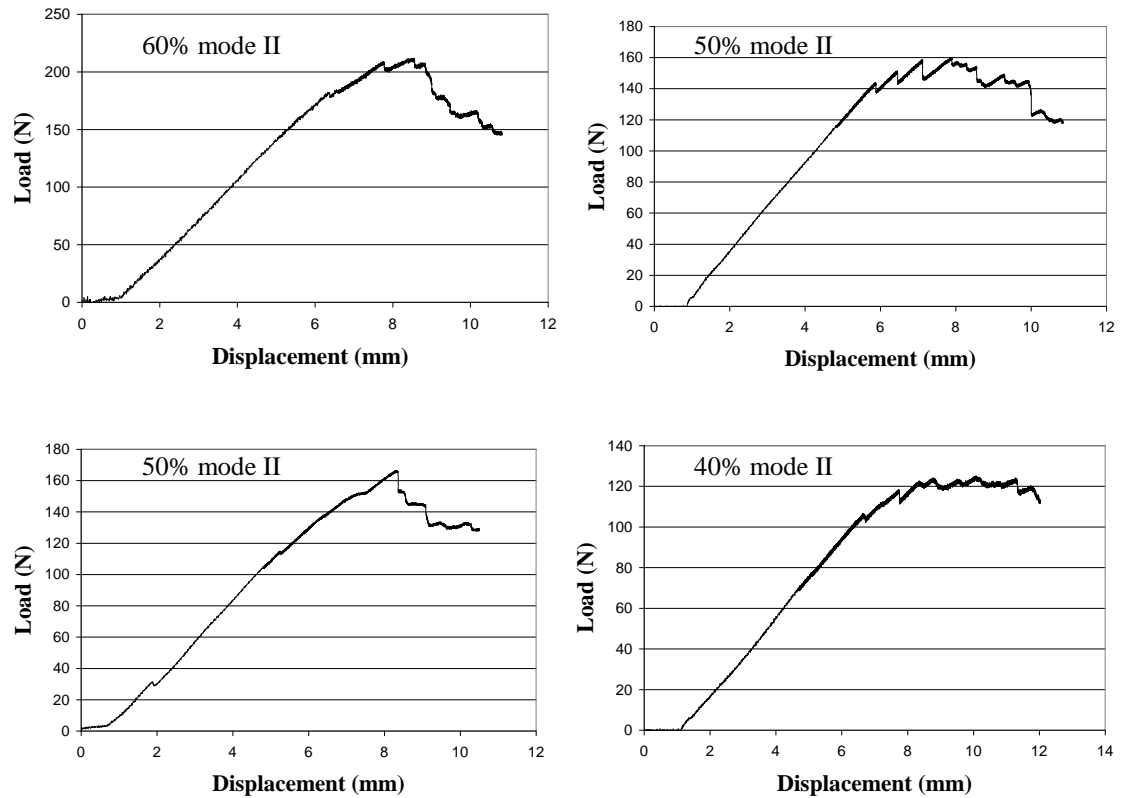
Figure 5.3.6: Typical load-displacement curves for delamination of PWLT subjected to mixed-mode testing.

Delamination of PWLT occurred by interply failure along the warp yarns for all loading modes. Delamination did not occur along a particular side of the warp yarn, but frequently alternated between one side of the yarn and the other. For higher mode II loading, the delamination often occurred along both faces of the warp yarn simultaneously. Transition across intersecting weft yarns occurred by both interply failure (around the weft yarn) and interyarn failure (through the weft yarn). Interyarn failure through weft yarns became more dominant for higher

mode II loading. Interply and interyarn failure along the warp yarns of PWLT is

shown in Figure 5.3.7.

(a)

EHT=20.00 kV   WD= 27 mm   Mag=   50 X
100µm ├────┤   Photo No.=71   Detector= QBSD
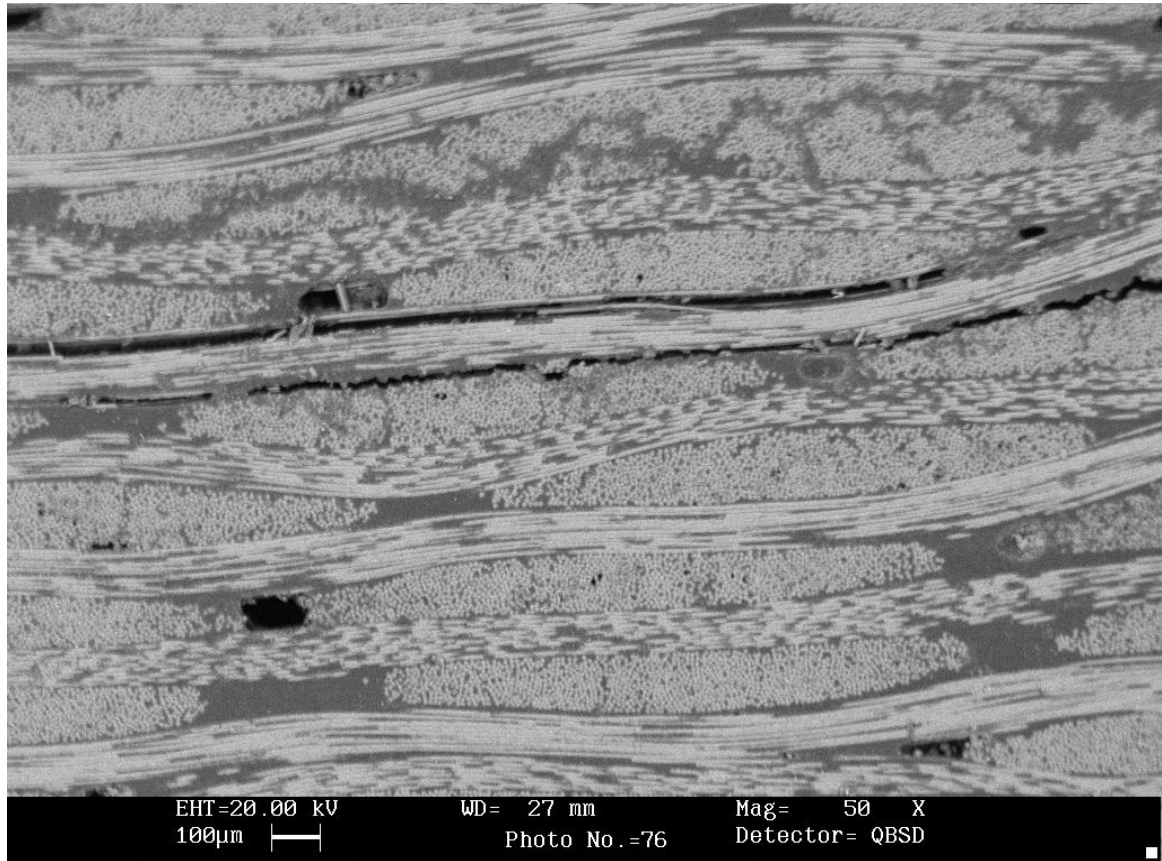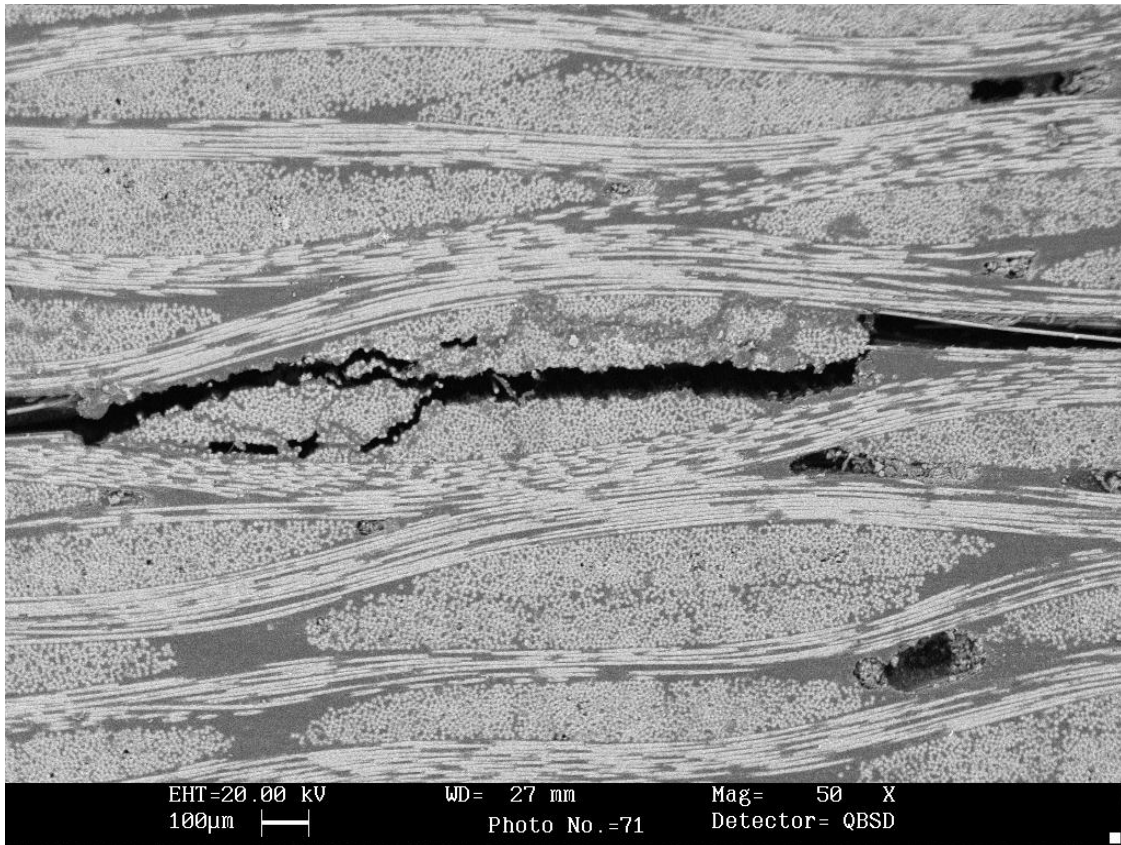
(b)

Figure 5.3.7. SEM micrographs showing delamination of PWLT along the warp yarns; (a) interply failure along both faces of a warp yarn and a weft yarn for 50% mode II loading; (b) interyarn failure through a weft yarn for 60% mode II loading.

5.4 Discussion

5.4.1 Crack Initiation and Growth

Crack initiation within the fabric composites occurred similarly as with the UD composites. Microcracks were observed to form ahead of the introduced crack initiator. The micro-cracks were observed to coalescence with further loading, to form a small continuous, but closed, crack. Similar with UD, this process could not be observed when white-out was used. Following initiation, crack growth

proceeded differently for the fabric composites than it did for the UD composites. Crack growth differed between 8HHT and PWLT, and also for delamination along the warp yarn dominated ply face of 8HHT and the weft yarn dominated ply face.

For delamination along the warp yarn dominated ply face of 8HHT, with further loading the initial crack grew incrementally upward toward and then along the warp yarn. The crack extended until it encountered the intersection of a weft yarn with the warp yarn, and became pinned at a resin-rich pocket. At a critical load, the crack opened and the load decreases sharply. This sequence of pinning and crack opening explains the saw-tooth pattern observed in the load-displacement curve. In addition to the existing crack opening, another small closed crack formed ahead of the open crack. With further loading, propagation of the crack occurred through a repeat of this process. The process of crack growth along the warp yarn dominated ply face of a satin weave fabric is illustrated in Figure 5.4.1. Corresponding points for each stage are shown along a typical load-displacement curve for the material.

Pre-existing crack between plies   Weft Yarn   Warp Yarn
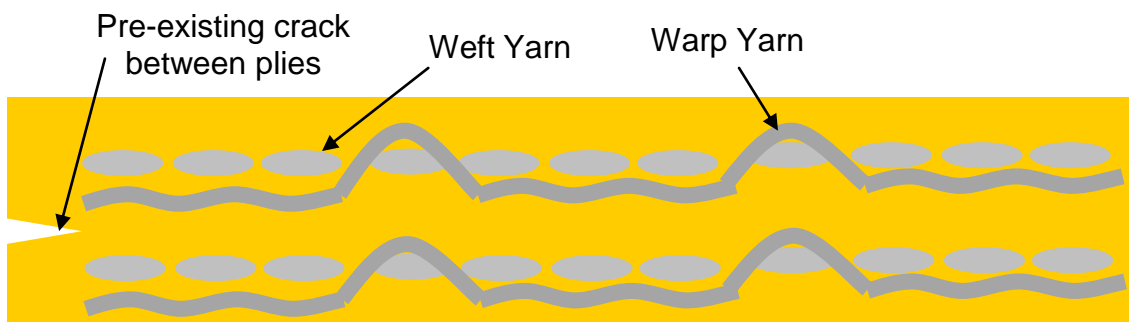
(A)
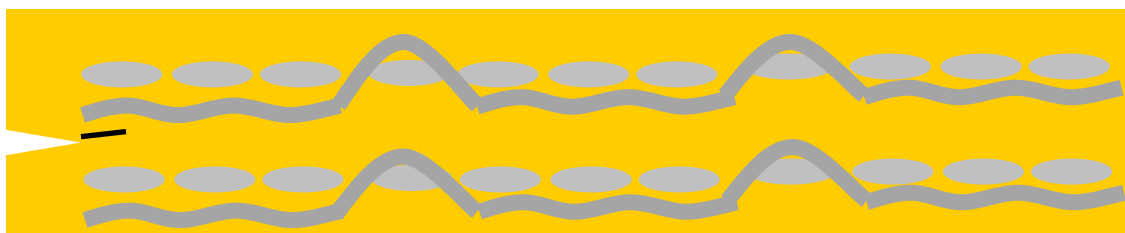
(B)
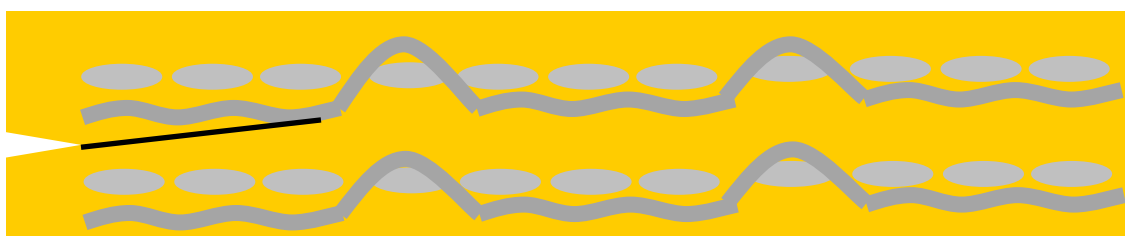
(C)
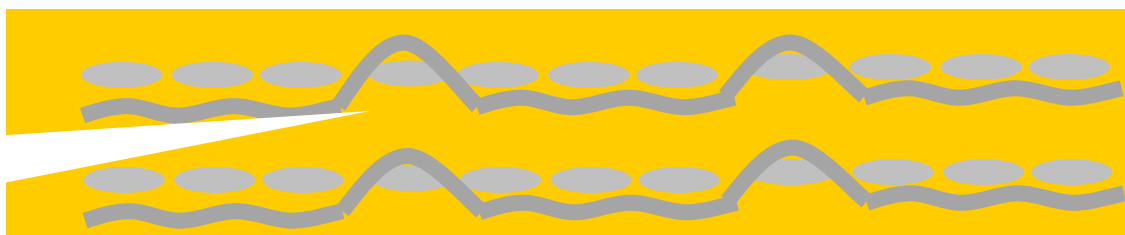
(D)
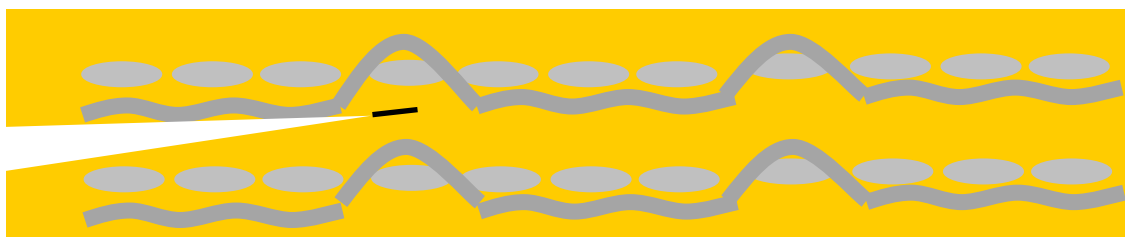
(E)
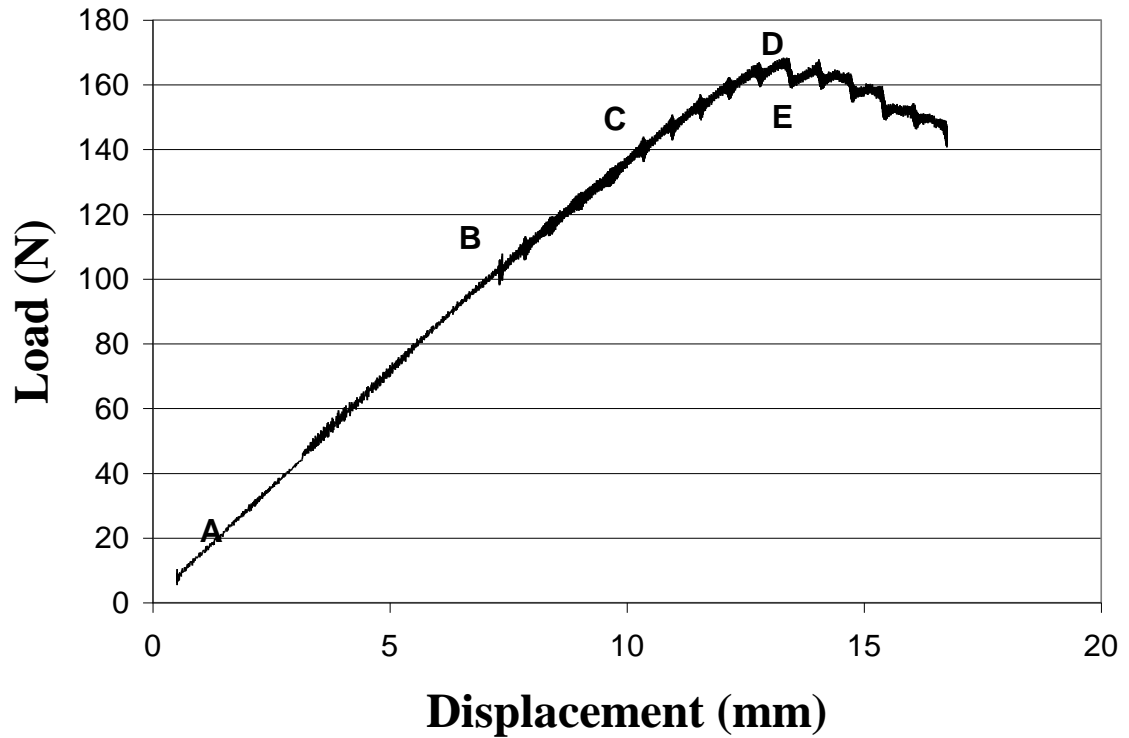
Figure 5.4.1: Illustration of the crack formation process along the warp face of a satin weave fabric (3-harness used for illustrated purposes); A) fabric composite with pre-existing crack; B) initial crack formation; C) incremental crack growth and pinning; D) crack opening; E) simultaneous formation of new closed crack.

For delamination along the weft yarn dominated ply face of 8HHT, further loading does not induce the initial crack to grow. Rather, a second crack initiates along the crest of the warp yarn at the warp/weft intersection ahead of the initial crack. This second crack then progresses backward along the warp yarn to unite with the first crack. Once the two cracks meet, the combined crack suddenly opens and there is a significant drop in load. While the crack at the crest of warp yarn is growing backward, it simultaneously also extends slightly forward along the warp yarn. With further loading, this sequence reiterates. The process is illustrated in

Figure 5.4.2. The forward and rearward growth of the crack can be directly observed during testing. Additionally, the pattern is validated by SEM examination of the fracture surface, in which hackle formation within the resin can be seen to proceed in opposing directions away from the peak.
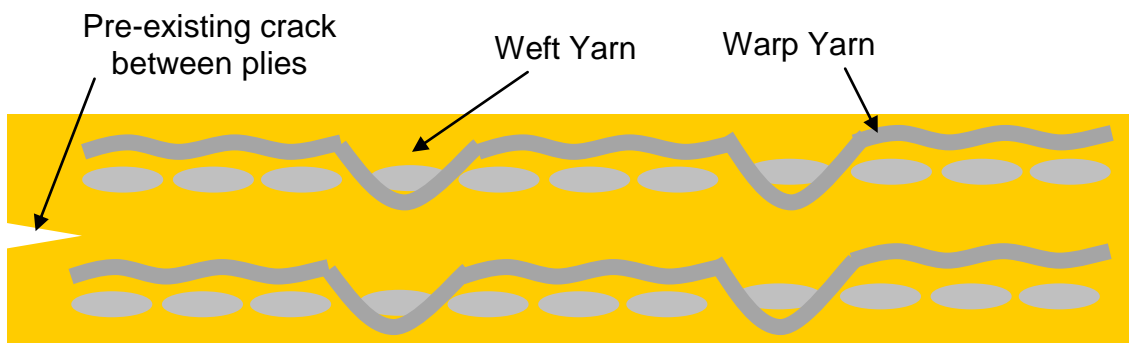
(A)
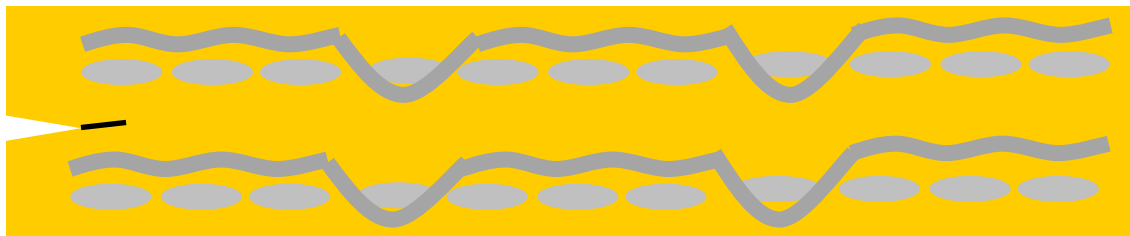
(B)

(C)
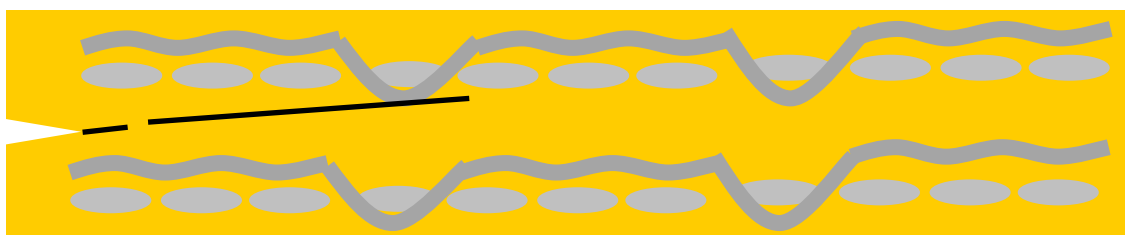
(D)
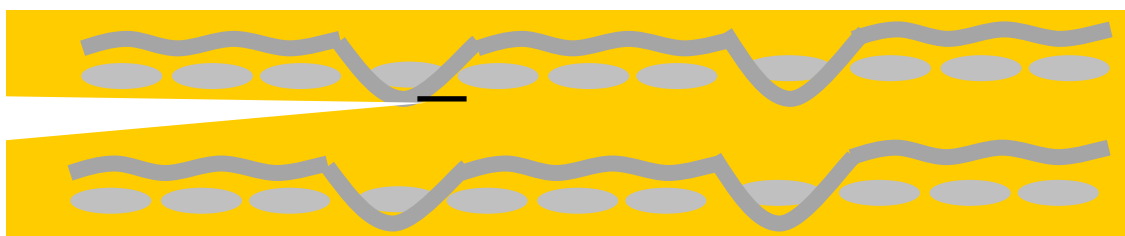
(E)
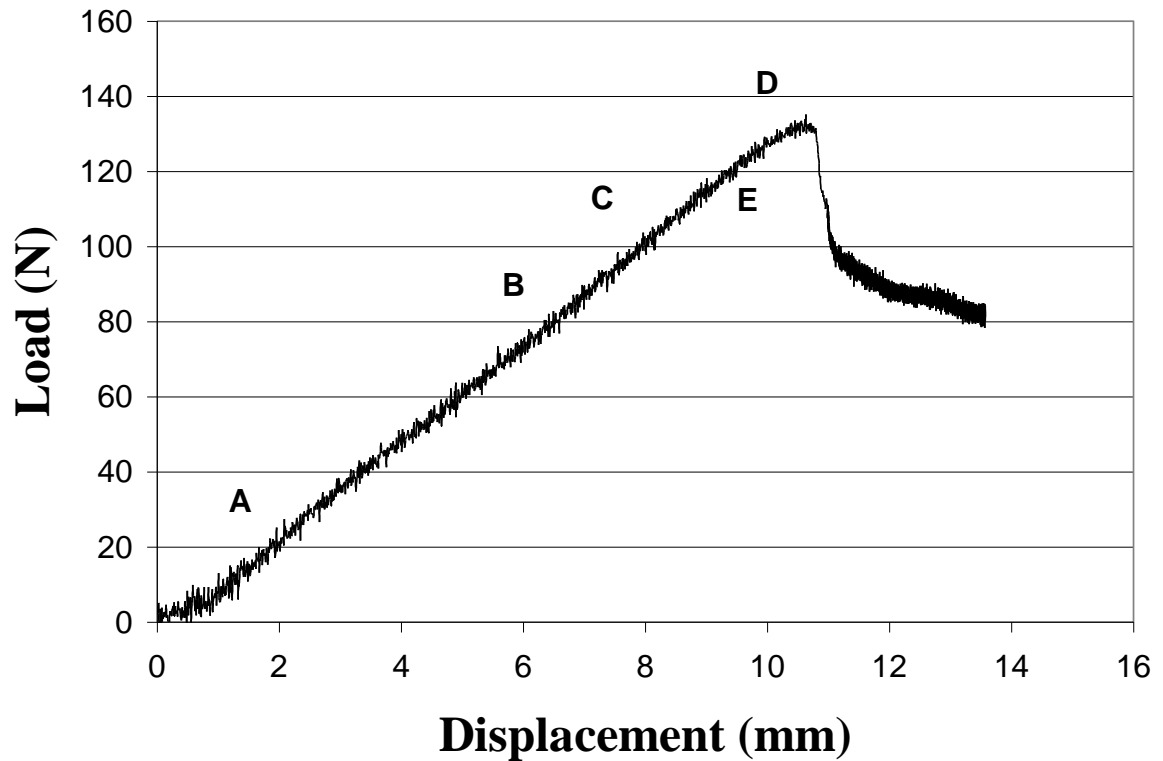
Figure 5.4.2: Illustration of the crack formation process along the warp face of a satin weave fabric (3-harness used for illustrated purposes); A) fabric composite with pre-existing crack; B) initial crack formation; C) formation of second crack at warp yarn peak; D) rear extension of second crack and slight forward extension; E) crack opening.

For delamination of the PWLT, crack growth was irregular and no clear pattern was discernable. As can be seen from Figure 5.3.6, the load-displacement curve also does not suggest a pattern to crack growth. The irregular nature of the crack formation of the PWLT is most probably a consequence of the brittle nature of the matrix.

The successive stages of fracture evolution described above for delamination of fabric composites will be referred to as the non-linear, visual, growth, opening

and propagation stages. The non-linear stage corresponds to the non-linear transition; the visual stage corresponds to the appearance of visible crack formation (micro-cracking and coalescence); the growth stage corresponds to visible growth of the crack that does not involve opening of the crack; the opening stage corresponds to the apparent opening of the crack and coinciding with the point of maximum loading; the propagation stage corresponds to crack propagation following the point of maximum loading. The approximate occurrence of each stage is shown in Figure 5.4.3 for a typical mixed-mode bend test load-displacement curve.

Figure 5.4.3: Illustration of the locations along a typical mixed-mode testing load-deflection curve of the stages of crack evolution.

5.4.2 Determining CSERR for Fabric Composites

There are a number of important consequences arising from the stages involved in crack initiation and growth in fabric composites. Crack jumping along the warp yarn dominated ply face and secondary fracture formation along the weft yarn dominated ply face render it difficult to clearly define the fracture tip in fabric composites. Another consequence is that the load at which the initiation CSERR is to be calculated is no longer clearly defined by ASTM D6671.

ASTM D6671 describes the load at which the CSERR is to be calculated as the lesser value of either the maximum load, or the load corresponding to a 5% offset from linearity. For UD composites, these values are typically very close and fundamentally represent the load at which the composite fails and the fracture opens. For the case of a woven fabric composite subjected to mixed-mode bending, the presence of resin-rich pockets result in a significant difference in the load at which fracture formation is first observed, and the load at which fracture opening occurs. The value for the CSERR calculated from the maximum load is frequently significantly greater than the value obtained by the 5% offset method.

Therefore, in accordance with ASTM D6671, the load resulting from 5% offset method would always be the load at which the CSERR would be calculated for fabric composites. This value however does not adequately reflect the considerably greater energy required to actually cause the fracture to open. Calculation of the CSERR is further complicated by how the fracture tip is defined when measuring fracture tip growth. Paris et al [43] defined the fracture tip as

the point at which micro-fracture coalescence has occurred. Coalescence however is difficult to measure accurately, as it occurs gradually and simultaneous with crack extension. Also, coalescence cannot be observed when white-out is applied to the specimen edge, per ASTM D6671.

Alternatively, defining the fracture tip as the tip of the opened fracture may provide a more appropriate value of the CSERR, reflecting the total energy required to induce complete fracture. This approach is not necessary for UD composites, as the difference in load between when a fracture becomes visible and when the fracture opens is typically very small. However, for fabric composites, the difference in load, and therefore calculated values for the CSERR, between when coalescence is first observed, and fracture opening occurs, can be appreciable. From the load-displacement curves shown In Figures 5.4.1 and 5.4.2, the appreciable load difference between the Growth stage and the Opening Stage is evident. As well, the Growth and Opening stages are clearly discernable when white-out is used, facilitating accurate measurement.

The methodology for calculating the CSERR for woven fabric composites requires reconsideration. Use of the load at which crack opening is observed is recommended. This will typically correspond to the maximum load measured, but not necessarily, as is the case with PWLT, so careful observation and accurate measurement is required. The 5% offset method should not be used, as this consistently under-estimates the CSERR. Paris et al [43] calculates the

CSERR for fabric composites from the peak load at which a load drop was first observed. This approach is also not recommended, as higher loads are required to induce crack opening.

5.4.3 Initiation CSERR

Initiation CSERR was calculated for delamination along both the weft and warp faces and for PWLT. These values were calculated using the loads corresponding to the point at which crack opening was observed to occur. Initiation CSERR as a function of mode mixture are presented in Figures 5.4.4 through 5.4.6 for these materials. For delamination of the 8HHT along the warp, transition from interyarn to interply failure occurs at approximately 40% mode II loading.
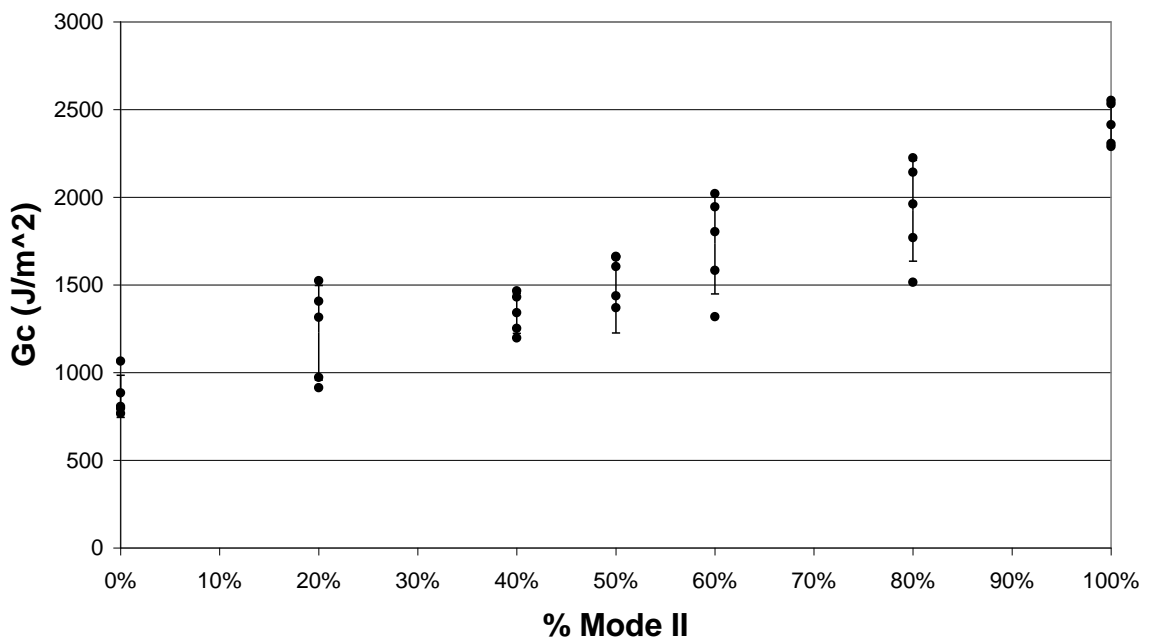
Figures 5.4.4: CSERR vs mode mixture for 8HHT along weft yarn dominated ply face.
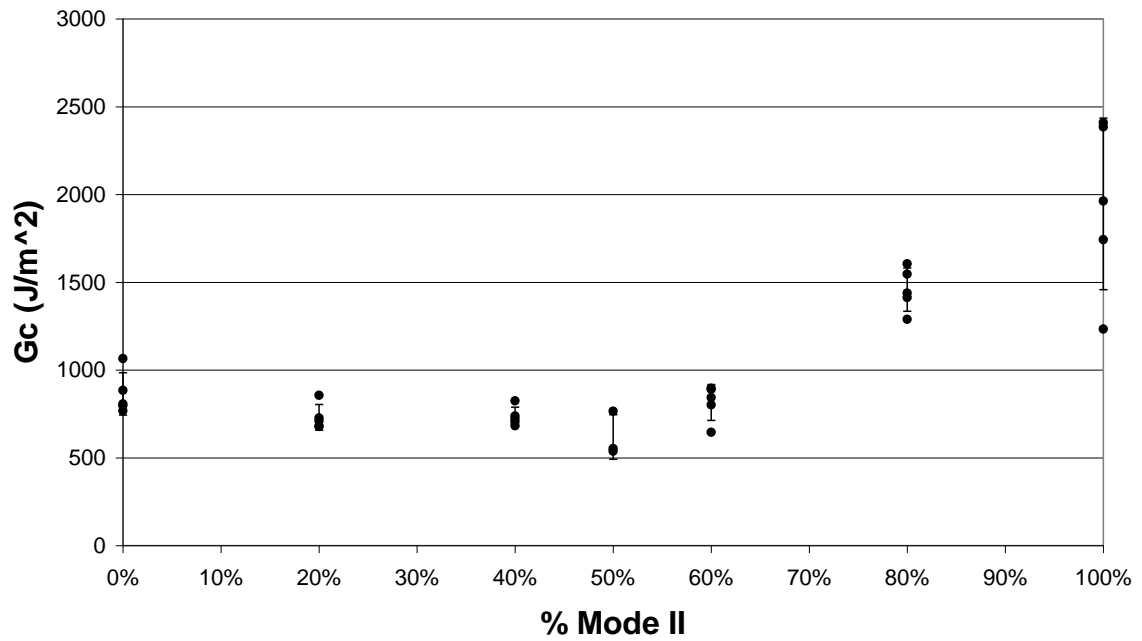
Figures 5.4.5: CSERR vs mode mixture for 8HHT along warp yarn dominated ply face.
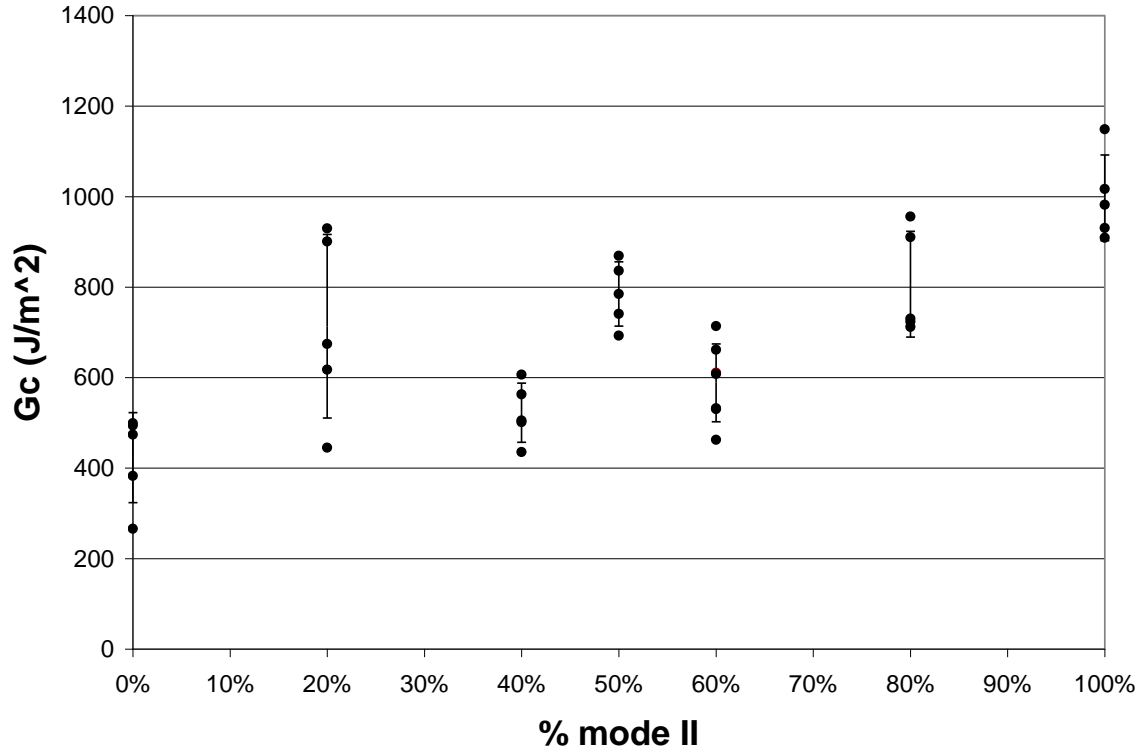
Figures 5.4.6: CSERR vs mode mixture for PWLT.

5.4.4 Fabric Composite Delamination Features

Below is a review of important aspects of delamination of fabrics that were observed to vary from the UD composites. These features provide insight into the effect of the unique aspects of fabric composite delamination on the material CSERR values.

5.4.4.1 Fiber Fracture

Examination of the fracture surface of the fabric specimens tested by mixed-mode bending frequently revealed the fracture of both individual filaments and entire yarns. Fracture consisted of transverse cracking through the filaments. Typical examples are shown in Figure 5.4.7.

(a)

EHT=20.00 kV WD= 27 mm Mag= 100 X
100µm Photo No.=115 Detector= QBSD
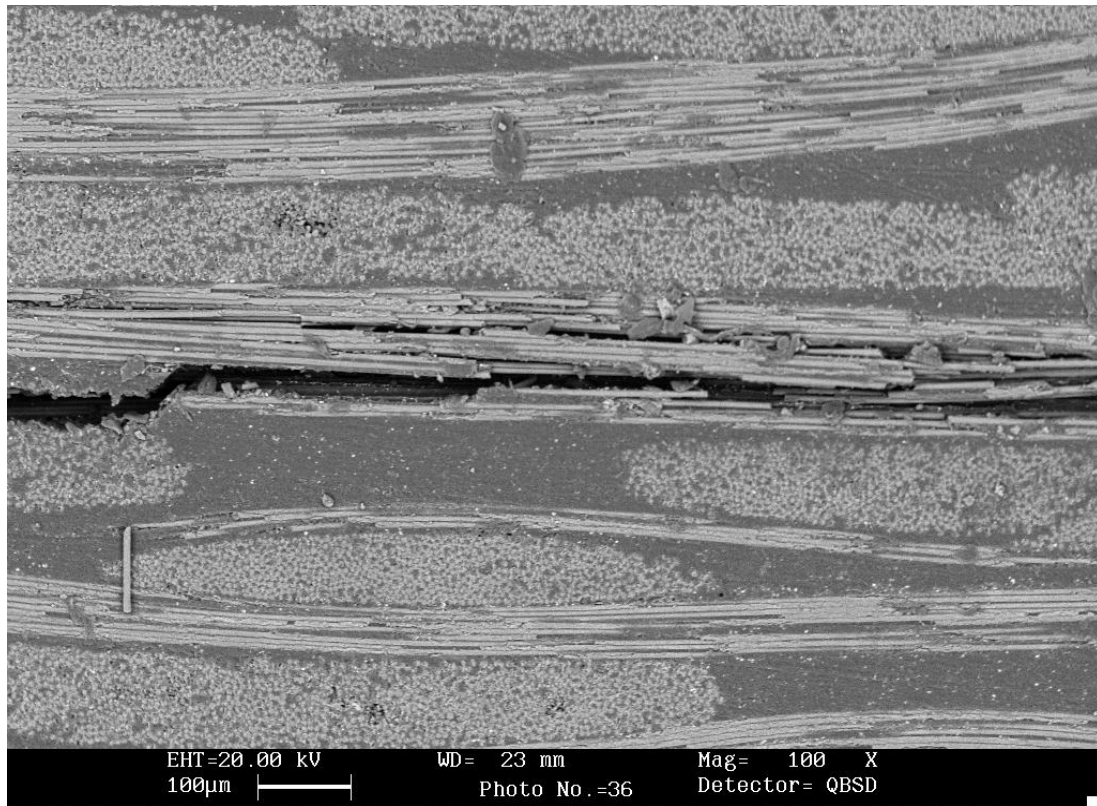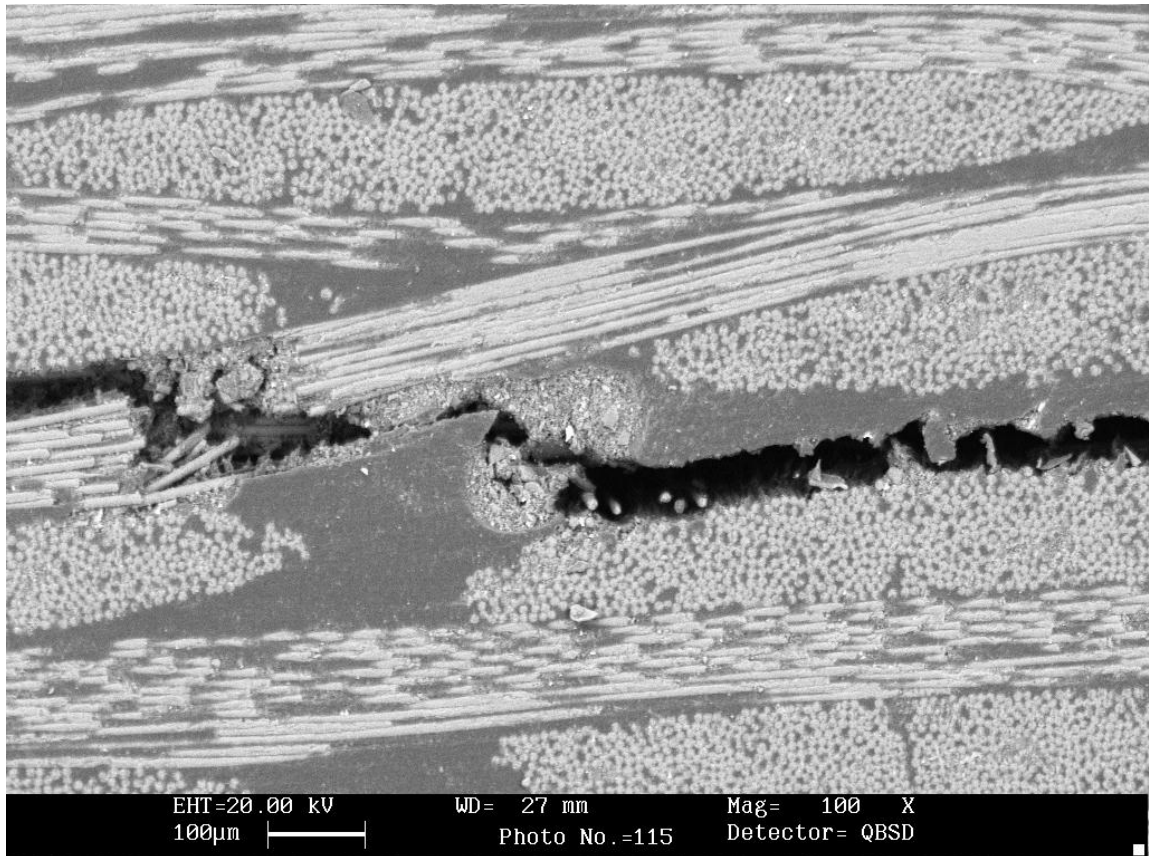
(b)

Figure 5.4.7: Fiber fracture in 8HHT; a) interyarn failure at 20% mode II loading resulting in filament fracture; b) interply fracture at 40% mode II loading involving fracture through a yarn.

This effect was observed to typically be associated with the transition between warp and weft yarns. Delamination within fabrics involves complex fracture paths along three-dimensional paths and complex states of stress. The complex stress state at the weft/warp transition in fabrics can cause abrupt variation in failure mechanism involving filament fracture. Figure 5.4.8 illustrates common fiber fracture behaviours observed in the fabric composites.
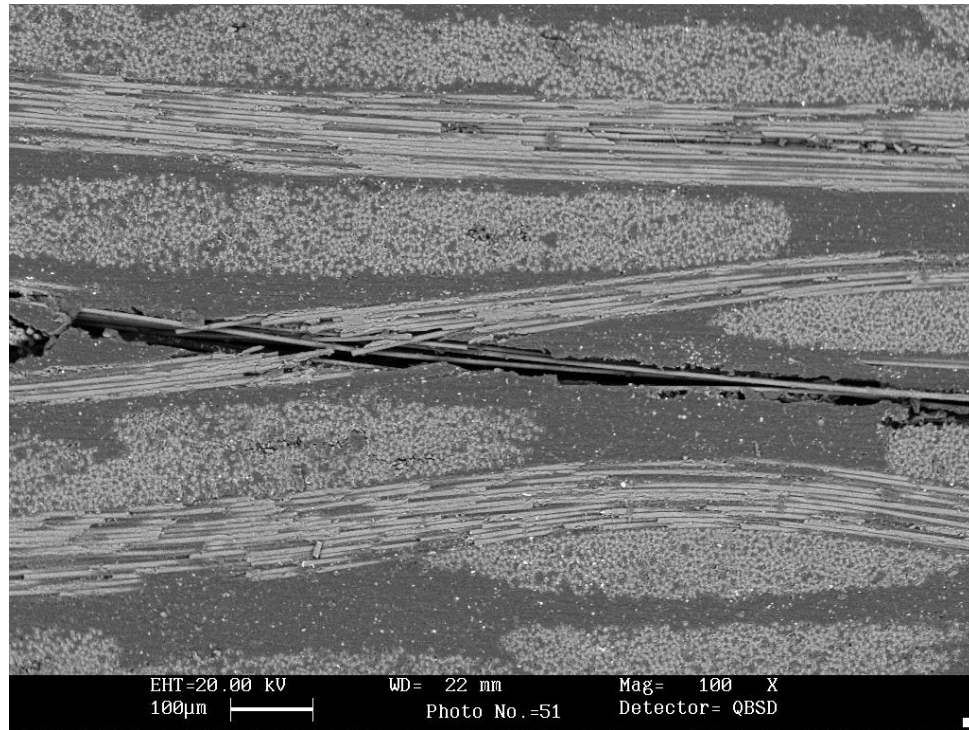
(a)
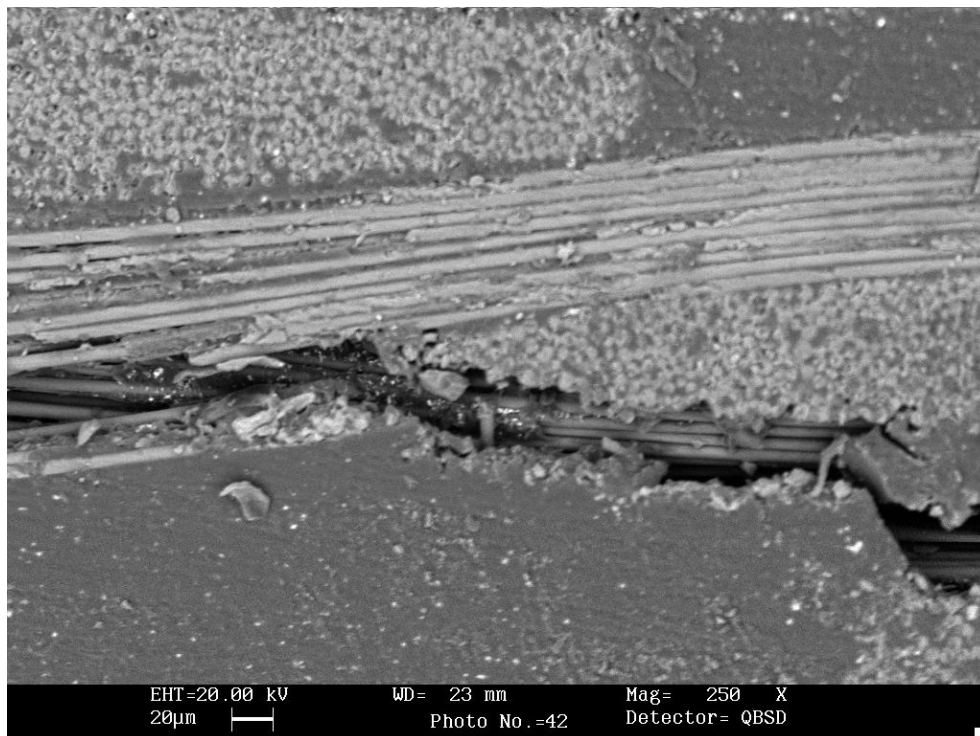
(b)

Figure 5.4.8: 8HHT at 40% mode II loading; a) extension of interply failure along a yarn cutting through an adjacent yarn; b) crack transitioning from a warp yarn to a weft yarn.

For interyarn failure of 8HHT along the warp face, fracture of the surface filaments is observed to increase in frequency and severity with increasing mode II loading. Figure 5.4.9 shows a surface view of fiber fracture for the case of pure mode I loading, and for the same material at 40% mode II loading (beyond which the failure is interply). Fracture of the surface filaments is appreciably more extensive at 40% mode II loading than for pure mode I loading. As the loading mode increases, the depth of cracking within the yarn transitioning from deep in the yarn toward to surface of the yarn, resulting in more extensive surface filament fracturing. By this gradual means, interyarn failure transitions to interply failure. CSERR values between mode I and 40% mode II loading presented in Figure 5.4.5 appear to be relatively insensitive to the degree of fiber fracture. Therefore fiber fracture does not appear to contribute significantly to energy absorption.
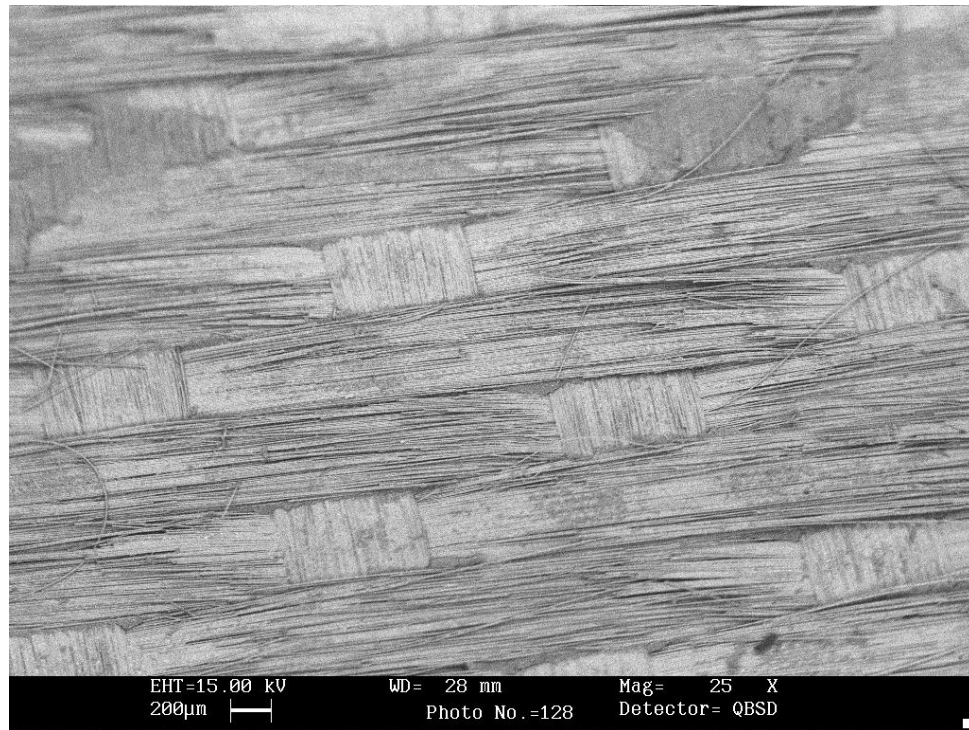
(a)
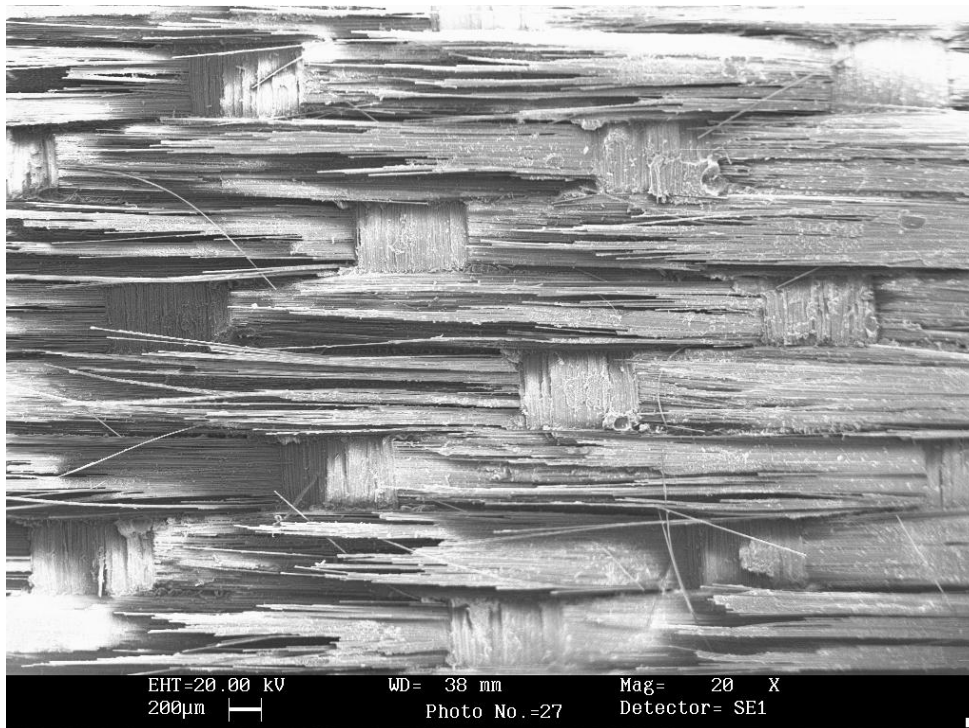
(b)

Figure 5.4.9: surface filament fracture associated with interyarn failure for 8HHT along the warp face; a) pure mode I loading; b) 40% mode II loading.

5.4.4.2 Resin Fracture

Resin fracture is observed both between plies, and within yarns between individual filaments.   Hackling frequency and hackle angle were observed to increase with an increasing percentage of mode II loading for both 8HHT and PWLT. Figure 5.4.10 shows intermittent hackle formation at low mode II loading, and frequent and more angular hackle formation at high mode II loading.
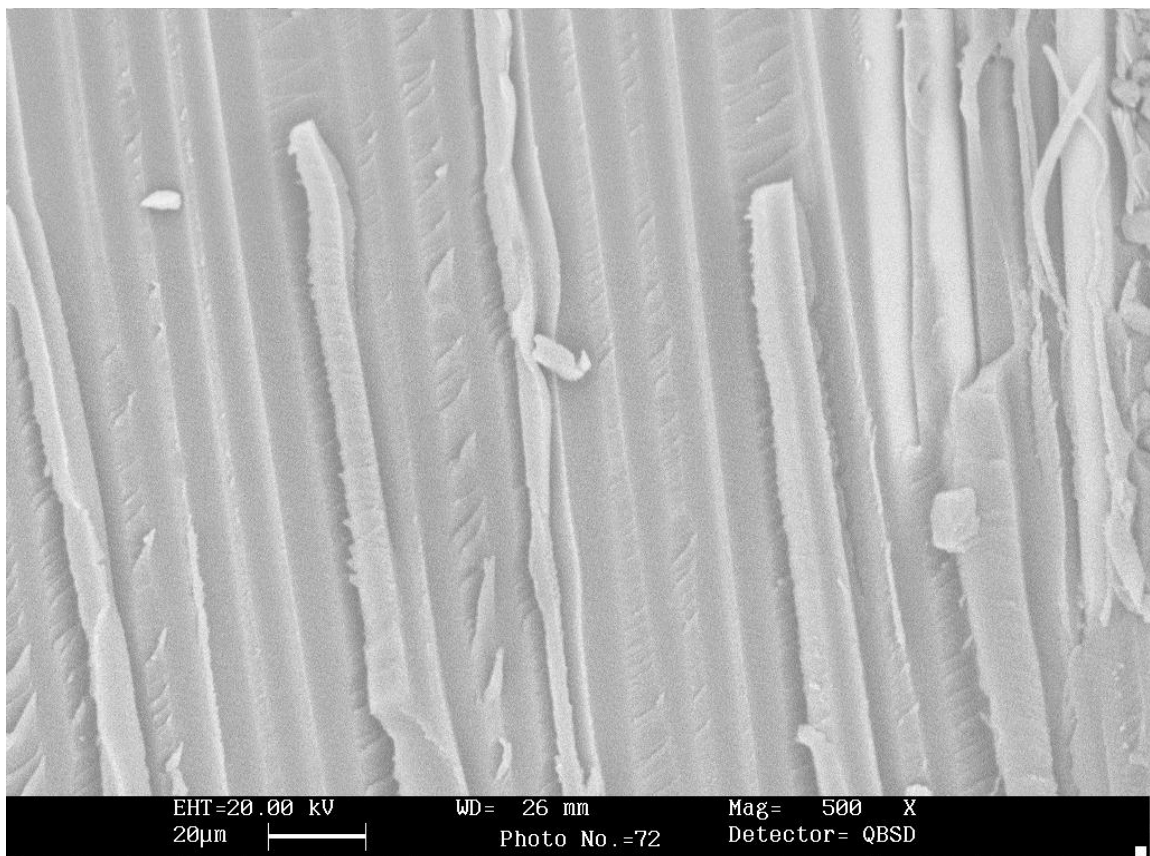
(a)
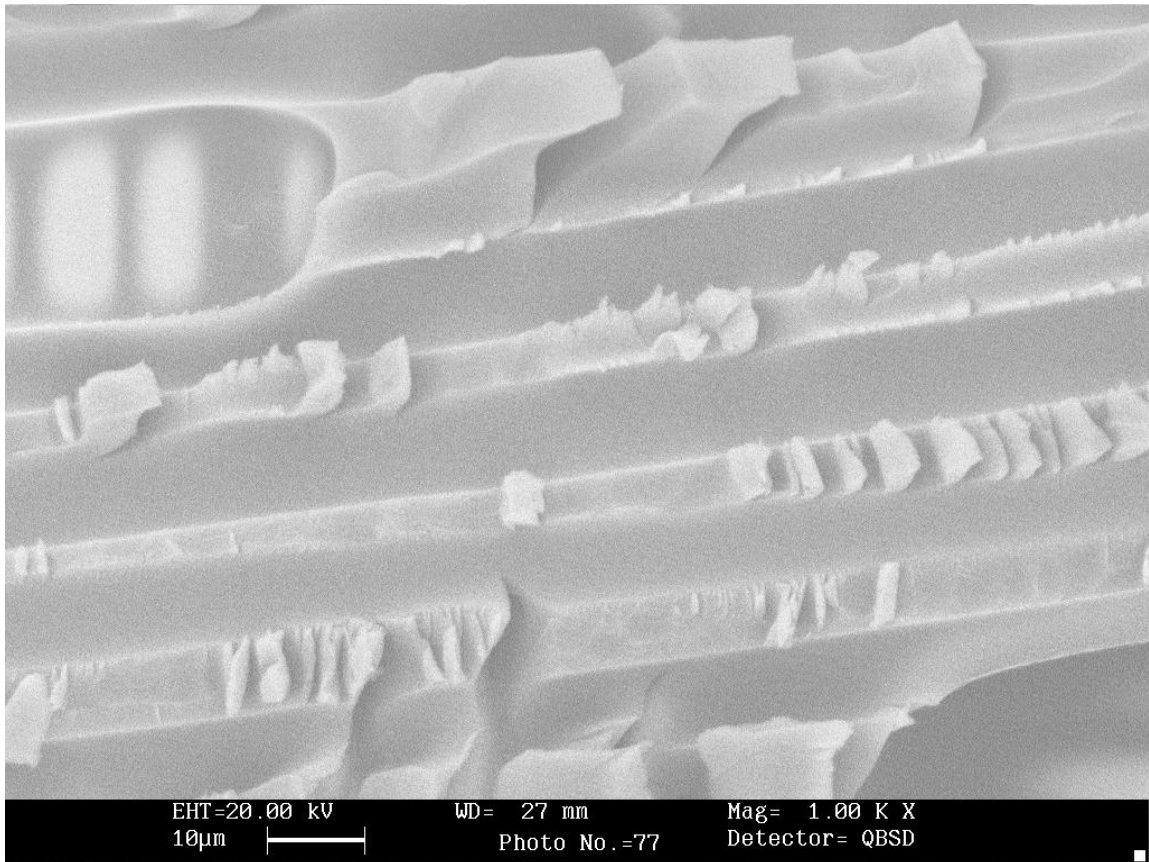
(b)

Figure 5.4.10: Detail of hackle appearance in PWLT; a) at 40% mode II loading; b) at 100% mode II loading

The fracture of resin through the resin rich pockets occurring at the intersection of warp and weft yarns could be directly observed. After a crack passes through a resin rich pocket, a portion of the resin-rich pocket remains. This region can be observed by SEM on the fractured surface, as shown in Figure 5.4.11. These resin regions are observed for the 8HHT under all mixed-mode loading conditions with the exception of pure mode I loading. They are not seen in PWLT. The relative size of the resin regions was observed to increase with increasing mode II loading.
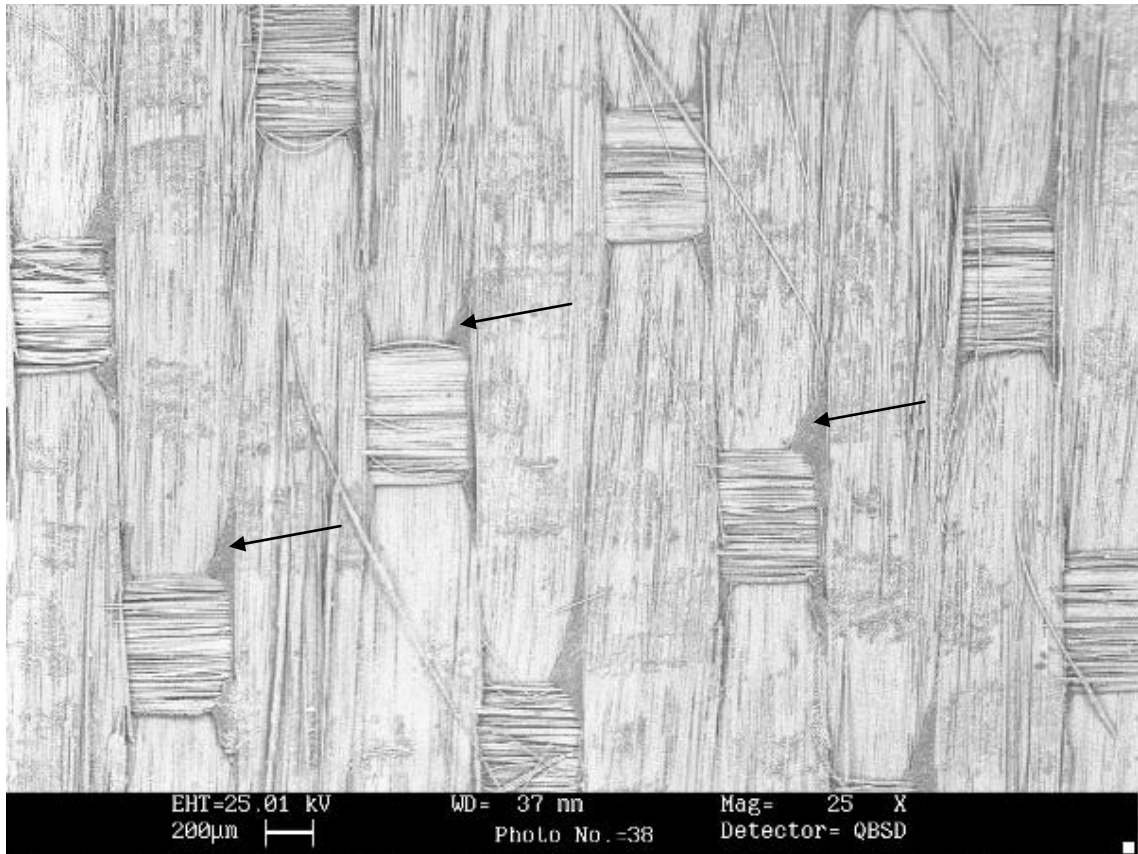
Figure 5.4.11: Resin-rich pockets at yarn intersection for 88HT at 80% mode II loading, indicated by the black arrows. The crack direction is from left to right.

5.4.4.3 Crack Path

In UD composites, delamination typically progresses along a single relatively linear crack path. In fabric composites, the crack path associated with delamination is increased due to the complex geometry of the material. Crack path increases are associated with the convoluted path of interply failure along warp yarns, the occurrence of interply and interyarn failure along both faces of warp yarns, and crack branching within warp and weft yarns during interyarn failure.

The path that the delaminating crack follows effects the CSERR associated with the fracture process. For a given failure mode, the longer the associated path length, the larger the surface area created, and therefore the greater the energy absorbed. The higher the total crack length associated with resin fracture, the greater the associated CSERR will be. Also, energy absorption is associated with overcoming pinning at the resin-rich pockets.

The intersection of weft and warp yarns provides for a number of potential crack paths through the resin-rich layer and around the weft yarns. Some of these involve higher energy absorption than others, due to a longer crack path, by inducing crack branching, or by requiring the crack to pass through a greater length of resin. Illustrations of the various crack paths observed for delamination through the intersection of a warp and weft yarn are provided in Figure 5.4.12. As mentioned, the ASTM specifications used to evaluate CSERR were created for UD composites, for which crack paths are assumed linear and for which there are no warp to weft yarn intersections. Therefore the CSERR of fabric composites would be expected to be higher than for UD composites fabricated from similar reinforcement and matrix materials.

(a) (b)

(c) (d)
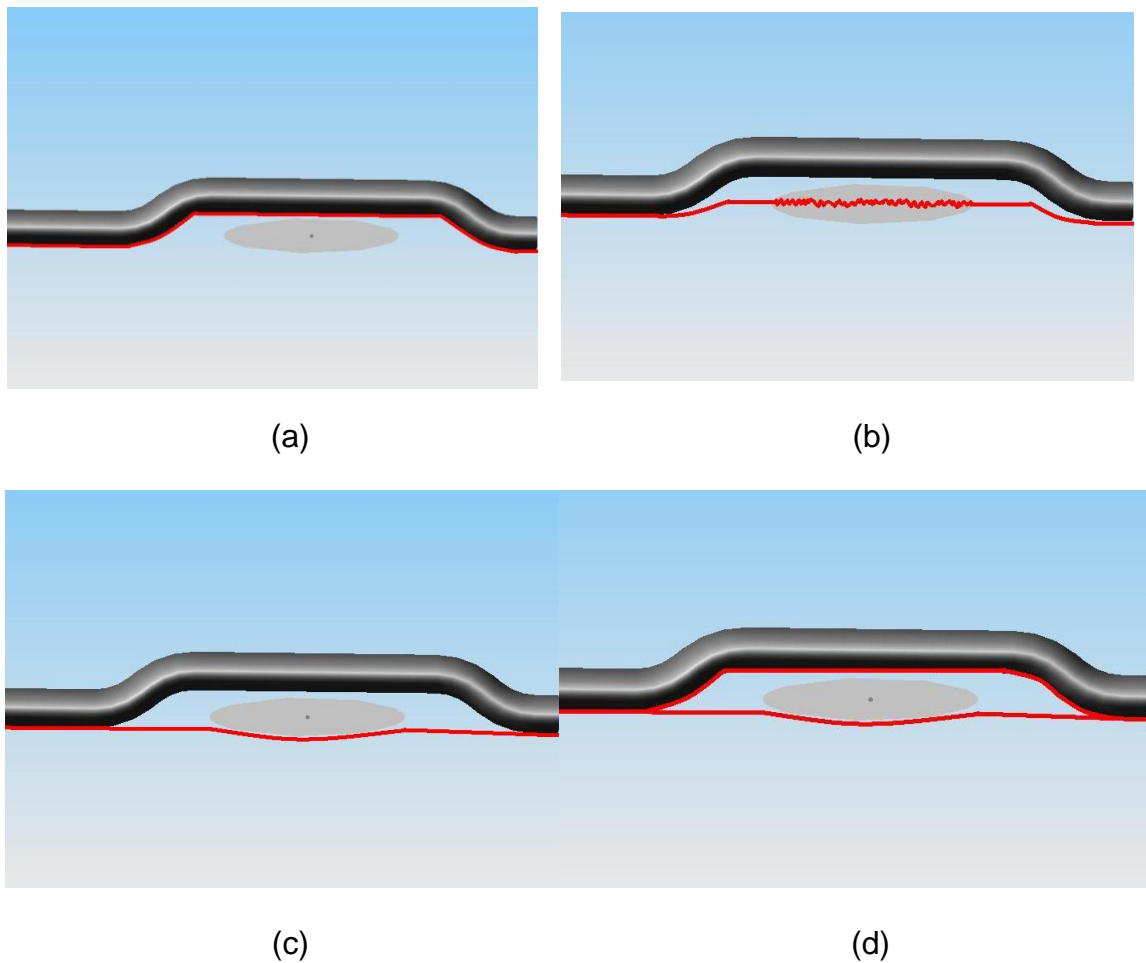
Figure 5.4.12: Crack paths associated with interply failure along a warp yarn at the intersection with a weft yarn; a) crack continues along warp yarn; b) crack proceeds by interyarn failure through weft yarn; c) crack progresses by interply failure around weft yarn; d) crack proceeds by interply failure along both warp and weft yarns.

5.4.4.4 Fiber-Resin Interface

Both interply and interyarn failure involved fiber-resin interface debonding. Fiber-resin debonding is observed for 8HHT and PWLT to involve a clean separation of the resin from the fibers. SEM micrographs of the observed fiber-resin debonding are shown in Figures 5.4.13 and 5.4.14.

EHT=20.00 kV   WD= 27 mm   Mag= 100 X
100µm ⊢——⊣   Photo No.=116   Detector= QBSD

(a)

EHT-20.00 kV   WD- 23 mm   Mag- 750 X
10µm ⊢——⊣   Photo No.=39   Detector= QBSD
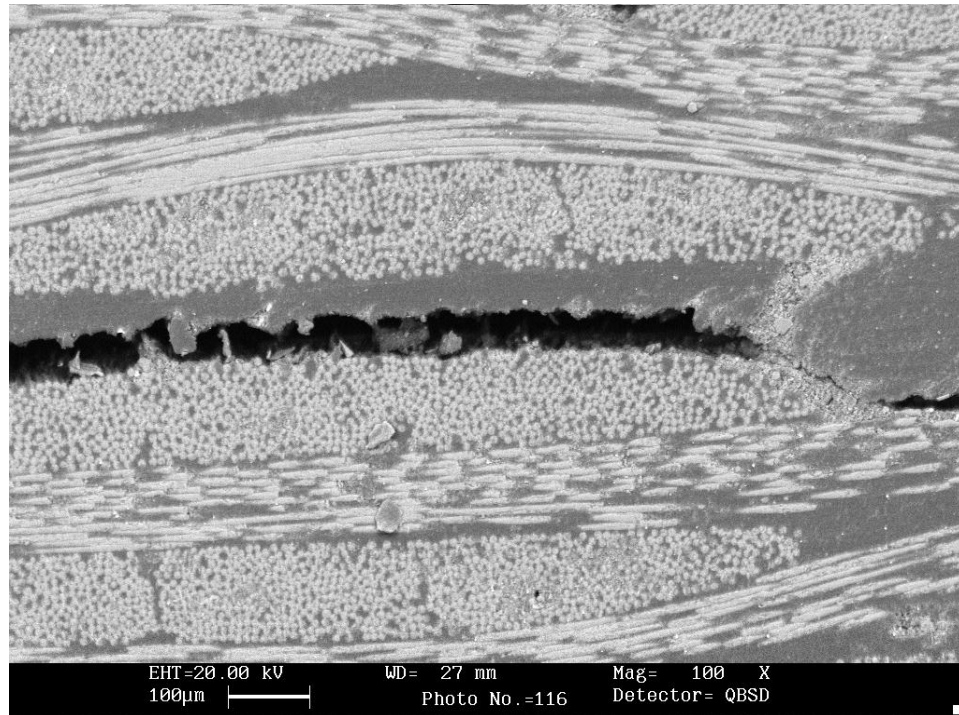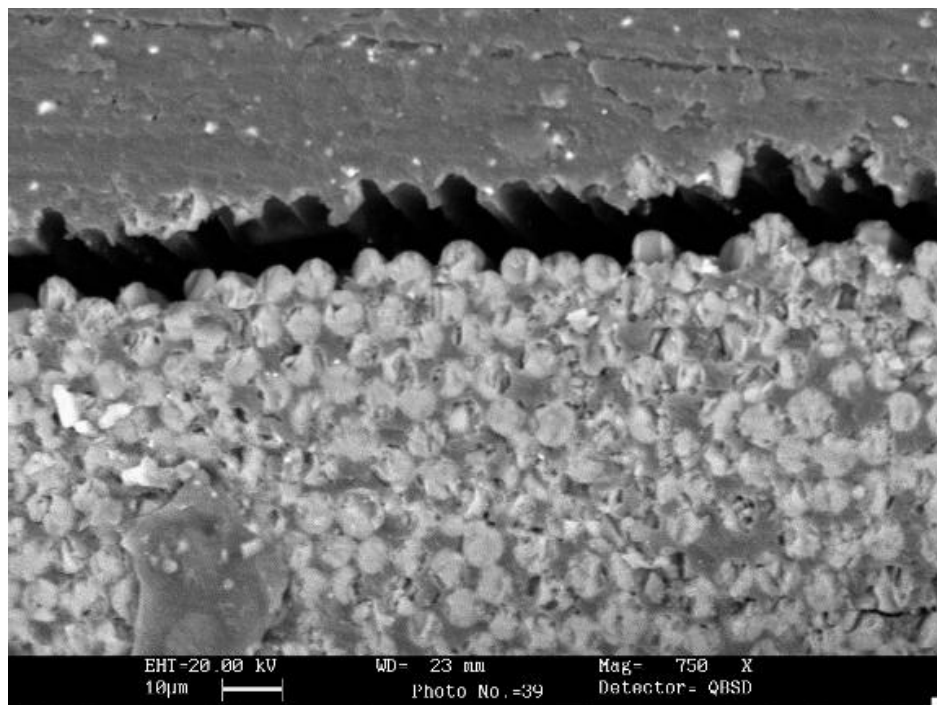
(b)

Figure 5.4.13: SEM edge micrograph of 8HHT specimen tested under 50% mode II loading showing fiber-resin interface debonding; a) low magnification; b) high magnification. The separation occurs cleanly between the resin and fiber.
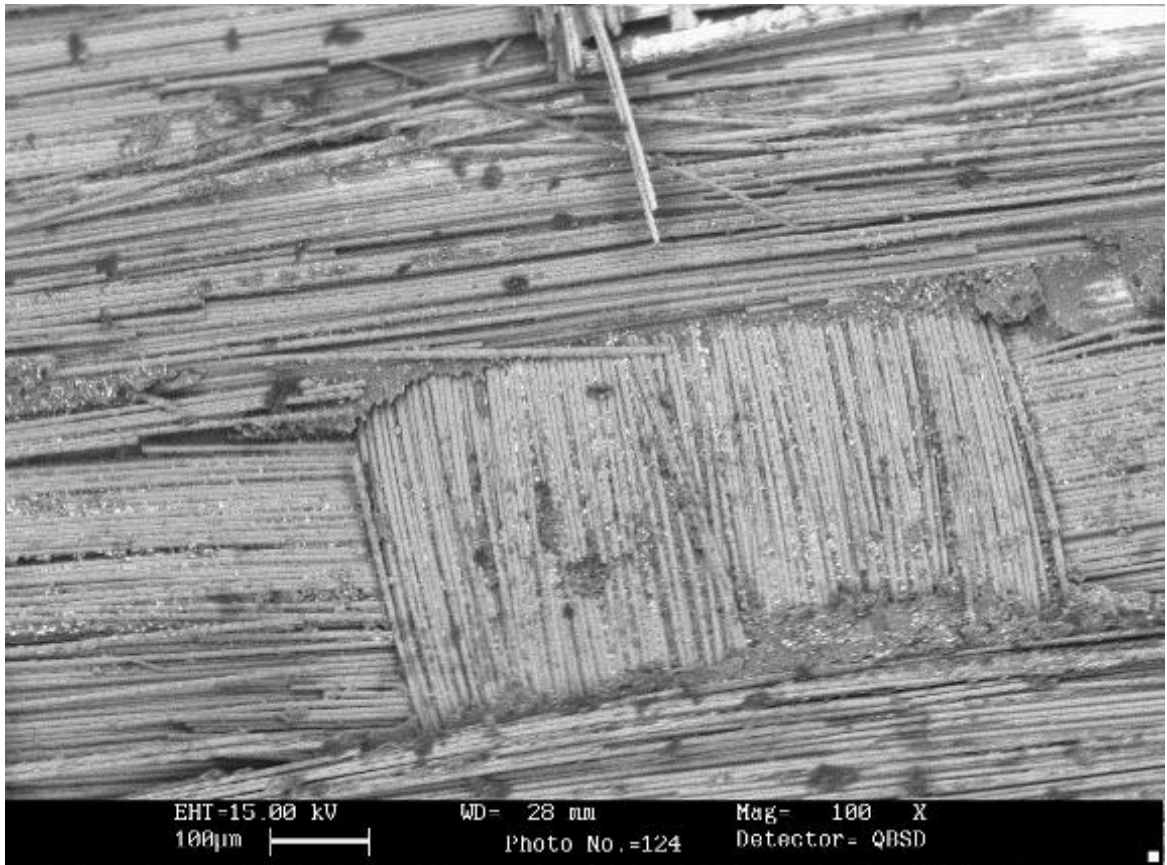
Figure 5.4.14: SEM surface micrograph of 8HHT specimen tested under 50% mode II loading showing fiber rich side of the fractured surfaces. Very little resin remains attached to the filaments.

5.5 Summary

Crack initiation and growth is a multi-stage process for fabric composites. The unique aspects of fabric crack formation require a reconsideration of the load at which a meaningful value for the CSERR should be calculated. Testing suggests that the load at which crack opening is observed would most accurately reflect the full energy absorbing properties of fabric composites. The delamination of satin weave composites is determined to be sensitive to specimen orientation. Delamination may occur along the predominately warp or weft ply face,

depending on which face experiences compression during the test. Delamination within fabric composites involves many complex failure mechanisms, which contribute to the energy absorption associated with delamination.

6. RESIN STUDIES

6.1 Introduction

Development of a mechanistic based mixed-mode failure criterion for CFP composites requires incorporation on the energy absorbing properties of the constituent materials. Therefore resin fracture properties were investigated. Mode I and mode II fracture testing was performed on the Crosslink epoxy used to fabricate the UD materials tested in this study, and as described in Chapter 4. The specific failure mechanisms involved in fracture under both loading conditions were evaluated and characterized. The CSERR for the epoxy under mode I and mode II loading was determined and correlated with the failure mechanisms observed in the tested UD composites.

Mode I loading was found consistently to result in cleavage failure. Hackle formation, a mode I induced tension fracture, was observed under mode II loading. Expressions are developed to describe hackle formation behaviour under mixed-mode loading in terms of the stress state at the crack tip. A model to predict variation in CSERR with loading mode based on the crack path increase associated with hackle formation is proposed. The model is correlated with data from this study. Good correlation is found between experimental data and the model.

6.1.1 Measuring Neat Resin CSERR

The concept of mode I CSERR, G_{IC}, is well understood and agreed upon by researchers. The meaning however of the mode II CSERR, G_{IIC}, has been challenging to understand and define. Mode II loading does not always result in mode II failure, which involves planes sliding relative to each other [10,68]. It has been suggested that G_{IIC} is not an independent material property, and can be derived from G_{IC} [68]. For many materials, mode II loading has been observed to result in mode I failure, involving tension induced cracking. For other materials, the mode II initiated failure quickly transitions to a mode I failure [10]. For these cases it has been proposed that mode I failure occurs because G_{IC} is exceeded before G_{IIC} and that therefore the measured CSERR does not accurately represent G_{IIC} [10,68].

For many materials in which mode I failure is observed under mode II loading, G_{IIC} is measured to be very close to the value of G_{IC} [69], suggesting that this is the case. Alternatively, this position has been disputed based on test results that have indicated that the G_{IIC} is independent of G_{IC} [22]. The testing suggests completely different failure mechanisms occur under Mode II loading when compared to Mode I loading, and these mechanisms are distinct and independent of the Mode I loading mechanisms.

Few tests exist to determine the mode II CSERR of a homogeneous polymer, and these are complex and difficult to perform [10]. Test methods to perform Mode II testing of neat polymers include the Center Slanted Cracked Circular

Plate test, the Single Edged Crack test, the Double Crack Punch Through Shear test [69], the Richard's Test [70], and the Asymmetric Bend test [65]. These test methods are not standardized. Limited research papers have been published for mode II and mixed-mode fracture testing of neat polymers. There is no agreement on the preferred test method, nor on the preferred test set-up for each method. Available test results are not consistent in the material property determined, and show a large range in the values measured. The cause of the variation is typically not explored and limited characterization of the failure mechanisms involved in fracture is provided.

The key research conducted in regards to mode II fracture testing of neat polymers can be briefly summarized. Kwon and Jar [10] in 2005 evaluated the mode I and mode II fracture properties of polyacrylonitrile-butadiene-styrene (ABS), a common brittle thermoplastic. The Richard's test was used to perform the mode II testing, using V-Notched Beam Method fixturing. Fracture energy was determined by calculating the Essential Work of Fracture (EWF). The EWF process is used to determine the portion of the total energy absorbed in the fracture process that is attributable to the formation of the crack surface [10]. The pure mode I EWF for ABS was measured as 13.1 kJ/m^2, while the pure mode II EWF was measured as 32.3 kJ/m^2.

Hashimoto [69] in 2007 evaluated the mode I and mode II fracture toughness of an acrylic resin, poly-methyl methacrylate (PMMA), a common brittle thermoplastic frequently referred to by the trade name Plexiglas. Three different

test methods were assessed and compared. The mode I CSIF, K_{IC}, was measured as 1.3 MPa(m)$^{\frac{1}{2}}$, and the mode II CSIF, K_{IIC}, ranged between 1.52-1.84 MPa(m)$^{\frac{1}{2}}$, depending upon the specific test arrangement used. Wakaro et al. [65] in 2005 evaluated the mode I and mode II fracture toughness of two epoxy resins that were a blend of bisphenol-A type epoxide resin and metyl-tetrahydro-phthalic anhydride. The Asymmetric Bend test was employed. For one epoxy, K_{IC} was measured to be 1.94 MPa(m)$^{\frac{1}{2}}$ and K_{IIC} was 1.52 MPa(m)$^{\frac{1}{2}}$, while for the other epoxy, K_{IC} was measured to be 1.99 MPa(m)$^{\frac{1}{2}}$ and K_{IIC} was 2.77 MPa(m)$^{\frac{1}{2}}$.

6.2 Methods

6.2.1 Specimen Preparation

A two part epoxy supplied by Crosslinks Technology (Toronto, Ontario, Canada) consisting of CLR 1180 resin and CLH 6560 hardener was used to manufacture neat polymer specimens. The resin is prepared by mixing 30 parts of CLH 6560 into 100 parts of CLR 1180. Neat polymer is cast by slowly pouring the liquid resin into a flat Teflon coated container. The resin is cured at room temperature for 24 hours until solidified, and then post-cured at 60 degrees Celsius for 4 hour to complete the full cure, per manufacturer's instructions.

Tensile properties of the polymer were evaluated in compliance with ASTM D638, Standard Test Method for Tensile Properties of Plastics. Shear properties of the polymer were evaluated in compliance with ASTM D5379/D5379M-98 Standard Test Method for Shear Properties of Composite Materials by the V-

Notched Beam Method. Mode I and Mode II fracture testing was also performed, and discussed in detail below.

6.2.2 Mode I Fracture Testing

Mode I fracture testing of the neat polymer was conducted in accordance with ASTM 5045, Standard Test Methods for Plane-Strain Fracture Toughness and Strain Energy Release Rate of Plastic Materials. ASTM 5045 is suitable for brittle polymers for which linear elastic behaviour is observed [2]. Therefore the test is valid for most thermosetting polymers, but is not valid for many thermoplastics. ASTM 5045 involves subjecting notched beam specimens to a 3-point loading configuration as shown in Figure 6.2.1.

For the testing conducted in this research, rectangular specimens 15 mm thick, 30 mm wide and 130 mm long were cut from the neat resin using a fine saw blade and edges were sanded with 600 grit paper. A 15 mm deep notch was introduced at the mid-section along one edge with a router and jig designed to maintain the dimensions for the notch as specified in the standard. A razor blade was slid along the notch to ensure a sharp initiation point. A 5000 Newton load cell was used to perform the testing. A standard 3-point bend fixture was used to support the specimens and to apply the load at the mid point of the specimen. Specimens were aligned on the fixture using a simple alignment block. Specimens were tested to fracture at a steady rate of 1 mm/min. Load and extension data were recorded and reviewed to confirm linear elastic behaviour.

The maximum load was noted and the mode I CSERR, G_{IC}, was calculated per the methodology described in ASTM 5045, and briefly described below.
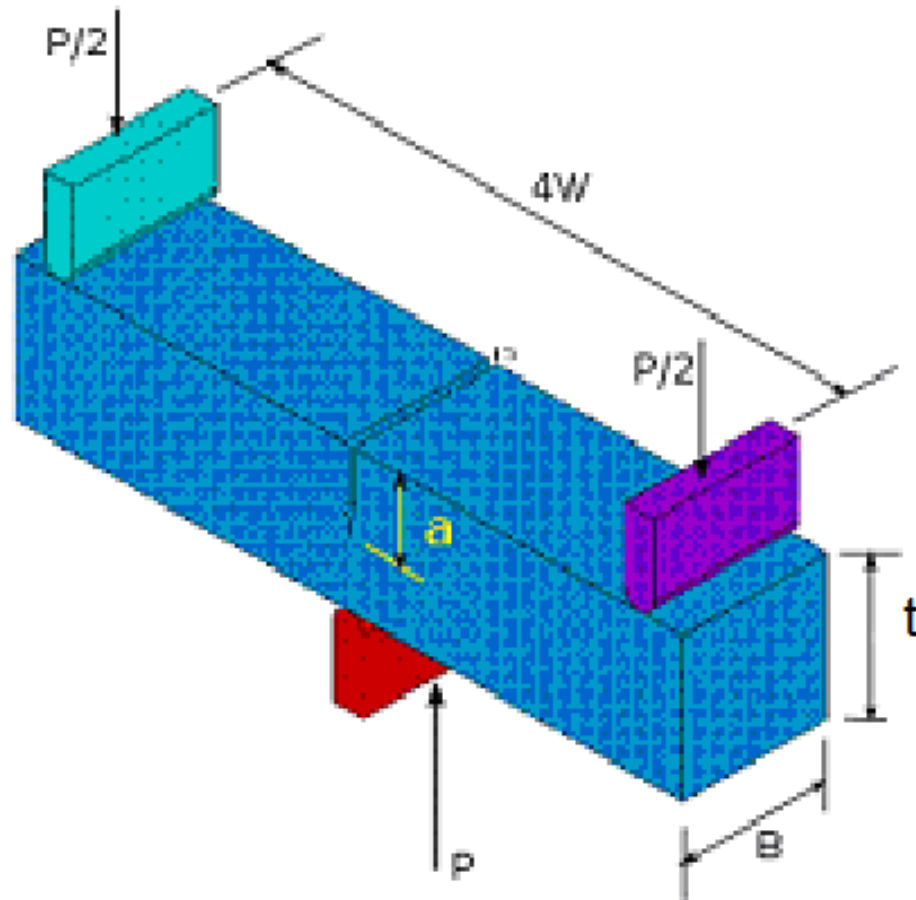
Figure 6.2.1: 3-point test set-up for rectangular beam specimen per ASTM 5045

For the case of linear elastic loading and displacement, the elastic strain energy input into the specimen resulting in fracture is given by:

$$U = \frac{1}{2} P_F d_F$$

(6.2.1)

The mode I CSERR can then be determined from the following expression:

$$G_{IC} = \frac{U}{Bt\phi}$$

(6.2.2)

where Φ is a calibration factor which accounts for the specimen compliance as a function of the ratio of the notch length, a, to the specimen width, W. Values of Φ are provided in ASTM 5045.

An alternative method to determine the mode I CSERR from the ASTM 5045 test procedure is to calculate the material mode I Critical Stress Intensity Factor (CSIF), K_{IC}, and to then evaluate the corresponding mode I CSERR. The CSIF is given by the following expression [71]:

$$K_{IC} = \frac{P_F}{B\sqrt{t}} f(x)$$

(6.2.3)

where the function $f(x)$ is given by [71]:

$$F(x) = 6\sqrt{\frac{a}{t}} \frac{1.99 - \frac{a}{t}\left(1 - \frac{a}{t}\right)\left(2.15 - 3.93x + 2.7\left(\frac{a}{t}\right)^2\right)}{\left(1 + \frac{2a}{t}\right)\left(1 - \frac{a}{t}\right)^{\frac{3}{2}}}$$

(6.2.4)

The relationship between the mode I CSIF, $K_{IC,}$ and the mode I CSERR, G_{IC}, is given for plane strain conditions by [6]:

$$G_{IC} = \frac{K_{IC}^{2}}{E}\left(1 - v^{2}\right) \tag{6.2.5}$$

For this testing, the mode I CSERR was calculated by both methods and compared to provide improved confidence in the results.

It is also necessary to calculate the CSIF to ensure the plane strain condition is met. The thickness of the specimen introduces plane strain conditions when the following condition is met:

$$B_{w} > 2.5\left(\frac{K_{IC}}{\sigma_{y}}\right)^{2} \tag{6.2.6}$$

6.2.3 Mode II Fracture Testing

Of the mode II fracture tests available for homogeneous resins, that generally regarded as the most useful is known as the Richard Type (RT) Test [69,70]. This method is applicable to both brittle and ductile materials. Specimens are subjected to in-plane shear loading conditions, and the mode II CSERR is evaluated by ensuring mode II failure occurs across the specimen gauge length. Here it is important to distinguish again between loading mode and fracture mode. A single fracture mode may dominate over a wide range of loading conditions. Mode I fracture, as noted above, commonly occurs in polymers under mode II loading. The Richard's Type test is designed to ensure mode II failure is maintained under mode II loading.

A number of test configurations have been proposed for the Richard's Type test [69], though the configuration that ensures mode II failure occurs is a function of the material tested. For a brittle thermoset polymer, the V-Notched Beam Method, utilizing the Iosipescu device, is recommended [10], as the use of the double edge notch specimen maintains a pure mode II stress state across the specimen gauge length than single edge notch specimens. The V-Notched test procedure is described in ASTM D5379/D5379M-98 Standard Test Method for Shear Properties of Composite Materials by the V-Notched Beam Method. The specimen geometry, test fixturing and testing configuration are shown in Figure 6.2.2.
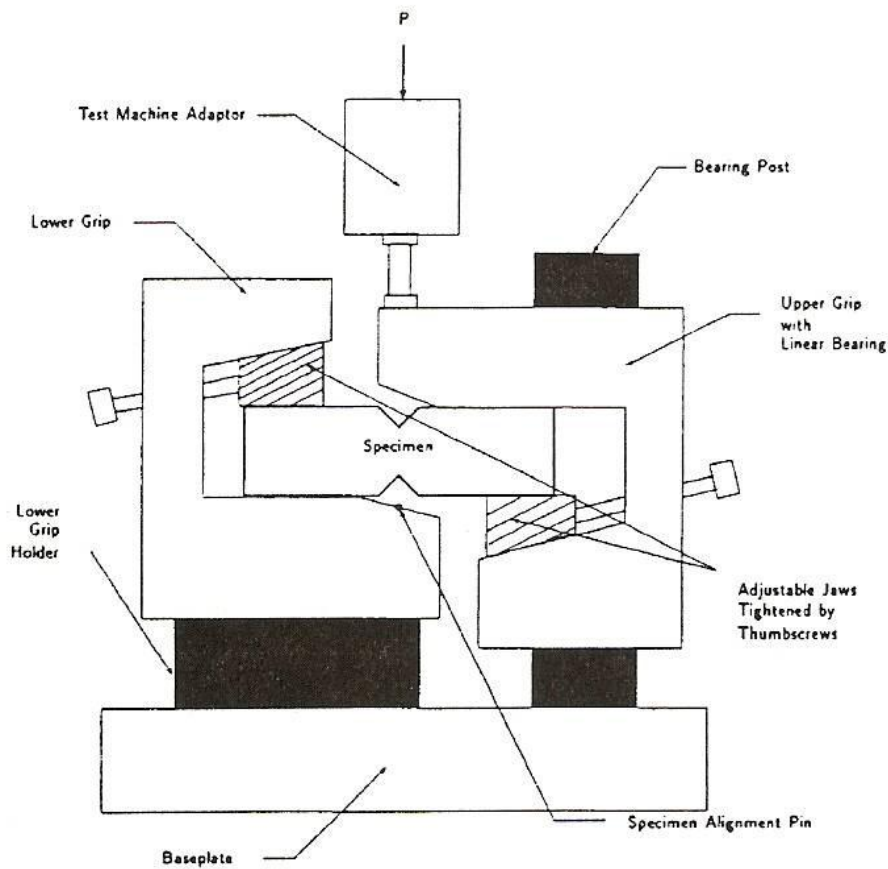
Figure 6.2.2: The Iosipescu device test set-up, showing fixturing, specimen configuration and load application.

For the testing conducted in this research, rectangular specimens 75 mm long and 25 mm wide were cut from the neat resin using a fine saw blade and edges were sanded with 600 grit paper. Notches were introduced along both edges with a router and jig. A razor blade was slid along the notch to ensure a sharp initiation point. Some materials show sensitivity to the specimen thickness due to the occurrence of plasticity effects, some to gauge length, and other materials to both [10], depending on the material evaluated. Therefore a range of specimens at various gauge lengths and thicknesses were testing. Specimens with a thickness of 2 mm, 3 mm, 4.5 mm and 6 mm were produced at a 11 mm gauge length. Specimens with gauge lengths of 5 mm, 10 mm, 15 mm and 20 mm were produced with 3 mm thickness. Values for G_{IIC} were determined for each specimen thickness and gauge length.

Specimens were placed into the Iospiescu fixture and secured with the alignment blocks. Load was applied to the specimens with a 5000 Newton load cell at a strain rate of 1 mm/min, until failure is observed to have occurred across the specimen gauge length, as indicated by a rapid decrease in the load. Data obtained from testing results in a record of load and extension. From this data, the maximum load is noted. The mode CSIF, K_{IIC}, is calculated from Equation 6.2.7 [69], which is applicable for single edge notch specimens, but will give a reasonable estimated value for the double notched specimen configuration. From this value, the mode II CSERR, G_{IIC}, is calculated using equation 6.2.5 and by substituting mode II values for CSERR and CSIF. The calculated value of G_{IIC} was based on an average of all values measured.

$$K_{IIC} = \frac{P_c \sqrt{\pi a}}{tB} \frac{1}{1-\left(\dfrac{a}{t}\right)} \sqrt{\frac{-0.23+1.40\left(\dfrac{a}{t-a}\right)}{1-0.67\left(\dfrac{a}{t-a}\right)+2.08\left(\dfrac{a}{t-a}\right)^2}} \qquad (6.2.7)$$

6.3 Results

Test results are summarized in Table 6.3.1. Tensile and shear properties of the Crosslink epoxy are based on averages obtained from 12 tensile specimens and 9 shear specimens. Mode I values for G_{IC} and K_{IC} are the average of 12 tested specimens. Values for G_{IIC} were evaluated for specimens of varying thickness and gauge length. Five specimens were tested for each thickness and gauge length combination.

Mechanical Properties			Fracture Properties		
Property	Value	1 std dev	Property	Value	1 std dev
Tensile Strength	51.8 MPa	4.2	G_{IC}	3588 J/m^2	1232.7
Elongation to Failure	8.85%	1.8	K_{IC}	3.20 MPa(m)$^{1/2}$	0.46
Young's Modulus	2.6 GPa	0.2	G_{IIC}	~6383 J/m^2	~210
Shear Strength	40.3 MPa	2.47	K_{IIC}	~3.87 MPa(m)$^{1/2}$	~0.090

Table 6.3.1: Measured properties of neat Crosslink epoxy.

Testing of calibration samples determined that the load frame was sufficiently massive with respect to the specimen loads that no calibration adjustment was necessary for mode I and mode II testing. Fracture surfaces of both the mode I and mode II specimens were examined by SEM following testing to evaluate the associated fracture morphology. Cleavage fracture was observed to have occurred for the mode I specimens, while hackling was observed for the mode II specimens, shown respectively in Figures 6.3.1 and 6.3.2.
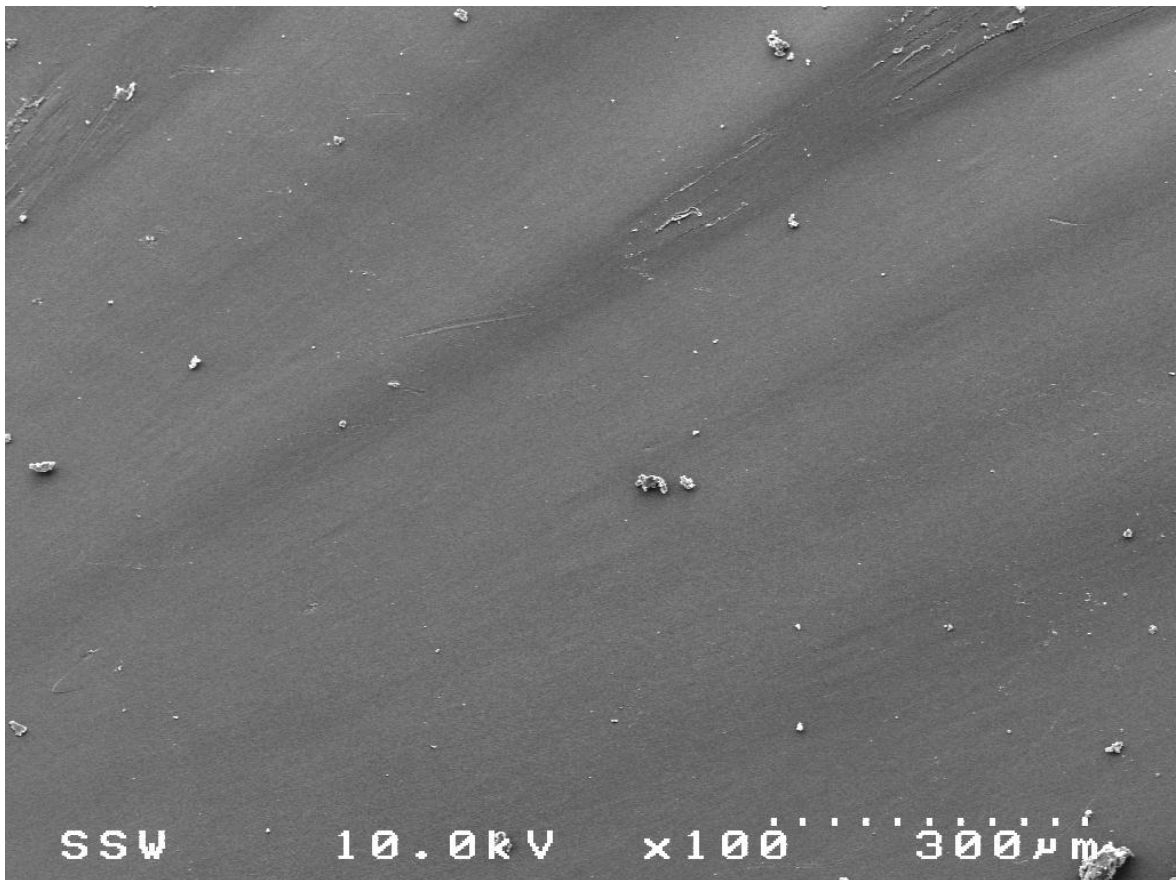
Figure 6.3.1: SEM of Crosslink epoxy following mode I testing, showing cleavage fracture.
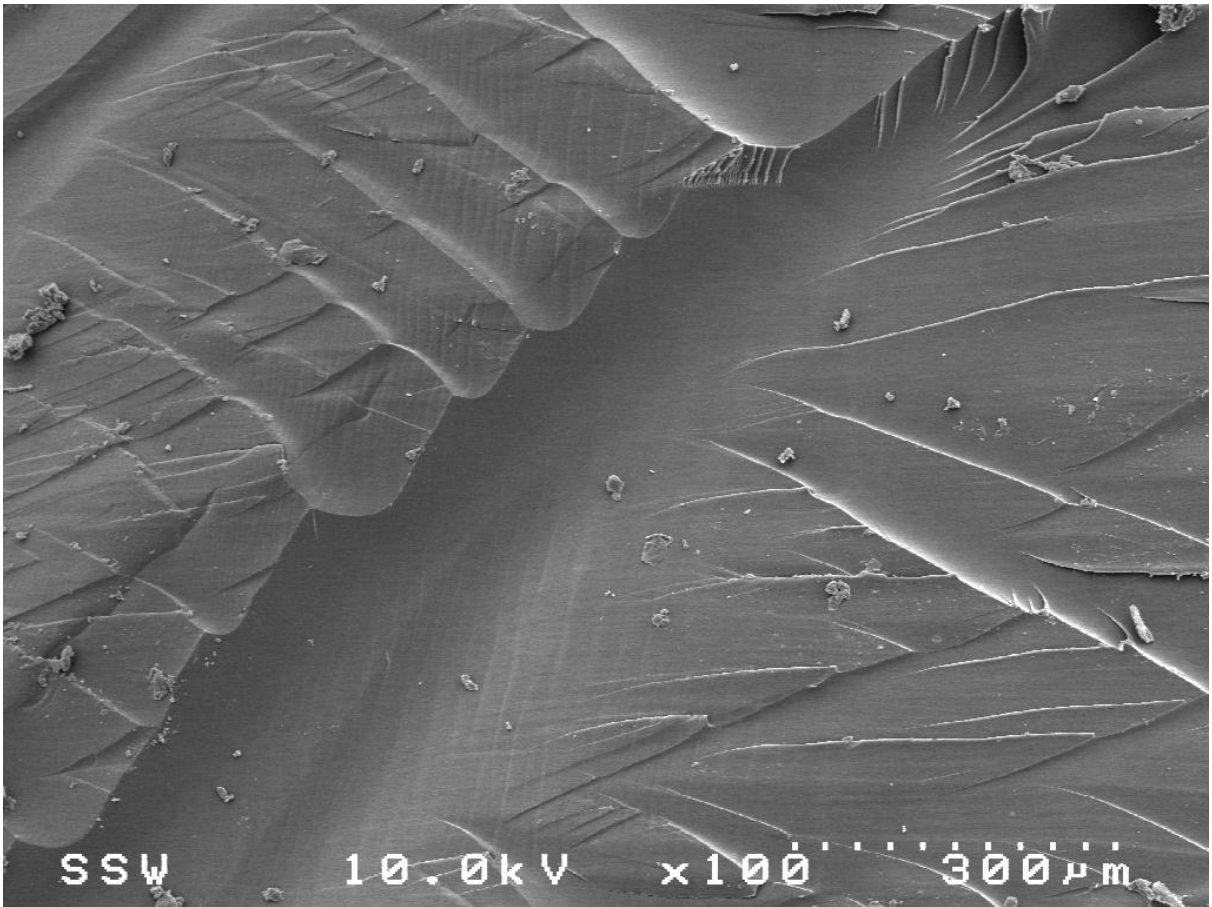
Figure 6.3.2: SEM of Crosslink epoxy fracture surface across gauge length following mode II testing, showing hackling.

6.4 Discussion

6.4.1 Understanding Mode I Failure Under Mode II Loading

As discussed, mode I induced failure may occur under mode II loading. Hackling is an important example of a mode I induced failure mechanism that is only observed to occur when a mode II loading component is present. As mentioned, it has been proposed that this is due to G_{IC} being exceeded before G_{IIC}. This would occur if G_{IIC} was sufficiently larger than G_{IC}. A comparison of G_{IIC} to G_{IC} for

thermosetting polymers can be made through an analysis of the crack tip plastic zone.

From Linear Elastic Fracture Mechanics (LEFM), for materials that experiences limited plasticity at the crack tip such as thermosetting polymers, the energy required to induce crack growth is proportional to the size of the material ahead of the crack tip experiencing plastic deformation [6]. Therefore the ratio of G_C for a given mode of loading as compared with G_{IC} should be approximately equal to the ratio of the corresponding plastic zones.

The plastic zone is frequently defined in terms of the plastic radius, r_P. A general form of the expressions for r_P as a function of loading mode can be derived using the Westergaard expressions for stress at the crack tip for mode I and mode II loading [6].

Westergaard Stress Functions - Mode I

$$\sigma_{xI} = \frac{K_I}{\sqrt{2\pi r}} \cos\left(\frac{\theta}{2}\right)\left[1 - \sin\left(\frac{\theta}{2}\right)\sin\left(\frac{3\theta}{2}\right)\right] \tag{6.2.7}$$

$$\sigma_{yI} = \frac{K_I}{\sqrt{2\pi r}} \cos\left(\frac{\theta}{2}\right)\left[1 + \sin\left(\frac{\theta}{2}\right)\sin\left(\frac{3\theta}{2}\right)\right] \tag{6.2.8}$$

$$\tau_{xyI} = \frac{K_I}{\sqrt{2\pi r}} \sin\left(\frac{\theta}{2}\right)\cos\left(\frac{\theta}{2}\right)\cos\left(\frac{3\theta}{2}\right) \tag{6.2.9}$$

Westergaard Stress Functions - Mode II

$$\sigma_{xII} = -\frac{K_{II}}{\sqrt{2\pi r}} \sin\left(\frac{\theta}{2}\right)\left[2 + \cos\left(\frac{\theta}{2}\right)\cos\left(\frac{3\theta}{2}\right)\right]$$ (6.2.10)

$$\sigma_{yII} = \frac{K_{II}}{\sqrt{2\pi r}} \sin\left(\frac{\theta}{2}\right)\cos\left(\frac{\theta}{2}\right)\cos\left(\frac{3\theta}{2}\right)$$ (6.2.11)

$$\tau_{xyII} = \frac{K_{II}}{\sqrt{2\pi r}} \cos\left(\frac{\theta}{2}\right)\left[1 - \sin\left(\frac{\theta}{2}\right)\sin\left(\frac{3\theta}{2}\right)\right]$$ (6.2.12)

Or simplifying,

$$\sigma_{xI} = \frac{K_I}{\sqrt{2\pi r}} f_1(\theta) \qquad \sigma_{yI} = \frac{K_I}{\sqrt{2\pi r}} f_2(\theta) \qquad \tau_{xyI} = \frac{K_I}{\sqrt{2\pi r}} f_3(\theta) \qquad \text{mode I}$$

$$\sigma_{xII} = \frac{K_{II}}{\sqrt{2\pi r}} f_4(\theta) \qquad \sigma_{yII} = \frac{K_{II}}{\sqrt{2\pi r}} f_5(\theta) \qquad \tau_{xyII} = \frac{K_{II}}{\sqrt{2\pi r}} f_6(\theta) \qquad \text{mode II}$$

The mode I and mode II values can be accumulated for the normal and shear stress components for a mixed-mode condition:

$$\sigma_x = \sigma_{xI} + \sigma_{xII}$$ (6.2.13)

$$\sigma_y = \sigma_{yI} + \sigma_{yII}$$ (6.2.14)

$$\tau_{xy} = \tau_{xyI} + \tau_{xyII}$$ (6.2.15)

Expressions for K_{IC} and K_{IIC} in terms of far field stresses [6] are:

$$K_I = \sigma_O \sqrt{\pi a} \tag{6.2.16}$$

$$K_{II} = \tau_O \sqrt{\pi a} \tag{6.2.17}$$

Substituting 6.2.16 and 6.2.17 into 6.2.13, 6.2.14 and 6.2.15 provides:

$$\sigma_x = \sigma_O \sqrt{\frac{a}{2r}} f_1(\theta) - \tau_O \sqrt{\frac{a}{2r}} f_4(\theta) \tag{6.2.18}$$

$$\sigma_y = \sigma_O \sqrt{\frac{a}{2r}} f_2(\theta) + \tau_O \sqrt{\frac{a}{2r}} f_5(\theta) \tag{6.2.19}$$

$$\tau_{xy} = \sigma_O \sqrt{\frac{a}{2r}} f_3(\theta) + \tau_O \sqrt{\frac{a}{2r}} f_6(\theta) \tag{6.2.20}$$

The ratio between the normal and shear far field stresses given in 6.2.16 and 6.2.17 is:

$$\frac{\sigma_O}{\tau_O} = \frac{K_I}{K_{II}} \tag{6.2.21}$$

An equivalent CSERR can be derived by comparing the expressions relating the mode I and mode II CSERR vs CSIF under plane strain conditions:

$$G_I = \frac{K_I^2}{E}\left(1 - \upsilon^2\right) \tag{6.2.22}$$

$$G_{II} = \frac{K_{II}^2}{E}\left(1 - \upsilon^2\right) \tag{6.2.23}$$

Substituting expressions for CSIF from Equation 6.2.16 and Equation 6.2.17:

$$G_I = \frac{\sigma_0^{2} \pi a}{E} \qquad (6.2.24)$$

$$G_{II} = \frac{\tau_0^{2} \pi a}{E} \qquad (6.2.25)$$

$$\frac{\sigma_0}{\tau_0} = \sqrt{\frac{G_I}{G_{II}}} \qquad (6.2.26)$$

The expression G_I/G_{II} is referred to as the mixed-mode ratio [72], and varies from 0 to infinity. The mode mixture, M, is given by G_{II}/G_C, where $G_C=G_I+G_{II}$ [72], and varies from a value of 0 for pure mode I loading, to a value of 1 for pure mode II loading.

Therefore:

$$\frac{G_I}{G_{II}} = \frac{1}{M} - 1 = \frac{1-M}{M} \qquad (6.2.27)$$

And therefore:

$$\frac{\sigma_o}{\tau_o} = \sqrt{\frac{1-M}{M}} \qquad (6.2.28)$$

Re-arranging terms and substituting for the far field shear stress in the general expressions above, we have mode I and mode II expressions for crack tip stress for any mixed-mode loading condition.

$$\sigma_x \Big/ \sigma_0 = \sqrt{\frac{a}{2r}} f_1(\theta) - \sqrt{\frac{aM}{2r(1-M)}} f_4(\theta) \qquad (6.2.29)$$

$$\sigma_y \Big/ \sigma_0 = \sqrt{\frac{a}{2r}} f_2(\theta) + \sqrt{\frac{aM}{2r(1-M)}} f_5(\theta) \qquad (6.2.30)$$

$$\tau_{xy} \Big/ \sigma_0 = \sqrt{\frac{a}{2r}} f_3(\theta) + \sqrt{\frac{aM}{2r(1-M)}} f_6(\theta) \qquad (6.2.31)$$

And introducing the full function expressions:

$$\sigma_x = \sigma_{xI} + \sigma_{xII} = \sigma_0 \sqrt{\frac{a}{2r}} \left\{ \begin{array}{l} \sqrt{1-M} \, \cos\left(\dfrac{\theta}{2}\right)\left[1 - \sin\left(\dfrac{\theta}{2}\right)\sin\left(\dfrac{3\theta}{2}\right)\right] \\ - \sqrt{M} \, \sin\left(\dfrac{\theta}{2}\right)\left[2 + \cos\left(\dfrac{\theta}{2}\right)\cos\left(\dfrac{3\theta}{2}\right)\right] \end{array} \right\} \qquad (6.2.32)$$

$$\sigma_y = \sigma_{yI} + \sigma_{yII} = \sigma_0 \sqrt{\frac{a}{2r}} \left\{ \begin{array}{l} \sqrt{1-M} \, \cos\left(\dfrac{\theta}{2}\right)\left[1 + \sin\left(\dfrac{\theta}{2}\right)\sin\left(\dfrac{3\theta}{2}\right)\right] \\ + \sqrt{M} \, \sin\left(\dfrac{\theta}{2}\right)\cos\left(\dfrac{\theta}{2}\right)\cos\left(\dfrac{3\theta}{2}\right) \end{array} \right\} \qquad (6.2.33)$$

$$\tau_{xy} = \tau_{xyI} + \tau_{xyII} = \sigma_0 \sqrt{\frac{a}{2r}} \left\{ \begin{array}{l} \sqrt{1-M} \, \sin\left(\dfrac{\theta}{2}\right)\cos\left(\dfrac{\theta}{2}\right)\cos\left(\dfrac{3\theta}{2}\right) \\ + \sqrt{M} \, \cos\left(\dfrac{\theta}{2}\right)\left[1 - \sin\left(\dfrac{\theta}{2}\right)\sin\left(\dfrac{3\theta}{2}\right)\right] \end{array} \right\} \qquad (6.2.34)$$

To derive an expression for plastic radius as a function of loading ratio, the approach described by Broek [6] is applied, in which 6.2.32, 6.2.33 and 6.2.34 are substituted into the expressions for principal stresses as a function of stress state [6]:

$$\sigma_1, \sigma_2 = \frac{\left(\sigma_x + \sigma_y\right)}{2} \pm \sqrt{\left[\frac{\left(\sigma_x - \sigma_y\right)}{2}\right]^2 + \tau_{xy}^2}$$

(6.2.35)

$$\sigma_3 = \nu\left(\sigma_1 + \sigma_2\right) \qquad \text{for plane strain}$$

(6.2.36)

The resulting expressions are then substituted into Von Mises Failure Criterion [6]:

$$2\sigma_y^2 = \left(\sigma_1 - \sigma_2\right)^2 + \left(\sigma_2 - \sigma_3\right)^2 + \left(\sigma_3 - \sigma_1\right)^2$$

(6.2.37)

Setting Poisson's ratio equal 0.3 for a thermosetting polymer, and solving in terms of the plastic radius, the general expression for plastic zone size as a function of mode mixture is derived:

$$r_p / \left(\frac{\sigma_y^2}{a}\right) = 2.84\sqrt{M}\sqrt{1-M}\cos\frac{\theta}{2}\sin\frac{\theta}{2} - 6\sqrt{M}\sqrt{1-M}\cos\frac{\theta}{2}\sin^3\frac{\theta}{2}$$
$$-5.84M\sin^2\frac{\theta}{2} + 6M\sin^4\frac{\theta}{2} + 1.42M + 1.42\sin^2\frac{\theta}{2} - 1.5\sin^4\frac{\theta}{2} + 0.08$$

(6.2.38)

These calculations were performed using MAPLE software, and are shown in Appendix B. Plotting Equation 6.2.38 for the plastic radius as a function of the

mode of loading produces the plastic zone shape relationship as shown in Figure

6.4.1.
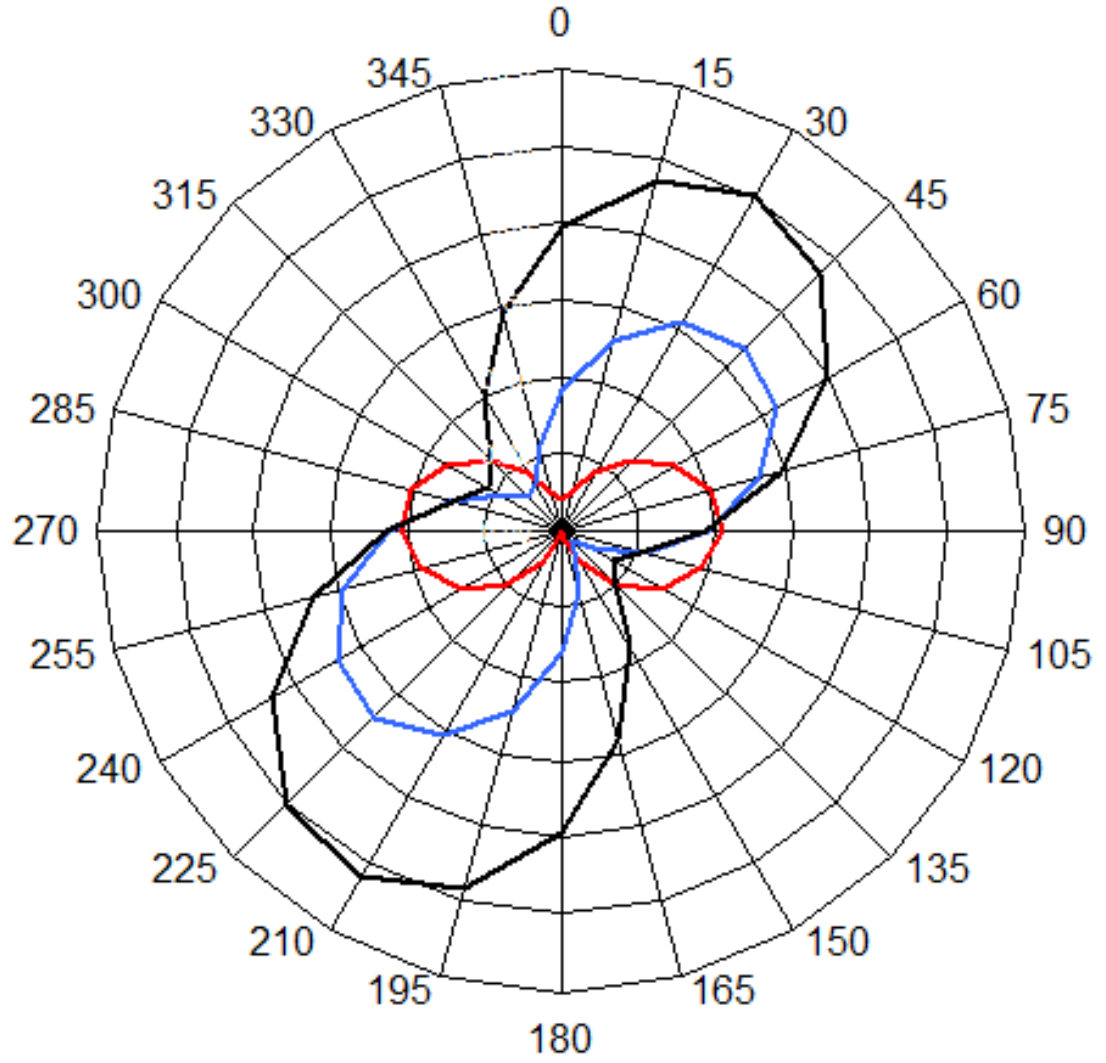
(a)
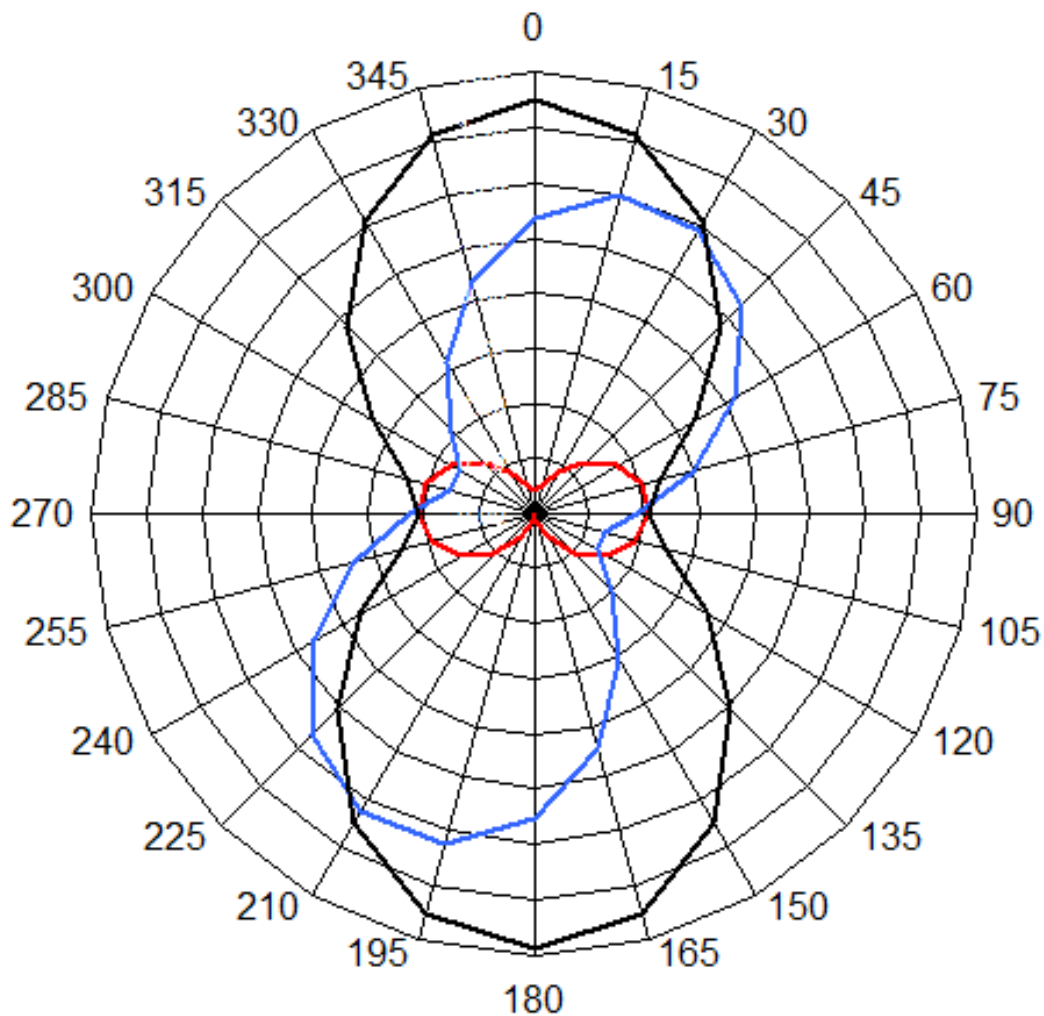
(b)

Figure 6.4.1: Shape and relative size of crack tip plastic radius as a function of mixed-mode loading, plotted over 360 degrees from an existing crack at the 180 degrees position; (a) for 0% (red), 30% (blue) and 50% (black) mode mixture percentages; (b) for 0% (red), 70% (blue) and 100% (black) mode mixture.

The shape of the pure mode I and pure mode II plastic zones are precisely as predicted [6], and as shown in Figure 2.2.5. The transition of the relative size and shape of the plastic zone between mode I and mode II occurs through a gradual increase in the plastic zone size and a rotation from a direction perpendicular to the crack direction to a direction aligned with the crack direction. The transitional shape and orientation correspond to that demonstrated by finite element analysis [73]. The orientation also corresponds to that measured by experimentation [74], as shown in Figure 6.4.2. The plastic zone size increases with mode II loading, and reaches a maximum for pure mode II loading. As mentioned, the CSERR is proportional to the volume of the plastic zone. Therefore it can be concluded that when a mode II loading component is present, thermosetting polymers may fail in mode I rather than mode II as a result of G_{IC} being exceeded prior to G_{IIC}.
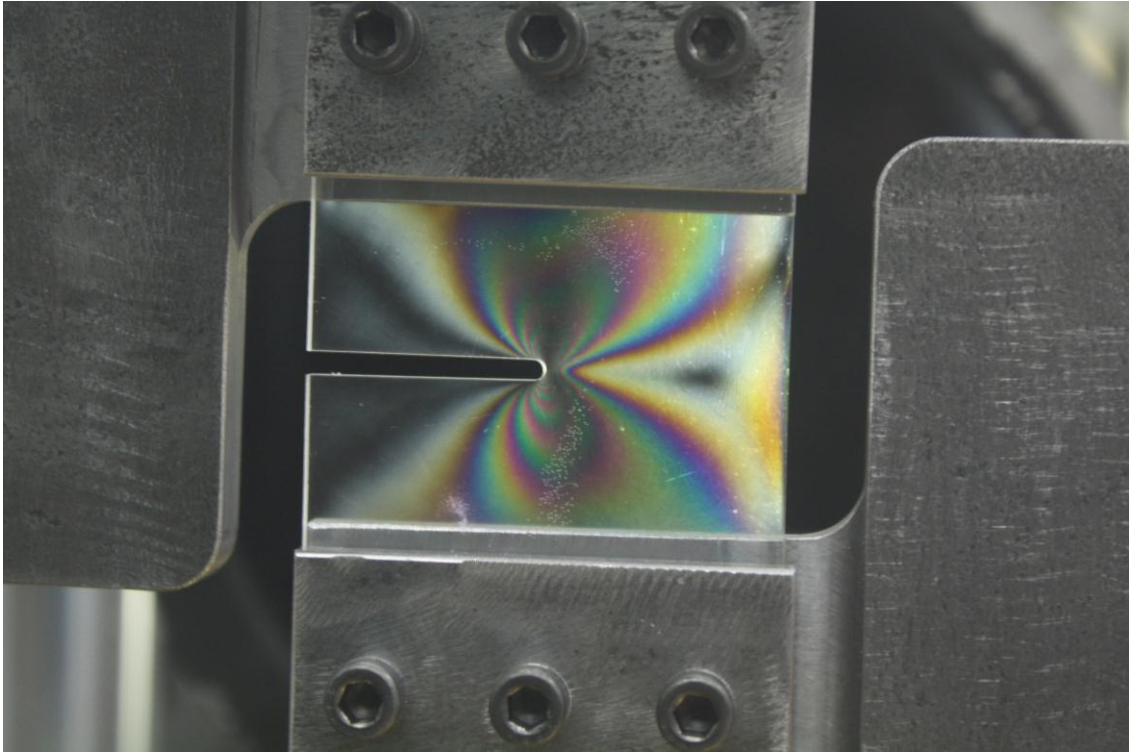
(a)
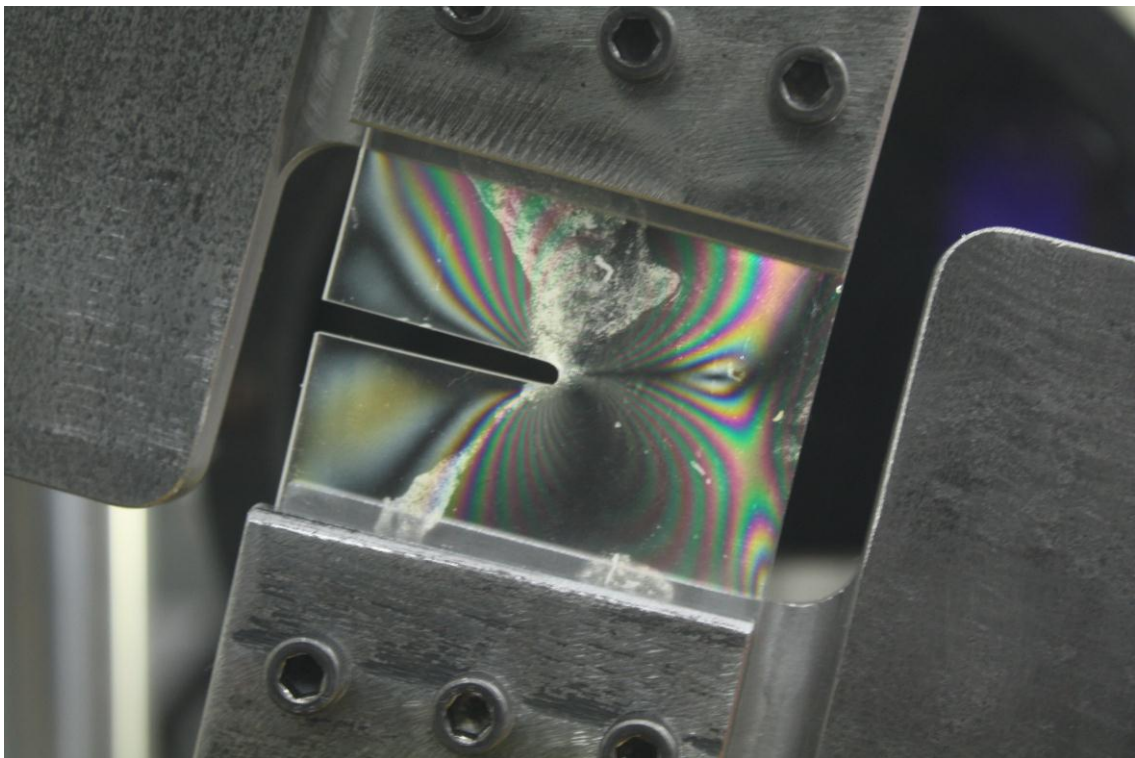
(b)
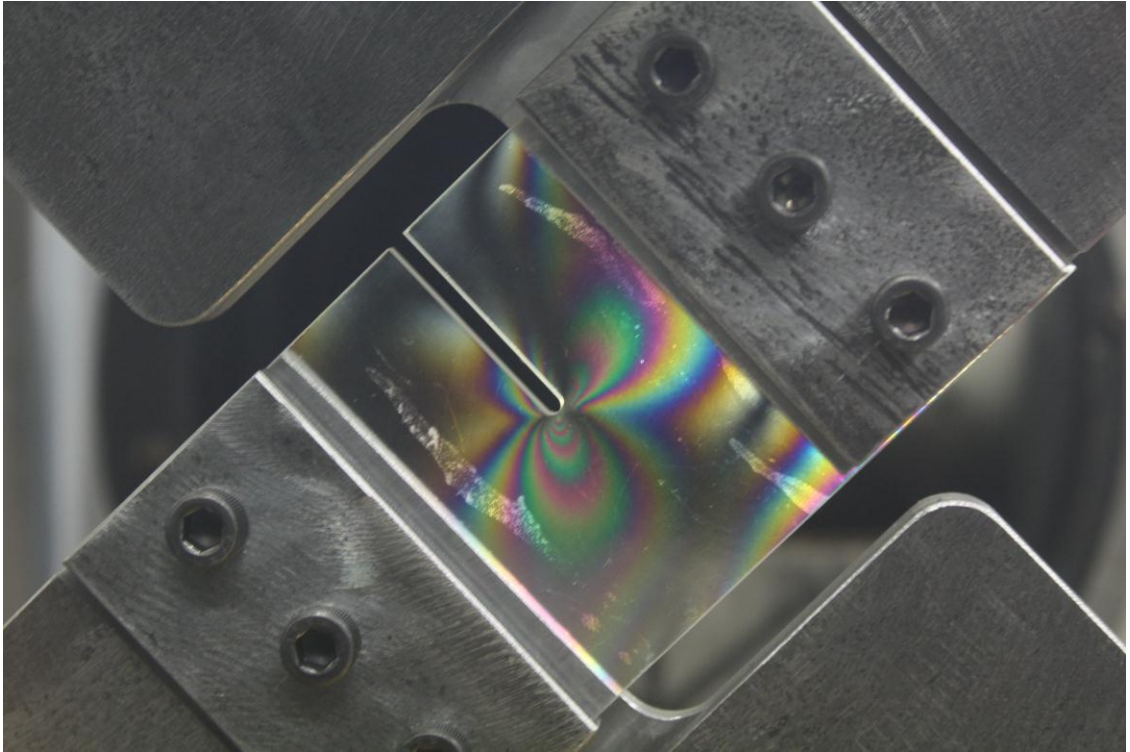
(c)
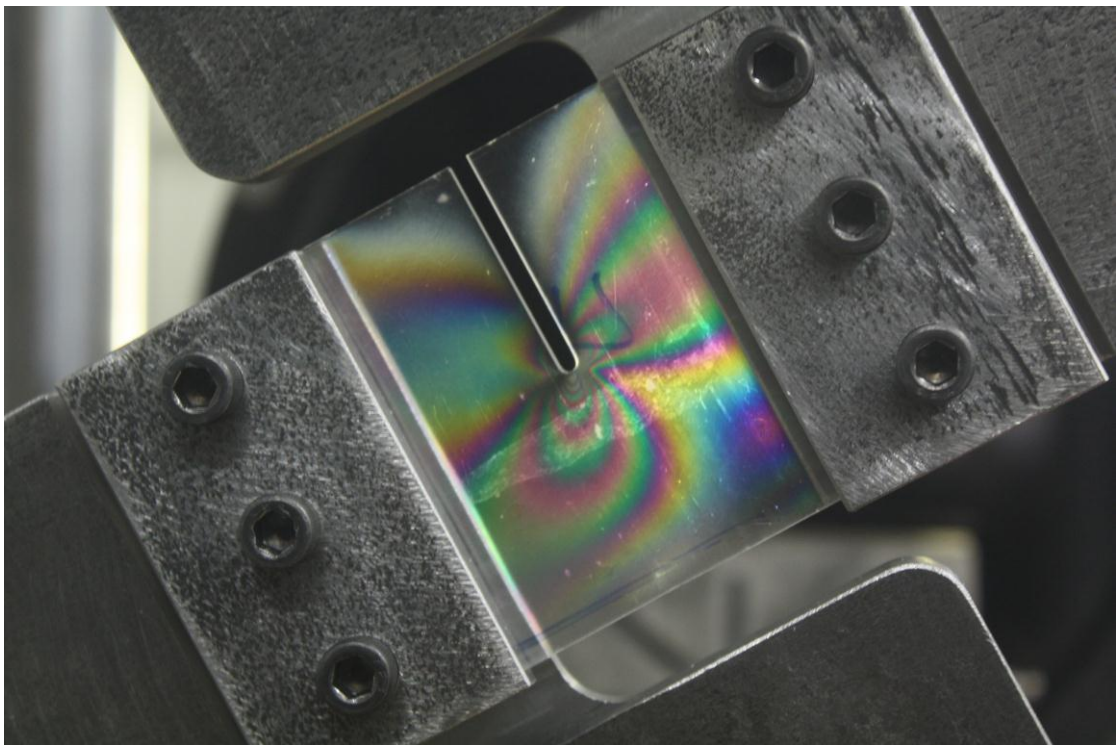
(d)
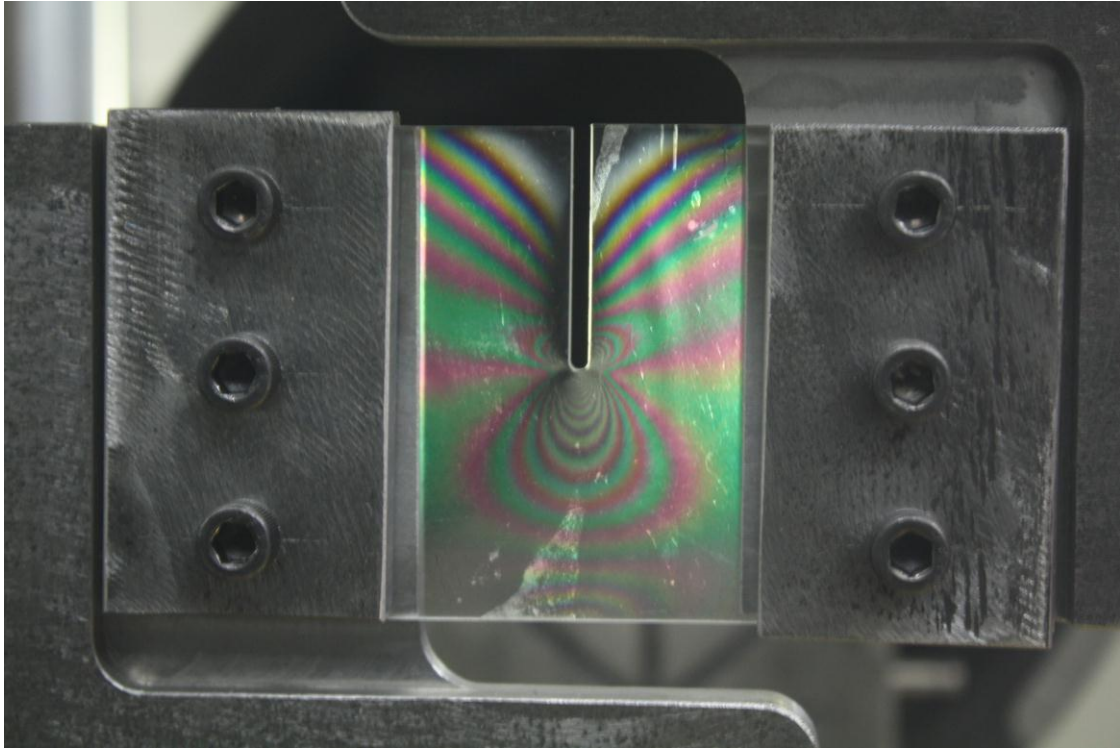
(e)

Figure 6.4.2: Polarized light study of the shape of the crack tip strain orientation as a function of the mixed-mode loading percentage; (a) pure mode I; (b) 15 degrees off-loading; (c) 45 degrees off-loading; (d) 75 degrees off-loading; (e) pure mode II [74].

6.4.2 Predicting CSERR as a Function of Hackling

From the analysis above, mode I failure may occur under mode II loading.   Mode I failure may involve propagation of a single crack, or the formation of hackling. Other author's have reported that mode II testing of neat resins typically results in the formation of a single crack, and the occurrence of hackling has not been reported [10,65,69]. Hackling was clearly observed in the mode II testing conducted in this study, as shown in Figure 6.3.4.

For the cases in which hackling occurs, as with the neat resin and UD composites tested in this study, the measured increase in G_C between mode I and mode II loading can be understood as a consequence of the increase in fracture surface area resulting from hackle formation. An expression can be developed to describe the angle at which hackling will occur for a given mixed-mode loading condition. As a tension induced failure, the angle of hackle formation corresponds to the principal stress direction. This lies between 0° and 45° for pure mode I and pure mode II loading, respectively. The angle of the principal stress direction for plane strain conditions is given by:

$$2\theta_p = \tan^{-1} \frac{2\tau_{xy}}{\sigma_x - \sigma_y}$$

(6.2.39)

Substituting the inverse of Equation 6.2.28, we have:

$$2\theta_p = \tan^{-1} \sqrt{\frac{M}{1-M}}$$

(6.2.40)

Hackle angle as a function of mixed-mode loading is shown in Figure 6.4.3.
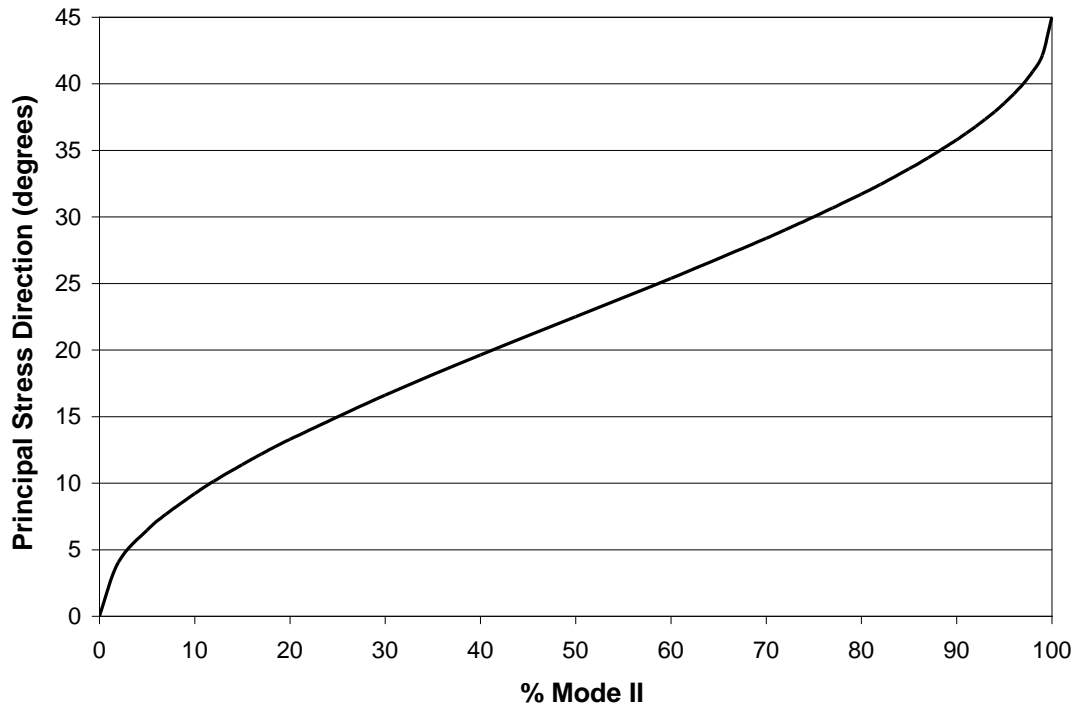
Figure 6.4.3: Graphical Representation of Principal Stress (Hackle Angle) as a Function of Percent Mode Mixture

The hackle angle is a function of the principal stress direction, and from Equation 6.2.40, principal stress direction is a function of mode mixture. The hackle angle increases with increasing mode II loading, increasing the associated crack path. Therefore crack path length is also a function of the loading mode. Increasing crack length corresponds to increasing fracture surface, and the associated CSERR increases proportionately. From simple geometry, a mathematical expression for the crack length as a function of principal stress direction is derived, as given below and shown in Figure 6.4.4.

$$L_{MM} = L_{M1}\left(\tan\theta_p + \frac{1}{\cos\theta_p}\right) \qquad (6.2.41)$$

Pure Mode I ———————————— Crack Length = L_{M1}

Pure Mode II   Crack Length = $L_{M1}(1+\sqrt{2})$

Mixed-mode θ Crack Length = $L_{M1}(\tan\theta + 1/\cos\theta)$
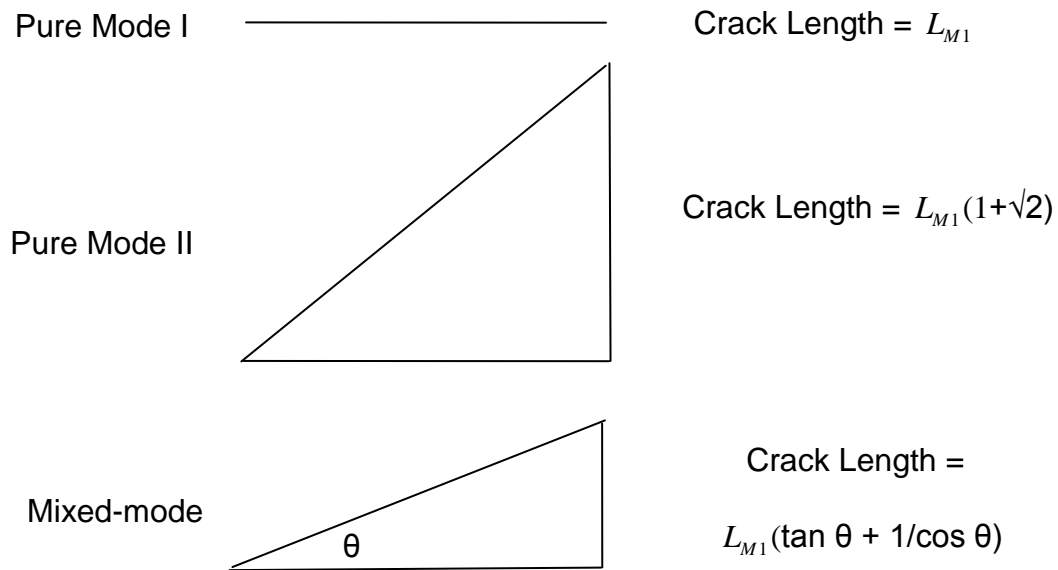
Figure 6.4.4: Crack path length as a function of loading mode and hackle angle.

Crack length as a function of mixed-mode loading is shown in Figure 6.4.5. The relationship shown in Figure 6.4.5 is the ideal case, where all material hackles perfectly. In practice, and as observed with the reinforced polymer tested in this study, some plastic deformation of the hackles may occur for high mode II loading, and hackles may intermittently occur for low mode II loading.
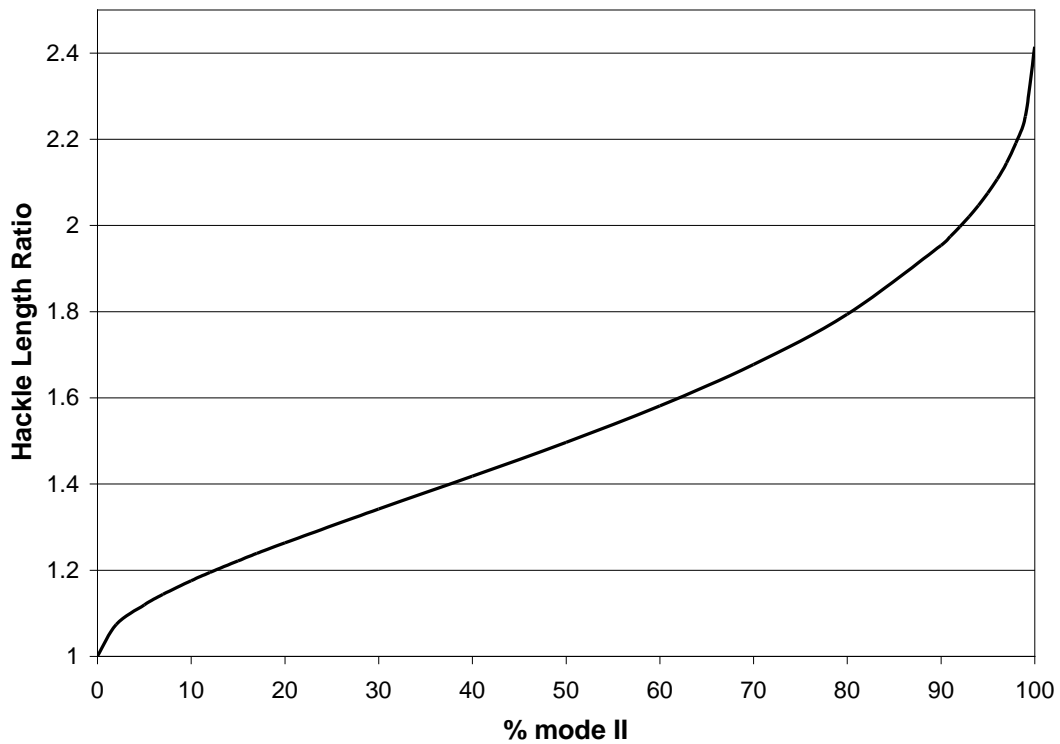
Figure 6.4.5: Graphical Representation of Crack Length as a Function of Loading Mode

Substituting Equation 6.2.40 into Equation 6.2.41 yields an expression for Figure 6.4.5

$$H_f = \tan\left(\frac{1}{2}\tan^{-1}\sqrt{\frac{M}{1-M}}\right) + \frac{1}{\cos\left(\frac{1}{2}\tan^{-1}\sqrt{\frac{M}{1-M}}\right)} \tag{6.4.42}$$

Where the term H_f will be referred to as the Hackle Function, and expresses the relationship between hackle angle and mode mixture, M, where M varies from 0 to 1 for pure mode I and pure mode II loading, respectively.

The supposition that the measured variation in CSERR with the mixed-mode loading condition is a function of the angle of hackle formation is supported by the experimental data presented in this study. For the case of mode II loading of a neat thermosetting polymer under ideal conditions in which all material hackles at 45° without gaps between the hackles, the crack length would be 1+√2 times, or 241% of that for cracking by cleavage under pure mode I loading (from Figure 6.4.5 and from the geometry for a right triangle). In practice, gaps are regularly seen between hackles, and so the actual value would be expected to be lower. For the Crosslink epoxy studied, and for which hackling was evident for mode II induced fracturing, G_{IIC} is estimated at 178% the value of G_{IC}. This supports hackling as responsible for the observed increase in CSERR, and that hackling is a mode I induced failure, without involving a mode II failure component.

Further support for the supposition could be provided by comparing the measured values of the CSERR as a function of mixed-mode loading for neat thermosetting polymers that exhibit hackling with that predicted by Figure 6.4.5. However, no published test data could be located. This is due to the fact that, as mentioned, mode II and mixed-mode testing of polymers typically results propagation of a single mode I induced crack [2,74], rather than resulting in hackle formation. This is demonstrated in Figure 6.4.6 for the case of a polymer specimen subjected to mixed-mode loading [74]. Further validation of the relationship would require development of a test method that more reliably producing hackling in neat polymers under mixed-mode loading conditions.
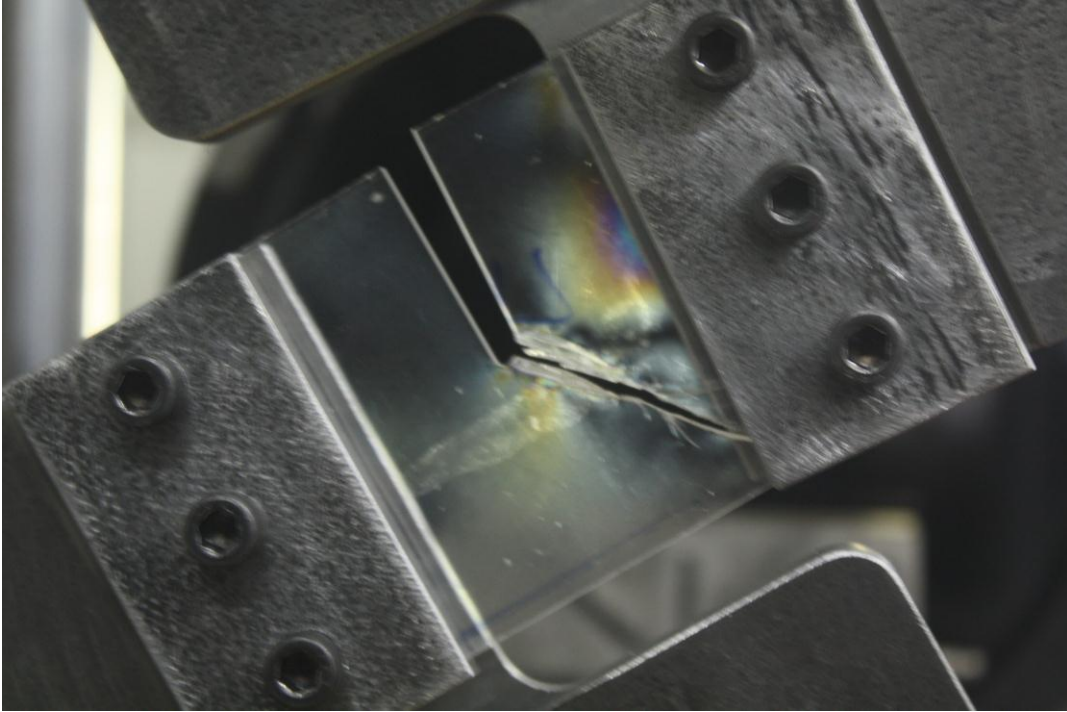
Figure 6.4.6: Typical propagation of a single tensile crack in a neat polymer subjected to mixed-mode testing [74].

In summary, the transition in CSERR with loading mode predicted by the increase in fracture surface resulting from hackle formation correlates well with available data. As other failure mechanisms often contribute to higher values of G_C than that observed for when only hackling occurs, the CSERR relationship predicted by hackling can be seen as a lower bound for reinforced thermosetting polymers. In the effort to produce a mechanistic failure criterion for reinforced thermosetting polymer composites, characterizing and quantifying the crack path increase associated with hackle formation as a function of mixed-mode loading provides an essential first step.

6.5 Summary

Hackle formation, a mode I induced tension fracture, was observed to occur for both neat epoxy and UD CFP composites subjected to mode II fracture testing. The occurrence of mode I failure under mode II loading in thermosetting polymers is explained using Westergaard expressions in terms of the crack tip plastic zone. The total crack length associated with hackle formation as a function of mixed-mode loading is predicted on the basis of principal stress direction. The measured increase in G_C with increased mode II loading for neat epoxy and UD CFP composites correlates well with the corresponding increase in crack length.

7. INTERFACE STUDIES

7.1 Introduction

Fiber-resin interfacial properties, and methods to accurately and reliably measure these, were investigated in an effort to develop a mixed-mode loading mechanistic failure criterion for CFP composites. The properties of interest are the interfacial bond strength, also referred to as the interfacial shear strength, and denoted τ_i [1], and the interfacial debond energy, G_{ic} [1]. Interfacial bond strength is a measure of the strength of the bond between the matrix and reinforcement, and is critical in determining whether crack deflection occurs. Interfacial debond energy is a measure of the energy required to debond the matrix and reinforcement, and is one of the key energy absorption properties associated with delamination in CFP composites.

Methods available to experimentally determine interfacial bond strength and interfacial debond energy of CFP's fall into three groups; direct methods, indirect methods, and composite lamina methods [2,75]. Though these methods attempt to measure the interfacial properties, many are actually fracture tests. Only the direct test methods are able to determine the interfacial bond strength and debond energy. Indirect test methods, such as the ball compression and variable curvature tests, provide only comparative information useful for ranking of the adhesion properties between various CFP's. Composite lamina test methods,

such as transverse flexural, 4-point shear and short beam shear tests, do not measure the interface properties alone [2].

Direct test methods include the embedded fiber compression (push-out), fiber pullout, microbond, micro-indentation, and fiber fragmentation tests. All of these methods are particularly sensitive to specimen preparation [2]. The push-out test is regarded as accurate for brittle resins, but the assumptions made in the model used to evaluate test results are less applicable to ductile resins [75]. As well, the push-out method requires sophisticated equipment, both in regards to the indenter and the load cell. The micro-indentation test is a version of the push-out test.

Pull-out test methods are common, but due to difficulty in embedding individual filaments a wide variety of specimen configuration and test methodologies exist. There is a lack of consistency in results between the various approaches [76]. Pull-out testing also requires extensive and repetitive specimen testing over a range of embedded lengths, rendering the test method labour intensive. The microbond test is a version of the pull-out test.

The fiber fragmentation test does not require sophisticated instrumentation or equipment and results are regarded as consistent. However, a transparent resin with a relatively high elongation to failure is required. Like all methods, the fiber-fragmentation method is regarded as sensitive to specimen preparation; and

similar to the pull-out method, consistently embedding a single filament in the resin is challenging [76,77].

Assumptions and analytical approach vary between the various models proposed. For example, authors frequently assume perfect bonding, no residual stresses, or frictionless debonding [78]. Others will attempt to account for frictional losses [77] or other effects. Consequently, there is a wide range in the available test configurations and resulting data. These methods have shown varied results in measuring interfacial debond properties. For example, Zhou [75] found G_{ic} values calculated for a glass/epoxy using the fragmentation test were 6 times higher than those obtained using push-out test, noting that the variation results from key differences in the models proposed. A 1993 round-robin exercise on interfacial measurements concluded that "different laboratories are unable to provide similar answers for the level of interfacial adhesion of a given composite system" and that "every laboratory now has its own model for the analysis of the fragmentation test" [79].

An extensive survey of the available literature strongly suggested that the fragmentation test provides the most consistent and accurate values for measuring both interfacial bond strength and debond energy [52,77,79]. The test method also involves the least complex specimen preparation, least complicated test set-up, and proved suitable for the resin system considered in this study. Therefore, the fragmentation test was selected to determine both the interfacial

bond strength and interfacial debond energy for the resin/fiber system being studied in this research.

The fragmentation test involves imposing a tensile strain to specimens consisting of filaments extracted from a fibrous yarn or tow that are embedded in a polymeric resin. Strain is increased until no additional filament fracturing occurs. Employing shear lag theory, it is assumed that the filament ends are unable to transfer tensile stresses, and therefore load is transferred from the matrix to the fibers solely via shear stress across the common interface. The maximum shear stresses exist at the fiber ends. The shear stress is then carried as a tensile stress by the remaining fiber length. The tensile stress increases from zero at the fiber ends to a maximum at some distance from the fiber end, while the shear stress decreases from the maximum at the fiber ends to near zero at the same distance from the fiber end. The principle is illustrated in Figure 7.1.1.
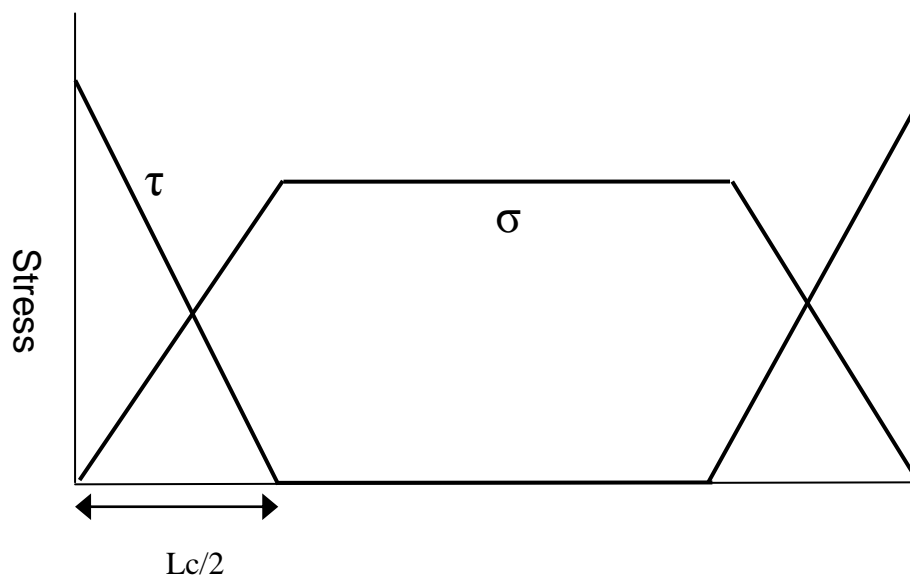
Figure 7.1.1: Tensile and shear stress distribution along the length of a fiber embedded in a matrix to axial loading

The filament length at either end of the filament over which the transfer in load occurs is equal to half of the critical transfer length, L_c. When the fiber is loaded beyond the tensile strength of the fiber, the fiber will fail somewhere along its length. The fragmented fiber will continue to carry load and fracture repeatedly. When the fiber length is equal to the critical transfer length, the maximum tensile loading at the center of the fiber is just equal to the failure strength of the fiber. At any length shorter than the critical transfer length, the fiber can no longer carry a tensile load that exceeds the strength of the fiber and therefore can no longer fail [79]. On completion of the fragmentation test, all filament segments will have a length, x, such that $L_c/2 < x < L_c$. For the case in which the shear yield strength of the matrix sufficiently exceeds the shear stress at the interface, then the relationship between the critical transfer length and the interfacial shear strength is expressed as [79]:

$$L_c = \chi \frac{\sigma_F d}{2\tau_i} \qquad (7.1.1)$$

The value of the non-dimensional correction factor, χ, accounts for the variations in the tensile strength and of the resulting fiber fragment lengths [79]. Equation 7.1.1 can be re-arranged to provide an expression for calculating the interfacial bond strength:

$$\tau_i = \chi \frac{\sigma_F d}{2L_c} \qquad (7.1.2)$$

Interfacial debond energy, G_{ic}, is determined from the fiber fragmentation test by considering that following the fracture of a filament, strain energy not consumed in the process of fracturing the filament is introduced to the resin-fiber interface. This additional energy results in debonding of the fractured ends of the filament from the surrounding resin. The principle is illustrated in Figure 7.1.2. The total length of the debonded filament on either side of the fracture is known as the Debond Zone, L_d. The length of the debond zone correlates to the interfacial debond energy. The zone is shorter where strong interfacial bonding is present and longer where the debond strength is weaker [19].
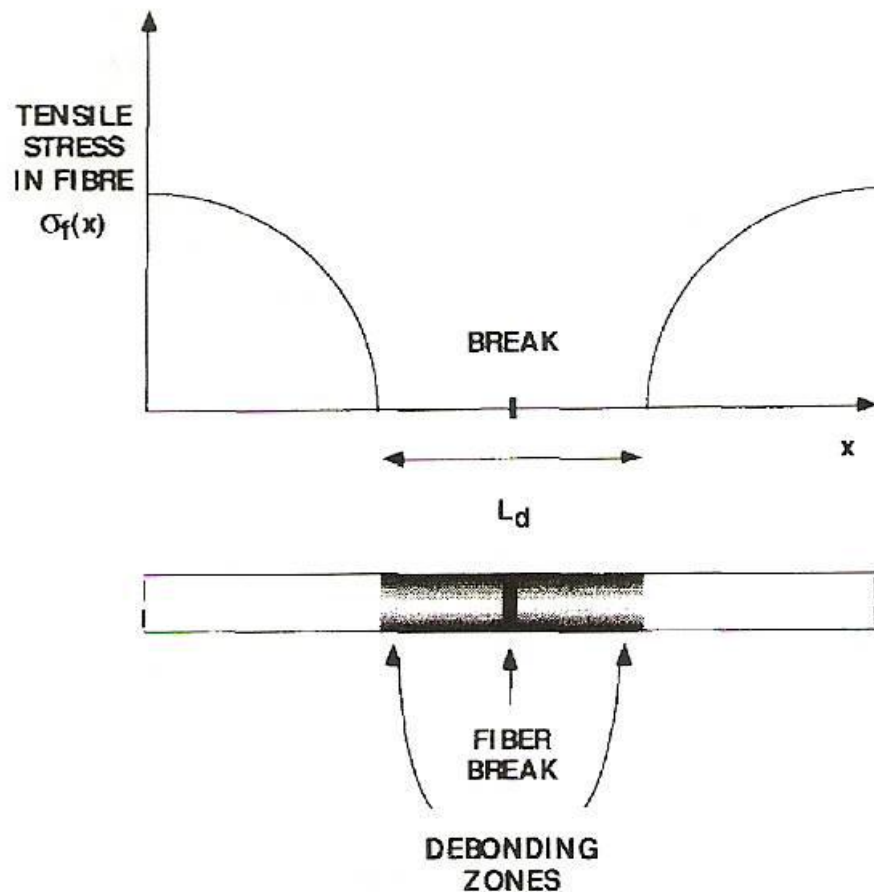
Figure 7.1.2: Tensile stress distribution along a fractured fiber. Debonded zone length, L_d, corresponds inversely to the interfacial bond energy.

Using the single fiber fragmentation test, Folkes [79] studied E-glass and thermoplastic composites and determined the interfacial bond strength to be between 20 and 46 MPa, with a dependence on the fibers used. Zhou [75] studied E-glass and epoxy composites with the fragmentation test and measured an interfacial bond strength of 30+/- 7 MPa for uncoated fibers and 43+/-11 MPa for fibers sized with a silane coupling agent. Zhou [75] also reported interfacial debond energy values for a glass/epoxy of 957 J/m^2 for fibers sized with a silane compound, and 571 J/m^2 for uncoated fibers. In general Zhou [19] reports G_{iC} values for glass/epoxy with a weak interface of approximately 200 J/m^2, while for a strong interface of approximately 1000 J/m^2. It has been reported that debond energy is also sensitive to filament diameter, varying from 400 to 1000 J/m^2 for filament diameters of 7 and 12 μm, respectively [19].

No studies were found that considered conducting the fragmentation test with multiple embedded filaments to determine whether or not the measured value of fiber bond strength is independent of the quantity of filaments embedded in the specimen. This is of interest as development of a methodology utilizing embedding multiple filaments would significantly simplify specimen preparation and consistency, and hence reduce variability in the measured property.

7.2 Methods

7.2.1 Specimen Preparation

Fiber fragmentation testing requires the resin to be transparent to permit post-test examination to determine L_c. As well, the resin must possess a strain to failure much higher than the filament to permit adequate filament fracturing. And lastly, the resin must possess shear strength higher than the interfacial bond strength to ensure fiber fragmentation is observed rather than resin fracture. The two-part epoxy supplied by Crosslinks Technology (Toronto, Ontario, Canada) and used to fabricate UD-L and UD-H meets these requirements. Fragmentation test specimens were prepared by embedding between 1 and 36 E-glass filaments in the epoxy resin. E-glass filaments were collected from a 17.8 oz/yd^2 UD fabric, style TG-18-U, supplied by J B Martin (St-Jean-sur-Richelieu, Quebec, Canada). The filaments had a diameter of 19 µm, as determined by SEM. The epoxy was prepared by slowly stirring 100 parts of CLR 1180 with 30 parts CLH6560.

Test specimens were fabricated using a Teflon block, into which four rectangular cut-outs were machined. The block was 250 mm long x 90 mm wide x 13 mm deep. The cut-outs were 200 mm long x 13 mm wide x 4 mm deep. The cut-out surfaces were polished with a polishing paste and polishing disk to minimize surface roughness of the specimens, thereby preserving specimen transparency. Slots 1.5 mm deep were introduced at either side of the cut-outs. A single cut-out version of the block is illustrated in Figure 7.3.1.
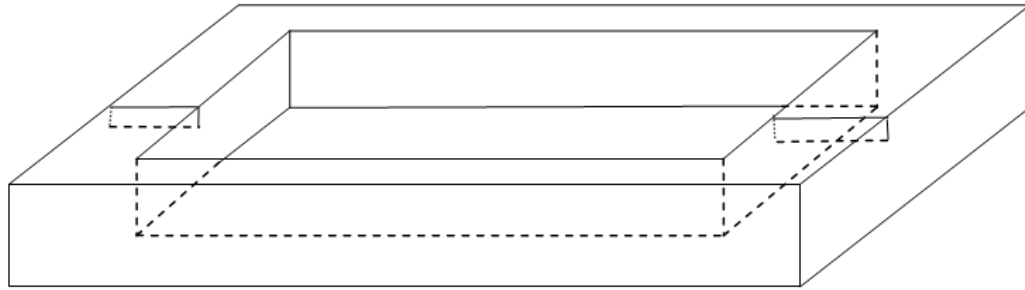
Figure 7.3.1: Teflon Block with Machined and Polished Cut-out and Slots for Fabricating Fragmentation Specimens.

To fabricate the specimens, the filaments were suspended through the slots and held in place at the filament ends with high temperature tape. The filaments were pulled tightly to ensure they remained within the middle region of each specimen. Resin was introduced into the cut-outs slowly with a syringe. Droplets were applied directly along the filaments to ensure good wetting. Exactly 7 cubic centimetres of resin was added to each cut-out to produce consistent specimens. The fixture, resin and filaments were cured at 60 C for 4 hours, per the manufacturer's instructions. Specimens were removed from the fixture following cooling.

Separation of the cured epoxy blocks from the Teflon required minimal force. The blocks were 3 mm thick, with the fibers embedded 0.5 mm below the top surface. The epoxy blocks were cut in half to 100 mm in length, and dog-bone specimens were machined from these. The specimens had a meniscus along

the edges, but machining removed the meniscus from the gauge length area. The free surface of the sample was not machined or polished, as this was found to reduce specimen transparency

7.2.2 Testing

The fragmentation test was performed by subjecting specimens to a tensile strain at a rate of 1 mm/min. During testing, the development of fractures within the filaments could be directly observed. The epoxy in the area of the fracture appeared to darken. The filaments were observed to fracture within the gauge length of the specimen. Testing proceeded with each specimen until no additional filament fracture was observed to occur. Specimens were then unloaded and removed from the fixture, and examined by optical transmission microscopy.

Interfacial bond strength was calculated using Equation 7.1.2. As mentioned, the non-dimensional correction factor, χ, that appears in Equation 7.1.2 accounts for the variations in the tensile strength of the fiber and resulting fragment lengths [79]. The value of the non-dimensional correction factor ranges from 0.67 to 0.97, and is a function of the fiber-matrix system being tested, and the selected experimental method. For the case where the fiber fragment lengths are assumed to vary uniformly between $\frac{1}{2} L_c$ and L_c, then $\chi = 0.75$ is typically taken as a mean value [79]. Substitution into Equation 7.1.2 provides:

$$\tau_i = \frac{3\sigma_F d}{8L_c}$$ (7.2.1)

The value for the tensile strength of the fibers was taken from the manufacturer's material specification data sheets.

To evaluate whether the measured interfacial shear strength is reasonable, the shear strength of the neat resin as determined in Chapter 6 was compared to the interfacial bond strength. The interfacial shear strength should be less than the resin shear strength, otherwise fragmentation testing would result in matrix failure rather than fiber fracture.

The interfacial debond energy was calculated using the expression proposed by X.-F. Zhou [19]:

$$G_{ic} = \frac{\dfrac{2\sigma_f{}^2 r_f \left(\dfrac{1}{\beta} - \dfrac{\beta E_f r_f{}^2}{16 G_f}\right) - 2E_f r_f \Gamma_f}{L_d} + r_f \sigma_f{}^2}{4E_f}$$ (7.2.2)

where the term β is defined as [19]:

$$\beta = \frac{1}{r_f}\sqrt{\frac{2G_m}{E_f \ln \dfrac{R}{r_f}}}$$ (7.2.3)

7.3 Results

Post-test examination of the fragmentation test specimens using optical transmission microscopy was able to discern individual filaments and the point of fracture through the filament. The regions of fiber-resin debonding on either side of each fractured filament were discernable. As shown in Figure 7.3.2, the point of fiber fracture appears as a short black region. Resin debonding is evident as the grey zone on either side of the fracture. For specimens with multiple embedded filaments, fracturing was observed to occur in clusters. All the filaments appeared to experience fracture at approximately the same locations along their length, as shown in Figure 7.3.3. The cause appears to be that initial random fracturing weakens the affected local area, inducing a cascading effect that results in fracturing of the remaining filaments at approximately the same location.
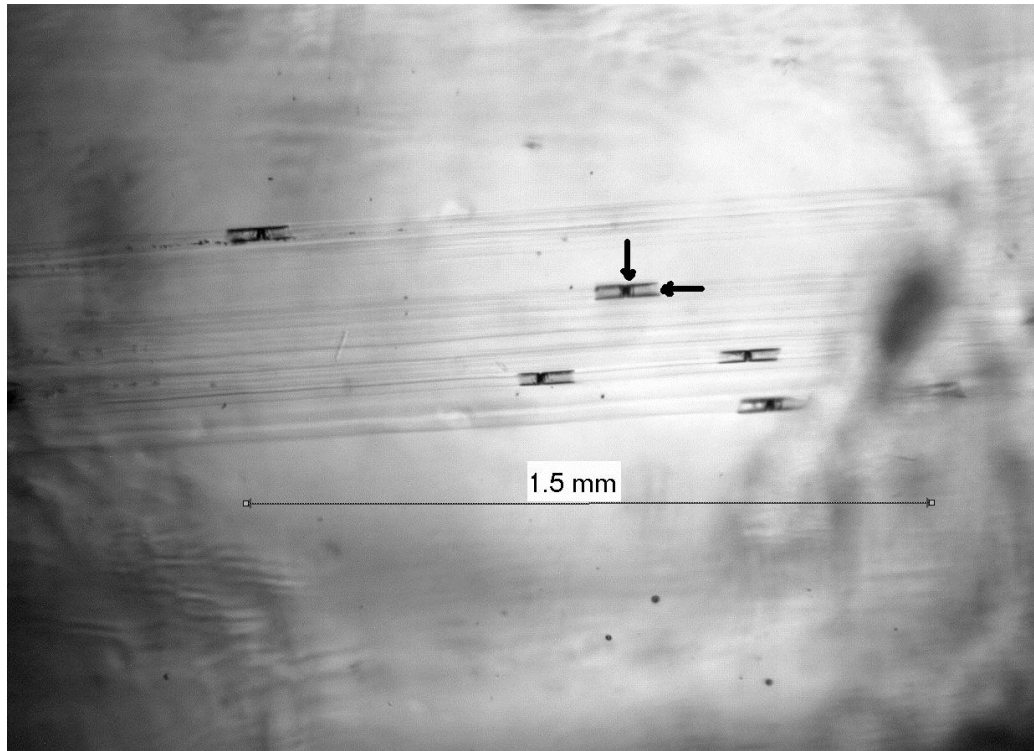
Figure 7.3.2: Fracture point (vertical pointer) and adjacent fiber-resin debond region (horizontal pointer) for individual filaments.
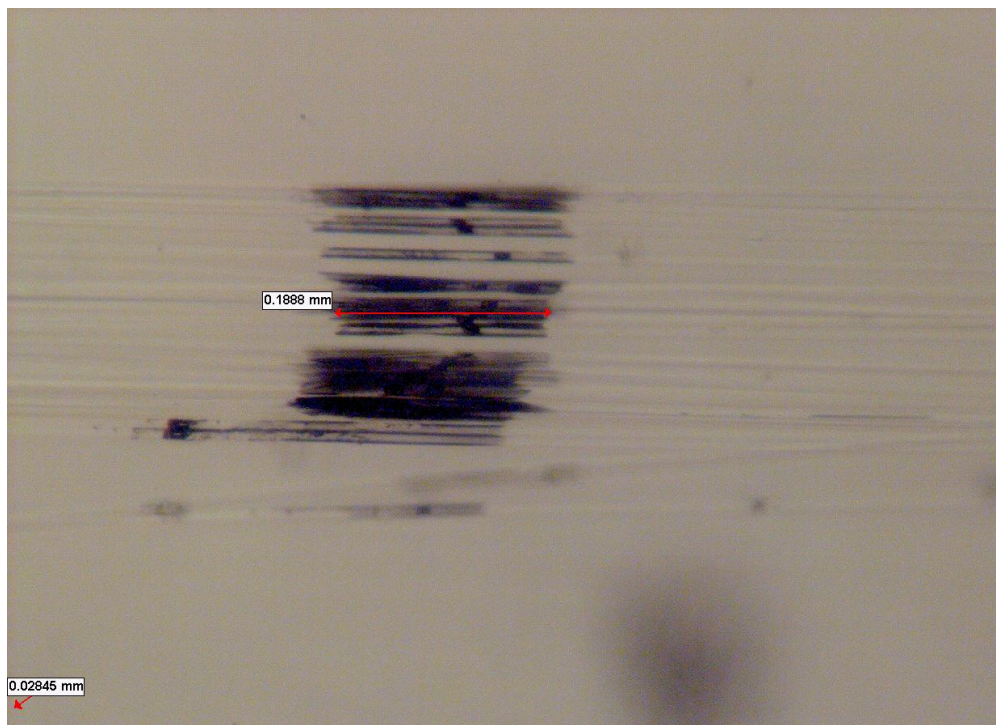
Figure 7.3.3: Typical appearance of fracture zone along a bundle of filaments.

The critical transfer length, L_c, and debond zone length, L_d, were directly measured using a graduated gauge synchronized with the microscope. The values for the critical transfer length vs the number of embedded filaments in a specimen is shown in Figure 7.3.4. A best exponential fit of the relationship between L_c to the number of embedded filaments is provided. The average critical transfer length increases with the number of filaments in the specimen. Debond lengths varied from 0.248 mm to 0.326 mm. The average debond length measured was 0.29 mm with a standard deviation of 0.025 mm.
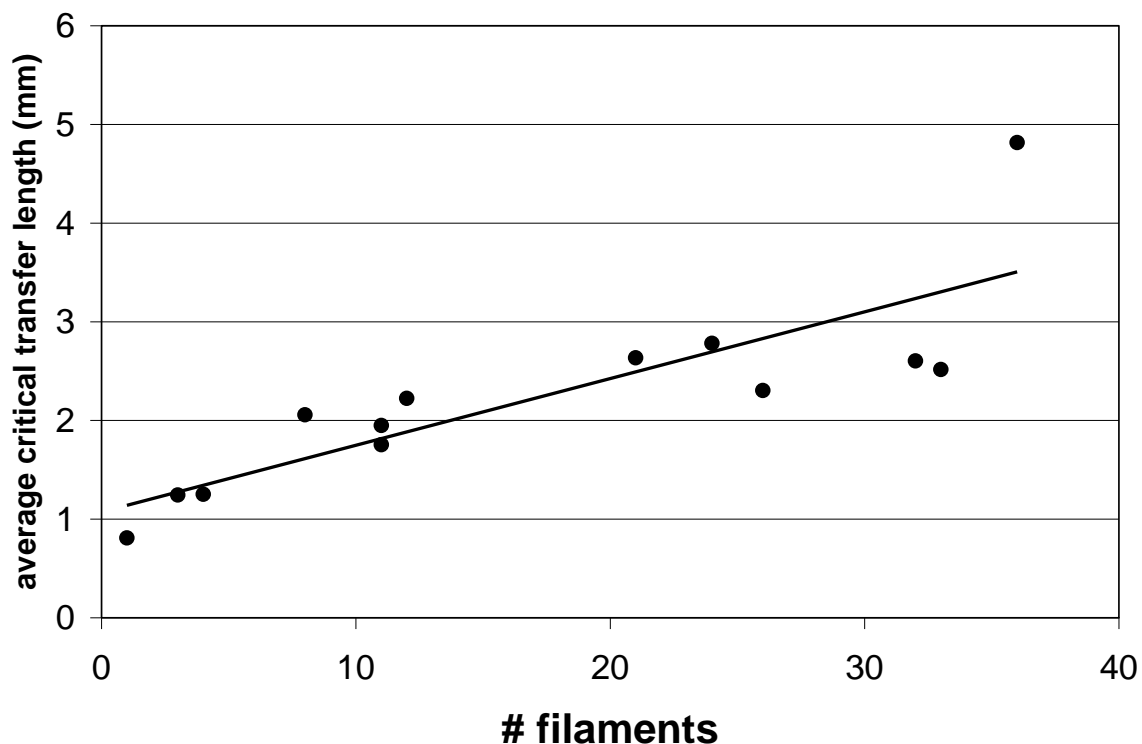
Figure 7.3.4: Average critical transfer length values measured vs the number of filaments in each specimen.

Non-fractured portions of the specimens were cross-sectioned, polished and viewed with both optical microscopy and scanning electron microscopy (SEM) to

determine the number of filaments embedded in each specimen and the average filament diameter. SEM confirmed a relatively tight grouping of embedded filaments. A typical cross-section is shown in Figure 7.3.5. From SEM, the average fiber diameter was determined to be 19 µm.
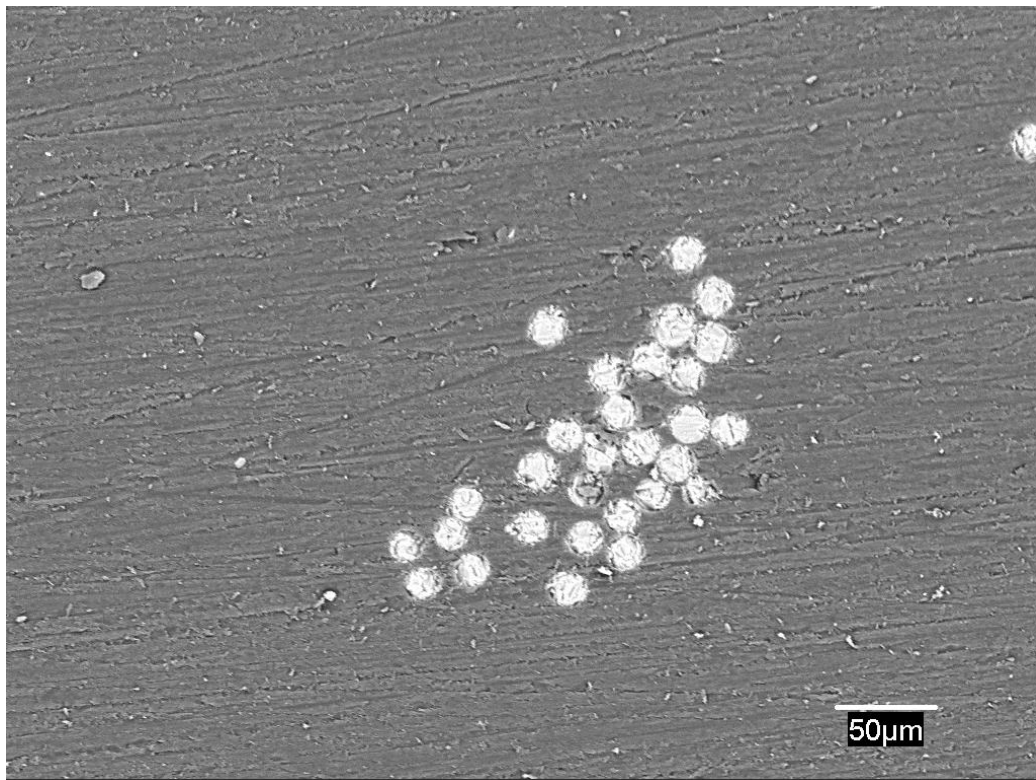
Figure 7.3.5: Cross-section of embedded filament cluster, showing tight grouping and distribution observed by SEM.

7.4 Discussion

7.4.1 Interfacial Debond Strength

The value of L_c was determined to vary with the number of embedded filaments, as shown in Figure 7.3.3. An interfacial bond strength of 22.0 MPa is calculated from single embedded filaments (0.8098 mm). The case of multi-filaments specimens can be evaluated by deriving an expression to describe multi-filament the relationship. Let the effective diameter, d_E, be the diameter of a filament corresponding to the equivalent area of the total filaments in a specimen. Equating the areas, we have:

$$\frac{\pi d^2_E}{4} = n\frac{\pi d^2}{4} \tag{7.4.1}$$

This simplifies to:

$$d_E = d\sqrt{n} \tag{7.4.2}$$

The interfacial bond strength can be calculated as a function of effective diameter by substituting Equation 7.4.2 into Equation 7.1.2:

$$\tau_i = \frac{3\sigma_F d\sqrt{n}}{8L_c} \tag{7.4.3}$$

Re-arranging terms provides an expression for the critical transfer length:

$$L_c = \frac{3\sigma_F d \sqrt{n}}{8\tau_i}$$
(7.4.4)

Letting the fixed term $3\sigma_F d/8\tau_i$ equal a parameter, Σ, this simplifies to:

$$L_c = \Sigma\sqrt{n}$$
(7.4.5)

Introducing Equation 7.4.5 into Equation 7.4.3 provides an expression for the interfacial bond strength that incorporates the relationship between L_c and the number of embedded filaments:

$$\tau_i = \frac{3\sigma_F d}{8\Sigma}$$
(7.4.6)

Applying an exponential fit to values of L_c, where $L_c = An^p$, as a function of the number of embedded filaments as shown in Figure 7.4.1 provides a values for Σ of 0.7978. A fiber-resin interfacial bond strength of 22.3 MPa is obtained by introducing terms into Equation 7.4.6, where the average filament diameter is 19 μ and the fracture strength of the glass filament is 2400 MPa, as provided by the manufacturers material specification data sheet. This value is lower than the

shear strength of the epoxy of 40.3 MPa. Therefore fiber fragmentation is confirmed as expected to occur, rather than resin shearing.

Note that the exponential fit is equal to 0.3827. This would be equal to 0.5 if d_E was equivalent to the effective area of the total filaments in a specimen. The variation is most probably due to the matrix between the filaments being constrained by the stiffer filaments, reducing the shear stress on the "inward-facing" faces of the filaments.
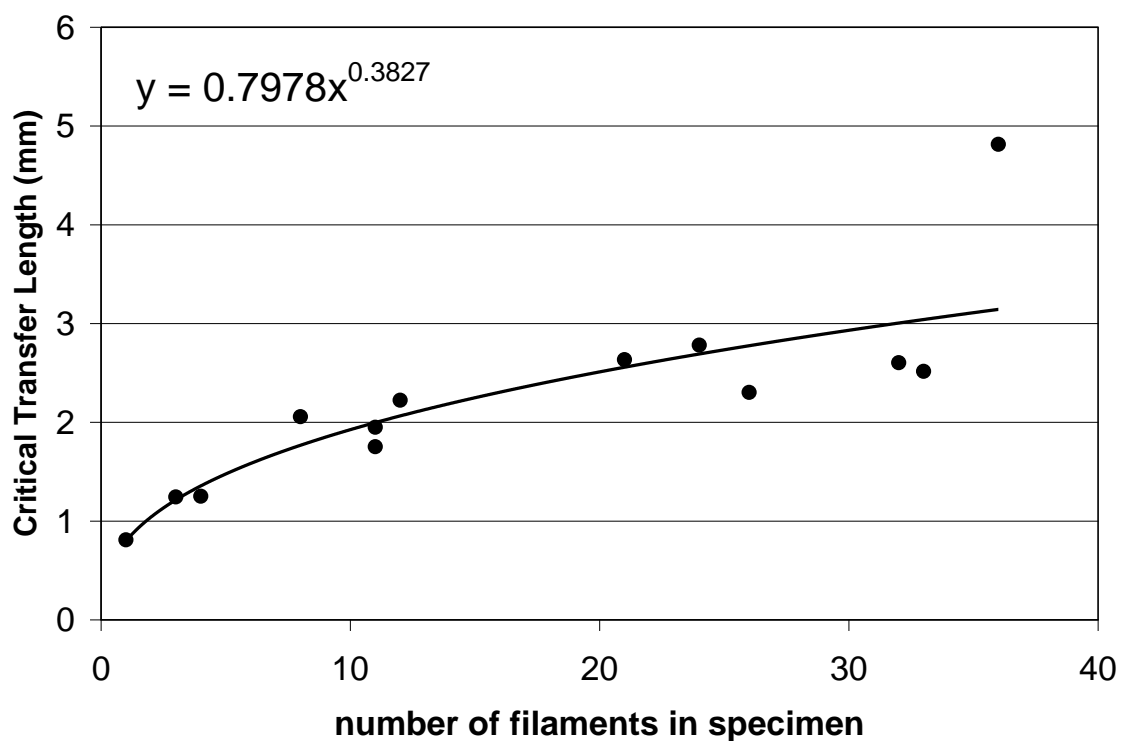
Figure 7.4.1: Plot of the critical transfer lengths measured vs the number of filaments in each sample.

These results suggest equivalence to the single filament testing when variation resulting from the scatter within the actual data is considered.

Based on this analysis for fiber-fragmentation test, the value of the critical transfer length is sensitive to the number of embedded filaments, increasing in length with an increase in the number of embedded filaments. Per Equation 7.1.1, Lc is a function of the diameter of the embedded filament. As demonstrated, increasing the number of embedded filaments is equivalent to increasing the diameter of a single embedded filament, so this relationship is expected. The analysis also shows that the value of the interfacial bond strength is insensitive to the number of embedded filaments. This is significant in that, as mentioned, a large variation in test results has been reported for testing conducted based on the use of single embedded filament.

Consistency in test results can be achieved through the use of multiple embedded filaments. Reliance on testing of individual filaments results in large variations between specimens as a result of the sensitivity of test results to specimen preparation. Embedding multiple filaments requires less handling of the filaments, reducing opportunities for variations to occur. As well, the use of multiple filaments will act to average the preparation variations on the test results. Therefore fewer specimens need to be tested to get statistically meaningful measurements. Additionally, specimen preparation is significantly simplified with multiple embedded filaments by removing the need to isolate and mount individual filaments.

7.4.2 Interfacial Debond Energy

Interfacial debond energy was calculated using Equation 7.2.2. This expression requires introduction of terms obtained from both the experimental data and data available from the literature. The fiber radius, r_f, and the fiber debond zone length, L_d, are directly measured from the fragmentation test. The E-glass filament Young's modulus, E_f, shear modulus, G_f, and fracture strength, σ_f, as well as the matrix shear modulus, G_m, were taken from the manufacturer's material specification data sheet. These values are 70 GPa, 38.4 GPa, 2.6 GPa, and 2.4 GPa, respectively. The matrix radius, R, is the radius of matrix affected by the stress on the filament and estimated as five times the filament radius [19]. The value for the strain to failure of the E-glass fibers was of 4.6% was obtained from the published manufacturer's product properties. The average energy associated with fiber fracture, Γ_f, is approximately 7.5 J/m^2 [75]. Therefore, the average interfacial debond energy for the fiber-resin system studied was determined to be 625 J/m^2 with a standard deviation of 19. In the methodology proposed by Zhou [19] to determine the interfacial debond energy, and as used in this study, frictional effects are not accounted for. In studying E-glass and epoxy systems, Zhou [77] estimated that frictional effects reduce debond energy by an average of 9.4%. Taking this effect into consideration, the average interfacial debond energy is 566 J/m^2. This value is in reasonable agreement with the values determined for similar resin/fiber systems by Zhou [77,79].

7.5 Summary

Values for the interfacial bond strength and debond energy were measured for the fiber-resin system used to fabricate the UD composites evaluated in this study. Measured values of interfacial debond energy are in reasonable agreement with the literature. The interfacial properties were determined using the fiber fragmentation test. The fiber fragmentation test was demonstrated to be insensitive to the number of embedded filaments. Therefore test set-up can be significantly simplified, which will increase consistency of experimental results.

8. MECHANISTIC FAILURE CRITERION

8.1 INTRODUCTION

Existing empirical mixed-mode failure criteria for UD CFP composites involve evaluation of parametric values. These values are deduced by curve fitting of CSERR data over a wide range of mixed-mode loading conditions, obtained by extensive testing of various composite materials. The method is labour intensive, and as well, these criteria have shown poor correlation for UD CFP composites other than those from which the parametric values were derived.

A mechanistic mixed-mode failure criterion for UD CFP composites is presented here that incorporates an understanding of the operative fracture mechanisms involved in material failure, and requires knowledge only of the reinforcement and matrix material properties related to fracture and the associated energy absorption. The advantage of a mechanistic failure criterion compared with empirical criteria is two fold. Firstly, as it incorporates an understanding of the material mechanics, it will be more generally applicable over a wider range of composite materials. Secondly, it can be used as a design tool to optimize energy absorption of the CFP composite by customizing selection of the constituent fiber and matrix materials.

As discussed in Chapter 2, delamination of CFP composites was observed to occur by either interyarn or interply failure. For both cases, there are only two

dominant energy absorbing mechanisms. These are fiber-resin interfacial debonding and resin fracture. The energy absorption associated with interfacial debonding is characterized by the interfacial debond energy. While that associated with resin fracture is characterized by the neat resin mode I CSERR. The proposed criterion involves integrating these energy absorption terms with respect to the relative ratio of their occurrence over the fracture surface. Therefore, the testing requirements for the criterion are limited to the evaluation of these properties for the resin-fiber systems of interest. From this limited data, the CSERR as a function of mixed-mode loading can be predicted for any UD CFP composite produced using these constituents as the reinforcement and matrix materials.

For the analysis on which the proposed criterion is based, the fiber-resin debond energy is assumed to be constant as a function of mixed-mode loading. It is additionally assumed that the fiber modulus is significantly greater than the resin modulus, Linear Elastic Fracture Mechanics (LEFM) applies to the fracture process, quasi-static loading and plane strain conditions exist, and no crack branching, crack migration or fiber bridging occurs. Hackle formation is assumed to occur between mode I and mode II along the resin fracture surface by the relationship derived in Chapter 6 and expressed in Equation 6.4.42. These assumptions will apply for CFP composites fabricated with reinforcement materials and thermosetting polymers typically used in industry. Thermosetting polymers are the only class of matrix material currently considered for the fabrication of blast mitigating CFP composite structures.

8.2 Constrained Resin

An effective resin mode I CSERR is used in the criterion to account for the constraints imposed on the resin by the surrounding reinforcing filaments in a CFP composite. As discussed in section 6.4.1, the plastic zone radius at the crack tip is proportional to the fracture toughness of a linear-elastic material [6]. Evaluation of the resin mode I CSERR involves the use of neat resin, in which plastic deformation of the crack tip is unconstrained. In a CFP composite, the high modulus of the reinforcing filaments induce constraints on the thin resin regions between the filaments. Deformation of the resin is restricted by the filaments, reducing the strain at which the yield strength of the resin is exceeded. This effectively restricts the size of the associated plastic zone radius and reduces the corresponding energy consumed by crack growth.

Both interply and interyarn failures impose different constraints on the resin adjacent to the reinforcing fibers. For interply failure, the plastic zone of the resin ahead of the crack tip is unconstrained on the resin rich side of the crack and constrained on the reinforcement side. While for interyarn failure, the resin is constrained on both sides of the crack. Figure 8.1.1 demonstrates the concept of an unconstrained plastic zone on the resin rich side of a propagating crack and of a constrained plastic zone on the fiber rich side (not drawn to scale).

Therefore a unique effective resin mode I CSERR will exist for both interply and interyarn failure. For interply failure, this value will be proportional to the combined size of the constrained and unconstrained plastic zones to the plastic zone size of neat resin. For interyarn failure, the value will be proportional to the

combined size of the unconstrained plastic zones of either side of the crack to the plastic zone size of neat resin.
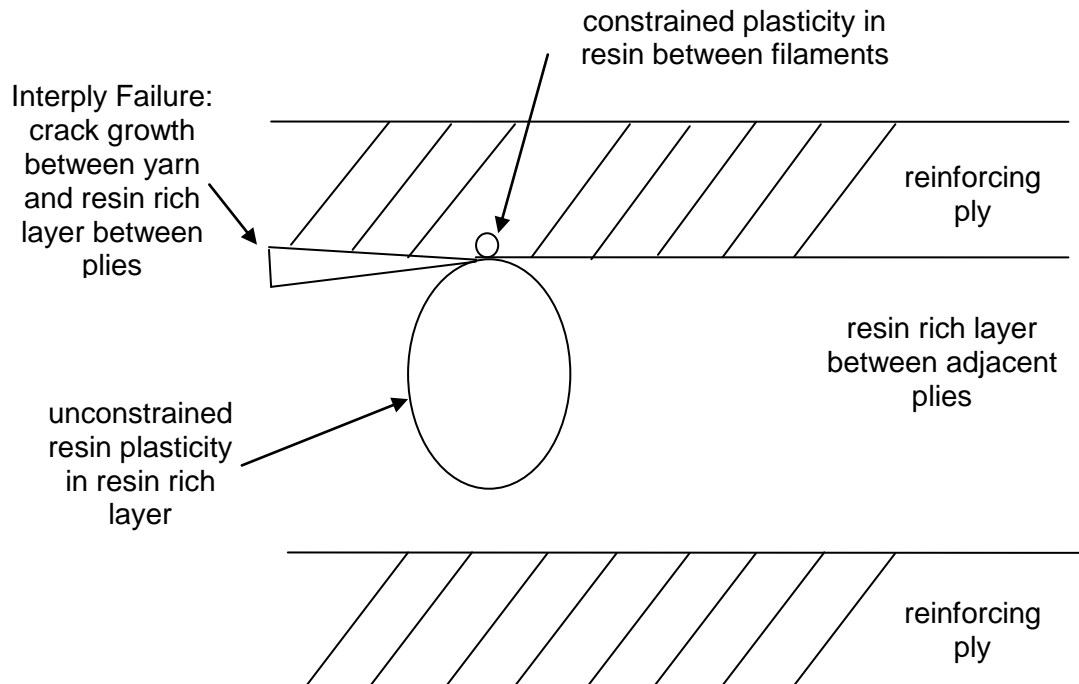
Figure 8.1.1: Illustration of interply crack growth in a UD CFP composite and constraint on the plastic zone development of the resin between yarn filaments.

Strain in the resin is constrained by the reinforcement in proportion to the ratio of the stiffness of each material. For the case of tensile loading in the direction of the filaments, the strain in the resin will be limited to that of the filaments. However, due to the very high modulus and proportions of the filaments compared to that of the resin, the stress experienced by the resin will be approximately the same as that in the filaments. Therefore the failure strength of the resin will be exceeded with the occurrence of relatively little plastic straining

within the resin. Similarly, due to the very thin resin region, the case will be similar for transverse and shear loading.

For the materials considered in this study, the resin and fiber Young's Modulus are 2.6 GPa and 70 GPa respectively. As the resin modulus is only 3.7% that of the fibers, the constrained resin plastic zone is only 3.7% of that associated with neat resin. The mode I CSERR of the neat epoxy was determined to be 3588 J/m^2. For the neat resin, half of the plastic zone is associated with either side of the crack. Therefore, half of the CSERR value is associated with the plastic zone on the one side of the crack tip, while the other half is associated with the plastic zone on the other side.

For interply failure, the resin on the resin rich side of the crack is unconstrained, and therefore contributes an effective CSERR of 3588 J/m^2 /2, or 1794 J/m^2. The constrained plastic zone on the fiber rich side of the crack however only contributes 3.7% of 1794 J/m^2, or 66 J/m^2. Therefore the total effective mode I CSERR for interply failure is equal to 1860 J/m^2. For the case of interyarn failure, for which the plastic zone is constrained on both sides of the crack face, the plastic zone development is very limited. The effective mode I CSERR for interyarn failure is equal to 3.7% of half the neat resin CSERR on either side of the crack tip, or 133 J/m^2.

The plastic zone at the crack tip can be demonstrated to be unconstrained on the resin rich side of the crack for interply failure by calculating the size of the plastic zone, and ensuring that it is less than the thickness of the resin rich layer. The

simplified relationship between the plastic zone radius, r_p, resin yield strength, σ_{ys}, and resin mode I CSIF, K_{IC}, under plane strain conditions is [6]:

$$r_p = \frac{K_{Ic}^2}{6\pi\sigma_{ys}^2}$$

(8.2.1)

Where the relationship between CSIF and CSERR is [6]:

$$K_c = \sqrt{\frac{EG_c}{1-\upsilon^2}}$$

(8.2.2)

The resin yield strength, mode I CSERR, and Young's Modulus for the resin used to fabricate the UD CFP composite materials in this study were experimentally determined to be 51.8 MPa, 3588 J/m^2 and 2.6 GPa respectively. For a Poisson's ratio of a typical epoxy of 0.3, K_{IC} has a value of 3.20 MPa (m)$^{1/2}$. Therefore the plastic radius of unconstrained resin is 202 μm. As this is less than the thickness of the resin rich layer of 300-340 μm, the crack tip plastic zone is verified as unconstrained along the resin rich side of the crack.

8.3 Calculating Ratio's of Fracture

The effective mode I CSERR of the resin for interply and interyarn failure have been determined. The interfacial debond energy is known. Prediction of the CSERR for a UD CFP composite requires summation of these energies over the relative ratio of their occurrence over the fracture surface. The ratio can be defined by considering the case of a simplified cross section of a delaminated UD CFP composite, as illustrated in Figure 4.4.2. Fiber debonding occurs along the

pockets from which filaments are extracted, while resin fracture occurs along the material between filaments.

With reference of Figure 4.4.2, the expression for calculating the predicted value of CSERR through summation of the energy terms over their respective ratio's of fracture surface area is:

$$(G_{IC})_{CO} = \frac{L_S (G_{IC})_R + 0.5\pi D_f G_{iC}}{L_S + D_f}$$

(8.3.1)

Where the term CO denotes composite, and R denotes resin.

The average spacing between filaments for interyarn and interply failure was determined by SEM, as reviewed in section 4.3.2. The filament spacing was determined to have an average value of 7 μm for interyarn failure, and an average value of 25 μm for interply failure. As the predicted value of CSERR is sensitive to these values, they need to be determined reasonably accurately. This can be achieved either experimentally or through calculation. Experimental values are given above for the CFP composite studied. These values may be consistent for other CFP composites, or vary with material properties. Further study would be required to determine this relationship.

An average spacing can be calculated based on geometry. Assuming an even distribution of filaments within the reinforced polymer (not completely accurate for a laminated structure for which a resin rich layer exists between plies), from

simple geometry the average spacing between filaments can be derived as a function of fiber volume fraction, V_f, and is given as:

$$L_s = \frac{D_f\left(5\sqrt{\pi} - \sqrt{V_f}\right)}{\sqrt{V_f}} \qquad (8.3.2)$$

For the CFP composite UD-L fabricated in this study, the fiber volume fraction was determined to be 48.4% by the commonly employed Water Displacement method. Applying Equation 8.3.2 for 19 µm filaments provides an average value for spacing between filaments of 5.18 µm. This compares favourably with the measured values for interyarn failure of 7 µm. As mentioned, the higher value of filament spacing for interply failure appears to be the consequence of filament spreading at the unconstrained ply edge. Therefore this value is difficult to predict by calculation.

8.4 Proposed Mechanistic Failure Criterion

Based on the above work a mechanistic failure criterion to predict CSERR as a function of mixed-mode loading for thermosetting UD CFP composites can be formulated. This criterion is a function of the fracture properties of the constituent components of the composite only, and applies to any configuration of composite constructed from constituents for which the properties are known. The properties which will require experimental determination are the resin mode I CSERR, G_{IC}, and the fiber-resin interfacial bond strength, τ_i, and interfacial debond energy, G_{ic}. Reasonable values for the resin yield strength, σ_y, Young's Modulus of the resin,

E_R, and Young's Modulus of the fiber, E_F, can typically be acquired through manufacturer material specification data sheets.

The method proposed to predict CSERR for a UD CFP composite involves integrating the energy terms for interfacial debond energy and resin fracture energy as a function of their respective surface areas, and incorporating terms to include effects from hackle formation and the degree of resin constraint. This approach provides a set of expressions describing the predicted CSERR values as a function of failure mechanism and mode mixture. One equation is produced for interyarn failure and is to be employed over the mixed-mode range predicted to experience interyarn failure. A second equation is produced for interply failure which applies over the remaining mixed-mode range.

Variables that are determined in previous sections are the hackle formation angle as a function of mixed-mode loading, H_f, and the ratios of fiber and resin dedond lengths, F_f and F_r, respectively. The ratio of fiber debond to resin fracture length is unique for interyarn and interply failure. Therefore they will be differentiated by adding the notation IY for interyarn and IP for interply, yielding F_{f-IY} and F_{r-IY}, and F_{f-IP} and F_{r-IP}. For a filament diameter of 19 µm, and for an average filament spacing of 7 µm for interyarn failure, and 25 µm for interply failure, the values of F_{f-IY}, F_{f-IP}, F_{r-IY} and F_{r-IP} are 1.456, 0.746, 0.073, 0.525, respectively.

For interyarn failure, the CSERR is predicted to be the accumulated values of the interfacial debond energy, G_{ic}, and the effective resin CSERR, multiplied by their respective areas. The effective resin CSERR is the resin mode I CSERR, G_{IC}, multiplied by the hackle factor and the resin constraint factor for interyarn failure. As reviewed in section 8.2, the resin constraint factor for interyarn failure is the ratio of the resin to the fiber Young's modulus, $E_R/E_{F.}$. Accumulating terms provides:

$$G_c = F_{f-IY}G_{ic} + F_{r-IY}G_{Ic}H_f\left(\frac{E_R}{E_F}\right)$$ (8.4.1)

Interply failure is calculated similarly, where the applicable terms for relative fracture surface area, F_{f-IP} and F_{r-IP}, are substituted for F_{f-IY} and F_{r-IY}, respectively, and where the constrained resin factor is modified to account for resin on only one side of the crack being constrained. Accumulating terms provides:

$$G_c = F_{f-IP}G_{ic} + F_{r-IP}G_{Ic}H_f\left(\frac{E_R + E_F}{2E_F}\right)$$ (8.4.2)

As discussed in section 4.3.1, the transition from interyarn to interply failure occurs by the interyarn crack progressing toward the yarn-resin interface with increasing mode II loading. Therefore, as the loading mode increases between pure mode I and the ratio at which interply failure occurs, the plastic zone at the crack tip will begin to extend into the resin rich layer. The result is a gradual decrease in the constraint imposed on the plastic zone, and correspondingly an

increase in the associated CSERR. This explains why an abrupt change in the CSERR at the mode mixture at which interyarn failure transitions to interply is not observed. This effect can be accounted for in Equation 8.4.1 by including another term.

A linear transition is assumed in the progress of the interyarn fracture toward the yarn surface with increasing mode mixture, and the ratio of fiber debond to resin fracture length is assumed to transition linearly between the interyarn and interply values. Letting any two terms be X and Y, therefore a linear transition from X to Y in terms of mode mixture, M, between pure mode I loading (M=0) and the mode mixture at which the transition from interyarn to interply occurs, M_t, can be expressed as:

$$X + (Y - X)\left(1 - \frac{M_t - M}{M_t}\right) \tag{8.4.3}$$

For the case in which these assumptions apply, and where the plastic radius is assumed to be equal to the starting depth of the crack in the yarn, substitution of Equation 8.4.3 into Equation 8.4.1 yields:

$$
\begin{aligned}
G_c = G_{ic}&\left(F_{f-IY} + \left(1 - \frac{M_t - M}{M_t}\right)\left(F_{f-IP} - F_{f-IY}\right)\right) + \\
F_{r-IY}G_{Ic}H_f&\left(\frac{E_R}{2E_F}\right) + G_{Ic}H_f\left(F_{r-IY} + \left(1 - \frac{M_t - M}{M_t}\right)\left(F_{r-IP} - F_{r-IY}\right)\right) \\
&\left(\frac{E_R}{2E_F} + \left(1 - \frac{M_t - M}{M_t}\right)\left(\frac{E_F - E_R}{2E_F}\right)\right)
\end{aligned} \tag{8.4.4}
$$

8.5 Predicting Transition of Fracture Mechanisms

A mechanistic based failure criterion needs to predict the transition between interyarn and interply failure as a function of the mode mixture, M_t. The transition will happen when crack deflection along the reinforcing yarn occurs. Crack deflection occurs at the mixed-mode loading percentage at which the shear stress at the crack tip exceeds the fiber-resin interfacial bond strength. For the tested material, the interfacial bond strength was measured to be 22.3 MPa. The shear stress at the crack tip as a function of mixed-mode loading can be derived from the Westergaard's expressions. The summation of the mode I and mode II Westergaard stress functions for shear stress is given as:

$$\tau_{xy} = \frac{K_I}{\sqrt{2\pi r}} \sin\left(\frac{\theta}{2}\right) \cos\left(\frac{\theta}{2}\right) \cos\left(\frac{3\theta}{2}\right) + \frac{K_{II}}{\sqrt{2\pi r}} \cos\left(\frac{\theta}{2}\right) \left[1 - \sin\left(\frac{\theta}{2}\right) \sin\left(\frac{3\theta}{2}\right)\right] \qquad (8.5.1)$$

For delamination, in which crack growth occurs longitudinally with the reinforcement direction, the value of θ is 0°. Therefore the first term in Equation 8.5.1 becomes zero. Re-arranging terms provides an expression for the mode II component of the stress intensity factor in terms of the applied shear stress and the plastic radius:

$$K_{II} = \tau_{xy} \sqrt{2\pi r} \qquad (8.5.2)$$

Setting the value of the distance from the crack tip, r, equal to plastic radius of 202 μ at which the stress state is the maximum (as determined in section 8.2), failure is predicted to occur when the mode II stress intensity factor is 0.794

$MPa(m)^{\frac{1}{2}}$. For the neat resin, the mode I CSIF were determined to be 3.20 $MPa(m)^{\frac{1}{2}}$. Applying the hackle factor, the mode II CSIF would be 4.97 $MPa(m)^{\frac{1}{2}}$. The CSIF will transition between these values for the composite in accordance with the relationship given in Equation 8.4.2, converting from CSIF and CSERR using Equation 8.2.2. The mode II component of the CSIF then is determined by multiplying these values by the mode mixture. Therefore the mode mixture at which the value of K_{II} is equal to 0.794 $MPa(m)^{\frac{1}{2}}$ can be determined. The mode mixture at which the stress at the crack tip is predicted to exceed the interfacial bond strength shear is at approximately 27% mode II loading. This compares well with the experimentally observed transition from interyarn to interply failure just following 25% mode II mode mixture.

The criterion is utilized by applying Equation 8.4.2 for mode mixtures greater than M_t , and by applying Equation 8.4.4 for mode mixtures less than M_t. The prediction of the transition between interyarn and interply failure at a specific mode mixture, M_t, suggests that a rapid change in CSERR would occur at the transition point. This however is not experimentally observed. As was noted earlier, as the mode II loading ratio is increased, the interyarn crack growth is observed to progress from deep into a yarn toward the surface. A smooth transition in the CSERR therefore occurs as the plastic zone gradually transitions from a constrained to an unconstrained condition. This is accounted for in equation 8.4.4.

8.6 Validating the Mechanistic Failure Criterion

To validate the accuracy of the criterion, the CSERR as a function of mixed-mode loading was predicted for UD-H and UD-L and compared to the experimental values obtained for these materials.   For UD-H, interply delamination does not occur as there is not resin-rich layer between the plies, and therefore only Equation 8.4.1 is applied. For UD-L, Equation 8.4.4 is applied for the mixed-mode region over which interyarn delamination was predicted to occur in section 8.5 (between 0% and 33% mode II loading), and Equation 8.4.2 is applied for the remaining mode mixtures. Predicted values are compared to the experimental data for UD-H and UD-L in Figures 8.5.1 and 8.5.2, respectively.   The experimental data is indicated with filled black circles.   A smoothed line plot is shown of the predicted values.
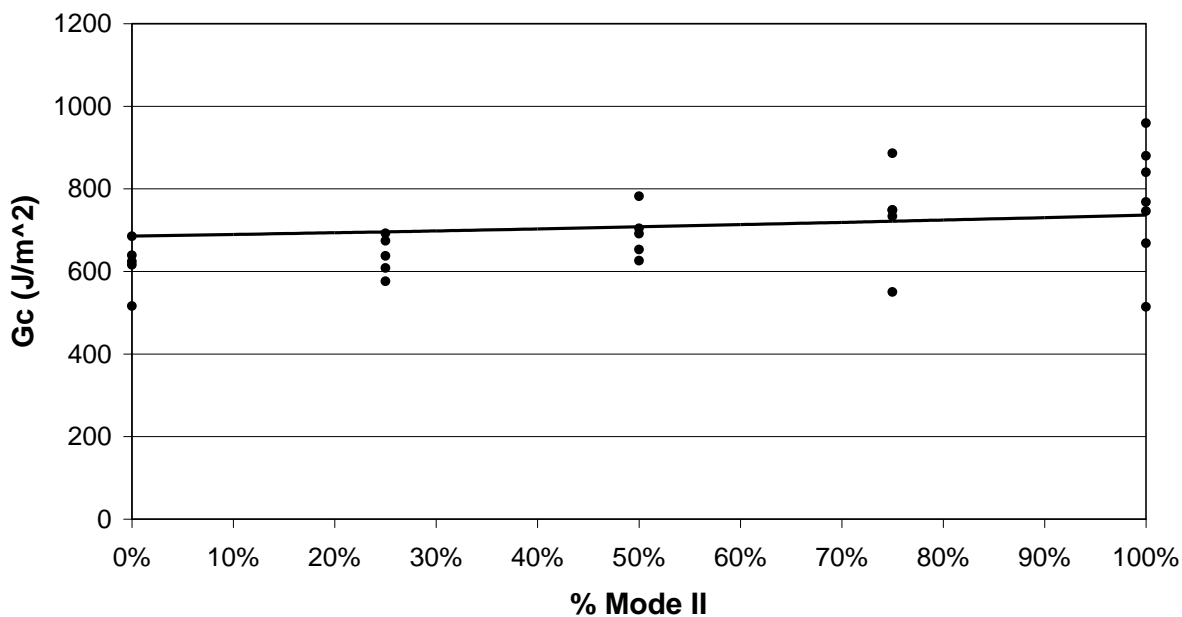
Figure 8.5.1: Measured CSERR (dots) vs predicted (line) for UD-H.
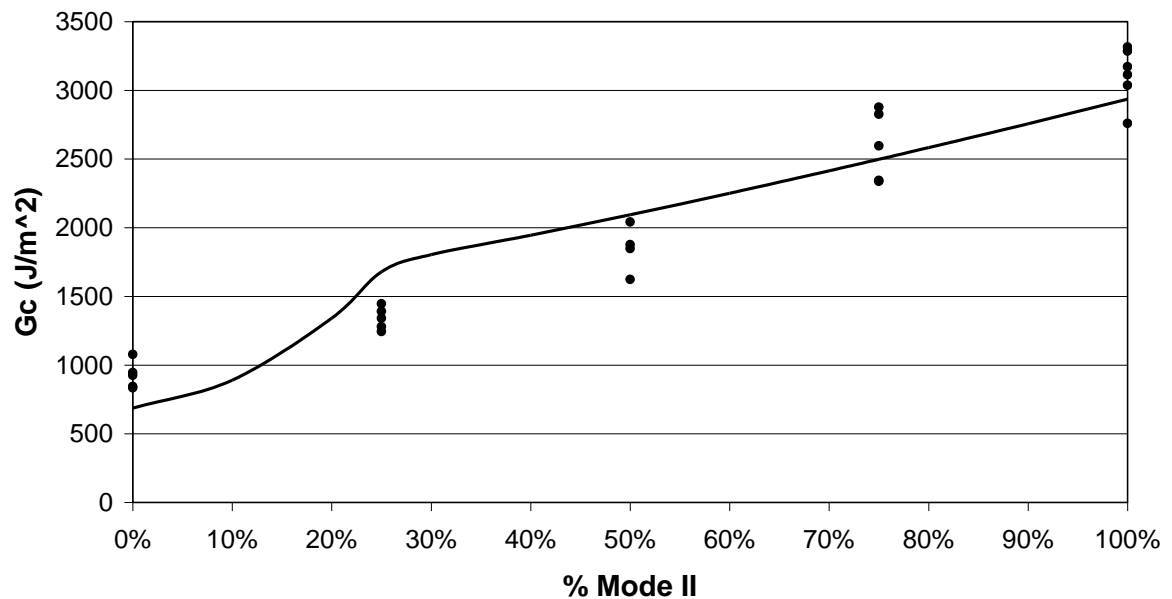
Figure 8.5.2: Measured CSERR (dots) vs predicted (line) for UD-L.

As indicated in Figure 8.5.1, the mechanistic failure criterion accurately predicts the CSERR for UD-H. The predicted values are in close agreement with the average experimental values. However, the scatter in the data is large and allows for a range in interpretation of the trend other than the average. As indicated in Figure 8.5.2, the mechanistic failure criterion accurately predicts the CSERR for UD-L. The kink in the predicted CSERR curve at 30% mode II loading reflects the simplified assumptions made in modelling the transition from interyarn to interply failure. A more detailed study is required to more accurately capture the behaviour of the material during the transition. In general, the predicted values accurately reflect the average measured values for both UD-H

and UD-L, indicating that the failure criterion successfully predicts CSERR as a function of mixed-mode loading for thermosetting UD CFP composite materials.

It is important to note that all proposed empirical criteria make no attempt to predict the CSERR of a CFP composite. Rather, they endeavour to predict the behaviour of the change in CSERR between pure mode I and pure mode II loading, requiring the measured value of G_{IC}, and frequently G_{IIC}, for a given CFP composite system. Therefore, not only have the empirical criteria been shown to not be accurate over a range of CFP materials. Therefore they are also not truly predictive. The requirement to fabricate the CFP material to be evaluated necessitates a test intensive and reiterative approach to design. This approach consists of selecting an assumed best performance material based on experience, fabricating and testing the material, interpreting the results using an inaccurate empirical criterion, using experience to select which material characteristic to change to improve the performance, and repeating the process until an acceptable material is derived at. This approach is expensive, time consuming, and does not produce an optimized material, but only an acceptable material.

The criterion proposed here is unique in that precise values of the CSERR as a function of mode mixture are predicted based only on the constituent material properties. Therefore the criterion provides a highly effective design tool. The mechanistic failure criterion can directly be employed to tailor selection of the most suitable fiber-resin combinations and their arrangement to best meet a

given design requirement. Not only is this process less expensive and time consuming that the traditionally employed reiterative testing method described above, but an optimized material design is achieved.

8.7 Summary

A mechanistic mixed-mode failure criterion for thermosetting UD CFP composites is proposed. The criterion is founded on an understanding of the operative fracture mechanisms involved in material failure. Prediction of CSERR as a function of mixed-mode loading requires knowledge only of the reinforcement and matrix fracture properties. The criterion includes consideration of resin fracture toughness, hackle formation, interfacial debonding, resin constraint, and the transition from interyarn to interply delamination. The criterion is demonstrated to accurately predicted CSERR by comparison with experimental data, supporting the validity of the criterion.

9. CONCLUSIONS

9.1 Conclusions

The proposed mechanistic failure criterion demonstrably predicts the CSERR as a function of mode mixture accurately for a thermosetting UD CFP composite. The criterion is concisely expressed as a number of mathematical equations. The CSERR values predicted by these expressions for the two UD CFP composite materials tested as part of this study show a high degree of correlation with the experimentally measured values. The level of agreement of the experimental and predicted results substantiate the validity, effectiveness, and accuracy of the model.

The proposed criterion provides a significant contribution to science in that criterion is founded on an understanding of the operative fracture mechanisms involved in material failure. This study provides significant insight into the behaviour of composite failure in regards to resin fracture toughness, hackle formation, interfacial debonding, resin constraint, and the transition from interyarn to interply delamination. These terms are incorporated into a non-empirical criterion that successfully predicts composite material failure. The criterion proposed also provides a useful design tool to the engineering community for the design of composite materials with optimized energy absorbing properties.

As a design tool, the criterion would be used in conjunction with finite element analysis modelling. The resin and filaments used in the composite, and the relative arrangement of these within the composite, could be tailor selected to optimize energy absorption of the composite. Resin-fiber combinations would be selected so that the interfacial shear strength were maximized, while optimizing the occurrence on interply failure in preference to interyarn failure. For components with a pre-determined fiber volume fraction, resins would be selected that possessed a high fracture toughness to plastic radius size ratio. While for designs in which the resin was pre-selected, a volume fraction which resulted in a resin rich layer thickness sufficient to permit full expression of the resin plastic zone would be determined.

9.2 Future Work

Further studies with additional thermoset resin/fiber composite systems are required to further substantiate the proposed criterion's applicability over a wider range of CFP composite materials. Further studies are also required to evaluate the consistency of the resin spacing between filaments for interply and interyarn failure for CFP composites and to more accurately model the transition between interyarn and interply failure.

Extending the criterion to be more generally applicable over a broader range of materials and conditions would require further studies of the additional failure mechanisms that occur in some CFP composites, of the behavior of

thermoplastic resins, of the failure mechanisms associated with fabric composites described in Chapter 5, and of the high strain rate sensitivity of composite delamination over a range of CFP composite materials.

BIBLIOGRAPHY

[1]   Hull D, Clyne TW, "An Introduction to Composite Materials", Cambridge University Press, 1996

[2]   ASM Handbook, Volume 21, Composites

[3]   Fink BK, Damage Tolerance of Thick-Section Composites Subjected to Ballistic Impact, Army Research Laboratory, Weapons and Materials Research Directorate, ARL-TR-2477, May 2001

[4]   Feresenbet E, Raghavan D, Holmes GA, The Influence of Silane Coupling Agent Composition on the Surface Characterization of Fiber and on Fiber-Matrix Interfacial Shear Strength, The Journal of Adhesion, 2003;79:7:643-665

[5]   MIL Handbook 17, Volume 2, Polymer Matrix Composites Materials Properties

[6]   Broek D, Elementary Engineering Fracture Mechanics; Springer, 2nd edition, 1982; ISBN-10: 9024726565, ISBN-13: 978-9024726561

[7]   Irwin GR, Fracture, Handbuch der Physik VI, 1958;551-590

[8]   Griffith AA, The Phenomena of Ruture and Flow in Solids, Philisophical Transactions of the Royal Society of London, 1921; A221:163-197

[9]   Crews JH, Reeder JR, A Mixed-mode Bending Apparatus for Delamination Testing, NASA Technical Memorandum 100662, 1988

[10] Kwon HJ, Jar P-YB, Fracture Toughness of Polymers in Shear Mode, Polymers, 2005;46:12480-12492

[11] Westergaard HM, Bearing Pressures and Cracks, Journal of Applied Mechanics, 1939;61:49-53

[12] Irwin GR, Plastic Zone Near a Crack and Fracture Toughness, Proceedings from the 7th Sgamore Conference, 1960;4-63

[13] MIL Handbook 17, Volume 1, Polymer Matrix Composites Guidelines for Characterization of Structural Materials

[14] Robinson P, Song DQ, The Development of an Improved mode III Delamination Test for Composites, Composites Science and Technology, 1994;52:2: 217-33

[15] Benzeggagh ML, Kenane M, Measurement of Mixed-Mode Delamination Fracture Toughness of Unidirectional Glass/Epoxy Composites with Mixed-Mode Bending Appartus, Composites Science and Technology, 1995;56: 439-449

[16] Araki W, et al, Fracture Toughness for Mixed-mode I/II of Epoxy Resin, Acta Meterialia, 53, 2005, pp. 869-875

[17] Nwosu SN, Hui D, Dutta P, Dynamic Mode I Delamination Fracture of Unidirectional Graphite/Epoxy Composites, Composties: Part B,2003;34: 303-316

[18] Agarwal BD, Broutman LJ, Analysis and Performance of Fiber Composites, Wiley-Interscience Publications, 1980

[19] Detassis M, Frydman E, Vrieling D, Zhou X-F, Wagner HD, Nairn JA, Interface Toughness in Fiber Composites by the Fragmentation Test, Composites Part A: Applied Science and Manufacturing,1996;27A: 769-773

[20] Kim J-K, Sham M-L, Impact and Delamination Failure of Woven-Fabric Composites, Composites Science and Technology, 2000;60: 745-761

[21] Singh S, Greenhalgh ES, Micromechanisms of Interlaminar Fracture in Carbon-Epoxy Composites at Multidirectional Ply Interfaces, 4th International Conference on Deformation and Fracture of Composites, 1998

[22] Sjogren A, Asp L, Greenhalgh ES, Hiley MJ, Interlaminar Crack Propagation in CFRP: Effects of Temperature and Loading Conditions on Fracture Morphology and Toughness, Composite Materials: Testing, Design, and Acceptance Criteria, ASTM STP 1416, 2002

[23] Reeder JR, An Evaluation of Mixed-Mode Delamination Failure Criteria, NASA Technical Memorandum 104210, 1992

[24] Ducept F, Davies P, Gamby D, Mixed-mode Failure Criteria for a Glass/Epoxy Composite and an Adhesively Bonded Composite/Composite Joint, International Journal of Adhension and Adhesives,2000;20: 233-244

[25] Villaverde, NB, Variable Mixed-Mode Delamination in Composite Laminate under Fatigue Conditions: Testing and Analysis, PhD Thesis, Universitat de Girona, October 2004

[26] Zhao S, Mixed-Mode Delamination Behaviour of Carbon/Epoxy Composites, Journal of Reinforced Plastics and Composites,1995;14: 804-826

[27] Hochard C, Aubourg P-A, Charles J-P, Modelling of the Mechanical Behaviour of Woven-Fabric CFRP Laminates up to Failure, Composites Science and Technology, 2001;61:221-230

[28] England AH, Crack Between Dissimilar Media, American Society of Mechanical Engineers – Transactions – Journal of Applied Mechanics,1965;32:2::400-402

[29] Barenblatti GI, Cherepanov GP, Brittle Cracks Under Longitudinal Shear, Journal of Applied Mathematics and Mechanics, 1961;25:6:1654-1666

[30] Erdogan F, Stress distribution in bonded dissimilar materials with cracks, American Society of Mechanical Engineers – Transactions – Journal of Applied Mechanics, 1965;32:2:403-410

[31] Wang SS, Wang HT, Interlaminar Crack Growth in Fiber Reinforced Composites During Fatigue, Journal of Engineering Materials and Technology, Transactions of the ASME,1979;101:1: 34-41

[32] O'Brien, T.K., et al, A Simple Test for the Interlaminar Fracture Toughness of a Composite, SAMPE journal, 18, July-August 1982

[33] O'Brien TK, Murri GB, Salpekar SA, Interlaminar Shear Fracture Toughness and Fatigue Thresholds for Composite Materials, NASA TM-89157, USAAVSCCOM TM 87-B-7, August 1987

[34] Caslini M, Zanotti C, O'Brien TK, Fracture Mechanics of Matrix Cracking and Delamination in Glass/Epoxy Laminates, NASA Technical Memorandum 89007, AVSCOM Technical Report 86-B-3, September 1986

[35] Crews JH, Shivakumar KN, Raju IS, Factors Influencing Elastic Stresses in Double Cantilever Beam Specimens, NASA TM-89033, 1986

[36] Martin RH, Delamination Failure in a Unidirectional Curved Composite Laminate, NASA Contractor Report 182018, April 1990

[37] Williams JG, Fracture Mechanics of Composite Failure, Proceedings from the Institution of Mechanical Engineers,1990;209-218

[38] Reeder JR, Crews JH, Nonlinear Analysis and Redesign of the Mixed-Mode Bending Delamination Test, NASA Technical Memorandum 102777, 1991

[39] Ducept F, Davies P, Gamby D, An Experimental Study to Validate Tests Used to Determine Mixed-mode Failure Criteria of Glass/Epoxy Compsites, Composites Part A,1997;28A:719-729

[40] Greenhalgh ES, Asp L, Singh S, Delamination Resistance, Failure Criteria and Fracture Morphology of 0/0, 0/5 and 0/90 Ply Interfaces in CFRP, 5th International Conference on Deformation and Fracture of Composites, 1999

[41]   Greenhalgh ES, Singh S, The Effect of Moisture, Matrix and Ply Orientation on Delamination Resistance, Failure Criteria and Fracture Morphology in CFRP, Composite Materials; Testing Design and Acceptance Criteria, ASTM STP1416, 2002

[42] Ebeling T, Hiltner A, Baer E, Delamination Failure of a Woven Glass Fiber Composites, Journal of Composite Materials, 1997;31:12:1318-1333

[43]   Paris I, Minguet PJ, O'Brien TK, Comparison of Delamination Characterization for IM7/8552 Composite Woven and Tape Laminates, ASTM Special Technical Publication 1436, 2003;372-390

[44] Naik NK, et al, Interlaminar Fracture Characterization for Plain Weave Fabric Composites, Journal of Materials Science, 2002;37:2983-2987

[45] Reeder JR, 3D Mixed-Mode Delamination Fracture Criteria – An Experimentalist's Perspective, American Society for Composites 21st Annual Technical Conference, Sept 2006

[46] Whitcomb JD, Analysis of Instability-Related Growth in a Through-Width Delamination, NASA TM 86301, September 1984

[47] Whitcomb JD, Parametric Analytical Study of Instability-Related Delamination Growth, Composites Science and Technology,1986;25:1:19-48

[48] Jensen HM, Mixed-mode Interface Fracture Criteria, Acta Metallurgica et Materialia,1990;38:12: 2637-2644

[49] Yan XQW, Du SY, Wang D, An Engineering Method of Determining the Delamination Fracture Toughness of Composite Laminates, Engineering Fracture Mechanics,1991; 39:4623-627

[50] Hahn HT, A Mixed-Mode Fracture Criterion for Composite Materials, Composite Technology Review,1983; 5:26-29

[51] Hahn HT, Johannesson T, A Correlation Between Fracture Energy and Fracture Morphology in Mixed-Mode Fracture of Composites, ICM 4,1983;1: 431-438

[52] Greenhalgh ES, Characterisation of Mixed-Mode Delamination Growth in Carbon-Fiber Composites, PhD Thesis, Imperial College of Science, Technology and Medicine, London (UK), 1998

[53] ASTM D5528, Standard Test Method for Mode I Interlaminar Fracture Toughness of Unidirectional Fiber-Reinforced Polymer Matrix Composites

[54] Lee SH, Noguchi J, Kim Y-B, Cheong S-K, Effect of Interleaved Non-Woven Carbon Tissue on Interlaminar Fracture Toughness of Laminated Composites: Part I – Mode II, Journal of Composite Materials,2002;36:18: 2153-2168

[55] ASTM D3039, Standard Test Method for Tensile Properties of Polymer Matrix Composite Materials

[56] Russell AJ, "On the Measurement of Mode II Interlaminar Fracture Energies", DREP Materials Report 82-0, December 1982

[57] Kanninen MF, An Augmented Double Cantilever Beam Model for Studying Crack Propagation and Arrest, International Journal of Fracture,1973;9:1:83-92

[58] Aliyu AA, Daniel IM, Effects of Strain Rate on Delamination Fracture Toughness of Graphite/Epoxy, Delamination and Debonding of Materials, ASTM STP 876, W.S. Johnson, Ed., American Society for Testing and Materials, 1985; 336-348

[59] Carlsson LA, Gillespie JW, Pipes RB, On the Analysis and Design of the End Notched Flexure (ENF) Specimen for Mode II Testing, Journal of Composite Materials,1986; 20: 594-604

[60] Williams JG, The Fracture Mechanics of Delamination Tests, Journal of Strain Analysis,1989;24: 207-214

[61] Wang Y, Williams JG, Corrections for Mode II Fracture Toughness Specimens of Composite Materials, Composites Science and Technology,1992;43:1992

[62] Kinloch AJ, Wang Y, The Mixed-Mode Delamination of Fiber-Composite Materials, Composites Science and Technology, 1992

[63] Moor DR, Pavan A, Williams JG, editors, Fracture Mechanics Testing Methods for Polymers, Adhesives and Composites, Elsevier Science Ltd and ESIS, 2001, ISBN 0 08 043689 7

[64] Stevanovic D, Kalyanasundaram S, Lowe A, On crack-initiation conditions for mode I and mode II delamination testing of composite materials, Composite Science and Technology,2000;60:1879-1887

[65] Wakako A, Nemoto K, Adachi T, Yamaji A, Fracture Toughness for Mixed-mode I/II of Epoxy Resin, Acta Materialia,2005;53:869-875

[66] Moor DR, Pavan A, Williams JG, Fracture Mechanics Testing Methods for Polymers, Adhesives and Composites, Elsevier Science Ltd and ESIS, 2001

[67] Stevanovic D, Kalyanasundaran S, Lowe A, Jar P-YB, Mode I and Mode II delamination properties of glass/vinyl-ester composite toughened by particulate modified interlayers, Composite Science and Technology, 2003;63:1949-1964

[68] O'Brien TK, Composite Interlaminar Shear Fracture Toughness, G_{IIC}: Shear Measurement or Sheer Myth?, ASTM Special Technical Publication, 1998;1330

[69] Hashimoto K, Consideration for Fracture Toughness Evaluation of Mode II Research reports of the Tokuyama Technical College, 2007;31

[70] Richard HA, A Loading Device for the Creation of Mixed-Mode in Fracture Mechanics, International Journal of Fracture,1983;22

[71] ASTM 5045, Standard Test Methods for Plane-Strain Fracture Toughness and Strain Energy Release Rate of Plastic Materials

[72] ASTM D6671, Standard Test Method for Mixed-mode I – Mode II Interlaminar Fracture Toughness of Unidirectional Fiber Reinforced Polymer Matrix Composites

[73] Noury PM, Shenoi RA, Sincliar I, On Mixed-Mode Fracture of PVC Foam, International Journal of Fracture,1998;92:131-151

[74] Rowles C, Mixed-Mode Experimental Study with Richard's Loading Device and Criteria, University of Western Ontario MME 9500 paper, 2011

[75] Zhou X-F, Wagner HD, Nutt SR, Interfacial Properties of Polymer Composites Measured the Push-Out and Fragmentation Tests, Composites Part A: Applied Science and Manufacturing,2001;32:1543-1551

[76] Li Z-F, Grubb DT, Single-Fibre Polymer Composites, Part I Interfacial Shear Strength and Stress Distribution in the Pull-Out Test, Journal of Materials Science,1994;29:189-202

[77] Zhou X-F, Nairn JA, Wagner HD, Fiber-Matrix Adhesion from the Single–Fiber Composite Test: Nucleation of Interfacial Debonding, Composites Part A: Applied Science and Manufacturing,1999;30:1387-1400

[78] Zhou L, Fracture Mechanics Analysis of the Fibre Fragmentation Test, Journal of Composite Materials,1995;29:881-902

[79] Folkes MJ, Kim J-K, Baillie C, Mai Y-W, Wong WK, Determination of Interfacial Shear Strength in Fibre-Reinforced Thermoplastic Composites, Polymer,1987;28:1309-1314

APPENDIX A: Data Interpretation

A.1. Mode I Data Reduction Techniques

ASTM D5528 recommends three data reduction techniques for calculating the Mode I CSERR, each of which are considered equal. These are the Modified Beam Theory (MBT), the Compliance Calibration Method (CCM) and the Modified Compliance Calibration Method (MCCM). Values of CSERR were determined by all three techniques for all mode I data.

It was found that the MBT tended to provide values for CSERR consistent with the values obtained based on the standard beam theory equations. As well, the values obtained with the MBT tended to decrease the scatter of the values compared to the standard beam theory equations. Both the CCM and the MCCM were observed to result in values that were not consistent with the values obtained based on the standard beam theory equations, and tended to increase the scatter in the CSERR values. Therefore all data presented was determined using the MBT data reduction technique.

A.2. Mode I CSERR Calculations

Values to determine the mixed-mode CSERR of the UD and fabric composites were determined through testing per ASTM D6671 - Standard Test Method for Mixed Mode I - Mode II Interlaminar Fracture Toughness of Unidirectional Fiber Reinforced Polymer Matrix Composites. The standard states that all mixed-

mode ratio's can be evaluated by the test method, permitting a single cohesive set of data to be developed. In practice, it was determined that mixed-mode ratio's lower than 20% mode II cannot be evaluated using the mixed-mode fixturing. As the lever position c is increased in value, there is a corresponding decrease in the mode II loading component. However, below approximately 20% mode II loading, the required position for c exceeds the beam length. If the beam length were to be increased beyond the configuration shown in ASTM D6671, pure mode I loading could never be achieved as this would require an infinite value for c.

To perform pure mode I testing, ASTM D6671 requires removal of the loading beam and for the specimen to be mounted directly in the grips without fixturing. This configuration is exactly that provided by ASTM D5528, Standard Test Method for Mode I Interlaminar Fracture Toughness of Unidirectional Fiber-Reinforced Polymer Matrix Composites. Though this is an ASTM recognized test, it is not ASTM D6671, and does not involve the same test set-up as ASTM D6671. The configuration for each test is significantly different. Also, and more importantly, the equations used to determine the CSERR also differ. Specifically, ASTM D5528 calculations include use of the measured displacement values, rather than of the material modulus, and involve selection of one of three data reduction processes, which are not included as part of the ASTM D6671 calculations.

As mentioned, the mode I value for CSERR varies significantly with the data

reduction method selected. Therefore ASTM D6671 does not necessarily permit consistent sets of data to be developed, due to the pure mode I exception. The CSERR curves presented in this research for UD-H, UD-L, PWLT and for 8HHT along the weft yarn dominated ply face suggest that the mode I CSERR values are consistent with the other mixed-mode CSERR values. However, for the 8HHT along the warp yarn dominated ply face, it is possible that the mode I values are higher than would be expected for a linear trend between pure mode I and 40% mode II loading. In summary, this research tends to support that ASTM D6671 does result in a consistent set of data for evaluating CSERR as a function of mixed-mode loading, despite the reliance on for the pure mode I case.

A.3 Mode II CSERR Calculations

Pure mode II testing can be performed both by the End Notched Flexural (ENF) Test and with the fixturing described in ASTM D6671 by setting the loading position, c, to zero. The value for the mode II CSERR can then be determined for each by applying the equations given in ASTM D6671, or by using the equations given for the ENF. The analytical approaches to develop these equations differ. To understand the possible effect of the two different test methods and the different calculation methods, mode II testing was performed by each technique for PWLT and 8HHT. The mode II CSERR was then determined using both calculations methods for the data from both test methods. The variance between test methods and calculation approaches is shown in Table A.3.1. To provide for a consistent set of data, mode II CSERR's presented in this study are the values obtained by testing with the ASTM D6671 fixturing, and

calculated using the ASTM D6671 equations.

Test Method	Calculation Method	% variance	
		PWLT	8HHT
3 point bend test	ENF vs 6671	2	7
ASTM D6671	ENF vs 6671	10	12

Table A.3.1: Summary of the observed variability in calculated values of the mode II CSERR, as a function of test method and calculation method.

A.4. Propagation CSERR vs Initiation CSERR

ASTM D6671 states that propagation CSERR values should be higher than initiation CSERR values. The standard states that this is due to the development of fiber bridging with propagation. In the event that the propagation CSERR values are lower than the initiation CSERR values, the standard suggests that the insert may be too thick. In this case, the ASTM states that specimen pre-cracking can be used. ASTM D6671 recommends that the thickness for the delamination insert is not greater than 13 μ. However, the thinnest commercially available insert was 20 μ.

There was a concern that the insert may not have been adequate to truly induce proper cracking. Therefore an evaluation was conducted into the effect of the insert. Values of the propagation CSERR were compared with those of initiation CSERR for each mode of loading. Increases in propagation CSERR with respect

to initiation CSERR of 9%, 1.7% and 6% were noted for PWLT and 8HHT delaminating along both the warp and weft yarn faces, respectively. This comparison confirmed that the insert was not functionally too thick.

A.5 Propagation CSERR Stability

It was observed that propagation values were not stable with crack length. Initial values for the propagation CSERR were determined for 1 mm of crack growth following the opening mode. Testing was continued and the crack was permitted to continue to grow. Propagation CSERR values were then determined for each additional 1 mm of crack growth. It was observed that typically the propagation CSERR continued to increase slowly with increasing crack length. Figure A.5.1 shows a plot of the propagation CSERR as a function of propagation crack length for a typical specimen. The data is presented for the mode I and mode II loading components of the CSERR and the total CSERR. The effect appears most significant for the mode I component. This implies that an increase in fiber bridging with increasing crack propagation would account for the behaviour. As mentioned however, significant fiber bridging was not observed.
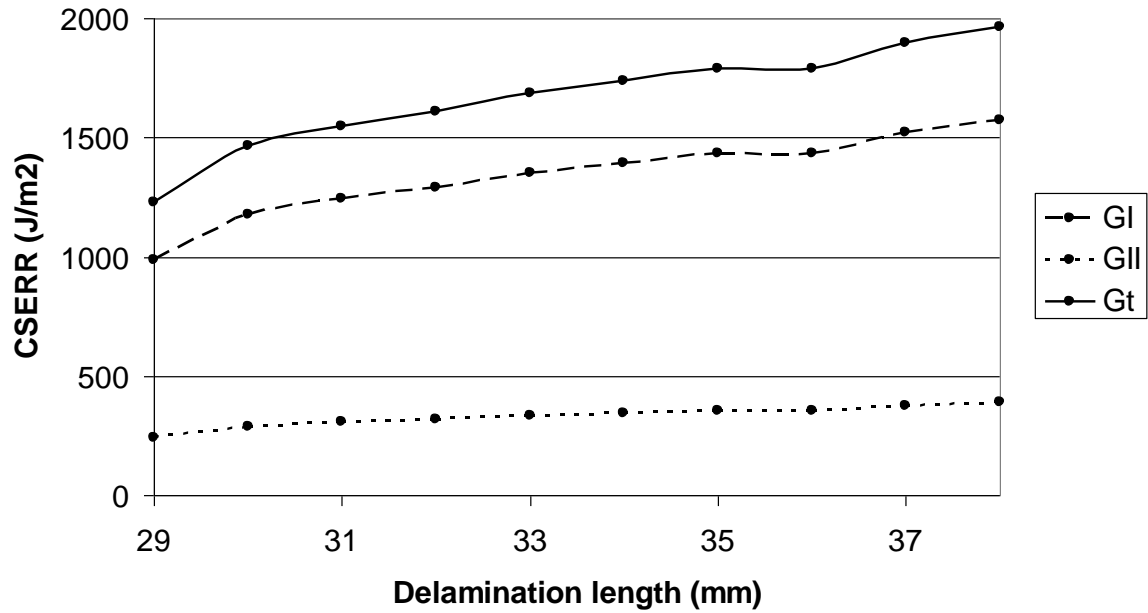
Figure A.5.1: Plot of the initiation CSERR (at 29 mm delamination length) and propagation CSERR values for specimen loaded at 20% mode II loading.

A.6 Mixed-Mode Correction Factors

Expressions for the mode I and mode II CSERR involve a number of correction

factors. The expression are:

$$G_{IC} = \frac{12[P(3c-L) + P_g(3c_g - L)]^2 (a + \chi h)^2}{16bL^2 E_{1f} I} \tag{A.6.1}$$

$$G_{IIC} = \frac{9[P(c+L) + P_g(c_g + L)]^2 (a + 0.42\chi h)^2}{16bL^2 E_{1f} I} \tag{A.6.2}$$

Where correction factors are E_{1f} (bending elastic modulus of the laminate in a

fiber direction), C_{sys} (compliance of the loading system), χ_c (crack length

correction parameter for crack tip rotation), Γ_c (transverse modulus correction parameter), C_{cal} (calibration specimen compliance), P_g (total weight of the lever and attached loading apparatus), c_g (distance from the center of gravity to the center roller, changing with lever load position); each is defined below:

$$E_{1f} = \frac{8(a_0 + \chi_C h)^3 (3c - L)^2 + [6(a_0 + 0.43\chi_C h)^3 + 3L^3)(c + L)^2}{16bL^2 bh^3 \left(\frac{1}{m} - C_{sys}\right)} \tag{A.6.3}$$

$$\chi_C = \sqrt{\frac{E_{11}}{11G_{13}}\left(3 - 2\left(\frac{\Gamma_C}{1} + \Gamma_C\right)^2\right)} \tag{A.6.4}$$

$$\Gamma_C = 1.18\left(\frac{\sqrt{E_{11}E_{22}}}{G_{13}}\right) \tag{A.6.5}$$

$$C_{sys} = \frac{1}{m_{cal}} - C_{cal} \tag{A.6.6}$$

$$C_{cal} = \frac{2L(c + L)^2}{E_{cal}b_{cal}t^3} \tag{A.6.7}$$

In practice, the correction factors were found to have minimal effect on the calculated values of the CSERR. Due to the relatively low loads applied to the specimens (1-2 kN) in comparison to the large load frame used (500 kN rated capacity), the machine compliance was negligible. Similarly, due to the low

weight of the fixturing compared to the applied loads (typically less than 3%), the lever weight corrections also had negligible effect on the calculated values for CSERR. An example of the CSERR calculated with and without correction factors for a tested specimen of PWLT at 80% mode II loading is given in Table A.6.1. The average effect on the value of the CSERR for all crack stages is approximately 0.9%.

| Crack Formation Stage	CSERR from simple beam theory (J/m^2)	CSERR with all corrections applied (J/m^2)	% variation
Non-Linear	559	571	2.1%
Initiation	634	644	1.6%
Growth	861	869	0.9%
Opening	904	911	0.8%
Propagation	927	933	0.6%
Propagation	1011	1013	0.2%
Propagation	1080	1078	-0.2%

Table A.6.1: Example of effect on value of CSERR by including all correction factors.

A.7 Calculating CSERR

As mentioned in Section 5.4.1, there are successive stages of fracture evolution,

referred to as the non-linear, visual, growth, opening and propagation stages. The non-linear stage corresponds to the non-linear transition; the visual stage corresponds to the appearance of visible crack formation (micro-cracking and coalescence); the growth stage corresponds to visible growth of the crack that does not involve opening of the crack; the opening stage corresponds to the apparent opening of the crack and coinciding with the point of maximum loading; the propagation stage corresponds to crack propagation following the point of maximum loading. The approximate occurrence of each stage is shown in Figure 5.4.3 for a typical mixed-mode bend test load-displacement curve.

The CSERR curves as a function of mode mixture presented in Figures 5.4.4 through 5.4.6 are for the opening stage, as mentioned in Section 5.4.3. Shapes of the relationship for CSERR with mode mixture are not consistent for the various stages. As well, values of the CSERR associated with each stage can vary significant. This is illustrated in Figures A.7.1 through A.7.5 by showing the non-linear, visual, growth, opening and propagation CSERR curves with mode mixture for 8HHT along the warp yarn face. Note that no values are available for pure mode II loading for the visual and propagation values as crack growth under pure mode II is unstable. Trendlines shown are for 2nd order polynomial fits.
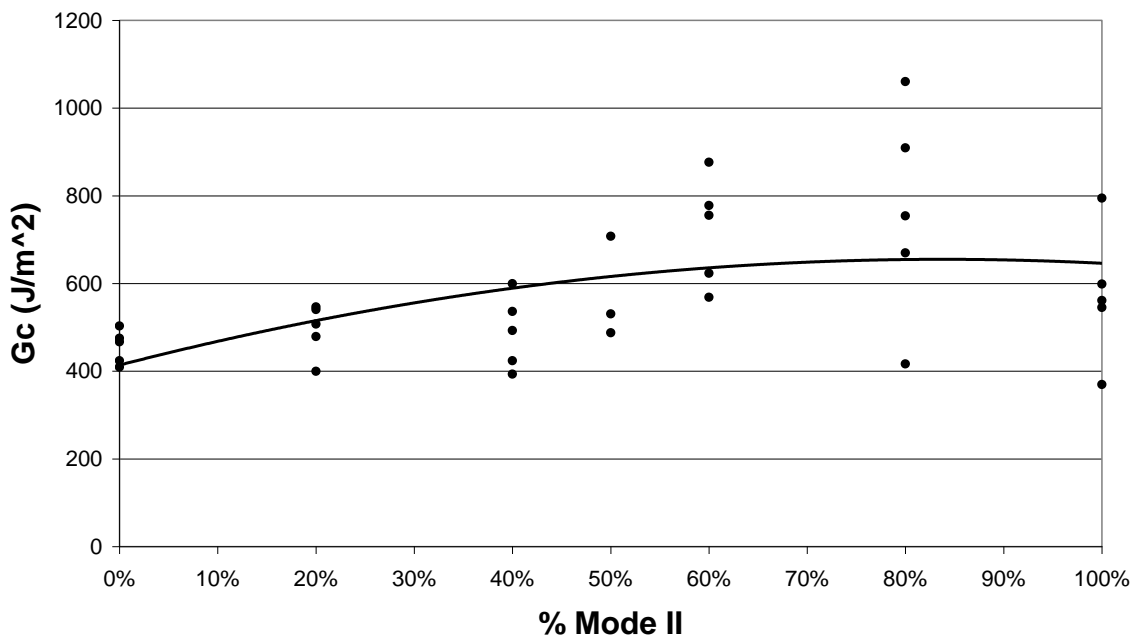
Figures A.7.1: Plot of the Non-linear CSERR with Mode Mixture for 8HHT along the Warp Yarn Face.
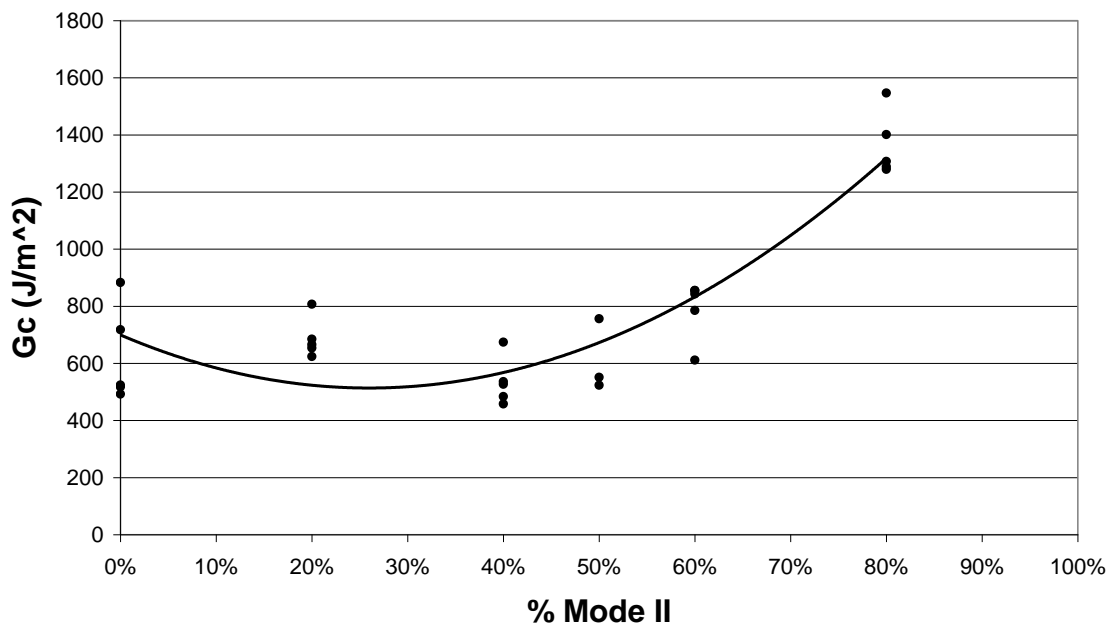
Figures A.7.2: Plot of the Visual CSERR with Mode Mixture for 8HHT along the Warp Yarn Face.
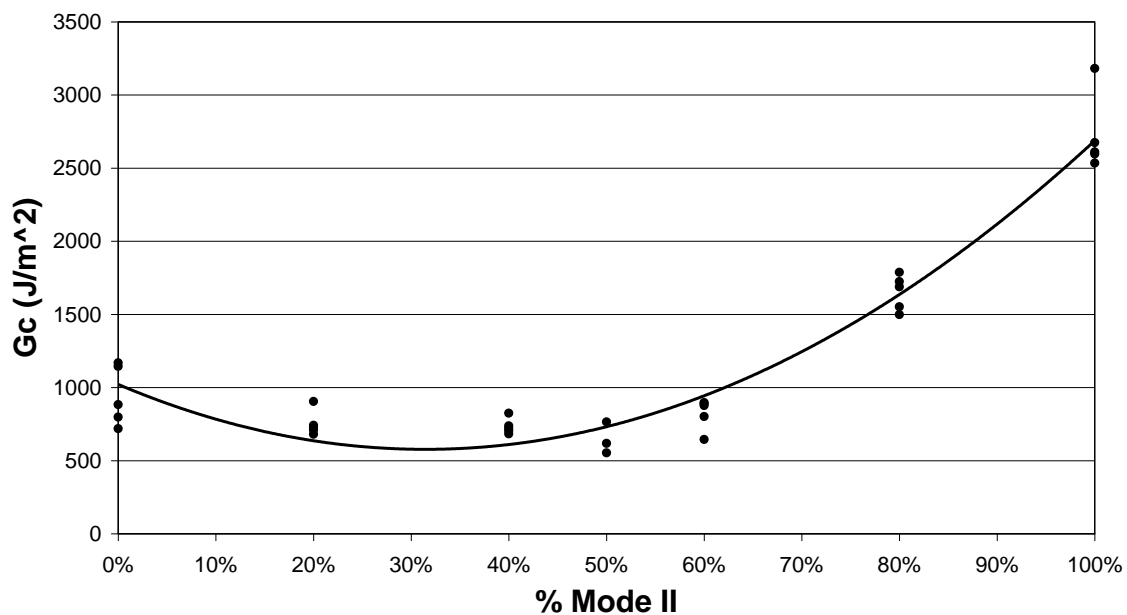
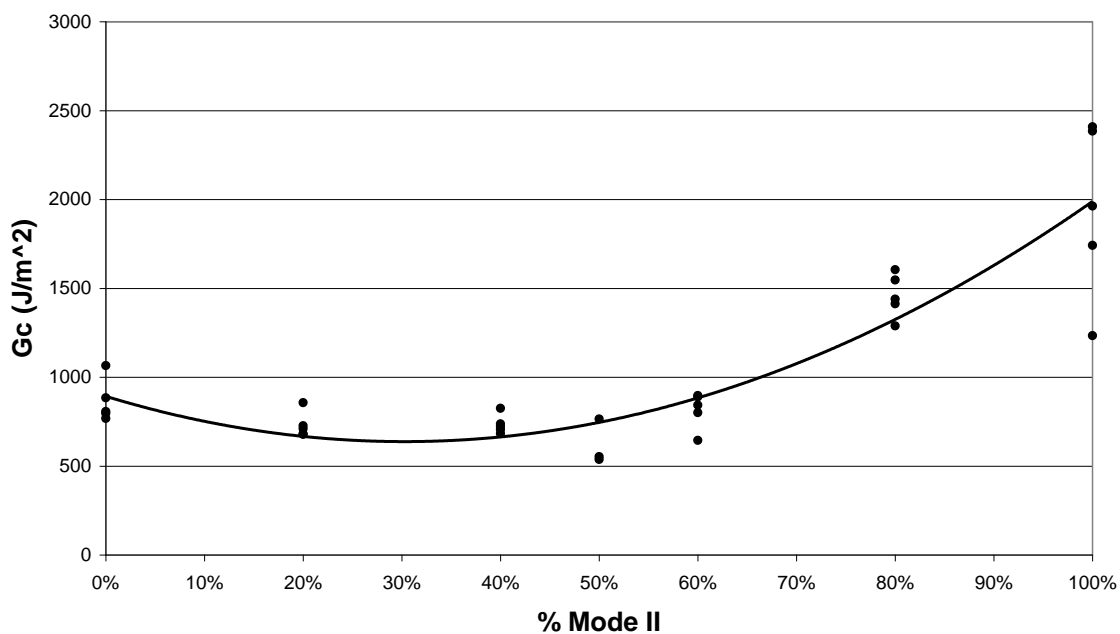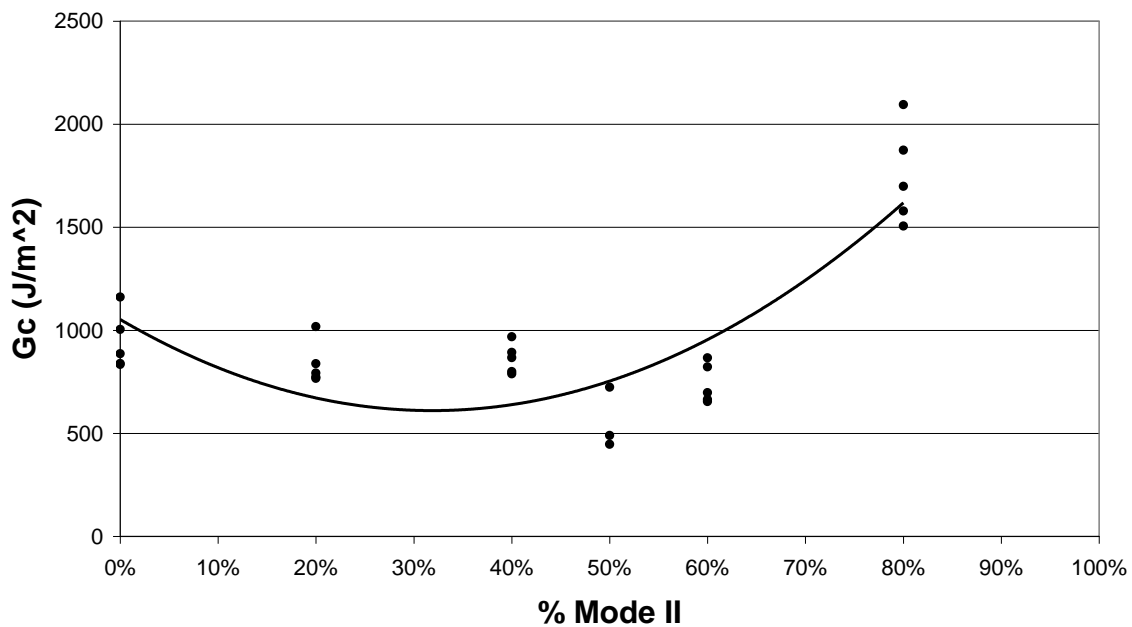Figures A.7.3: Plot of the Growth CSERR with Mode Mixture for 8HHT along the Warp Yarn Face.

Figures A.7.4: Plot of the Opening CSERR with Mode Mixture for 8HHT along the Warp Yarn Face.

Figures A.7.5: Plot of the Propagation CSERR with Mode Mixture for 8HHT along the Warp Yarn Face.

APPENDIX B: Mixed-Mode Plastic Zone Maple Calculations

> *restart*;
> $eq1 := (A - B)^2 + (B - C)^2 + (C - A)^2 - 2 \cdot 1^2 = 0;$

$eq1 := (A - B)^2 + (B - C)^2 + (C - A)^2 - 2 = 0$

> $eq2 := A = \dfrac{(X + Y)}{2} + \text{sqrt}\left(\left(\dfrac{(X - Y)}{2}\right)^2 + Z^2\right);$

$eq2 := A = \dfrac{1}{2} X + \dfrac{1}{2} Y + \dfrac{1}{2} \sqrt{X^2 - 2 X Y + Y^2 + 4 Z^2}$

> $eq3 := B = \dfrac{(X + Y)}{2} - \text{sqrt}\left(\left(\dfrac{(X - Y)}{2}\right)^2 + Z^2\right);$

$eq3 := B = \dfrac{1}{2} X + \dfrac{1}{2} Y - \dfrac{1}{2} \sqrt{X^2 - 2 X Y + Y^2 + 4 Z^2}$

> $eq4 := C = 0.3 \cdot (X + Y);$

$eq4 := C = 0.3 X + 0.3 Y$

> $eq5 := X = (1 - M)^{0.5} \cdot \dfrac{\text{sqrt}(1)}{\text{sqrt}(2 \cdot R)} \cdot \cos\left(\dfrac{\theta}{2}\right) \cdot \left(1 - \sin\left(\dfrac{\theta}{2}\right)\right.$
$\left. \cdot \sin\left(\dfrac{3 \cdot \theta}{2}\right)\right) - (M)^{0.5} \cdot \dfrac{\text{sqrt}(1)}{\text{sqrt}(2 \cdot R)} \cdot \sin\left(\dfrac{\theta}{2}\right) \cdot \left(2 + \cos\left(\dfrac{\theta}{2}\right)\right.$
$\left. \cdot \cos\left(\dfrac{3 \cdot \theta}{2}\right)\right);$

$eq5 := X$
$$= \dfrac{1}{2} \dfrac{(1 - M)^{0.5} \cos\left(\dfrac{1}{2} \theta\right) \left(1 - \sin\left(\dfrac{1}{2} \theta\right) \sin\left(\dfrac{3}{2} \theta\right)\right) \sqrt{2}}{\sqrt{R}}$$
$$- \dfrac{1}{2} \dfrac{M^{0.5} \sin\left(\dfrac{1}{2} \theta\right) \left(2 + \cos\left(\dfrac{1}{2} \theta\right) \cos\left(\dfrac{3}{2} \theta\right)\right) \sqrt{2}}{\sqrt{R}}$$

> $eq6 := Y = (1 - M)^{0.5} \cdot \dfrac{\text{sqrt}(1)}{\text{sqrt}(2 \cdot R)} \cdot \cos\left(\dfrac{\theta}{2}\right) \cdot \left(1 + \sin\left(\dfrac{\theta}{2}\right)\right.$
$\left. \cdot \sin\left(\dfrac{3 \cdot \theta}{2}\right)\right) + (M)^{0.5} \cdot \dfrac{\text{sqrt}(1)}{\text{sqrt}(2 \cdot R)} \cdot \sin\left(\dfrac{\theta}{2}\right) \cdot \cos\left(\dfrac{\theta}{2}\right)$
$\left. \cdot \cos\left(\dfrac{3 \cdot \theta}{2}\right);$

$eq6 := Y$

$$= \frac{1}{2} \frac{(1-M)^{0.5} \cos\left(\frac{1}{2}\theta\right) \left(1 + \sin\left(\frac{1}{2}\theta\right) \sin\left(\frac{3}{2}\theta\right)\right) \sqrt{2}}{\sqrt{R}}$$

$$+ \frac{1}{2} \frac{M^{0.5} \sin\left(\frac{1}{2}\theta\right) \cos\left(\frac{1}{2}\theta\right) \cos\left(\frac{3}{2}\theta\right) \sqrt{2}}{\sqrt{R}}$$

> $eq7 := Z = (1-M)^{0.5} \cdot \frac{\text{sqrt}(1)}{\text{sqrt}(2 \cdot R)} \cdot \sin\left(\frac{\theta}{2}\right) \cdot \cos\left(\frac{\theta}{2}\right) \cdot \cos\left(\frac{3 \cdot \theta}{2}\right)$
> $\qquad + (M)^{0.5} \cdot \frac{\text{sqrt}(1)}{\text{sqrt}(2 \cdot R)} \cdot \cos\left(\frac{\theta}{2}\right) \cdot \left(1 - \sin\left(\frac{\theta}{2}\right) \cdot \sin\left(\frac{3 \cdot \theta}{2}\right)\right);$

$eq7 := Z = \frac{1}{2} \frac{(1-M)^{0.5} \sin\left(\frac{1}{2}\theta\right) \cos\left(\frac{1}{2}\theta\right) \cos\left(\frac{3}{2}\theta\right) \sqrt{2}}{\sqrt{R}}$

$$+ \frac{1}{2} \frac{M^{0.5} \cos\left(\frac{1}{2}\theta\right) \left(1 - \sin\left(\frac{1}{2}\theta\right) \sin\left(\frac{3}{2}\theta\right)\right) \sqrt{2}}{\sqrt{R}}$$

> $eq1$

$(A-B)^2 + (B-C)^2 + (C-A)^2 - 2 = 0$

> $eq8 := subs\left(\left\{A = \frac{(X+Y)}{2} + \text{sqrt}\left(\left(\frac{(X-Y)}{2}\right)^2 + Z^2\right), B\right.\right.$
> $\qquad = \frac{(X+Y)}{2} - \text{sqrt}\left(\left(\frac{(X-Y)}{2}\right)^2 + Z^2\right), C = 0.3 \cdot (X+Y)\right\},$
> $\qquad eq1\Big);$

$eq8 := X^2 - 2XY + Y^2 + 4Z^2 + \left(0.2000000000X\right.$

$$\left. + 0.2000000000Y - \frac{1}{2}\sqrt{X^2 - 2XY + Y^2 + 4Z^2}\right)^2 + \Big($$

$$-0.2000000000X - 0.2000000000Y$$

$$\left. - \frac{1}{2}\sqrt{X^2 - 2XY + Y^2 + 4Z^2}\right)^2 - 2 = 0$$

>

$$
\begin{aligned}
eq9 := subs\bigg(\bigg\{ & X = (1 - M)^{0.5} \cdot \frac{\mathrm{sqrt}(1)}{\mathrm{sqrt}(2 \cdot R)} \cdot \cos\left(\frac{\theta}{2}\right) \cdot \left(1 - \sin\left(\frac{\theta}{2}\right)\right. \\
& \left. \cdot \sin\left(\frac{3 \cdot \theta}{2}\right)\right) - (M)^{0.5} \cdot \frac{\mathrm{sqrt}(1)}{\mathrm{sqrt}(2 \cdot R)} \cdot \sin\left(\frac{\theta}{2}\right) \cdot \left(2 + \cos\left(\frac{\theta}{2}\right)\right. \\
& \left. \cdot \cos\left(\frac{3 \cdot \theta}{2}\right)\right), Y = (1 - M)^{0.5} \cdot \frac{\mathrm{sqrt}(1)}{\mathrm{sqrt}(2 \cdot R)} \cdot \cos\left(\frac{\theta}{2}\right) \cdot \bigg(1 \\
& + \sin\left(\frac{\theta}{2}\right) \cdot \sin\left(\frac{3 \cdot \theta}{2}\right)\bigg) + (M)^{0.5} \cdot \frac{\mathrm{sqrt}(1)}{\mathrm{sqrt}(2 \cdot R)} \cdot \sin\left(\frac{\theta}{2}\right) \\
& \cdot \cos\left(\frac{\theta}{2}\right) \cdot \cos\left(\frac{3 \cdot \theta}{2}\right), Z = (1 - M)^{0.5} \cdot \frac{\mathrm{sqrt}(1)}{\mathrm{sqrt}(2 \cdot R)} \cdot \sin\left(\frac{\theta}{2}\right) \\
& \cdot \cos\left(\frac{\theta}{2}\right) \cdot \cos\left(\frac{3 \cdot \theta}{2}\right) + (M)^{0.5} \cdot \frac{\mathrm{sqrt}(1)}{\mathrm{sqrt}(2 \cdot R)} \cdot \cos\left(\frac{\theta}{2}\right) \cdot \bigg(1 \\
& - \sin\left(\frac{\theta}{2}\right) \cdot \sin\left(\frac{3 \cdot \theta}{2}\right)\bigg)\bigg\}, eq8 \bigg);
\end{aligned}
$$

> $R_{solve} := solve(eq9, R);$

$R_{solve} :=$

$$
2.840000000\sqrt{1. - 1.M} \, \cos(0.50000000000\theta) \, \sqrt{M}
$$

$$
\sin(0.50000000000\theta)
$$

$$
- 6.\sqrt{1. - 1.M} \, \cos(0.50000000000\theta) \, \sin(0.50000000000\theta)^3
$$

$$
\sqrt{M} - 5.840000000M \sin(0.50000000000\theta)^2
$$

$$
+ 6.M \sin(0.50000000000\theta)^4
$$

$$
+ 1.420000000\sin(0.50000000000\theta)^2 + 0.08000000000
$$

$$
+ 1.420000000M - 1.500000000\sin(0.50000000000\theta)^4
$$

>

CURRICULUM VITAE

THOMAS BRUCE

EMPLOYMENT EXPERIENCE

Senior Survivability Engineer
General Dynamics Land Systems –Canada, April 2002 – Present

- Project lead for advanced proto-type ground combat vehicle development
- Lead test engineer for mine blast testing of R&D concept vehicles

Area Manager, Manufacturing
General Motors Defense, April 1996 – April 2002

- Manage manufacturing operations related to armoured vehicle build, including cutting, forming, welding, machining and radiography departments

Manufacturing Engineer
General Motors Defense, April 1994 - April 1996

- Evaluate and resolve manufacturing concerns

EDUCATION

Professional Engineer
Professional Engineers of Ontario, 1996

- Registered as a Professional Engineer within the province of Ontario
- Registration number 90460627

Masters of Engineering Science, Materials
University of Western Ontario, 1991-1993

Conduct research on the production of amorphous carbon films and the characterisation of their interfacial chemistry to evaluate the mechanism of film adhesion

Bachelor of Engineering, Metallurgy
Technical University of Nova Scotia, 1983-1989

PUBLICATIONS

1. E-glass and Epoxy Resin-Fiber Interfacial Shear Strength, SAMPE conference proceedings, 2007

2. Mixed-mode Testing of Woven Fabric Polymer Composites, SAMPE conference proceedings, 2007

3. Characterisation of Low Energy Ion Deposited Diamond-like Films, University of Western Ontario, 1994

4. Adhesion of Diamond-like Films to ZnS, University of Western Ontario, 1993

5. Interfacial Interactions of Ion Beam Deposited Diamond-like Carbon Films on Germanium and Zinc Sulfide, University of Western Ontario, 1992

6. Metallographic Preparation and Microstructural Characterisation of Terfenol-D, Defence Research Establishment report No. DL/92/6, 1991

7. Field Metallography for Military Applications, Defence Research Establishment report No. DL/92/2, 1990

8. Replication of Martensitic Microstructures for Naval Applications, Defence Research Establishment report No. DL/91/3, 1990

9. Published Oral Presentation given at the 4th Annual International CRAD Meeting on Submarine Pressure Hull Fabrication and Inspection, 1989

10. Metallurgical Evaluation of an HY 80 Steel Weldment used by the TTCPPTP1 Operating Assignment on Fracture Control for Naval Structures, Defence Research Establishment report No. DL/91/1, 1989